MOLECULES IN MAGNETIC FIELDS

By

TODD ALAN KEITH, M.Sc

A Thesis

Submitted to the School of Graduate Studies

in Partial Fulfilment of the Requirements

for the Degree

Doctor of Philosophy

McMaster University

MOLECULES IN MAGNETIC FIELDS

DOCTOR OF PHILOSOPHY (1993)
(Chemistry)

McMASTER UNIVERSITY
Hamilton, Ontario, Canada

TITLE: Molecules in Magnetic Fields

AUTHOR: Todd Alan Keith, M.Sc. (University of Minnesota)

SUPERVISOR: Professor R.F.W. Bader

NUMBER OF PAGES: xiii, 220 (8)

ABSTRACT

This thesis is primarily an investigation of those properties of closed-shell molecules which result from interaction with an external magnetic field. Throughout, emphasis is placed on the observable, magnetically induced current density distributions. The insistence that measurable magnetic response properties such as the NMR shielding tensors and diamagnetic susceptibility tensors be *interpreted*, physically, in terms of the corresponding induced current distributions has led to new, and more accurate, methods of *predicting* these properties. These methods are described in Chapter 1. The fundamental features of the induced vector current fields are investigated in Chapter 2 through a formal topological analysis of a divergenceless three-dimensional vector field with magnetic symmetry together with actual analyses of several induced molecular current distributions. In chapter 3 the experimentally measurable molecular magnetic susceptibility and nuclear magnetic shielding tensors are analyzed in terms of the corresponding tensors for atoms in molecules to address the physical basis for the empirical models which have been developed to explain experimental results. An atomic magnetic response tensor is entirely determined by the charge and induced current density distributions within the atom and on its surface. The physical significance of the atoms of theory is reiterated through the agreement of the theoretical group magnetic susceptibilities in the hydrocarbons with the empirically defined group increments of Pascal. In chapter 4, advances in methods of calculating properties of atoms in molecules are described.

ACKNOWLEDGEMENTS

About four years ago I became aware of the unique research being carried out in Professor R.F.W. Bader's laboratory. I thank Mr. James T. Cheeseman and Dr. James R. Cheeseman for their scientific awareness, which made mine possible. After reading, and rereading, many of the publications from Professor Bader's laboratory I was convinced that a fundamental *physical* theory of *chemistry* was being discovered, and I wanted to contribute. With the help of many people I have been able to do so for the past two and a half years. I thank the fine people of McMaster University and Ontario for the financial support which made my stay at McMaster possible. I thank the members of Professor Bader's research group, past and present, for their friendship, advice and most of all, tolerance. In chronological order they are: Dr. J.R. Cheeseman, Dr. K.E. Laidig, Mr. P.F. Zhou, Mr. P.J. Krug, Mr. D.A. Legare, Dr. P.L.A. Popelier, Dr. I. Bytheway and Dr. R.G.A. Bone. I am particularly grateful to Keith Laidig for getting me started, and to Jim Cheeseman and Joanne Hiscocks, for keeping me going. I thank Dr. R.D. Amos and the other members of the Cambridge University theory group for CADPAC, without which much of the progress I have made would have been more difficult.

Above all, I thank Professor R.F.W. Bader. It is not possible to adequately express here all that he has done for me, and for science, so I will not try. The future will speak.

To my Mom and Dad

TABLE OF CONTENTS

Chapter 2

Analysis of the Magnetic Field Induced Current Density Distributions

Chapter 3

Magnetic Susceptibility and Nuclear Magnetic Shielding Tensors

Chapter 4

Computational Improvements for the Theory of Atoms in Molecules

Appendix

LIST OF FIGURES

LIST OF TABLES

INTRODUCTION

In this work the fundamental phenomena associated with the interaction of closed-shell molecules with external magnetic fields are investigated, namely, diamagnetism, nuclear magnetic resonance and electronic current induction. Throughout, emphasis is placed on the observable, magnetically induced current density distributions as a means for both understanding and predicting magnetic phenomena. The requirement that measurable magnetic response properties such as the NMR shielding tensors and diamagnetic susceptibility tensors be *interpreted*, physically, in terms of the corresponding induced current distributions has led to new, and more accurate, methods of *predicting* these properties. In chapter 1, these methods are described, and they are perhaps the most important result of this work, for without accurate observation and prediction there can be no understanding. The new methods employ multiple or continuous gauge transformations in order to calculate the induced currents and the molecular properties they determine from conventional coupled-perturbed Hartree-Fock wavefunctions. They are expected to be relatively simple to generalize beyond Hartree-Fock.

The fundamental features of magnetically induced vector current fields are investigated in Chapter 2 through a formal topological analysis of a divergenceless three-dimensional vector field with magnetic symmetry, together with analyses of several induced molecular current distributions made available by the methods described in Chapter 1. The results of chapter 2 demonstrate that, unlike free atoms, an induced current distribution in a molecule is a fully three-dimensional vector field whose associated trajectories can exhibit four basic flow patterns, all of which are commonly observed. The topological analysis has also

brought to the fore the vorticity of the induced current, its curl vector field, which exhibits a shell structure in striking analogy with a property of the electron density distribution, and which may lead to better understanding and prediction of the induced current flow in terms of other molecular properties.

In chapter 3 molecular magnetic susceptibility and nuclear magnetic shielding tensors are analyzed in terms of the corresponding tensors of atoms in molecules in order to address the physical basis for the empirical models which have been developed to explain experimental observations. An atomic magnetic response tensor is entirely determined by the charge and induced current density distributions within the atom and on its surface. The physical significance of the atoms of theory in interpreting and predicting magnetic phenomena is explicitly demonstrated through the agreement of the theoretical isotropic group magnetic susceptibilities in the normal hydrocarbons with the uniquely defined, empirical group increments of Pascal. The induced current distributions in an atom, and hence its magnetic properties, are shown to be transferable between molecules in a manner paralleling the transferability of the electron density distribution. With the exception of those for protons, nuclear magnetic shielding tensors are confirmed to be essentially atomic properties. Much of the original work presented in this work either implicitly or explicitly employs the theory of atoms in molecules, a theory which is generally well known in the chemical community and is well documented in the literature. However, for those readers not familiar with the theory of atoms in molecules, those aspects of it which are particularly relevant to the work presented here are summarized in Chapter 4, which describes computational improvements that have been made in applying the theory, as well as in the Appendix.

1. CALCULATION OF MAGNETIC RESPONSE PROPERTIES

1-1 Introduction

In this first chapter, new approaches to solving the long-standing "gauge problem" in ab-initio magnetic response calculations are presented. In particular, straightforward and relatively accurate methods for calculating the magnetically induced first-order current density distributions in molecules as well as the observable properties determined by these distributions are described. The methods employ gauge transformations in real space in order to calculate the magnetic properties from conventional coupled-perturbed Hartree Fock (CPHF)[1] wavefunctions. The methods are judged to be superior to conventional methods based on the relatively good agreement of the calculated magnetic susceptibility and nuclear magnetic shielding tensors with corresponding experimental results as well as the relatively high degree of satisfaction of the continuity equation for the current density distribution.

The first method, IGAIM (Individual Gauges for Atoms In Molecules),[2] takes advantage of the theory of atoms in molecules[3] by calculating the current density distribution throughout the space of the molecule - an atom at a time. In the IGAIM method, conventional CPHF calculations for the three components of the angular momentum and linear momentum perturbations are first performed, and then the induced current distributions within each atom of the molecule are calculated by performing a gauge transformation which shifts the gauge origin of the magnetic vector potential to the atom's nucleus, in analogy with the simple free atom calculation. The molecular magnetic response tensors are calculated from the atomic current distributions as a sum of atomic contributions.

The other methods[4] are extensions of the IGAIM method to the limit of a *continuous*, real space gauge transformation. In these methods a gauge transformation *function* is chosen as a continuous parametric function of real space, one which guarantees the symmetry properties of the current distribution and effectively employs a different gauge origin for each point in real space in order to calculate the current distributions and the dependent magnetic response tensors. The continuous gauge transformation methods, like IGAIM, use conventional CPHF first-order wavefunctions, but unlike IGAIM they are easily implemented into existing conventional CPHF programs, such as CADPAC.[5] In addition to their relatively good accuracy in predicting molecular magnetic properties, the continuous gauge transformation methods possess an important advantage over the IGAIM method and any other methods which are commonly used in that they not only allow for the more efficient calculation of the molecular properties, but they also make readily

possible the relatively accurate determination, display and analysis of the full three-dimensional molecular induced current distributions. Thereby, these methods enable one to study the topology of the $\mathbf{J}^{(1)}(\mathbf{r})$ distribution[6] and its relation to other molecular magn tic properties.[7,8]

1-2 The CPHF Induced Current Density

Invoking the non-relativistic and Born-Oppenheimer approximations, the first-order electronic current density induced in a closed-shell molecule with n electrons by a static and uniform perturbing magnetic field **B** is expressed in terms of the ground state wavefunction $\psi^{(0)}$ and its corresponding first-order correction $\psi^{(1)}$ as[1,9]

$$\mathbf{J}^{(1)}(\mathbf{r}) = -(en/m)\int d\tau' \left\{ \psi^{(0)*}\hat{\mathbf{p}}\psi^{(1)} + \psi^{(1)*}\hat{\mathbf{p}}\psi^{(0)} \right\} - (e^2/mc)\mathbf{A}(\mathbf{r})\rho^{(0)}(\mathbf{r}) \qquad (1)$$

where $\rho^{(0)}(\mathbf{r})$ is the unperturbed electron density, $\hat{\mathbf{p}}$ is the linear momentum operator, $\mathbf{A}(\mathbf{r})$ is a vector potential (assumed first-order in B) describing **B** through Maxwell's equation, $\nabla\cdot\mathbf{B} = 0 \rightarrow \mathbf{B}=\nabla\times\mathbf{A}(\mathbf{r})$, and the integration is over the spins of all n electrons and the spatial coordinates of (n - 1) electrons.

Within the CPHF framework[1] the zero-order function $\psi^{(0)}$ is a Slater determinant of n/2 doubly occupied molecular orbitals $\phi_i^{(0)}$ while the function $\psi^{(1)}$ is a Slater determinant composed of the first-order corrections, $\phi_i^{(1)}$, to these orbitals. From eqn. (1), the CPHF first-order induced current density is given by[1]

$$\mathbf{J}^{(1)}(\mathbf{r}) = -(2e/m)\sum_{i=1}^{n/2}\left\{\phi_i^{(0)*}\hat{\mathbf{p}}\phi_i^{(1)} + \phi_i^{(1)*}\hat{\mathbf{p}}\phi_i^{(0)} \right\} - (e^2/mc)\mathbf{A}(\mathbf{r})\rho^{(0)}(\mathbf{r})$$

$$= \mathbf{J}_p^{(1)}(\mathbf{r}) + \mathbf{J}_d^{(1)}(\mathbf{r}) \qquad (2)$$

where $\rho^{(0)}(\mathbf{r})$ is now the ground state Hartree-Fock electron density. The part of $\mathbf{J}^{(1)}(\mathbf{r})$ in eqn. (2) depending on both $\phi_i^{(0)}$ and $\phi_i^{(1)}$ is normally called the "paramagnetic" contribution, $\mathbf{J}_p^{(1)}(\mathbf{r})$, while the part which depends on $\rho^{(0)}(\mathbf{r})$ is called the "diamagnetic" contribution $\mathbf{J}_d^{(1)}(\mathbf{r})$.

Using the formalism first described by Lipscomb et al,[1] the $\phi_i^{(1)}$ can be determined as an expansion in the basis of unperturbed Hartree-Fock virtual molecular orbitals $\phi_p^{(0)}$, as in eqns. (3)

$$\phi_i^{(1)} = \sum_{p=n/2+1} C_{pi}^{(1)} \phi_p^{(0)} \qquad (3)$$

where the expansion coefficients $C_{pi}^{(1)}$ are the solutions to the set of coupled equations, the first-order CPHF equations, given in eqns. (4)

$$(\varepsilon_p^{(0)} - \varepsilon_i^{(0)})C_{pi}^{(1)} + \langle\phi_p^{(0)}|\hat{H}^{(1)}|\phi_i^{(0)}\rangle +$$

$$\sum_{j=1}^{n/2} \sum_{q=n/2+1} [(qi|pj)-(ji|pq)]C_{qj}^{(1)} = 0 \qquad (4)$$

The operator $\hat{H}^{(1)}$ in these equations is the imaginary first-order correction to the one-electron part $\hat{H}$ of the Fock operator $\hat{F}$ due to the **B** perturbation while the quantities $\varepsilon_p^{(0)}$ and $\varepsilon_i^{(0)}$ are the orbital energies of the p^{th} virtual molecular orbital and i^{th} occupied molecular orbital, respectively. The quantities (qi|pj) and (ji|pq) in eqn. (4) represent, in the conventional notation, two electron integrals over the corresponding molecular orbitals.

The first-order CPHF equations given in eqns. (4) follow from the requirement that the *canonical* Hartree-Fock equations, $\hat{F}\phi_i=\varepsilon_i\phi_i$ (i=1,...,n/2),

be satisfied to first-order in the B perturbation, as in eqns. (5)

$$\hat{F}^{(0)}\phi_i^{(1)} + \hat{F}^{(1)}\phi_i^{(0)} = \varepsilon_i^{(0)}\phi_i^{(1)} + \varepsilon_i^{(1)}\phi_i^{(0)} \qquad (5)$$

while maintaining the orthonormality of the n/2 occupied orbitals through second-order.

When the vector potential is chosen as $\mathbf{A}(\mathbf{r})=(1/2)\mathbf{B}\times\mathbf{r}$ to describe the magnetic field then

$$\hat{H}^{(1)} = (e/2mc)\mathbf{B}\cdot\mathbf{r}\times\hat{\mathbf{p}} = (e/2mc)\mathbf{B}\cdot\hat{\mathbf{L}} \qquad (6)$$

where $\hat{\mathbf{L}}$ is the angular momentum operator with respect to the arbitrary origin of $\mathbf{r}$.

1-3 Gauge Transformations

As is well known, the vector potential $\mathbf{A}(\mathbf{r})$ is not unique. The addition of the gradient of any scalar function $f(\mathbf{r})$ to $\mathbf{A}(\mathbf{r})$, a gauge transformation, leaves the physical field B unchanged, since $\nabla\times\nabla f(\mathbf{r})=0$. Since observable magnetic response properties such as the induced current density are determined by interactions with B, they should be invariant to any gauge transformation of $\mathbf{A}(\mathbf{r})$.

The exact CPHF first-order current density is invariant to gauge transformations of $\mathbf{A}(\mathbf{r})$,[9] the simplest example of which is a shift in the origin $\mathbf{r}_0$ of the electronic position vector $\mathbf{r}$ by an amount $\mathbf{d}$ such that $\mathbf{r}' = \mathbf{r} - \mathbf{d}$. For such a gauge transformation $f(\mathbf{r}) = -(1/2)(\mathbf{B}\times\mathbf{d})\cdot\mathbf{r}$. The origin $\mathbf{r}_0$ will hereafter be called the *gauge origin*. It is immediately evident from eqn. (6) that such a gauge transformation changes $\hat{H}^{(1)}$ into

$$\hat{H}^{(1)\prime} = \hat{H}^{(1)} + \delta\hat{H}^{(1)} = \hat{H}^{(1)} - (e/2mc)\mathbf{B}\cdot\mathbf{d}\times\hat{\mathbf{p}} \qquad (7)$$

and the first-order corrections to the orbitals into

$$\phi_i^{(1)'} = \phi_i^{(1)} + \delta\phi_i^{(1)} = \phi_i^{(1)} + \sum_{p=n/2+1} \delta C_{pi}^{(1)} \phi_p^{(0)} \qquad (8)$$

with the changes in the first-order coefficients $\delta C_{pi}^{(1)}$ being determined by the set of coupled equations given in eqns. (9),

$$(\varepsilon_p^{(0)} - \varepsilon_i^{(0)}) \delta C_{pi}^{(1)} + \langle \phi_p^{(0)} | \delta \hat{H}^{(1)} | \phi_i^{(0)} \rangle +$$

$$\sum_{j=1}^{n/2} \sum_{q=n/2+1} [(qi|pj) - (ji|pq)] \delta C_{qj}^{(1)} = 0 \qquad (9)$$

These equations follow from substituting the expressions for the $\phi_i^{(1)'}$ and the transformed perturbation $\hat{H}^{(1)'}$ into eqns. (4) and the fact that the set of $\phi_i^{(1)}$ satisfy eqns. (4) for $\hat{H}^{(1)}$.

Because the shift in gauge origin by **d** is the same for every orbital, the stationary first-order CPHF wavefunction for any gauge origin and any perturbing field **B** can be obtained by first solving a set of six CPHF equations: three for the components of the angular momentum operator $\hat{\mathbf{L}}$ using any single gauge origin, eqns. (4), to obtain the set of $\phi_i^{(1)}$: $\phi_i^{(1)L_x}$, $\phi_i^{(1)L_y}$ and $\phi_i^{(1)L_z}$; and three for the components of the linear momentum operator $\hat{\mathbf{p}}$: $\phi_i^{(1)\hat{p}_x}$, $\phi_i^{(1)\hat{p}_y}$ and $\phi_i^{(1)\hat{p}_z}$ resulting from any shift in origin, eqns. (7).

The change in the CPHF first-order wavefunction resulting from a gauge transformation of $\mathbf{A}(\mathbf{r})$ clearly changes the paramagnetic part of $\mathbf{J}^{(1)}(\mathbf{r})$, eqn. (2), but in the exact CPHF case the diamagnetic term, $\mathbf{J}_d^{(1)}(\mathbf{r})$, changes in the opposite manner leaving the total $\mathbf{J}^{(1)}(\mathbf{r})$ unchanged.[9] In approximate CPHF calculations - for example, an expansion of the molecular orbitals in a finite

set of basis functions - the current density is not, in general, invariant to gauge transformations of $\mathbf{A}(\mathbf{r})$.[9] Thus, the effects of such transformations on $\mathbf{J}^{(1)}(\mathbf{r})$ are of *practical* interest and their analysis may lead to an improvement in the calculation of this property and the dependent molecular properties.

From the equations given above, the general expression for the CPHF $\mathbf{J}^{(1)}(\mathbf{r})$ obtained for any shift $\mathbf{d}(\mathbf{r})$ in gauge origin from the arbitrary one used to calculate the set of $\phi_i^{(1)L_x}$ is given in eqn. (10) for a magnetic field applied along the x-axis. Of course, a similar expression obtains for any magnetic field direction.

$$\mathbf{J}^{(1)}(\mathbf{r}) = (2e/m)\sum_{i=1}^{n/2}(Be/2mc)\Big\{\phi_i^{(0)*}\hat{\mathbf{p}}\phi_i^{(1)L_x} + \phi_i^{(1)L_x*}\hat{\mathbf{p}}\phi_i^{(0)}$$

$$-d_y(\mathbf{r})[\phi_i^{(0)*}\hat{\mathbf{p}}\phi_i^{(1)p_z} + \phi_i^{(1)p_z*}\hat{\mathbf{p}}\phi_i^{(0)}]$$

$$+d_z(\mathbf{r})[\phi_i^{(0)*}\hat{\mathbf{p}}\phi_i^{(1)p_y} + \phi_i^{(1)p_y*}\hat{\mathbf{p}}\phi_i^{(0)}]\Big\}$$

$$-(e^2/2mc)\mathbf{B}\times(\mathbf{r}-\mathbf{d}(\mathbf{r}))\rho^{(0)}(\mathbf{r}) \qquad (10)$$

It is to be noted that the shift in gauge origin $\mathbf{d}$ has now been made an explicit *parametric* function of $\mathbf{r}$, $\mathbf{d}(\mathbf{r})$. By choosing a particular function $\mathbf{d}(\mathbf{r})$, hereafter termed a *gauge transformation function*, one necessarily subjects each of the first-order orbitals $\phi_i^{(1)}$ and the corresponding CPHF current density $\mathbf{J}^{(1)}(\mathbf{r})$ to the consequences of a gauge transformation, eqns. (9) and (10). It should be clear that one *cannot* perform a similar gauge transformation of $\mathbf{A}(\mathbf{r})$ to obtain a *stationary* first-order CPHF wavefunction

with a different gauge origin for each molecular orbital. In order to obtain a stationary CPHF wavefunction with a different gauge origin for each orbital, it is necessary to solve the CPHF equations, eqns. (4), using a separate $\hat{H}^{(1)}$, eqn. (6), for each orbital in order to ensure self-consistency. This corresponds to assigning multiple origins in the orbital Hilbert space, as is done in the IGLO method (using non-canonical CPHF with localized orbitals),[10] and is to be sharply contrasted with the use of a change of gauge origin in real space, *the space in which* **B** *is defined*, which corresponds to a gauge transformation. In the limit of the exact CPHF solutions - for example, the use of a complete basis set expansion of the molecular orbitals - a gauge transformation corresponds to subjecting both the Hamiltonian and state function to a unitary transformation.[9]

1-4 Relation of Induced Current Density to Other Magnetic Response Properties

As emphasized by Jameson and Buckingham,[11] the induced current density distribution $\mathbf{J}^{(1)}(\mathbf{r})$ is related to the measurable magnetic susceptibility tensor χ and nuclear magnetic shielding tensor σ^N (for a nucleus with magnetic dipole moment μ^N) according to eqns. (11) and (12), respectively[1]

$$\mathbf{B}\cdot\chi = (1/2c)\int d\mathbf{r}\{\mathbf{r}\times\mathbf{J}^{(1)}(\mathbf{r})\} \tag{11}$$

$$\mu^N\cdot\sigma^N\cdot\mathbf{B} = (-1/c)\mu^N\cdot\int d\mathbf{r}_N\{\mathbf{r}_N\times\mathbf{J}^{(1)}(\mathbf{r})/r_N^3\} \tag{12}$$

where the origin of $\mathbf{r}$ in eqn. (11) is arbitrary in the exact CPHF case or when demanded by symmetry - since then the integrated current is identically zero -

and the origin of $\mathbf{r}_N$ in eqn. (12) is the nucleus N.

Eqns. (11) and (12) show that in an approximate CPHF calculation, the accuracies of χ and σ^N are determined by the accuracy with which $\mathbf{J}^{(1)}(\mathbf{r})$ is calculated. Eqn. (10) determines the $\mathbf{J}^{(1)}(\mathbf{r})$ distribution, and ultimately χ and σ^N, for any gauge transformation function $\mathbf{d}(\mathbf{r})$. The essential question then arises, "What function $\mathbf{d}(\mathbf{r})$ gives the most accurate $\mathbf{J}^{(1)}(\mathbf{r})$ distribution, and hence χ and σ^N tensors, for a given level of approximation - finite basis set, for example - within the CPHF approximation?"

1-5 Multiple Gauge Transformations - The IGAIM Method

In the IGAIM method[2] χ and σ_N are calculated by expressing eqns. (11) and (12) in terms of a summation over contributions from each atom Ω in a molecule[3] using the nucleus as gauge origin to calculate $\mathbf{J}^{(1)}(\mathbf{r})$ throughout the basin of the corresponding atom. The nucleus is the "natural gauge origin" for a free atom because then $\psi^{(1)}$ is identically zero and thus $\mathbf{J}^{(1)}(\mathbf{r})$ is determined entirely by the ground state electron density $\rho^{(0)}(\mathbf{r})$. Thus, IGAIM uses *multiple* gauge transformations to calculate the $\mathbf{J}^{(1)}(\mathbf{r})$ distribution, χ and σ^N, with $\mathbf{d}(\mathbf{r})$ being set equal to $\mathbf{R}_\Omega$, the position vector of nucleus Ω, for all $\mathbf{r}$ in a given atomic basin.

A description of the IGAIM method together with calculated results for the isotropically averaged suceptibility $\bar{\chi}$ and carbon NMR shielding $\bar{\sigma}^C$ has been published.[2] In that publication, comparisons of the IGAIM results are made with corresponding conventional CPHF single gauge origin results and experimental results for a fairly large number of molecules. In all cases, the IGAIM method was shown to yield significantly more accurate results than

the conventional CPHF approach. A copy of the IGAIM publication[2] appears as Appendix 1-A of this chapter.

While the IGAIM method yields relatively accurate molecular magnetic properties, there are difficulties associated with it: 1) numerical integration is required to calculate the separate atomic contributions and thus the method is computationally intensive; 2) the current density is relatively poorly described near the boundaries of the atom, resulting in a discontinuous display of $\mathbf{J}^{(1)}(\mathbf{r})$ and making a study of its topology difficult; and 3) the symmetry properties of the induced current distribution are not guaranteed.

1-6 Continuous Gauge Transformations - The CGT Methods

It is possible that the use of a *continuous* function for $\mathbf{d}(\mathbf{r})$, as opposed to the discontinuous one used in IGAIM, could preserve or improve upon the accuracy of the calculated molecular properties, in addition to simplifying their calculation by allowing for the use of easily evaluated expressions. The use of a continuous gauge transformation function $\mathbf{d}(\mathbf{r})$ would yield a continous and potentially more accurate description of the *molecular* current density distribution, particularly in the vicinities of the interatomic surfaces.

An important physical constraint on the function $\mathbf{d}(\mathbf{r})$, one not met by that used in the IGAIM method, is that it should guarantee the symmetry properties of the molecular current distribution - that is, $\mathbf{d}(\mathbf{r})$ should be both continuous and transform as the totally symmetric irreducible representation of the molecular point group. Of course, the current density

vector field itself does not belong to the totally symmetric irreducible representation but it should be clear from eqn. (10) that $\mathbf{d}(\mathbf{r})$ must. The symmetry properties of the $\mathbf{J}^{(1)}(\mathbf{r})$ field are discussed in chapter 2.

An obvious choice for the function $\mathbf{d}(\mathbf{r})$ would be the one which causes the transverse part - the components of $\mathbf{J}^{(1)}(\mathbf{r})$ perpendicular to $\mathbf{B}$ - of the exact $\mathbf{J}_p^{(1)}(\mathbf{r})$ to vanish, since in approximate CPHF calculations it is the paramagnetic term which is the least accurately determined and only the transverse component of the current determines the diagonal components of the magnetic response tensors χ and σ^N. Unfortunately, in order to determine $\mathbf{d}(\mathbf{r})$ in this case, it is necessary to know the exact $\mathbf{J}_p^{(1)}(\mathbf{r})$ and therefore this approach is of no *direct* use. Choosing the function $\mathbf{d}(\mathbf{r})$ so as to make the transverse part of the approximate $\mathbf{J}_p(\mathbf{r})$ vanish is possible in principle, but is computationally very difficult.

Alternatively, setting $\mathbf{d}(\mathbf{r}) = \mathbf{r}$ causes both the exact and approximate $\mathbf{J}_d^{(1)}(\mathbf{r})$ to vanish everywhere, eqn. (10), while clearly guaranteeing the symmetry properties of the current distribution. With moderately sized basis sets this method, termed CGTR (Continuous Gauge Transformation - $\mathbf{r}$), yields magnetic susceptibilities which are generally in good agreement with experiment, whereas the corresponding CPHF results using a single "optimum" gauge origin are, as is well known, significantly in error, especially for larger molecules. Table 1-1 lists calculated results for $\bar{\chi}$, the isotropically averaged magnetic susceptibility, obtained using two basis sets, 6-311++G(2d,2p)[12] for all molecules, and a large uncontracted set of (12s8p4d/8s4p)[13] for the smaller molecules. Corresponding results are also listed for the IGAIM method as well as experiment in Table 1-1. The magnetic

susceptibilities calculated using the smaller of the two basis sets with the CGTR method are consistently slightly lower than those calculated using IGAIM. This difference becomes much smaller for the larger basis set, being within the experimental uncertainty in $\bar{\chi}$, and both methods converge to a common value. The conventional CPHF results are, of course, much improved using the larger basis set, but are, in some cases, still significantly in error.

In general, the IGAIM results calculated using the smaller basis set are closer to the convergent value of $\bar{\chi}$ than the corresponding CGTR results and thus IGAIM is judged to be more accurate than CGTR in calculating magnetic susceptibilities with basis sets roughly of the 6-311++G(2d,2p) size and smaller.

The basis for the advantage of both the IGAIM method and the CGTR method over the conventional CPHF method in calculations of $\bar{\chi}$ can be seen from the results given in Table 1-2, which lists the separate paramagnetic and diamagnetic contributions to the perpendicular component of the magnetic suscpetibility tensor, $\chi_{\perp}$ for the CO_2 molecule. The axial component, $\chi_{\parallel}$, can easily be calculated "exactly" for any given basis set because the paramagnetic contribution vanishes identically for any axial gauge origin. Thus, all methods use the same value for $\chi_{\parallel}$. Use of a single oxygen nucleus as gauge origin in a conventional CPHF calculation yields very large paramagnetic and diamagnetic contributions to $\chi_{\perp}$, contributions which fail to cancel properly and the result is a gross overestimation of $\bar{\chi}$. Use of the carbon nucleus, the centre of electronic charge, as the single gauge origin dramatically reduces both contributions to $\chi_{\perp}$ and the calculated result for $\bar{\chi}$ is much closer to the experimental value but is still significantly in error.

Use of the IGAIM method results in the near vanishing of the paramagnetic contribution to $\chi_\perp$ and the result for $\bar{\chi}$ is in agreement with the experimental value within the experimental error. Finally, with the CGTR method the diamagnetic contribution to $\chi_\perp$ is identically zero and $\chi_\perp$ is thus equal to the paramagnetic contribution. The CGTR result for $\bar{\chi}$ is also in agreement with the experimental result within experimental error.

The results in Tables 1-1 and 1-2 are understandable by first recognizing that the error in $\chi_\perp$ for any gauge is due primarily to the paramagnetic contribution, which depends on the first-order wavefunction(s), and by assuming that the error in the calculated paramagnetic contribution, for a given basis set, is proportional to its magnitude. Thus, both the IGAIM method and the CGTR method yield more accurate results than the methods using any single gauge origin because the calculated magnitudes of $\chi_\perp$(para), and therefore the errors in $\chi_\perp$(para), are much smaller. Since the magnitude of $\chi_\perp$(para) is smaller for IGAIM than for CGTR, the results for $\bar{\chi}$ using the small basis set are closer to the convergent result using IGAIM.

A stringent requirement on $\mathbf{J}^{(1)}(\mathbf{r})$ is that it be everywhere divergenceless,[9] eqn. (13)

$$\nabla\cdot\mathbf{J}^{(1)}(\mathbf{r}) = 0 \tag{13}$$

which is simply the continuity equation for the electronic current in a stationary state. This equation can be inferred from the relationship between the second-order magnetic field perturbed energy $E^{(2)}$ and $\mathbf{J}^{(1)}(\mathbf{r})$ given in eqn. (14)

$$E^{(2)} = -(1/4c)\mathbf{B}\cdot\int d\mathbf{r}\{\mathbf{r}\times\mathbf{J}^{(1)}(\mathbf{r})\} = -(1/2c)\int d\mathbf{r}\{\mathbf{A}(\mathbf{r})\cdot\mathbf{J}^{(1)}(\mathbf{r})\} \tag{14}$$

a relationship which will be derived in chapter 3. The energy $E^{(2)}$, like $\mathbf{J}^{(1)}(\mathbf{r})$, is an observable quantity (it is proportional to χ) and thus should also be independent of gauge transformations of $\mathbf{A}(\mathbf{r})$. Thus, for the general gauge transformation $\mathbf{A}(\mathbf{r}) \rightarrow \mathbf{A}(\mathbf{r})' = \mathbf{A}(\mathbf{r}) + \nabla f(\mathbf{r})$,

$$E^{(2)'} - E^{(2)} = 0 = \int d\mathbf{r}\{\nabla f(\mathbf{r}) \cdot \mathbf{J}^{(1)}(\mathbf{r})\} = -\int d\mathbf{r}\{f(\mathbf{r}) \nabla \cdot \mathbf{J}^{(1)}(\mathbf{r})\} = 0 \qquad (15)$$

an equation which follows in part from the vanishing of $\mathbf{J}^{(1)}(\mathbf{r})$ at infinity. Since the function $f(\mathbf{r})$ is entirely arbitrary, the only way that eqn. (15) can be true is if eqn. (13) is true. Eqn. (13) in turn requires that the integral of $\mathbf{J}^{(1)}(\mathbf{r})$ over all space must vanish, as given in eqn. (16)

$$\int d\mathbf{r} \mathbf{J}^{(1)}(\mathbf{r}) = 0 \qquad (16)$$

and the current is seen to be conserved for the total system, eqn. (16), as a consequence of being conserved locally, eqn. (13).

The divergenceless condition given in eqn. (13) is satisfied relatively well by both IGAIM and CGTR. For a moderately sized basis set or larger, such as the 6-311++G(2d,2p) set, values of $\nabla \cdot \mathbf{J}^{(1)}(\mathbf{r})$ at critical points in the $\mathbf{J}^{(1)}(\mathbf{r})$ field which are not zero by symmetry are generally at least two orders of magnitude lower using IGAIM or CGTR than they are using the single origin method and are small enough to unambiguously study the topology of the induced current density[6] and its relation to χ and σ^N.[7,8]

Forcing $J_d(\mathbf{r})$ to be zero for all $\mathbf{r}$ in the CGTR method demands that $J_p(\mathbf{r})$ alone must approach the requirement of zero divergence, rather than attempting to achieve this result through the cancellation of two very large terms, as is the case with the conventional CPHF method. The integrated values of $\mathbf{J}^{(1)}(\mathbf{r})$

typically yields values of 10^{-3} au or less for nonsymmetric molecules containing first-row atom indicating good numerical satisfaction of the integral condition given in eqn. (15) for both the IGAIM and CGTR methods, whereas the corresponding results for the conventional CPHF method is usually at least two orders of magnitude larger. A fairly simple but difficult case is presented by OCS for a magnetic field applied perpendicular to the internuclear axis, but even here the IGAIM and CGTR methods with the medium basis set yield integrated currents per unit field of 0.011 and 0.019 au respectively for the component of $\mathbf{J}^{(1)}(\mathbf{r})$ perpendicular to both $\mathbf{B}$ and the internuclear axis (the other integrated components are zero by symmetry alone), while the use of a single gauge origin on carbon yields a large value of 4.24 au.

It is found that the CGTR method fails to yield satisfactory values for the magnetic shielding σ^N (with the exception of protons) unless prohibitively large basis sets are employed in the calculations. This is a result of the very large magnitude of $\mathbf{J}^{(1)}(\mathbf{r})$ in the immediate vicinity of a nucleus with core electrons and the $1/r_N^3$ dependence of the shielding property density,[11] eqn. (12). As a first step towards overcoming this difficulty, the *empirical* expression given in eqn. (17) for the gauge transformation function $\mathbf{d}(\mathbf{r})$ is proposed

$$\mathbf{d}(\mathbf{r}) = \mathbf{r} - \sum_{\Omega}(\mathbf{r}-\mathbf{R}_\Omega)\exp[-\alpha_\Omega(\mathbf{r}-\mathbf{R}_\Omega)^4] \qquad (17)$$

where the sum is over all nuclei in the molecule. This function effectively shifts the gauge origin from the point $\mathbf{r}$ towards the nearest nucleus, the magnitude of the shift decreasing with the distance of the point $\mathbf{r}$ from the

nucleus. Clearly, the parameter α_Ω must be assigned equivalent values for symmetrically equivalent nuclei to guarantee the symmetry properties of the current distribution. In this work a single value of 2 for α_Ω was used for all nuclei. The reasons for choosing this functional form for $\mathbf{d}(\mathbf{r})$ are as follows: 1) the success of the IGAIM method in shielding calculations relative to the conventional method demonstrates that in the region of a given nucleus the current density is best described with the gauge origin at the nucleus. 2) At a given point in a non-nuclear region of a molecule, the current density is relatively accurately described with the gauge origin near the point, as demonstrated by the success of the CGTR results for $\bar{\chi}$, a property which is insensitive to the current in the nuclear regions of the molecule. 3) Because of its simple form, the molecular values of χ and σ^N are readily calculated from eqns. (10) through (12), just as they are with the CGTR method.

Use of the gauge transformation function given in eqn (17), a method termed CGTRD (Continuous Gauge Transformation - $\mathbf{r}$ Damping), yields good results for $\bar{\sigma}^C$ while leaving essentially unchanged the $\bar{\chi}$ results of the CGTR method, Table 1-1. This is demonstrated clearly in Table 1-3 where calculated as well as experimental isotropic carbon shielding results for a broad range of molecules are shown. In all cases the CGTRD method yields much more accurate results than the conventional single-origin method. Unlike the magnetic susceptibility, the carbon shielding calculated using the CGTRD method with the smaller basis set is closer to the convergent result than the IGAIM method and thus the CGTRD method is judged to be more accurate for carbon shielding than IGAIM when using basis sets roughly of the size 6-

311++G(2d,2p). The CGTRD method, like IGAIM (and the CGTR method), also yields good results for proton shielding using moderate sized basis sets. The value of 24.0 ppm given in Table 1-3 for the isotropic proton shielding in benzene compared to the experimental (gas-phase) value of 23.7 ppm and the conventional CPHF value of 16.9 ppm, being a case in point. Lazzeretti et al[20] report a value of 22.7 ppm using a single origin at the charge centroid and an extremely large basis consisting of 474 primitives contracted to 396 basis functions.

Using the CGT methods one can obtain relatively accurate displays of the full $\mathbf{J}^{(1)}(\mathbf{r})$ distribution using moderately sized basis sets, even for large molecules, as illustrated in Fig. 1-1 for the benzene molecule. Shown in Fig. 1-1a is a display of the current distribution induced in the plane of the nuclei by a field applied parallel to the principal symmetry axis, a display determined using the CGTRD method with the small basis set.[12] It is judged to be accurate based on the good satisfaction of the continuity equation, eqn. (13), and the good agreement of the corresponding calculated values $\bar{\chi}$ and $\bar{\sigma}^{N}$ with experiment. The display in Fig. 1-1a is to be contrasted with that shown in Fig. 1-1b which is determined with a single gauge origin at the charge centroid using the same basis set. The map in Fig. 1-1b correctly predicts the paramagnetic current flow in the ring interior and the diamagnetic flow encompassing the entire molecule, both regions of flow being centred about the symmetry axis through the gauge origin. However, the remaining regions of current flow are qualitatively as well as quantitatively inaccurate, as also reflected in the results for $\bar{\chi}$, $\bar{\sigma}^{C}$ and $\bar{\sigma}^{H}$ in Tables 1-1 and 1-3. In particular, the current in Fig. 1-1b exhibits *three-dimensional* sources and

sinks in the vicinities of each carbon nucleus and thus seriously violates the requirement of zero divergence of the $\mathbf{J}^{(1)}(\mathbf{r})$ field, eqn. (13). The current distribution calculated using the IGAIM method is illustrated in Fig. 1-1c. It is essentially indistinguishable from that shown in Fig. 1-1a in the region of the carbon nucleus which serves as the gauge origin, but shows deviations near the interatomic surfaces of the corresponding atom with neighbouring carbon atoms. In particular the C-C "bonded", closed current loops in Fig. 1-1a have lost their symmetry with respect to the interatomic surfaces in Fig. 1-1c and now appear as spirals centered off the σ_d symmetry plane. As will be shown in chapter 2, a critical point of the current distribution which serves as origin or terminus for spiralling trajectories is only possible for a critical point which does not lie on a symmetry plane parallel to the **B** field.

Thus, the CGTRD method preserves the advantages of the IGAIM method in the region of a nucleus, and extend the same quality in the calculated current distribution to all regions of space. Fig. 1-1c also demonstrates the serious decline in the quality of the molecular current distribution which occurs if one chooses a gauge which does not guarantee the symmetry properties of the distribution, as in Fig. 1-1a and Fig. 1-1b. It should be recalled that this failure is not reflected in the molecular properties determined using the IGAIM method because the properties are calculated an atom at a time.

The analysis of the $\mathbf{J}^{(1)}(\mathbf{r})$ distributions made possible through the use of the CGT methods is presented in chapter 2.

1-7 Previous Methods

There have, of course, been many other ab-initio methods proposed to

overcome the "gauge-problem" in magnetic response calculations since Lipscomb et al pioneering applications of conventional CPHF in 1963.[1] Of these, only two appear to be consistently used. The first was proposed (for CPHF) by Ditchfield[21] and is called the GIAO (Gauge Invariant Atomic Orbitals) method.[22] The GIAO method takes advantage of the fact that each unperturbed, and hence perturbed, molecular orbital is usually approximated as a linear combination of nuclear centered *basis functions*. In the GIAO method each basis function is modified by a phase factor ($\exp[-ieB\times R_{\Omega}\cdot r/\hbar 2c]$) prior to the CPHF calculation so that the total molecular magnetic properties are invariant to the choice of the common gauge origin. For a given basis set, the GIAO method yields results in much better agreement with experiment than the conventional CPHF method, at least for shielding calculations. Due to the added complexity of the basis functions, however, the solution of the CPHF equations using the GIAO method is considerably more difficult than the conventional method, particularly with respect to the evaluation of the two-electron integrals.[21] Until the recent computational developments by Pulay et al,[19] these difficulties severely limited the applicability of the GIAO method. Even with these new developments, however, the computational difficulty associated with the GIAO method is still significant and has prevented its extension to calculations of the computationally more demanding magnetic susceptibility tensor.

The second commonly used method was proposed by Kutzelnigg et al and is called the IGLO (Individual Gauges for Localized Orbitals) method.[10] In the IGLO method, the molecular orbitals are localized prior to the CPHF and each is assigned a separate gauge origin, usually at the charge centroid of the

orbital. The first-order corrections to the localized orbitals are then determined from the corresponding *non-canonical* CPHF equations. Because non-canonical CPHF is used and because of the use of multiple origins in the orbital space, the solution of the CPHF equations in the IGLO method is, like GIAO, significantly more difficult than the conventional CPHF method and requires, for practical purposes, that certain terms be neglected or approximated.[10] The IGLO method has been widely applied to calculations of nuclear magnetic shielding as well as magnetic susceptibility tensors.[10]

The computational advantage of the CGT methods over the GIAO and IGLO methods is clear, for the CGT methods are essentially no more difficult to apply than the conventional CPHF method itself and yet yield results for χ and σ^N comparable to either GIAO or IGLO, as the results in Tables 1-1, 1-3 and 1-4 show. In Tables 1-1 and 1-3 results for $\bar{\chi}$ and $\bar{\sigma}^C$ from IGLO and GIAO (for shielding) calculations are given, when available in the literature, for comparison with the IGAIM, CPHF and experimental results. Unfortunately, direct comparison of the methods is not entirely justified in most cases due to the use of different basis sets and/or geometries. In particular, all of the IGLO results and some of the GIAO results were calculated using experimentally determined geometries while the IGAIM and CGT results were all calculated using the theoretically optimized geometries. The geometry is particularly important for shielding and it is generally held that the experimental geometry yields more accurate results, all other things being equal.[10,17,18] In Table 1-4 shielding anisotropies calculated using the CGTRD method, the GIAO method and the IGLO method are compared for several molecules.

The conclusion to be drawn from the comparison of results for the GIAO, IGLO and CGTRD methods in Tables 1-1, 1-3 and 1-4 is that the three methods generally give comparable, and quite accurate, results considering the approximations assumed in the calculations. There is clearly inadequate information available, at this point, to determine which method is the "best" from the standpoint of accuracy.

In the opinion of the author, however, the continuous gauge transformation methods are certainly preferable for computational reasons. In the IGLO and GIAO methods the solution of the CPHF equations is complicated relative to conventional CPHF due, effectively, to the introduction of multiple origins in the orbital Hilbert space. In the continuous gauge transformation methods, the gauge transformations are performed after the conventional CPHF calculations have been carried out and thus the only additional "complication" relative to the conventional method of calculating χ and σ^N lies in the evaluation of the corresponding one-electron integrals from eqns. (10)-(12). This additional effort is negligible, however, and the continuous gauge transformation methods are practically as straightforward as the conventional method. In addition, the continous gauge transformation methods enable one to study the induced molecular current distributions in an unambiguous and straighforward manner,[6] as will be demonstrated in chapter 2. To the author's knowledge, no detailed analyses of the IGLO or GIAO calculated current distributions have been done.

1-8 Comments

This work has laid the foundation for an entirely new approach to

calculating magnetic response properties of molecules. The approach was motivated by and takes direct advantage of the underlying physics of molecular interaction with a magnetic field, by calculating the molecular properties in terms of the induced current density distributions. Future work should clearly focus on optimizing the gauge transformation function $\mathbf{d}(\mathbf{r})$, which has not yet been investigated in detail. The "gauge problem" is, of course, not unique to calculating magnetic properties of molecules. It is ubiquitous in physics. Thus, one should not be dismayed by the use of the gauge transformation function, but rather exploit it.

Ideally, one would want to discover that gauge transformation function which results in the vanishing of the exact paramagnetic transverse current so that the principal elements of the molecular magnetic response tensors could be determined entirely by the ground state charge distribution. Clearly such a function *exists* for every molecule, but the important question is: is it a "universal" function?

Because the continuous gauge transformation methods employ conventional CPHF wavefunctions, it is expected that the incorporation of the many factors commonly neglected in magnetic response calculations will be relatively straightforward. Such factors include electron correlation, solvent effects and molecular vibration.

1-9 References

1. R.M. Stevens, R.M. Pitzer and W.N. Lipscomb, *J. Chem. Phys.*, **38**, 550 (1963). W.N. Lipscomb, *Adv. Magn. Res.*, **2**, 137 (1966); W.N. Lipscomb, *MTP Intern. Rev. Sci.*, **1**, 167 (1972).

2. T. A. Keith and R. F. W. Bader, *Chem. Phys. Lett.*, **194**, 1 (1992).

3. R.F.W. Bader, *Atoms in Molecules - A Quantum Theory*, (Oxford Univ. Press, Oxford, 1990).

4. T. A. Keith and R. F. W. Bader, *Chem. Phys. Lett.*, submitted.

5. R. D. Amos and J. E. Rice, *CADPAC: The Cambridge Analytic Derivatives Package* - Version 4.0, (Cambridge, UK., 1987)

6. T. A. Keith and R. F. W. Bader, *J. Chem. Phys.*, submitted.

7. R. F. W. Bader and T.A. Keith, *J. Chem. Phys.*, submitted.

8. T.A. Keith and R.F.W. Bader, *J. Chem. Phys.*, to be submitted.

9. S.T. Epstein, *The Variation Method in Quantum Chemistry*, (Academic Press, New York, 1974).

10. W. Kutzelnigg, *Israel. J. Chem.*, **19**, 193 (1980); W. Kutzelnigg, U. Fleischer and M. Schindler, *Nucl. Magn. Reson., Basic Principles Progr.*, **23**, 165 (1990).

11. C.J. Jameson and A.D. Buckingham, *J. Chem. Phys.*, **73**, 5684 (1980).

12. R. Krishnan, J.S. Binkley, R. Seeger and J.A. Pople, *J. Chem. Phys.*, **72**, 650 (1980); T. Clark, J. Chandreshakar, G.W. Spitznagel and P.v.R. Schleyer, *J. Comp. Chem.*, **4**, 294 (1983); M.J. Frisch, J.A. Pople and J.S. Binkley, *J. Chem. Phys.*, **80**, 3265 (1984).

13. F. B. van Duijneveldt, *IBM Res. Rept.*, RJ945 (1971). Polarizaation functions added by the author.

14. B.R. Appleman and B.P. Dailey, *Adv. Mag. Res.*, **7**, 231 (1974).

15. *Handbook of Chemistry and Physics*, 72nd Edition (CRC Press, Cleveland), Ed. D.R. Lide, 938 (1991-1992).

16. A.K. Jameson and C.J. Jameson, *Chem. Phys. Lett.*, **134**, 461 (1974).

17. C.J. Jameson, *Nucl. Magn. Res. Spectry. Per. Rept.*, 48 (1990)

18. D.B. Chesnut and C.G. Phung, *J. Chem. Phys.*, **91**, 6238 (1989).

19. K. Wolinshi, J.F. Hinton and P. Pulay, *J. Am. Chem. Soc.*, **112**, 8251 (1990)

20. P. Lazzeretti, M. Malagoli and R. Zanasi, *J. Mol. Struct.(Theochem)*, **234**, 127 (1991).

21. R. Ditchfield, *Mol. Phys.*, **27**, 789 (1974).

22. Although of no *direct* scientific importance, perhaps, it is nonetheless useful to recognize that the name "Gauge Invariant Atomic Orbitals" is grossly inaccurate in describing the method. First of all the basis functions used in the expansion of the molecular orbitals are *not* atomic orbitals. An atomic orbital clearly has meaning only for an isolated atom. Secondly, the modified basis functions in the GIAO method are not gauge invariant. It is precisely their defined gauge *dependence* that is important. The method should be renamed GDBF (Gauge Dependent Basis Functions).

Figure 1-1

a) A display of the magnetically induced current density distribution in the nuclear plane of the benzene molecule for a field applied out of the plane and parallel to the principal symmetry axis. The map was calculated using the CGTRD method with the small basis set.[12] The positions of the nuclei are indicated by crosses and the intersections of the interatomic surfaces with the plane are also shown. The directions of current flow are indicated within the atomic basins of a single C-H group. There is paramagnetic (counterclockwise) current flow in the ring interior and in the vicinity of each carbon nucleus, on its ring side.

b) A similar display of the current density distribution, but calculated using a single gauge origin at the centre of symmetry. Three dimensional sources and sinks are denoted by dots in one of the carbon basins.

c) A similar display of the current density distribution, but calculated with a single gauge origin at the position of a carbon nucleus. The well behaved current trajectories are in the basin of the gauge origin.

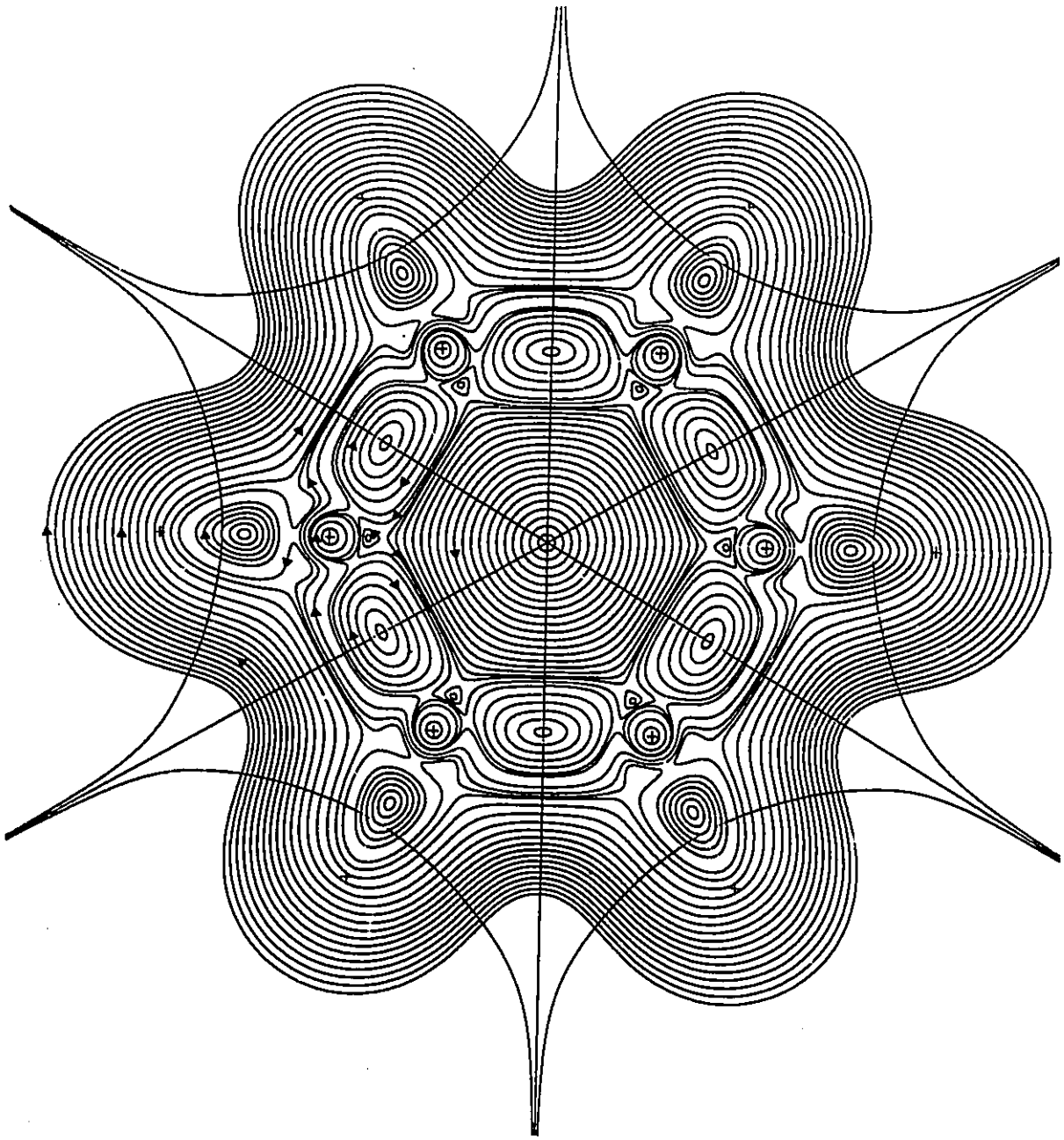

a

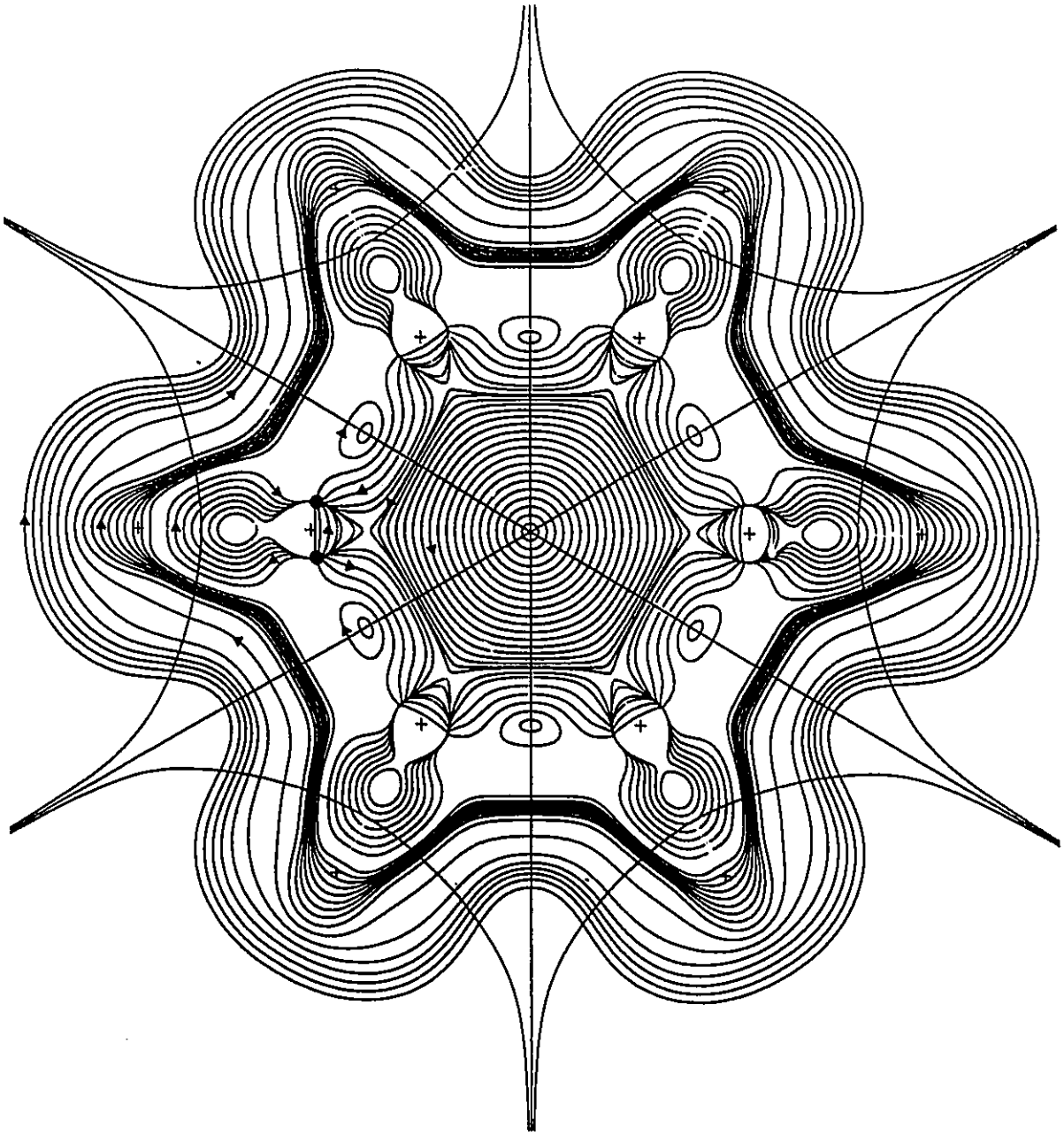

b

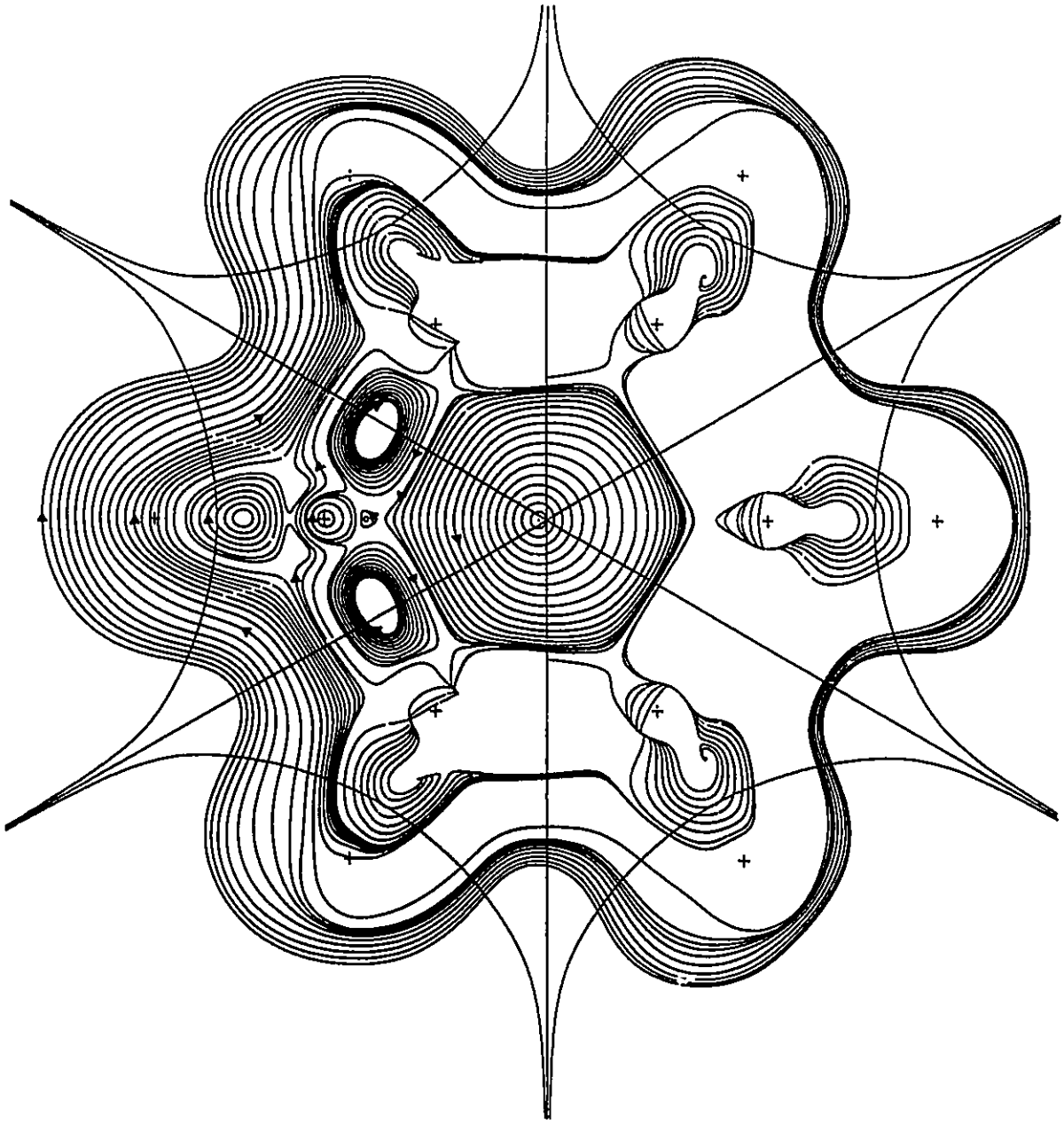

C

Table 1-1[a]

Isotropic Magnetic Susceptibilities $\bar{\chi}$ Calculated Using CPHF With a Single Gauge Origin (CONV), Multiple Gauge Origins (IGAIM), Continuous Gauge Transformations (CGT). Comparisons with experimental and IGLO results. Units are cgs-ppm.

Molecule[b]	$\bar{\chi}$(CONV)[c]	$\bar{\chi}$(IGAIM)	$\bar{\chi}$(CGTR)[d]	$\bar{\chi}$(CGTRD)[e]	$\bar{\chi}$(EXPT)[f]	$\bar{\chi}$(IGLO)[g,h]
N_2 S	-14.2	-12.5	-12.1	-12.1	-12.6(g)	NA
N_2 L	-12.8	-12.7	-12.8	-12.8	-12.6(g)	
HCN S	-20.7(C)	-16.7	-16.2	-16.2	-16.8(g)	NA
HCN L	-17.3(C)	-16.9	-16.9	-16.9	-16.8(g)	
CO_2 S	-31.7	-21.8	-21.0	-21.0	-21.0(g)	NA
CO_2 L	-25.0	-22.1	-21.9	-21.9	-21.0(g)	
CH_4 S	-19.3	-18.2	-17.1	-17.2	[-18.7, -17.4(g)]	-19.0[g]
CH_4 L	-18.9	-18.7	-18.7	-18.7	-18.7(g)	
C_2H_2 S	-24.9	-22.2	-21.7	-21.7	-21(g)	NA
C_2H_2 L	-23.1	-22.7	-22.7	-22.7	-21(g)	
C_2H_4 S	-24.3	-20.7	-20.1	-20.1	[-19.7, -18.8(g)]	-22.6[h]
C_2H_4 L	-21.5	-21.0	-20.9	-20.9	[-19.7, -18.8(g)]	
C_2H_6 S	-33.1	-28.5	-27.2	-27.2	[-27.4, -26.8(g)]	-30.0[g]
C_2H_6 L	-29.9	-29.0	-28.7	-28.7	[-27.4, -26.8(g)]	
C_3H_6 S	-48.2	-41.5	-40.8	-40.8	[-39.9, -39.2(g)]	-43.5[h]
C_3H_8 S	-51.2	-40.0	-39.1	-39.2	[-40.5, -38.6(g)]	-41.8[g]
C_4H_{10} S	-74.9	-52.2	-50.7	-50.9	-50(g)	-56.2[h]

C_5H_{12}	S	-109.7	-63.6	-61.0	-61.2	-63.1(g)	-67.8[h]
Butadiene	S	-58.1	-35.4	-33.1	-33.2	-32.1(g)	NA
Propene	S	-43.7(C2)	-32.0	-30.3	-30.4	-31.5(g)	NA
C_6H_6	S	-87.7	-59.7	-57.5	-57.6	-54.8(g)	-68.0[h]
CS_2	M	-127.7	-46.7	-43.3	-44.3	-47.8(g)	-48.4[g]
CSO	M	-80.5(C)	-36.4	-34.1	-34.6	-32.4(g)	-37.2[g]
CH_3F	S	-24.1(F)	-18.8	-15.9	-15.9	-18(g)	-19.4[g]
CH_3F	L	-19.5(F)	-18.9	-18.7	-18.8	-18(g)	
CF_4	M	-46.0	-33.0	-27.2	-27.2	-36 ± 5(g)	-34.6[g]
CH_3CN	S	-38.5(C1)	-28.7	-26.7	-26.7	-27.6 (l)	-29.9[g]
CH_3NH_2	S	-32.1(C)	-25.2	-23.6	-23.6	-27.0 (l)	NA
CH_3OH	S	-27.7(O)	-21.8	-19.7	-19.7	-21.9 (g)	-22.6[h]
Allene	S	-38.9	-28.5	-26.3	-26.3	-25 (g)	-31.9[h]
Oxirane	S	-42.3(O)	-31.6	-30.1	-30.1	-30.7 (g)	NA
c-C_3H_4	S	-40.3(C3)	-28.0	-26.6	-26.6	-29 (g)	NA
HCOOH	S	-32.1(C)	-21.3	-18.5	-18.5	-19.9 (l)	NA
Isobut	S	-71.3(C2)	-53.2	-51.8	-51.8	-51.7 (g)	-56.0[h]
Neopent	S	-90.5	-65.8	-63.9	-63.9	-63.1 (g)	-70.0[h]
CH_3CH_2OH	S	-47.0(C1)	-34.4	-32.3	-32.3	-33.7 (l)	NA

[a] All CPHF calculations for the CONV, IGAIM, CGTR and CGTRD methods were performed at the corresponding theoretical equilibrium molecular geometry.

[b] S, M and L denote small,[12] medium and large[13] basis set results, respectively. The medium basis set is a partial decontraction of the small set, ie, 6-11111++G(2d,2p).

[c] Single gauge origin is at charge centroid unless otherwise indicated by

centre given in brackets.

[d] The gauge transformation function for the CGTR method is $\mathbf{d}(\mathbf{r}) = \mathbf{r}$.

[e] The gauge transformation function for the CGTRD method is in eqn. (17).

[f] The references for the experimental values can be found in References 2, 10, 14 and 15.

[g] IGLO Basis III. (11s7p2d/6s2p) -> [7s6p2d/4s2p]. For First Row Atoms. Experimental Geometry. Reference 10.

[h] IGLO Basis II. (9s5p1d/5s1p) -> [5s4p1d/4s1p]. For First Row Atoms. Experimental Geometry. Reference 10.

Table 1-2[a]

Paramagnetic and Diamagnetic Contributions to Magnetic Susceptibility of CO_2 Calculated Using CPHF with a Single Gauge Origin (CONV), IGAIM and CGTR.

Units are cgs-ppm.

Method(Origin)	$\chi_\perp$(para)	$\chi_\perp$(dia)	$\chi_\perp$(total)	$\chi_\parallel$	$\bar{\chi}$
CONV(O)	+183.8	-238.2	-54.5	-26.0	-45.0
CONV(C)	+83.4	-117.9	-34.5	-26.0	-31.7
IGAIM	+0.6	-20.3	-19.7	-26.0	-21.8
CGTR	-18.5	0.0	-18.5	-26.0	-21.0
Expt.					-21.0[b]

[a] All CPHF calculations performed with the 6-311++G(2d,2p)[12] basis set at the corresponding theoretical equilibrium geometry.

[b] Reference 14.

Table 1-3[a]

Isotropic Carbon Nuclear Magnetic Shieldings $\bar{\sigma}^C$ Calculated Using CPHF With a Single Gauge Origin (CONV), IGAIM and Continuous Gauge Transformation (CGTRD). Comparisons with experiment, IGLO and GIAO. Units are ppm.

Molecule[b]	$\bar{\sigma}^C$(CONV)[c]	$\bar{\sigma}^C$(IGAIM)	$\bar{\sigma}^C$(CGTRD)	$\bar{\sigma}^C$(EXPT)[d]	$\bar{\sigma}^C$(IGLO)	$\bar{\sigma}^C$(GIAO)
CO_2 S	78.9	57.9	59.6	58.8(g)	50.7[e]	62.7[g]
CO_2 L	62.2	57.3	59.2	58.8(g)		
CH_4 S	198.5	197.4	196.2	195.1(g)	193.8[e]	196.4[g]
CH_4 L	196.0	195.5	195.3	195.1(g)		
HCN S	89.5(C)	79.9	80.3	82.1(g)	72.1[e]	81.6[g]
HCN L	80.4(C)	78.8	78.8	82.1(g)		
C_2H_2 S	124.2	119.3	118.7	117.3(g)	116.1[e]	119.9[g]
C_2H_2 L	120.4	118.1	118.1	117.3(g)		
C_2H_4 S	70.8	66.4	65.0	64.5(g)	58.3[e]	67.9[g]
C_2H_4 L	64.1	63.4	63.1	64.5(g)		
C_2H_6 S	189.8	186.3	185.2	180.9(g)	180.9[e]	186.2[g]
C_2H_6 L	184.4	183.4	183.2	180.9(g)		
C_3H_6 S	205.1	200.2	199.3	185.0(g)	200.0[f]	197.1[h]
C_3H_8_C1 S	182.3	178.7	177.4	170.8(g)	174.5[e]	178.6[g]
C_3H_8_C2 S	188.2	177.3	176.1	169.1(g)	173.2[e]	177.5[g]
C_4H_{10}_C1 S	181.7	179.9	178.8	173.5(g)	176.2[f]	179.7[g]
C_4H_{10}_C2 S	180.8	169.5	168.4	160.0(g)	168.1[f]	170.1[g]
C_5H_{12}_C1 S	181.0	180.8	178.9	173.2(g)	173.5[f]	NA

C_5H_{12}_C2 S	181.3	172.3	169.6	162.5(g)	165.9[f]	NA
C_5H_{12}_C3 S	177.9	162.8	159.3	150.4(g)	156.6[f]	NA
C_6H_6 S	71.9	61.5	60.2	57.9(g)	60.4[f]	57.7[h]
C_6H_6(proton) S	16.9	24.1	24.0	23.7(g)	24.0[f]	24.2[h]
Butadiene_C1 S	75.8	73.8	73.5	75.3(g)	NA	NA
Butadiene_C2 S	64.8	51.6	50.2	54.7(g)	NA	NA
Propene_C1 S	79.3(C2)	76.1	74.8	71.9(g)	NA	NA
Propene_C2 S	64.7(C2)	52.9	51.6	52.6(g)	NA	NA
Propene_C3 S	178.5(C2)	176.0	174.9	168.9(g)	NA	NA
CSO M	59.1(C)	20.7	21.2	30.0(g)	10.0[e]	NA
CH_3F S	140.0(C)	130.2	128.7	116.8(g)	122.1[e]	126.2[h]
CH_3F L	129.8(C)	126.2	126.0	116.8(g)		
CF_4 M	98.1(C)	82.8	81.9	64.5(g)	76.5[e]	NA
Neopent_C1 S	172.2(C2)	166.4	165.4	155.4(g)	159.6[f]	NA
Neopent_C2 S	189.5(C2)	169.3	168.1	158.2(g)	167.7[f]	NA
Isobut_C1 S	176.4(C2)	172.2	170.4	162.4(g)	172.8[f]	NA
Isobut_C2 S	187.8(C2)	171.5	170.3	161.6(g)	169.9[f]	NA
CH_3OH S	155.8(C)	148.0	146.7	137.0(g)	144.6[f]	149.3[g]
CH_3CH_2OH_C1 S	NA	141.0	139.8	127.6(g)	NA	NA
CH_3CH_2OH_C2 S	NA	178.0	176.9	168.5(g)	NA	NA
CH_3CN_C1 S	86.8(C1)	72.5	71.6	73.8(g)	64.4[e]	75.1[g]
CH_3CN_C2 S	205.0(C2)	194.7	193.8	187.7(g)	189.1[e]	194.5[g]
Allene_C1 S	122.0	119.5	118.3	115.4(g)	118.4[f]	118.3[g]
Allene_C2 S	-22.4	-34.8	-36.9	-29.2(g)	-36.1[f]	-31.8[g]
HCOOH S	50.2(C)	32.2	31.3	23.7(g)	NA	38.0[g]

Oxirane S	NA	161.1	160.0	152(1)	154.1[e]	156.4[h]
CH_3NH_2 S	173.9(C)	167.0	165.7	158.3(g)	162.2[e]	166.8[h]
c-C_3H_4_C1 S	NA	79.2	78.0	84(1)	72.7[f]	73.1[h]
c-C_3H_4_C3 S	NA	197.0	195.7	195(1)	189.1[f]	194.0[h]

[a] All CPHF calculations for the CONV, IGAIM and CGTRD methods were performed at the corresponding theoretical equilibrium molecular geometry.

[b] S, M and L denote small,[12] medium and large[13] basis set results, respectively. The medium basis set is a partial decontraction of the small set, ie., 6-11111++G(2d,2p).

[c] Single gauge origin is at charge centroid unless otherwise indicated by centre given in brackets. In some cases, values for the gauge origin at the shielded carbon can be found in Appendix 1-A.[2]

[d] The references for the experimental values can be found in references 2, 10, 16 and 17.

[e] IGLO Basis III. (11s7p2d/6s2p) -> [7s6p2d/4s2p]. For First Row Atoms. Experimental Geometry. Reference 10.

[f] IGLO Basis II. (9s5p1d/5s1p) -> [5s4p1d/4s1p]. For First Row Atoms. Experimental Geometry. Reference 10.

[g] 6-311G** basis[12] at the corresponding theoretical equilibrium geometry. Reference 18.

[h] 6-311+G(2d,2p)[12] basis at the experimental geometry. Reference 19.

Table 1-4[a]

Shielding Anisotropies for First Row Nuclei Calculated Using the CGTRD, IGLO and GIAO methods.

Mol.	$\Delta\sigma$(CGTRD)[b]	$\Delta\sigma$(EXPT)[c]	$\Delta\sigma$(IGLO)[d]	$\Delta\sigma$(GIAO)
CH_3F_C	90	90(g)	92	91[e]
CH_3F_F	-81	-90(g)	-66	-67[e]
C_6H_6_C	195	181(s)	NA	195[e]
C_6H_6_H	-5.0	-3.9(s)	NA	-5.4[e]
C_3H_6_C	56	48 ± 3(s)	57	56[e]
C_3H_4_C3	108	94	NA	108[e]
Oxirane_C	50	37	48	45[e]
C_2H_4_C	173	153(s)	180	169[f]
CH_3CN_C1	309	311 ± 30(s)	NA	330[f]
CH_3CN_C2	15	5 ± 10(s)	NA	14[f]
Allene_C1	98	95(s)	NA	99[f]
Allene_C2	80	58(s)	NA	79[f]

[a] The shielding anisotropy is defined as: $\Delta\sigma = \sigma_{11} - (1/2)[\sigma_{22} + \sigma_{33}]$ where $\sigma_{11} > \sigma_{22} > \sigma_{33}$.

[b] The CGTRD results were obtained with the 6-311++G(2d,2p) basis set[12] at the corresponding theoretical equilibrium geometry.

[c] References 18 and 19.

[d] Reference 10. IGLO basis III: (11s7p2d/6s2p) -> [7s6p2d/4s2p].

Experimental geometry.

[e] References 19. 6-311+G(2d,2p) basis set[12] at the experimental geometry.

[f] Reference 18. 6-311G** basis set[12] at the corresponding theoretical equilibrium geometry.

Appendix 1-A

A copy of the IGAIM publication. Reference 2.

Calculation of magnetic response properties using atoms in molecules

T.A. Keith and R.F.W. Bader
Department of Chemistry, McMaster University, Hamilton, Ontario, Canada L8S 4M1

Received 18 February 1992; in final form 14 April 1992

A new method (IGAIM – individual gauges for atoms in molecules) is presented for relatively accurate ab initio calculations of molecular magnetic response properties. The current density induced within an atom in a molecule by an external magnetic field is well described by the coupled, perturbed Hartree–Fock method when the gauge origin of the vector potential is placed at its nucleus, the natural origin for the free atom, even though it may be poorly described in the rest of the molecule. Since the molecular magnetic susceptibility and nuclear magnetic shielding tensors can be expressed in terms of the induced current density as a sum of separately determined atomic contributions, these properties are, in general, accurately predicted even with basis sets that are insufficient for conventional CPHF.

1. Introduction

The standard approach to calculating molecular responses to external magnetic fields is the coupled perturbed Hartree–Fock (CPHF) method [1]. It is well established that conventional CPHF calculations are, in general, successful in accurately predicting magnetic susceptibility and nuclear magnetic shielding tensors of closed-shell molecules if large basis sets are used [1,2]. The size of the basis sets required are much larger than those necessary for correspondingly accurate predictions of ground state one-electron molecular properties, however, and this limits meaningful application of conventional CPHF to small molecules. The use of basis sets of insufficient size also yields values for magnetic response properties that are dependent upon the gauge origin of the vector potential used to describe the uniform magnetic field.

There is a long history of proposals, as recently reviewed by Kutzelnigg et al. [3], to reduce the basis set error associated with CPHF, all of which attempt to emulate an important property of a closed-shell atom. The nucleus of a ^1S atom, its centre of electronic charge, acts as a natural gauge origin in that the resulting expressions for the magnetic properties are totally determined by the unperturbed wavefunction. This paper demonstrates that the nucleus also serves as a "natural" gauge origin for an atom in a molecule [4] in that the contributions to its magnetic properties from the perturbed wavefunctions are significantly reduced. Relatively accurate molecular properties are then obtained as a sum of separately determined atomic contributions.

Correspondence to: T.A. Keith, Department of Chemistry, McMaster University, Hamilton, Ontario, Canada L8S 4M1.

2. Theory

The response of a closed-shell molecule to an external, uniform magnetic field $\boldsymbol{B}$ is the appearance of an electronic current density $\boldsymbol{j}(\boldsymbol{r})$ which yields a magnetic dipole moment proportional to the external field, as measured through a magnetic susceptibility tensor χ. The induced current density distribution also describes an inhomogenous magnetic field within the molecule which partially shields each nucleus N from the external field to determine a set nuclear magnetic shielding tensors σ^N. Both σ^N and χ are second-order properties calculable from the induced first-order current density $\boldsymbol{j}^1(\boldsymbol{r})$, which is conveniently expressed in terms of the ground state

wavefunction ψ^0 and its imaginary first-order correction ψ^1 as a sum of a paramagnetic term $j_p^1(r)$, that depends on both ψ^0 and ψ^1, and a diamagnetic term $j_d^1(r)$, that denends only on the ground state charge density $\rho^0(r)$.

$$j^1(r)=j_p^1(r)+j_d^1(r)\,, \tag{1}$$

$$j_p^1(r)=\frac{n\hbar e}{mi}\int d\tau'\,(\psi^1\nabla\psi^0-\psi^0\nabla\psi^1)\,, \tag{2}$$

$$j_d^1(r)=-(e^2/mc)A\rho^0(r)\,. \tag{3}$$

In these equations, $A=\frac{1}{2}B\times(r-r_0)$ is the vector potential, with arbitrary gauge origin r_0, which describes the uniform magnetic field B and $\int d\tau'$ implies a summation over all spin variables and an integration over the spatial coordinates of all n electrons but one. Since $j(r)$ and all magnetic response properties derived from it are observable quantities it is necessary that $j^1(r)$ be independent of the arbitrary gauge origin, a condition which is met when ψ^1 is exactly determined by its expansion in the complete set of eigenfunctions of the unperturbed Hamiltonian [5]. Both $j_p^1(r)$ and $j_d^1(r)$ are separately gauge dependent but their sum $j^1(r)$ is gauge invariant. The gauge dependence of $j_d^1(r)$ is explicit through the presence of A while the gauge dependence of $j_p^1(r)$ is implicit in ψ^1.

Epstein [6] has shown that gauge invariance is obtained in approximate methods when certain stationarity conditions on the expectation value of the Hamiltonian are satisfied. Within the coupled, perturbed Hartree–Fock (CPHF) method, as commonly employed in the calculation of second-order properties, these conditions are met if a complete basis is used in the expansion of the molecular orbitals. Since this is not a practical possibility, one always finds a gauge origin dependence in the calculated values of $j^1(r)$, σ^N and χ using the CPHF method. In the case of a closed-shell atom, $j_p^1(r)$ vanishes throughout the atom when the gauge origin is taken at the nucleus, the natural gauge origin, for then ψ^1 is everywhere identically zero. In a molecule no single gauge origin will make $j_p^1(r)$ vanish over all space. However, it is possible to choose a gauge origin which significantly reduces the magnitude of $j_p^1(r)$ over a particular region of space. When $\rho^0(r)$ is accurately determined, the error in $j^1(r)$ comes from $j_p^1(r)$ and this error is reduced by reducing the magnitude of $j_p^1(r)$.

In a conventional CPHF calculation placing the gauge origin at the molecular centre of electronic charge usually yields the most accurate results for the magnetic susceptibility tensor χ, while placing the gauge origin at nucleus N yields relatively accurate results for the nuclear magnetic shielding tensor σ^N [2,7]. Even with an optimum choice of gauge origin, however, a conventional CPHF calculation is limited to relatively small systems because of the size of the basis set that must be employed to obtain useful results. For this reason, several variations of the conventional CPHF method have been developed to further reduce the magnitude of the terms arising from $j_p^1(r)$. An improvement in accuracy over conventional CPHF is realized in the GIAO method [8] (gauge independent atomic orbitals), which assigns an individual nuclear-centered gauge origin to each atomic-like basis function used in the expansion of the molecular orbitals. Since each basis function has its own phase within a given molecular orbital, however, this method complicates the evaluation of the electron–electron interaction integrals and results in a significant increase in the required computation time. In the IGLO method [3,9] (individual gauges for localized orbitals) the canonical molecular orbitals are transformed into a localized set and an individual gauge origin is placed at the negative charge centroid of each orbital. A closely related method is LORG [10], which also used localized orbitals, each with a local gauge. These methods also introduce new coupling terms not present in the conventional CPHF. In the IGLO method, unlike the GIAO method, these are either easily calculated or are small enough to be treated in an approximate manner. From an operational point of view the IGLO method has been demonstrated to be the most practical for the calculation of magnetic response properties [3]. Three methods have recently appeared for obtaining near or exact gauge invariance [11–13], one of which uses correlated wavefunctions [12].

2.1. The IGAIM method

In the approach developed here the natural origin exhibited by a closed-shell atom is used to advantage in the calculation of molecular current density dis-

tributions, by extending its use to an atom in a molecule [4]. In order to calculate $j^1(r)$ accurately throughout a molecule it is sufficient to determine $j^1(r)$ accurately over each spatially defined atom in the molecule using its nucleus as origin in a set of separate conventional CPHF calculations. This approach (IGAIM – individual gauges for atoms in molecules) amounts to constructing the induced current density distribution of a molecule from its constituent atoms. The IGAIM method differs from GIAO, IGLO and other methods which employ multiple gauge origins, in that the gauge origins are determined by properties of the charge density in real space rather than by the behavior exhibited by the basis functions in the Hilbert space of the molecular wavefunction.

The principal topological property of an atomic or molecular charge distribution is that the charge density $\rho(r)$ exhibits a local maximum at the position of each nucleus. The nuclei are, as a consequence, the attractors in the gradient vector field of the charge density. Using this property, one obtains a disjoint partitioning of the real space of a molecule into atomic basins, each basin being the region of space traversed by all the trajectories of $\nabla\rho(r)$ that terminate at a given nucleus, fig. 1. This definition of an atom [4] builds on and preserves the homeomorphism exhibited by the gradient vector fields of a bound and a free atom, thereby maximizing the similarity in the properties of their charge distributions. It is a property of an atomic basin that it is bounded by a surface $S(r)$, of zero flux in the gradient vector field of $\rho(r)$ as given as follows:

$$\nabla\rho(r)\cdot n(r)=0 \quad \forall r\in S(r)\,. \tag{4}$$

Eq. (4) is the defining equation for a subsystem Ω, whose expectation values are defined by quantum mechanics [4] and whose properties are additive, i.e., the molecular expectation value of a property M is given by the sum of its atomic contributions $M(\Omega)$. It has been demonstrated that these characteristics of an atom in a molecule are retained in the presence of an externally applied electromagnetic field [14] and in particular, as discussed below, field-induced properties such as the polarizability and magnetic susceptibility are expressible as a sum of atomic contributions. Unlike the application of an external electric field which causes first-order changes in the charge density and results in a shift in the interatomic surfaces [15], the first-order correction to $\rho(r)$ vanishes for an applied magnetic field, as in this case ψ^1 is purely imaginary. Thus for magnetic field strengths of practical value, the calculated charge density exhibits no discernible change even in terms of the positions and properties of its critical points and the associated interatomic surfaces.

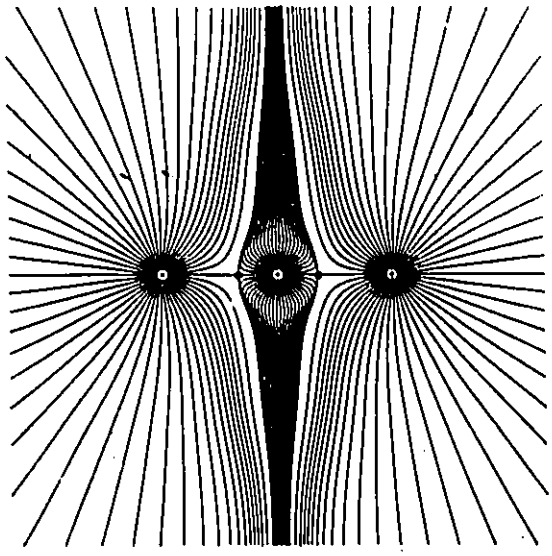

Fig. 1. A planar display of the trajectories of the gradient vector field of the electronic charge density for carbon dioxide. The region of R^3 traversed by the set of trajectories which terminate at a given nucleus is the associated atomic basin. Neighbouring basins are separated one from another by the trajectories which terminate at the bond critical point, denoted by a dot, and define the interatomic surface, a two-dimensional manifold embedded in R^3.

Figs. 2a–2d demonstrate the basis of the IGAIM method. In fig. 2a the induced current density distribution for the carbon dioxide molecule is shown in a plane of the nuclei for a uniform magnetic field applied perpendicular to this plane. This distribution is calculated from a CPHF first-order wavefunction determined with the gauge origin at the carbon nucleus, the centre of electronic charge, using a large uncontracted Gaussian basis set, [13s8p5d]. This basis set and choice of origin yields values for the mean magnetic susceptibility χ, and the mean carbon nuclear magnetic resonance shielding value σ^C, in good agreement with experiment, table 1. The first-order correction to the wavefunction ψ^1 van-

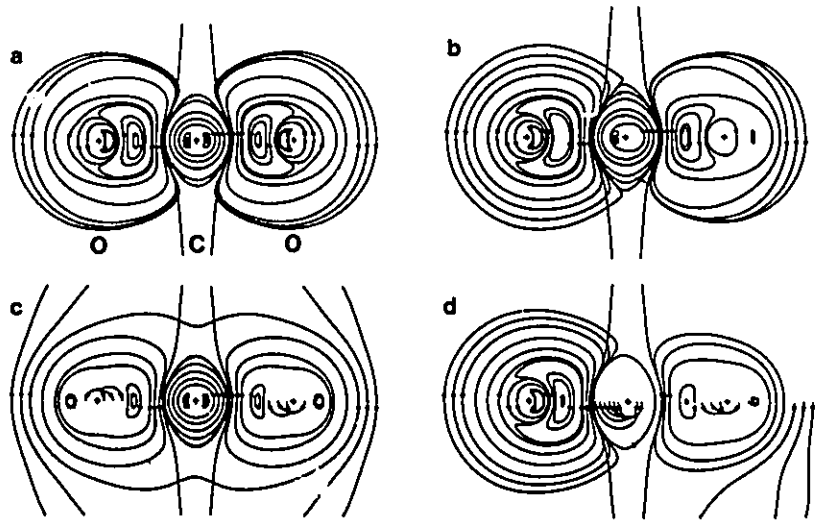

Fig. 2. Current density distributions for carbon dioxide induced by a field applied perpendicular to the indicated plane overlaid with the intersections of the interatomic surfaces. (a, b) Calculated using the large basis set with origins at the C and left hand O nuclei respectively; (c, d) calculated using the small basis set for corresponding origins. In systems with significant charge transfer most current loops are entirely closed within each atomic basin. Thus in CO_2 the *total* current density is partitioned into regions where it is primarily diamagnetic, clockwise loops in the O basins, or paramagnetic, counter-clockwise loops in the C basin. The induced magnetic field at the C nucleus by the current distribution within its basin reinforces the applied field and contributes to a relative downfield shift of the C NMR signal.

Table 1
Mean magnetic susceptibility χ and carbon NMR shielding σ^C for CO_2 calculated using conventional CPHF and IGAIM with large and small basis sets. Units are cgs-ppm for χ and ppm for σ^C

Method [basis]$_{gauge}$	χ	σ^C
CPHF [13s8p5d]$_C$	−23.2	62.2 [a]
CPHF [13s8p5d]$_O$	−24.3	62.2
CPHF [5s4p2d]$_C$	−31.6	78.9 [a]
CPHF [5s4p2d]$_O$	−45.0	78.9
IGAIM [5s4p2d]	−21.8	57.9
IGAIM [13s8p5d]	−22.1	57.1
experiment	−21.0 [b]	58.8 [c]

[a] The shielding is gauge invariant in this case since the carbon nucleus lies at a center of inversion.
[b] Ref. [16]. [c] Ref. [17].

ishes for a field applied parallel to the molecular axis and thus only the perpendicular components to the magnetic properties depend upon $j^1_p(r)$. The local vanishing of the divergence of $j^1(r)$, as required for the satisfaction of the equation of continuity, requires that the current loops be closed. The current density distribution of fig. 2a meets this criterion throughout the molecule and in this sense, is well behaved. Also shown in table 1 are the χ and σ^C values obtained when the gauge origin is placed at an oxygen nucleus, using the same large basis set. The resulting current distribution is shown in fig. 2b. The distribution over the basin of the gauge origin is similar to that shown in fig. 2a. The results for χ differ by 5% from those obtained with the carbon nucleus as gauge origin and this gauge origin dependence, while relatively small, is reflected in a corresponding deterioration in the description of the current density over the basins of the other oxygen and carbon atoms, fig. 2b.

Fig. 2c shows the current density distribution determined with the gauge origin at the carbon nucleus using a relatively small standard Gaussian basis set (12s6p2d), contracted to [5s4p2d], the 6-311++G(2d, 2p) basis [#1]. Note that the current density distribution over the basin of the carbon atom

[#1] 6-311 G: ref. [18]; ++, diffuse functions: ref. [19]; 2d2p, polarization functions: ref. [20].

in this figure is similar to that in fig. 2a obtained using the larger basis set with the same gauge origin, while the distributions over the oxygen atoms are quite different and clearly ill-behaved, as current loops within their basins fail to close. Fig. 2d shows the current density distribution obtained using the same small basis set with gauge origin at one of the oxygen nuclei. The current distribution within the basin of the gauge origin is well behaved and again similar to the corresponding oxygen distribution shown in fig. 2a or 2b obtained using the larger basis set. The distributions over the basins of the other two atoms however, are not well behaved and differ radically from those shown in fig. 2a. Unsurprisingly, the corresponding conventional CPHF values of χ and σ^C are in serious error for either gauge origin, table 1. This is evident not only in terms of the poor agreement with experiment, but also from the extreme gauge dependence in the values of the calculated χ.

Table 1 also lists the value of χ and σ obtained by summing the atomic contributions (in a manner described below) determined using both the large and small basis sets. The results reflect what the maps have illustrated, that the current density, and hence the properties it determines, are best described an atom at a time, with the nucleus as gauge origin. In fact a small basis set is able to reproduce the results obtained using a much larger set, when the properties are determined in this manner.

2.2. Atomic contributions to magnetic properties

The molecular magnetic susceptibility tensor component $\chi_{\alpha\beta}$ and the set of nuclear magnetic shielding tensor components $\sigma^N_{\alpha\beta}$ are related to the first-order current density induced by a magnetic field in the β direction, $j^1_\beta(r)$, as follows, where r is the real space position vector relative to an arbitrary origin (not necessarily the gauge origin), r_N is the real space position vector relative to nucleus N and the integrations are over all of real space,

$$\chi_{\alpha\beta}=\frac{1}{2cB}\int \mathrm{d}r\,[r\times j^1_\beta(r)]_\alpha=\int \mathrm{d}r\,\chi_{\alpha\beta}(r)\,, \qquad (5)$$

$$\sigma^N_{\alpha\beta}=-\frac{1}{cB}\int \mathrm{d}r_N\,[r_N\times j^1_\beta(r)/r_N^3]_\alpha$$

$$=\int \mathrm{d}r\,\sigma^N_{\alpha\beta}(r)\,. \qquad (6)$$

The property densities $\chi_{\alpha\beta}(r)$ and $\sigma^N_{\alpha\beta}(r)$ defined in this manner [21] may be used to define atomic contributions [4,14] $\chi_{\alpha\beta}(\Omega)$ and $\sigma^N_{\alpha\beta}(\Omega)$, such that their sum equals the molecular values $\chi_{\alpha\beta}$ and $\sigma^N_{\alpha\beta}$. Thus $\sigma^N_{\alpha\beta}(\Omega)$, the contribution of atom Ω to the $\alpha\beta$ component of the shielding tensor of nucleus N, is defined by the integration of $\sigma^N_{\alpha\beta}(r)$ over the basin of atom Ω,

$$\sigma^N_{\alpha\beta}(\Omega)=-\frac{1}{cB}\int_\Omega \mathrm{d}r_N\,[r_N\times j^1_\beta(r)/r_N^3]_\alpha$$

$$=\int_\Omega \mathrm{d}r\,\sigma^N_{\alpha\beta}(r)\,. \qquad (7)$$

Using this expression the shielding tensor of any particular nucleus N in a molecule can be understood in terms of separate contributions from each atom in a molecule.

The magnetic susceptibility density $\chi_{\alpha\beta}(r)$ given in eq. (5) is origin dependent. The atomic contribution $\chi_{\alpha\beta}(\Omega)$ should however, be origin independent if it is to reflect the characteristics of the atom and thus be compared among different molecules, i.e. it should be defined only in terms of properties of the atom. This may be accomplished while preserving the additivity of the atomic contributions, and the resulting expression for $\chi_{\alpha\beta}(\Omega)$ is as follows, its detailed derivation being given elsewhere,

$$\chi_{\alpha\beta}(\Omega)=\frac{1}{2cB}\Big[\int_\Omega \mathrm{d}r\,[r_\Omega\times j^1_\beta(r)]_\alpha$$

$$+\sum_{l=1}^{m}\Big((R_{\mathrm{cp},l}-R_\Omega)\times\int_l \mathrm{d}S\cdot j^1_\beta(r)\,r_\Omega\Big)_\alpha\Big]$$

$$=\chi^{\mathrm{int}}_{\alpha\beta}(\Omega)+\chi^{\mathrm{ct}}_{\alpha\beta}(\Omega)\,. \qquad (8)$$

This expression is obtained through the substitution $r=r_\Omega+R_\Omega$ where the origin for r_Ω is the nucleus of Ω whose position vector is R_Ω. The first term, $\chi^{\mathrm{int}}_{\alpha\beta}(\Omega)$, represents the α component of the induced "internal" magnetic moment of atom Ω per unit

magnetic field applied in the β direction. The second term involves the summation over each of the m groups connected to atom Ω through a bond critical point of the charge density with position vector $R_{cp,i}$ and lying in the atomic surface of atom Ω. In this term the i^{th} surface integral is the average position-weighted flux of $j^1_\beta(r)$ through the interatomic surface between Ω and group i. The $\chi^{cl}_{\alpha\beta}(\Omega)$ term shows how the current flow between atom Ω and the remainder of the molecule contributes to the magnetic susceptibility tensor and provides a basis for the ring-current model.

The atomic contributions $\chi_{\alpha\beta}(\Omega)$ and $\sigma^N_{\alpha\beta}(\Omega)$ are both determined entirely by the induced current density distribution $j^1_\beta(r)$ of the atom. Since this distribution is accurately determined by the IGAIM method, so too are $\chi_{\alpha\beta}(\Omega)$ and $\sigma^N_{\alpha\beta}(\Omega)$ and the corresponding molecular properties obtained by their summation.

Table 2
Calculated and experimental values of mean magnetic susceptibility χ. Units are cgs-ppm

Molecule	χ (IGAIM)	χ (exp.)	χ (CPHF) [a]
H_2	−3.9	−3.9(g) [b]	−4.0(coec)
LiH	−7.6	−7.6(g) [c]	−8.5(Li)
CH_4	−18.2	−18.7(g) [d], −17.4(g) [d]	−19.3(coec)
NH_3	−16.9	−16(g) [c]	−17.4(N)
H_2O	−13.9	−13.1(g) [c]	−13.9(O)
HF	−10.5	−10.3(g) [c]	−10.4(F)
HCN	−17.3	−16.8(g) [c]	−20.7(C)
N_2	−12.5	−12.6(g) [c]	−14.2(coec)
CO	−12.3	−12.7(g) [c]	−14.4(coec)
CO_2	−21.8	−21.0(g) [c]	−31.7(coec)
CS_2	−46.7	−47.8(l) [c]	−153.9(coec)
CSO	−36.6	−32.4(g) [c]	−96.6(C)
F_2	−12.6	−9.7(g) [c]	−21.0(coec)
H_2CO	−8.4	−6.9(g) [d]	−13.0(O)
C_2H_2	−22.2	−21(g) [c]	−24.9(coec)
C_2H_4	−20.7	−19.7(g) [d], −18.8(g) [d]	−24.3(coec)
C_2H_6	−28.5	−27.4(g) [d], −26.8(g) [d]	−33.1(coec)
c-C_3H_4	−27.6	−29(g) [c]	−40.3(C3)
allene	−28.5	−25(g) [d]	−38.9(coec)
c-C_3H_6	−41.5	−39.9(g) [d], −39.2(g) [d]	−48.2(coec)
propene	−32.0	−31.5(g) [d]	−43.7(C2)
C_3H_8	−40.0	−40.5(g) [d], −38.6(g) [d]	−51.2(coec)
butadiene	−35.4	−32.1(g) [d]	−58.1(coec)
C_4H_{10}	−52.2	−50.0(g) [d]	−74.9(coec)
C_5H_{12}	−63.6	−63.1(g) [b]	−109.7(coec)
C_6H_6	−59.7	−54.8(g) [d]	−87.7(coec)
CH_3NH_2	−25.3	−27.0(l) [b]	−32.1(C)
CH_3OH	−22.0	−21.9(g) [b]	−27.7(O)
CH_3F	−18.8	−18(g) [c]	−24.1(F)
CH_2F_2	−22.3	−24.0(g) [c]	−37.9(C)
CHF_3	−27.8	−30±4 [d]	−49.2(C)
CF_4	−33.1	−36±5 [d]	−59.0(coec)
CH_3CN	−30.2	−27.6(l) [c]	−38.5(C1)
c-C_2H_4O	−32.2	−30.7(g) [d]	−42.3(O)
CH_3CH_2OH	−34.2	−33.7(l) [d]	−47.0(C1)
HCOOH	−21.3	−19.9(l) [d]	−32.1(C)

[a] The gauge origin is denoted in parentheses; (coec) centre of electronic charge.
[b] Ref. [24]. [c] Ref. [16]. [d] Ref. [25].

3. Results

All CPHF calculations were done using CADPAC [22] modified to produce a set of first-order wavefunctions in a format suitable for calculation of the atomic contributions using PROAIM [23]. One set of first-order wavefunctions was obtained for each symmetrically unique atom in a molecule by solving the CPHF equations with the gauge-origin placed at the nucleus of the atom. The computation time required to solve the set of CPHF equations for a single gauge origin, using CADPAC, is about 10% of the total time required to perform the unperturbed SCF calculation and transform the two-electron integrals from the AO basis of the MO basis. All of the molecules presented here were geometry optimized at the same basis set used from the CPHF calculations.

Calculated and experimental mean magnetic susceptibilities χ are given in table 2 for molecules of varying size and magnetic response behavior. The calculated values are obtained using the 6-311++g(2d, 2p) basis set [18–20] by the IGAIM method and by the conventional CPHF method with the indicated gauge origins. In general, the IGAIM results are in excellent agreement with experiment even with this relatively small basis set, while the conventional CPHF results are significantly in error. The basis set was chosen because it is known to yield relatively accurate ground state charge distributions. Based upon a comparison of results for methane, ethane and propane [3], the IGAIM results are comparable to or slightly better than those obtained using the IGLO method which uses a basis of (11s7p2d) contracted to [7s6p2d].

Shown in table 3 are the IGAIM calculated absolute mean chemical shielding values for the carbon nuclei σ^C in a set of compounds for which corresponding experimental gas phase values have recently been obtained at low pressure [17,26]. Also shown are the conventional CPHF values, obtained with the carbon nucleus as gauge origin. In all cases the values calculated using the IGAIM method are in better agreement with experiment than those of the conventional CPHF method. Absolute agreement with experimental values is not to be expected since the experimental values were obtained at 300 K and include the effects of rotation and vibration, among other effects which the CPHF method neglects. While the basis set is adequate for susceptibility calculations, it does not provide an accurate enough description of the unperturbed wavefunction in the region of the carbon nuclei where the shielding density is largest. The IGAIM results are again comparable to those obtained by the IGLO method [3].

Table 3
Calculated and experimental mean carbon shielding σ^C in ppm

Molecule	σ^C (IGAIM)	σ^C (CPHF)	σ^C (exp.)
CH_4	197.4	198.5	195.1 [a]
HCN	79.9	89.5	82.1 [a]
C_2H_2	119.3	127.0	117.2 [a]
C_2H_4	66.4	73.4	64.5 [a]
C_2H_6	186.3	192.3	180.9 [a]
C_3H_4(C1)	119.5	130.2	115.2 [a]
C_3H_4(C2)	−34.8	−22.4	−29.3 [a]
c-C_3H_6	200.2	211.1	185.0 [b]
C_3H_8(C_1)	178.7		170.8 [b]
C_3H_8(C_2)	177.3		169.1 [b]
C_4H_{10}(C_1)	179.9		173.5 [b]
C_4H_{10}(C_2)	169.5		160.0 [b]
C_6H_6	61.5	82.1	57.9 [b]
CO	−7.4	−11.9	1.0 [a]
CO_2	57.9	78.9	58.8 [a]
CS_2	−41.1	51.9	−8.0 [a]
CSO	21.9	78.2	30.0 [a]
CH_3NH_2	167.0	173.9	158.3 [a]
CH_3OH	148.0	155.8	136.6 [a]
CH_3F	130.2	140.0	116.8 [a]
CF_4	86.0	122.3	64.5 [a]
CH_3CN(C1)	72.5	86.8	73.8 [a]
CH_3CN(C2)	194.7	205.0	187.7 [a]
EtOH(C1)	141.0		127.6 [b]
EtOH(C2)	178.0		168.5 [b]
HCOOH	32.2	50.2	23.7 [b]

[a] Ref. [17]. [b] Ref. [26].

4. Conclusion

The use of the natural gauge origin for each atom in a molecule yields relatively accurate estimates of molecular magnetic response properties, as corresponding sums of separately determined atomic contributions. This practical application of the theory of atoms in molecules enables one to treat larger molecules than would otherwise be possible using conventional CPHF and a basis set of given size. The atomic contributions themselves are subject to physical interpretation and provide a deeper understand-

ing of the response of a molecule to a magnetic field. This is to be demonstrated in a separate paper along with the ability of atoms in molecules to recover Pascal's transferable group contributions [24] to the magnetic susceptibility for the methyl and methylene groups in normal hydrocarbons.

Acknowledgement

The authors would like to thank Dr. K.E. Laidig for his help in modifying CADPAC [22] to obtain the wavefunctions in a format suitable for PROAIM [23].

References

[1] W.N. Lipscomb, Advan. Magn. Res. 2 (1966) 137; MTP Intern. Rev. Sci. 1 (1972) 167.
[2] F. Keil and R. Ahlrichs, J. Chem. Phys. 71 (1979) 2671; P. Lazzeretti, R. Zanasi and B. Cadioli, J. Chem. Phys. 67 (1977) 382; P. Lazzeretti and R. Zanasi, J. Chem. Phys. 68 (1978) 832.
[3] W. Kutzelnigg, U. Fleischer and M. Schindler, Nucl. Magn. Reson. Basic Principles Progr. 23 (1990) 165.
[4] R.F.W. Bader, Atoms in molecules – a quantum theory (Oxford Univ. Press, Oxford, 1990).
[5] D.W. Davies, The theory of the electric and magnetic properties of molecules (Wiley, New York, 1990).
[6] S.T. Epstein, The variation method in quantum chemistry (Academic Press, New York, 1974).
[7] S.I. Chan and T.P. Das, J. Chem. Phys. 37 (1962) 1527.
[8] R. Ditchfield, Mol. Phys. 27 (1974) 789.
[9] W. Kutzelnigg, Israel J. Chem. 19 (1980) 193.
[10] A.E. Hansen and T.D. Bouman, J. Chem. Phys. 82 (1985) 5035.
[11] P.J. Stephens and K.J. Jalkanen, J. Chem. Phys. 91 (1989) 1379.
[12] T. Helgaker and P. Jørgensen, J. Chem. Phys. 95 (1991) 2595.
[13] J. Geertsen, Chem. Phys. Letters 188 (1992) 326.
[14] R.F.W. Bader, J. Chem. Phys. 91 (1989) 6989.
[15] K.E. Laidig and R.F.W. Bader, J. Chem. Phys. 93 (1990) 7213; R.F.W. Bader, T.A. Keith, K.M. Gough and K.E. Laidig, Mol. Phys. (1992), to be published.
[16] B.R. Appleman and B.P. Dailey, Advan. Magn. Res. 7 (1974) 231.
[17] A.K. Jameson and C.J. Jameson, Chem. Phys. Letters 134 (1987) 461.
[18] R. Krishan, J.S. Binkley, R. Seeger and J.A. Pople, J. Chem. Phys. 72 (1980) 650.
[19] T. Clark, J. Chandreshakar, G.W. Spitznagel and P. von R. Schleyer, J. Comput. Chem. 4 (1983) 294.
[20] M.J. Frisch, J.A. Pople and J.S. Binkley, J. Chem. Phys. 80 (1984) 3265.
[21] C.J. Jameson and A.D. Buckingham, J. Chem. Phys. 73 (1980) 5684.
[22] R.D. Amos and J.E. Rice, CADPAC: the Cambridge analytic derivatives package, Cambridge, UK.
[23] F.W. Biegler-Konig, R.F.W. Bader and T.-H. Tang, J. Comput. Chem. 13 (1982) 317.
[24] L.N. Mulay and E.A. Bordeaux, Theory and applications of molecular diamagnetism (Wiley, New York, 1976).
[25] M. Schindler and W. Kutzelnigg, J. Am. Chem. Soc. 105 (1983) 1360.
[26] C.J. Jameson, Nucl. Magn. Reson. Spectry. Per. Rept. (1990) 48.

2. ANALYSIS OF THE MAGNETIC FIELD INDUCED CURRENT DENSITY DISTRIBUTIION

2-1 Introduction

Schrödinger introduced the electronic charge and current densities and the quantum equation of continuity relating them

$$(d\rho(\mathbf{r})/dt) = -\nabla\cdot\mathbf{J}(\mathbf{r}) \qquad (1)$$

in his fourth paper[1] on "wave mechanics". In this paper he expressed the hope that the definitions and statements it contained would prove useful in the elucidation of the magnetic properties of atoms and molecules, and in explaining the flow of electricity in solid bodies. The electronic charge density $\rho(\mathbf{r})$ is the measureable expectation value of a quantum observable, the charge density operator $\hat{\rho}(\mathbf{r})$[2]

$$\hat{\rho}(\mathbf{r}) = -e\sum_i \delta(\hat{\mathbf{r}}_i - \mathbf{r}) \qquad (2)$$

while the operator for the electronic current density, in analogy with the classical result, is expressible as the product of $\hat{\rho}(\mathbf{r})$ and the observable for

the electronic velocity, $\hat{\pi}(\mathbf{r})/m$.

$$\hat{J}(\mathbf{r}) = (-e/2m)\sum_i \{\hat{\pi}(\mathbf{r}_i)\delta(\hat{\mathbf{r}}_i - \mathbf{r}) + \delta(\hat{\mathbf{r}}_i - \mathbf{r})\hat{\pi}(\mathbf{r}_i)\} \quad (3)$$

The velocity operator for the i^{th} electron in the presence of a magnetic field B is given by

$$\hat{\pi}(\mathbf{r}_i)/m = \{\hat{\mathbf{p}}_i + (e/c)\mathbf{A}(\mathbf{r}_i)\}/m \quad (4)$$

where $\hat{\mathbf{p}}_i = -i\hbar\nabla_i$ is the corresponding linear momentum operator and $\mathbf{A}(\mathbf{r}_i)$ is a vector potential related to B by, $\mathbf{B} = \nabla_i \times \mathbf{A}(\mathbf{r}_i)$. For uniform B, the vector potential $\mathbf{A}(\mathbf{r}_i)$ can be expressed most simply as $(1/2)\mathbf{B}\times\mathbf{r}_i$, where the (common) origin of the $\mathbf{r}_i$ is arbitrary. Making use of eqn. (4), the single-particle current density $\mathbf{J}(\mathbf{r})$ describing the flow of N electrons in a magnetic field is given by

$$\mathbf{J}(\mathbf{r}) = \langle\psi|\hat{\mathbf{J}}|\psi\rangle = -(eN/2m)\int d\tau' \{\psi^*\hat{\pi}\psi + (\hat{\pi}\psi)^*\psi\}$$

$$= -(eN/2m)\int d\tau' \{\psi^*\hat{\mathbf{p}}\psi + (\hat{\mathbf{p}}\psi)^*\psi\} + (e/mc)\rho(\mathbf{r})\mathbf{A}(\mathbf{r}) \quad (5)$$

where $\int d\tau'$ implies a summation over all electronic spin coordinates and an integration over the spatial coordinates of all electrons but one.

The topology of $\rho(\mathbf{r})$ is made quantitative through the flow of the trajectories of its associated gradient vector field $\nabla\rho(\mathbf{r})$.[3] This field, in addition to defining an atom Ω in a molecule through the requirement of zero flux of the $\nabla\rho(\mathbf{r})$ field through the atomic surface $S(\Omega)$,[3] eqn. (6)

$$\nabla\rho(\mathbf{r})\cdot\mathbf{n}(\mathbf{r}) = 0 \qquad \forall\ \mathbf{r} \in S(\Omega,\mathbf{r}) \quad (6)$$

defines a system's atomic connectivity to yield a description of its structure and structural stability.[3] The basic aspects of the theory of atoms in molecules relevant to this work are summarized in Chapter 4 and in the Appendix. In addition, the topology of the divergence of the $\nabla\rho$ field, the laplacian of the charge density, recovers the basic tenets of

electronic structure models and enables one to predict reactive sites in a molecule. The essential features of the topology of $\rho(\mathbf{r})$ in the CO_2 molecule are shown in Fig. 2-1.

The topology of the vector current field $\mathbf{J}(\mathbf{r})$ defined in eqn. (5) should also be of interest since this field determines the magnetic properties of a closed-shell electronic system in a magnetic field.[4] Fig. 2-1 depicts some basic features of the $\mathbf{J}(\mathbf{r})$ field for the CO_2 molecule.

2-2 The First Order Magnetically Induced Current Density $\mathbf{J}^{(1)}(\mathbf{r})$

In a perturbation expansion of the magnetic field induced current $\mathbf{J}(\mathbf{r})$ with respect to the field strength B the first-order term in the expansion is (see chapters 1 and 3)

$$\mathbf{J}^{(1)}(\mathbf{r}) = -(en/m)\int d\tau' \left\{ \psi^{(0)*}\hat{\mathbf{p}}\psi^{(1)} + \psi^{(1)*}\hat{\mathbf{p}}\psi^{(0)} \right\} - (e^2/mc)\mathbf{A}(\mathbf{r})\rho^{(0)}(\mathbf{r})$$

$$= \mathbf{J}_p^{(1)}(\mathbf{r}) + \mathbf{J}_d^{(1)}(\mathbf{r}) \qquad (7)$$

where $\psi^{(1)}$ is the first-order correction to the unperturbed molecular wavefunction due to presence of the magnetic field and the separate terms $\mathbf{J}_p^{(1)}(\mathbf{r})$ and $\mathbf{J}_d^{(1)}(\mathbf{r})$ are called the "paramagnetic" and "diamagnetic" contributions to $\mathbf{J}^{(1)}(\mathbf{r})$ respectively. Unlike the total current $\mathbf{J}^{(1)}(\mathbf{r})$, these terms are not unique but depend on the arbitrarily chosen gauge of the vector potential $\mathbf{A}(\mathbf{r})$ (see chapter 1). The zeroth and second-order terms in the expansion of $\mathbf{J}(\mathbf{r})$ vanish identically and the higher-order terms are negligible relative to $\mathbf{J}^{(1)}(\mathbf{r})$ unless the field strength is very large. The first-order current density given in eqn. (7) determines the commonly measured second-order molecular magnetic reponse properties, namely the magnetic

susceptibility and nuclear magnetic shielding tensors,[4] as will be shown in chapter 3.

This chapter delineates and classifies the possible flows of the first-order vector current field $\mathbf{J}^{(1)}(\mathbf{r})$ in terms of the critical points of the field as well its symmetry properties. The topological analysis is based in part on the general scheme given by Reyn[5] for the classification of the critical points exhibited by a system of three linear differential equations. Gomes' pioneering analysis of the current density topology[6] was limited by having to rely on the incomplete information contained in relatively inaccurate planar displays of $\mathbf{J}^{(1)}(\mathbf{r})$ which were present in the literature. The availability of relatively accurate current distributions for polyatomic molecules made possible by the IGAIM[7] and continuous gauge transformation[8] methods described in chapter 1 enables one to unambiguously locate and analyze the critical points for the full three-dimensional $\mathbf{J}^{(1)}(\mathbf{r})$ field.

2-3 Topological Analysis of $\mathbf{J}^{(1)}(\mathbf{r})$

The current density distribution $\mathbf{J}^{(1)}(\mathbf{r})$ is a continuous vector field whose direction of flow is conveniently represented in terms of its trajectories, curves in real space which are parallel to $\mathbf{J}^{(1)}(\mathbf{r})$ at each point $\mathbf{r}$. Since the $\mathbf{J}^{(1)}(\mathbf{r})$ field is continuous, each point $\mathbf{r}$ at which $\mathbf{J}^{(1)}(\mathbf{r})$ does not vanish lies on a single trajectory. As an example, a representative set of trajectories of the $\mathbf{J}^{(1)}(\mathbf{r})$ field are shown in Fig. 2-2 for a plane containing the nuclei in the CO_2 molecule, where the applied magnetic field is perpendicular to the plane. While the diamagnetic and paramagnetic contributions to $\mathbf{J}^{(1)}(\mathbf{r})$, defined in eqn. (7), are gauge dependent and have no

separate physical significance, the trajectories of the *total* current can exhibit diamagnetic or paramagnetic behaviour in terms of the direction, with respect to the applied field, of the magnetic field generated by the induced current in the region encompassed by the trajectories. In Fig. 2-2, the direction of flow for the outer set of current trajectories contained within the basin of the carbon atom is counter clockwise and the field induced at the carbon nucleus by this current acts in concert with the applied field **B**, which is directed out of the plane of the paper. This current is paramagnetic. A smaller set of paramagnetic trajectories is found in this plane within each oxygen basin, on the bonded side of the nucleus. The primary current flow in the oxygen basins is however, diamagnetic, the current flowing in a clockwise direction inducing a field in the region enclosed by the current which is directed into the plane of the paper. The remainder of this chapter is concerned with the problem of analyzing such molecular current distributions in more detail.

The first-order induced current density is linearly proportional to the field strength B, so the trajectories of $\mathbf{J}^{(1)}(\mathbf{r})$ and their display, as in Fig. 2-2, are independent of B. For very large field strengths, when higher-order terms in the expansion of $\mathbf{J}(\mathbf{r})$ with respect to B become significant, the trajectories of $\mathbf{J}(\mathbf{r})$ will depend on B and the *structure* they determine will exhibit changes at certain "catastrophic" field strengths. Although this work considers only the first-order term $\mathbf{J}^{(1)}(\mathbf{r})$, it clearly provides a foundation for studies including higher order terms of $\mathbf{J}(\mathbf{r})$, studies in which the field strength will be an important parameter. The flow of the trajectories of $\mathbf{J}^{(1)}(\mathbf{r})$ depend on the orientation of the molecule with respect to the applied

field. In this work, the study of the dependence of $\mathbf{J}^{(1)}(\mathbf{r})$ on molecular orientation is restricted to the unique directions defined by the principal axes of the corresponding molecular magnetic susceptibility tensor. In addition to the orientation dependence, $\mathbf{J}^{(1)}(\mathbf{r})$ depends, of course, on the geometry of the molecule. In particular, the symmetry of the molecular geometry is most important in determining the structure of the $\mathbf{J}^{(1)}(\mathbf{r})$ field. In this work, all molecules are considered at their theoretically determined equilibrium molecular geometries.

The vector field $\mathbf{J}^{(1)}(\mathbf{r})$ is everywhere divergenceless because of the equation of continuity, eqn. (1), for stationary states. This equation was also inferred in chapter 1 and is stated explicitly again here because of its importance

$$\nabla\cdot\mathbf{J}^{(1)}(\mathbf{r}) = 0 \tag{8}$$

Applying Gauss' theorem to an integral of eqn. (8) over an infinitesimal volume δV,

$$\int_{\delta V} d\mathbf{r}\nabla\cdot\mathbf{J}^{(1)}(\mathbf{r}) = \int_{\delta S} d\mathbf{S}\cdot\mathbf{J}^{(1)}(\mathbf{r}) = 0 \tag{9}$$

one sees that the continuity condition for the current requires that there be no *three-dimensional* sources or sinks for the trajectories of the $\mathbf{J}^{(1)}(\mathbf{r})$ field, points at which neighboring trajectories either all originate or all terminate, respectively. The divergenceless condition does *not* preclude the existence of *one-* or *two-dimensional* sources and sinks for the trajectories, however. This fact, which is true for any divergenceless field, has only recently become appreciated in physics[10] and is of importance in understanding the topology of $\mathbf{J}^{(1)}(\mathbf{r})$, as will soon become clear.

Maps of magnetically induced first-order current density distributions in molecules were first illustrated in the pioneering computational studies of Lipscomb and co-workers.[11] The topological study of both the total current $\mathbf{J}^{(1)}(\mathbf{r})$ and its orbital contributions, was initiated in important papers by Gomes.[6] Orbital current densities are not divergenceless and, as a consequence, their topologies are considerably more complex than the topology exhibited by the total current considered here. Lazzeretti et al have displayed and discussed the magnetically induced current densities in benzene[12] and the cyclopropenyl cation[13] $C_3H_3^+$ to examine the physical basis of the ring-current model, as well as in ethene,[14] acetylene[15] and cyclopropane.[16] Their analyses were based on relatively inaccurate $\mathbf{J}^{(1)}(\mathbf{r})$ distributions which were calculated using the conventional single gauge origin CPHF method (see chapter 1). Thus, several false conclusions were drawn in their studies, conclusions which will be corrected in this work.

As is true of any vector field, the topology, or *structure*, of the $\mathbf{J}^{(1)}(\mathbf{r})$ field, *hereafter labeled* $\mathbf{J}(\mathbf{r})$ to simplify the presentation, is reflected by the flow of its trajectories in the neighborhood of its *critical* points, points where $\mathbf{J}(\mathbf{r})$ vanishes. For example, critical points in the current distribution of CO_2 are labeled in Fig. 2-2. Critical points are also occasionally referred to as fixed, stagnation, singular, equilibrium or null points. The $\mathbf{J}(\mathbf{r})$ field in the neighbourhood of a critical point at $\mathbf{r}_c$ can be described by a truncated Taylor series expansion about $\mathbf{r}_c$ as

$$\mathbf{J}(\mathbf{r}) = (\mathbf{r}-\mathbf{r}_c)\cdot(\nabla\mathbf{J})_{r=r_c} + (1/2)(\mathbf{r}-\mathbf{r}_c)(\mathbf{r}-\mathbf{r}_c):(\nabla\nabla\mathbf{J})_{r=r_c} + \cdots \qquad (10)$$

In the *linear approximation* only the first term in the expansion is considered and the description of the flow of $\mathbf{J}(\mathbf{r})$ about a critical point reduces to the

solution of a system of three coupled, linear differential equations whose corresponding 3x3 real coefficient matrix is given by the elements of $(\nabla \mathbf{J})_{r=r_c}$.

For a system of three linear differential equations, Reyn[5] has given an excellent pictorial description of all possible types of flow of the solution trajectories about a critical point in terms of the eigenvalues of the coefficient matrix. Since the $\nabla \mathbf{J}$ tensor is, in general, asymmetric its eigenvectors are dependent upon the coordinate system in which $\nabla \mathbf{J}$ is defined, though its eigenvalues are invariant to this choice. To unambiguously characterize $\nabla \mathbf{J}$, it is usefully expressed as a sum of two irreducible tensors, $\nabla \mathbf{J}_a$ and $\nabla \mathbf{J}_s$, where the elements of these tensors are

$$[\nabla \mathbf{J}_a]_{mn} = (1/2)(\partial J_m/\partial x_n - \partial J_n/\partial x_m) \tag{11}$$

and

$$[\nabla \mathbf{J}_s]_{mn} = (1/2)(\partial J_m/\partial x_n + \partial J_n/\partial x_m) \tag{12}$$

The tensor $\nabla \mathbf{J}_a$ is antisymmetric and transforms upon rotation of the coordinate system as a vector. The three independent elements of $\nabla \mathbf{J}_a$ are proportional to the components of the curl of $\mathbf{J}(\mathbf{r})$, $\nabla \mathbf{x} \mathbf{J}(\mathbf{r})$. It will be shown later that the flow of the vector field $\nabla \mathbf{x} \mathbf{J}(\mathbf{r})$, defining the "vorticity" of the current density, is of importance in relating the flow of the $\mathbf{J}(\mathbf{r})$ field to a property of the electronic charge density. The tensor $\nabla \mathbf{J}_s$ is a traceless, rank-two symmetric tensor with five independent elements. Since $\nabla \mathbf{J}_s$ is real and symmetric, it can always be diagonalized to yield a set of eigenvectors which are independent of the coordinate system in which $\nabla \mathbf{J}$ is initially defined. The $\nabla \mathbf{J}_s$ eigenvectors provide a unique coordinate system for the expression of the full asymmetric tensor $\nabla \mathbf{J}$. In this coordinate

system the $\nabla \mathbf{J}$ tensor will be labeled $\nabla \mathbf{J}'$ and appears as

$$\nabla \mathbf{J}' = \begin{matrix} \alpha_1 & c_1 & c_2 \\ -c_1 & \alpha_2 & c_3 \\ -c_2 & -c_3 & \alpha_3 \end{matrix} \tag{13}$$

where the vector $\mathbf{c}$ is $\nabla \times \mathbf{J}(\mathbf{r})/2$, whose components c_1, c_2 and c_3 are the upper triangular elements of $\nabla \mathbf{J}'_a$. The diagonal elements of $\nabla \mathbf{J}'$ are the eigenvalues of $\nabla \mathbf{J}_s$.

The eigenvectors $\mathbf{u}_i$ and eigenvalues λ_i of $\nabla \mathbf{J}'$ at a critical point, together with $\nabla \times \mathbf{J}(\mathbf{r})$, describe the flow of the trajectories of $\mathbf{J}(\mathbf{r})$ in the neighborhood of the point in the linear approximation.

It is known that if the corresponding 3x3 coefficient matrix obtained by linearization of a three-dimensional vector field has three non-zero eigenvalues, then the linear approximation is sufficient to describe the flow of the field trajectories in the neighborhood of the critical point.[10] However, this is no longer necessarily true when one or more of the eigenvalues is zero if the vector field is devoid of any local physical contraints.[10]

The constraint on the $\mathbf{J}(\mathbf{r})$ field that it be *everywhere* divergenceless, eqn. (8), leads to the important result that the linear approximation *is* sufficient to describe the local flow in the case of one zero eigenvalue for the $\nabla \mathbf{J}'$ tensor. To the author's knowledge, this general result for a divergenceless field has not been shown in the literature and so a proof is given here.

Let the two nonzero eigenvalues of $\nabla \mathbf{J}'$ be λ_u and λ_v, with eigenvectors $\mathbf{u}$ and $\mathbf{v}$ respectively. The eigenvector with zero eigenvalue will be labeled $\mathbf{w}$.

Because $\tau(\mathbf{r})$ is divergenceless the two nonzero eigenvalues must be equal and opposite and, as will be shown below, are either both pure real or both pure imaginary, $\lambda = \lambda_v = -\lambda_u$. Translating the critical point $\mathbf{r}_c$ to the origin for convenience, $\mathbf{r}_c = 0$, the components of the current $\mathbf{J}(\mathbf{r})$ at any point $\mathbf{r}(x_u, x_v, x_w)$ in the neighborhood of the critical point are $J_u(\mathbf{r}) = \lambda x_u$ and $J_v(\mathbf{r}) = -\lambda x_v$ for the nonzero roots. The neighbourhood is taken to be sufficiently small so that the the higher-order terms of $J_u(\mathbf{r})$ and $J_v(\mathbf{r})$ are negligible. The third component, $J_w(\mathbf{r})$, is predicted to be zero in the linear approximation and the objective is to determine if there are nonlinear contributions to $J_w(\mathbf{r})$ in the considered neighbourhood of $\mathbf{r}_c$. Since the divergence of $\mathbf{J}(\mathbf{r})$ vanishes everywhere, $\partial J_w(\mathbf{r})/\partial x_w$ must be zero at $\mathbf{r}$ just as it is at $\mathbf{r}_c$, independent of the linear approximation, because $\partial J_u(\mathbf{r})/\partial x_u = -\partial J_v(\mathbf{r})/\partial x_v$. Since $\mathbf{r}$ is an arbitrary point within the neighbourhood of $\mathbf{r}_c$ the only way this can be true is if $J_w(\mathbf{r})$ is constant in the neighbcurhood. Since the neighborhood contains $\mathbf{r}_c$, where $J_w(\mathbf{r}_c) = 0$, then the constant must be zero and thus $J_w(\mathbf{r}) = 0$ everywhere in this neighbourhood, as predicted by the linear approximation.

Thus, the linear approximation is sufficient to predict the flow of $\mathbf{J}(\mathbf{r})$ about a critical point with one zero eigenvalue for the $\nabla\mathbf{J}'$ tensor. In such a case, the flow of $\mathbf{J}(\mathbf{r})$ in the neighborhood of $\mathbf{r}_c$ will be clearly be *planar* with the total current $\mathbf{J}(\mathbf{r})$ being zero along the axis of the eigenvector $\mathbf{w}$ with zero eigenvalue since along this axis $x_u = x_v = 0$, and thus $J_u(\mathbf{r}) = J_v(\mathbf{r}) = J_w(\mathbf{r}) = 0$. A critical point of the $\mathbf{J}(\mathbf{r})$ field whose $\nabla\mathbf{J}'$ tensor has one zero eigenvalue is thus *non-isolated*.

The case of two zero eigenvalues for $\nabla\mathbf{J}'$ is not possible for a

divergenceless field, while for three zero eigenvalues, the linear approximation is, in general, insufficient to describe the local flow in the absence of particular symmetry constraints.

The eigenvalues λ of $\nabla J'$ are the roots of the secular equation

$$-\lambda^3 - \{c^2 + \alpha_1\alpha_2 + \alpha_1\alpha_3 + \alpha_2\alpha_3\}\lambda + [c_1^2\alpha_3 + c_2^2\alpha_2 + c_3^2\alpha_1 + \alpha_1\alpha_2\alpha_3] = 0 \qquad (14)$$

where the expression in square brackets is the determinant of $\nabla J'$. Since $J(r)$ is divergenceless, eqn. (8), the three eigenvalues of $\nabla J'$ must sum to zero. Thus, the possible types of critical points of $\nabla J'$, expressed as (r,s) in terms of rank r, the number of nonzero eigenvalues and signature s, the algebraic sum of their signs, are (3,+1), (3,-1), (2,0) and (0,0). It is possible for two of the eigenvalues to be complex and in such a case the signature refers to the real parts of these eigenvalues.

The absence of (3,+3) or (3,-3) critical points in the $J(r)$ field, critical points at which all trajectories in the neighbourhood of the point originate or terminate, respectively, is another way of stating what has already been inferred from eqn. (9), that the $J(r)$ field can possess no three-dimensional sources or sinks.

When the terms in square brackets in eqn. (14) do not sum to zero, the $\nabla J'$ tensor is nonsingular. In this case all of the eigenvalues of $\nabla J'$ are nonzero and the critical point is of type (3,+1) or (3,-1). In this situation $J(r)$ is nonvanishing in all directions removed from the critical point and the point is thus *isolated* from other critical points.

If the three eigenvalues of $\nabla J'$ at a (3,+1) or (3,-1) critical point are all real then the critical point lies in a *surface* of trajectories which either all originate or all terminate respectively, at the point, a surface

which is locally tangent to the plane defined by the two eigenvectors having eigenvalues of the same sign. Such (3,±1) critical points will be referred to as *surface points*. The eigenvector associated with the eigenvalue having the unique sign defines a pair of anti-parallel trajectories which are perpendicular to the surface at the critical point and originate there if it is (3,-1) and terminate there if it is (3,+1). The phase portraits, Fig. 2-2a, for such (3,+1) and (3,-1) critical points can be linked together, surface trajectories originating at (3,+1) points and terminating at (3,-1) points, with the unique trajectories at each point exhibiting the opposite behavior.

The other possible type of flow about (3,±1) critical points of the $J(\mathbf{r})$ field occurs when one eigenvalue of $\nabla J'$ is real while the other two are complex conjugates of one another. The eigenvector with real eigenvalue defines a pair of trajectories perpendicular to the complex eigenplane at $\mathbf{r}_c$, the trajectories originating at this point if the real part of the complex eigenvalues is positive and terminating there if it is negative. A set of trajectories *spiralling* about the critical point lies (locally) in the complex eigenplane, originating there if it is (3,+1) and terminating there if it is (3,-1). The phase portraits of such critical points, Fig. 2-3b, can again be linked to one another, spiral trajectories originating at a (3,+1) and terminating at a (3,-1) with the unique trajectories again exhibiting the opposite behaviour. The unique pair of trajectories for such (3,±1) critical points serve as axes of revolution for trajectories which spiral away from the complex eigenplane of a (3,+1) point and toward the plane of a (3,-1). These trajectories are closed, although not in simple loops, and do not originate or terminate at critical points. (3,±1) critical points with a pair of complex

eigenvalues will be referred to as *spiral points*.

When the terms in square brackets in eqn. (14) sum to zero and the $\nabla \mathbf{J}'$ tensor is singular, at least one of the eigenvalues of $\nabla \mathbf{J}'$ equals zero, the other two $\lambda_\pm$ being of equal magnitude and of opposite sign and given by

$$\lambda_\pm^2 = -(c^2 + \alpha_1\alpha_2 + \alpha_1\alpha_3 + \alpha_2\alpha_3) \qquad (15)$$

The $\lambda_\pm$ eigenvalues are thus either both real, both imaginary or both zero.

If the $\lambda_\pm$ are nonzero then the critical point is of type (2,0) and, according to the argument presented above, must be non-isolated. It lies on a continuous path of (2,0) critical points, which has been referred to by Gomes as a *stagnation path*.[6] Its direction at a given point along the path is defined by the eigenvector of $\nabla \mathbf{J}'$ with zero eigenvalue.

If the $\lambda_\pm$ are imaginary then the (2,0) critical point lies at the *center* of a set of closed current loops whose direction of flow about the point, clockwise or counterclockwise, is determined by $\nabla \times \mathbf{J}(\mathbf{r})$ at the critical point. The phase portrait for such a critical point is shown in Fig. 2-3c. Of course, $\nabla \times \mathbf{J}(\mathbf{r})$ determines the direction of flow about a spiral point as well. A critical point with a phase portrait such as is shown in Fig. 2-2c is called a *center point* and it lies on a *centre stagnation path*. This is the pattern of flow lines found for a closed-shell atom, with the nucleus lying on the center stagnation path. The center critical point is ubiquitous in the core current distributions induced in atoms and molecules, and elsewhere in molecules with the appropriate symmetry and orientation.

If the $\lambda_\pm$ defined by eqn. (15) are real then the local flow of $\mathbf{J}(\mathbf{r})$ appears as in the phase portrait shown in Fig. 2-3d, a phase portrait which is identical to that generated by the trajectories of the gradient of a scalar

field in the neighbourhood of a saddle point. The same name is applied to this type of (2,0) critical point in a non-gradient vector field such as $J(r)$. A *saddle point* of $J(r)$ is nonisolated and it lies on a *saddle stagnation path*. Two unique pairs of $J(r)$ trajectories are generated by the eigenvectors of $\nabla J'$ associated with the non-zero eigenvalues, the pair associated with the positive eigenvalue originating at the critical point, the other pair terminating there. These unique trajectories serve to separate four (possibly connected) regions of current flow. The $J(r)$ trajectories from these regions can approach, but must ultimately avoid, the saddle critical point.

Neither a center nor a saddle stagnation path can originate or terminate at a point which is not a critical point, since it is composed of (2,0) critical points, which are necessarily non-isolated. It must either be a closed path of (2,0) points or originate and terminate at infinity or at a (0,0) critical point. A (0,0) critical point, one with three zero eigenvalues for $\nabla J'$, thus usually, but not necessarily, lies at the origin or terminus of two or more stagnation paths.

This completes the description of the possible critical points of the $J(r)$ field. Their phase portraits, as shown in Fig. 2-3, in conjuction with a display of the stagnation paths traced out by the non-isolated critical points, summarize the three-dimensional flow of current in a molecule. The set of isolated critical points and stagnation paths have been referred to by Gomes as a *stagnation graph*.[6]

2-4 The Vorticity of $J^{(1)}(r)$

The properties of the vector field defined by the antisymmetric component

∇J_a of $\nabla J(\mathbf{r})$ provide an understanding of the direction of the current flow about a center stagnation path or a spiral point. Its elements, as given in eqn. (11), define the curl of $\mathbf{J}(\mathbf{r})$, whose lines of flow are termed the *vorticity lines.*[17] Since the divergence of a curl is everywhere zero the topology of the $\nabla \times \mathbf{J}(\mathbf{r})$ field is similar, in terms of the possible types of critical points, to that of the $\mathbf{J}(\mathbf{r})$ field itself. From eqn. (7), the general expression for the curl is

$$\nabla \times \mathbf{J}^{(1)}(\mathbf{r}) = (2ie\hbar/m)\int d\tau' \nabla\Psi^{(0)} \times \nabla\Psi^{(1)} -$$

$$(e^2/mc)\{\mathbf{B}\rho^{(0)}(\mathbf{r}) + (1/2)(\mathbf{B}\nabla\rho^{(0)}(\mathbf{r})\cdot\mathbf{r} - \mathbf{r}\nabla\rho^{(0)}(\mathbf{r})\cdot\mathbf{B})\} \qquad (16)$$

Only the terms involving $\rho^{(0)}(\mathbf{r})$ and $\nabla\rho^{(0)}(\mathbf{r})$ are different from zero for a closed-shell atom when the nucleus is chosen as gauge origin. The term $\nabla\rho^{(0)}(\mathbf{r})\cdot\mathbf{B}$ vanishes for the symmetry plane perpendicular to $\mathbf{B}$ in this case and, since $\nabla\rho^{(0)}(\mathbf{r})$ and $\mathbf{r}$ are antiparallel vectors, one obtains

$$\nabla \times \mathbf{J}^{(1)}(\mathbf{r}) = (e^2/mc)\{|\nabla\rho^{(0)}(\mathbf{r})||\mathbf{r}| - \rho^{(0)}(\mathbf{r})\}\mathbf{B} \qquad (17)$$

Thus, the direction of flow of the vorticity lines is perpendicular to the symmetry plane, being parallel to $\mathbf{B}$ for large r and antiparallel to $\mathbf{B}$ in the immediate region of the nucleus. Since most $\nabla \times \mathbf{J}(\mathbf{r})$ trajectroies curl back on themselves to form closed loops, the resulting pattern of the direction of flow lines through the symmetry plane is one of alternating shells, within which the lines of flow are alternately antiparallel to and parallel to the applied field $\mathbf{B}$. In three dimensions, adjacent shells are separated from one another and enclosed within separatrix surfaces defined by trajectories which originate and terminate at a closed saddle stagnation path of the $\nabla \times \mathbf{J}(\mathbf{r})$ field lying at the boundary between the two shells in the symmetry plane. A closed

center stagnation path of the $\nabla x\mathbf{J}(\mathbf{r})$ field lies in the symmetry plane within each shell.

These properties of $\nabla x\mathbf{J}(\mathbf{r})$ in a symmetry plane are illustrated in Fig. 2-4 and Fig. 2-5. What is interesting is that there is a pair of subshells with opposing flow lines for each quantum shell of an atom. These atomic patterns are homeomorphic with the corresponding pattern of alternating negative (charge concentration) and positive (charge depletion) regions generated by $\nabla^2\rho$, the Laplacian of the electron density. They also exhibit the same periodicity in their radii, contracting across a period and the outer shell expanding down a family. The shell structure exhibited by $\nabla x\mathbf{J}(\mathbf{r})$ for the free atom, like the shell structure of the atomic Laplacian, persists in the molecule and herein lies its importance. If molecule formation results in the creation of a centre or spiral point within an atomic basin, then the associated local trajectories of current will be diamagnetic or paramagnetic depending upon whether the critical point is formed in an outwardly or inwardly directed (relative to $\mathbf{B}$) region of flow of the $\nabla x\mathbf{J}(\mathbf{r})$ field, as can be seen by consideration of Stoke's theorem.[17]

$$\oint d\mathbf{S}\cdot\nabla x\mathbf{J}^{(1)}(\mathbf{r}) \;=\; \int d\mathbf{s}\cdot\mathbf{J}^{(1)}(\mathbf{r}) \qquad (18)$$

For example, a centre point created within the second of the inner-most pair of shells will be encircled by a set of paramagnetic current loops because $\nabla x\mathbf{J}(\mathbf{r})$ is parallel to $\mathbf{B}$ within this shell. In the general case when no symmetry plane is present, the relevant quantity which exhibits the shell structure analagous to $\nabla^2\rho$ is $\mathbf{B}\cdot\nabla x\mathbf{J}(\mathbf{r})$.

2-5 Group Theoretical Classification of $\mathbf{J}^{(1)}(\mathbf{r})$

A method is given here for the classification of the induced current distribution in an isolated molecule using molecular point groups. This information complements its topological classification. The group theoretical classification of a $\mathbf{J}^{(1)}(\mathbf{r})$ field involves constructing the appropriate so-called magnetic group.[18]

For a closed-shell system a $\mathbf{J}^{(1)}(\mathbf{r})$ field exhibits the same symmetry properties as does $\mathbf{B}\cdot\mathbf{L}$, the component of the angular momentum vector in the magnetic field direction. Thus, the current distribution generated by a magnetic field applied parallel to the z axis, the principal symmetry axis, transforms as Γ_z, where Γ_z is the one-dimensional irreducible representation in the group $\mathcal{G}$ for a rotation R_z of the molecule about z. Just as the electron density $\rho(\mathbf{r})$ is invariant to all of the symmetry operations of the molecular point group $\mathcal{G}$, the induced vector current $\mathbf{J}^{(1)}(\mathbf{r})$ for an isolated molecule transforms as the totally symmetric representation of the related magnetic group $\mathcal{G}'$.

The magnetic group $\mathcal{G}'$ is always isomorphic with $\mathcal{G}$ or a subgroup of $\mathcal{G}$. For the groups $\mathcal{C}_n$, $\mathcal{C}_{nh}$ and $\mathcal{S}_n$, groups which do not possess a secondary symmetry axis perpendicular to z nor a symmetry plane containing z, $\mathcal{G}'$ is identical to $\mathcal{G}$. This follows since a rotation of the molecule about z transforms as A, A′ or A_g in these groups, as does the current density.

For the remaining point groups $\mathcal{G}'$ is isomorphic with $\mathcal{G}$ for a field applied along the principal symmetry axis. To obtain $\mathcal{G}'$ in these cases, one introduces an antiunitary operator[19] $\mathcal{R}$ which reverses the sign of $\mathbf{J}^{(1)}(\mathbf{r})$ at each point in space, but does not act on the space coordinates. Its

properties are described by Hamermesh.[18]

To obtain the magnetic group $\mathcal{G}'$ isomorphic to $\mathcal{G}$ for a field applied along the principal symmetry axis z one first recognizes that the current distribution transforms as Γ_z, the irreducible representation for the rotation of the molecule about the z axis. The kernel subgroup of Γ_z in $\mathcal{G}$,[18] denoted by $\mathcal{K}(\mathcal{G},\Gamma_z)$, is obtained by taking all of the symmetry operations of $\mathcal{G}$ with character +1 in Γ_z. The current distribution induced by the application of a magnetic field along the z axis is thus invariant to the operations of the kernel subgroup $\mathcal{K}$, in this case a subgroup whose index in $\mathcal{G}$ is always equal to 2.[18] The magnetic group is then obtained by adding to the unitary set of operations in $\mathcal{K}$, an equal number of antiunitary operations. These latter elements are obtained by first generating the coset $A\mathcal{K}$ where A is any one of the remaining symmetry operations in $\mathcal{G}$ with character -1 in Γ_z, followed by their multiplication by the time-reversal operator $\mathcal{R}$, the elements in $\mathcal{R}(\mathcal{G} - \mathcal{K})$. The elements in $\mathcal{K}$ and $\mathcal{R}A\mathcal{K}$ yield a set of operations comprising the magnetic group $\mathcal{G}'$, under which the current transforms as the totally symmetic irreducible representation A, with Γ_z of $\mathcal{G}$ becoming Γ_A of $\mathcal{G}'$. The group $\mathcal{G}'$ obtained in this manner is labelled $\mathcal{G}(\mathcal{K})$.

As examples from this and the following chapter, consider first ethene of $\mathcal{D}_{2h}$ symmetry where the three rotations transform as B_{1g}, B_{2g} and B_{3g}, all of which are associated with a $\mathcal{C}_{2h}$ kernel subgroup. These three representations appear as the totally symmetric representation in a magnetic group $\mathcal{D}_{2h}(\mathcal{C}_{2h})$. Consider next a field applied along the three-fold axis in ethane, where $\mathcal{G} = \mathcal{D}_{3d}$. The molecular rotation about this axis and the associated induced current transform as A_{2g}. The kernel subgroup is $\mathcal{S}_6$ and the current

distribution transforms as A_g of the $\mathcal{D}_{3d}(\mathcal{G}_0)$ magnetic group.

The magnetic group appropriate for a field applied perpendicular to a three-fold or higher symmetry axis is not derived from the molecular point group $\mathcal{G}$ for which the corresponding rotations transform as a degenerate irreducible representation Γ_d, but from one of lower symmetry $\mathcal{G}''$, in which the degeneracy is broken. The appropriate group $\mathcal{G}''$ for the construction of the magnetic group $\mathcal{G}'(\mathcal{K})$ in such a case is then the largest subgroup of $\mathcal{G}$ in which the corresponding molecular rotation belongs to a one-dimensional irreducible representation. In ethane for example, molecular rotations about the x and y axes transform together as E_g in $\mathcal{D}_{3d}$. For a magnetic field applied perpendicular to both the C_3 axis and a C_2 axis the pertinent subgroup $\mathcal{G}''$ and its associated kernel are $\mathcal{C}_{2h}$ and $\mathcal{C}_i$ respectively, and the magnetic group is $\mathcal{C}_{2h}(\mathcal{C}_i)$. The current induced by a such a field transforms as does the A_u irreducible representation of this magnetic group, as illustrated in the following chapter. For a field applied along a C_2 axis in ethane one has the case referred to above where $\mathcal{G}' = \mathcal{G} = \mathcal{C}_{2h}$.

2-6 Symmetry Constraints on the Topology of $\mathbf{J}^{(1)}(\mathbf{r})$

The presence of certain symmetry elements in a magnetic group dictates the presence and/or possible types of critical points which can be present in the $\mathbf{J}(\mathbf{r})$ field - with respect to the symmetry elements. In this section several general cases are considered. Specific examples are given in section 2-7 when actual molecular current distributions are analyzed.

First, consider a unitary center of inversion. Since the inversion operation reverses the direction of the current vector, there must always exist a critical point of the $\mathbf{J}(\mathbf{r})$ field at a unitary center of inversion.

Next, consider the symmetry axis of a unitary proper rotation which is parallel to the applied field. Clearly, at any point along the axis the current must either be parallel to it or vanish. Let the symmetry axis be the z-axis. Then, the $\nabla \mathbf{J}$ tensor appears as

$$\nabla \mathbf{J} = \begin{matrix} \partial J_x/\partial x & \partial J_x/\partial y & 0 \\ \partial J_y/\partial x & \partial J_y/\partial y & 0 \\ 0 & 0 & \partial J_z/\partial z \end{matrix} \qquad (20)$$

with eigenvalues given by the equation

$$-\lambda^3 - \lambda[(\partial J_x/\partial x)(\partial J_y/\partial y) + (\partial J_x/\partial x)(\partial J_z/\partial z) + (\partial J_z/\partial z)(\partial J_z/\partial z)]$$
$$-(\partial J_z/\partial z)[(\partial J_x/\partial y)(\partial J_y/\partial x) - (\partial J_x/\partial x)(\partial J_y/\partial y)] = 0 \qquad (21)$$

Thus, a critical point lying on a unitary symmetry axis parallel to the magnetic field can be of any type - in the absence of other relevant symmetry elements. If the critical point is of type (2,0), then the stagnation path it lies on must be confined to the symmetry axis. This will occur if $(\partial J_z/\partial z)$ equals zero or the terms in brackets multiplying $(\partial J_z/\partial z)$ in eqn. (21) is zero along the length of the stagnation path. Unless demanded by greater symmetry, such as an antiunitary symmetry plane containing the symmetry axis, such a stagnation path would be unstable to any perturbation (symmetric or not) and is unlikely to occur.

Next, consider an antiunitary symmetry plane which is parallel to the applied magnetic field. The operation for an antiunitary symmetry plane is reflection followed by reversal of the current direction. Clearly, at any point on such a plane the current density must either be perpendicular to it or vanish. Let the symmetry plane be the xz plane with the field along the x-axis. Then the x and z components of $\mathbf{J}(\mathbf{r})$ must be zero everywhere in the

plane and the ∇J tensor takes the following form

$$\nabla J = \begin{matrix} 0 & \partial J_x/\partial y & 0 \\ \partial J_y/\partial x & 0 & \partial J_y/\partial z \\ 0 & \partial J_z/\partial y & 0 \end{matrix} \qquad (22)$$

with eigenvalues λ given by the equation

$$-\lambda^3 + \lambda[(J_y/\partial z)(\partial J_z/\partial y) + (\partial J_x/\partial y)(\partial J_y/\partial_x)] = 0 \qquad (23)$$

Thus, a critical point lying in an antiunitary symmetry plane parallel to the applied magnetic field must be of type (2,0), ie. a saddle or center, or of type (0,0). If the critical point is of type (2,0) then the eigenvector (x,y,z) with zero eigenvalue is defined by the equations

$$(\partial J_x/\partial y)y = (\partial J_z/\partial y)y = 0 \qquad (24a)$$

$$(\partial J_y/\partial x)x + (\partial J_y/\partial z)z = 0 \qquad (24b)$$

and is thus directed in the xz symmetry plane. Since a (2,0) critical is necessarily non-isolated, the considered point lies on a stagnation path, and the stagnation path is confined to the symmetry plane. Similarly, it follows that a stagnation path cannot cross such a plane, though it may originate or terminate at a (0,0) point in the plane.

Consider next a unitary symmetry plane which is perpendicular to the applied magnetic field. Then, at any point in the symmetry plane the current density vector is perpendicular to the applied field. Let the field again be along the x-axis so the symmetry plane is the yz plane. The ∇J tensor at any critical point in the symmetry plane takes the form

$$\nabla J = \begin{matrix} \partial J_x/\partial x & 0 & 0 \\ 0 & \partial J_y/\partial y & \partial J_y/\partial z \\ 0 & \partial J_z/\partial y & \partial J_z/\partial z \end{matrix} \qquad (25)$$

with eigenvalues λ given by the equation

$$-\lambda^3 - \lambda[(\partial J_x/\partial x)(\partial J_y/\partial y)+(\partial J_x/\partial x)(\partial J_z/\partial z)+(\partial J_y/\partial y)(\partial J_z/\partial z)-(\partial J_y/\partial z)(\partial J_z/\partial y)]$$

$$+(\partial J_x/\partial x)[(\partial J_y/\partial y)(\partial J_z/\partial z) - (\partial J_y/\partial z)(\partial J_z/\partial y)] = 0 \qquad (26)$$

Thus, any type of critical point is possible, in principle, in such a plane. If the final term is zero then the point will be of type (2,0), which will necessarily occur if the point also coincides with an antiunitary symmetry plane parallel to the field but is unlikely to occur otherwise. In any case, the stagnation path of a (2,0) critical point in a unitary symmetry plane perpendicular to the magnetic field must be locally perpendicular to the plane. If the critical point is a spiral point (two of the eigenvalues λ are complex) then the symmetry plane must coincide with the complex eigenplane while if the critical point is a surface point then the surface must be locally perpendicular to the symmetry plane. Since the current is confined to the plane and all critical points in the plane are isolated (on the plane), one can employ the Poincare-Hopf index theorem to the set of critical points, using the Euler characteristic of +1 for open planar surfaces.[20] The relevant critical points of a *planar* vector field have the following indices:[20] center +1, saddle -1, spiral +1, surface -1.

The sum of the indices of the critical points in a unitary symmetry plane perpendicular to the applied magnetic field must equal one. The Poincare-Hopf index theorem provides a useful check of a critical point analysis of the $\mathbf{J}(\mathbf{r})$ field in this case.

Clearly, all points on the axis defined by the intersection of two mutually orthogonal antiunitary symmetry planes parallel to the applied field must be critical points. Let the magnetic field be along the x-axis. Then

the ∇J tensor has the following simple form

$$\nabla J = \begin{matrix} 0 & 0 & 0 \\ 0 & 0 & \partial J_y/\partial z \\ 0 & \partial J_z/\partial y & 0 \end{matrix} \qquad (27)$$

with eigenvalues given by the equation

$$-\lambda^3 + \lambda[(\partial J_y/\partial z)(\partial J_z/\partial y)] \qquad (28)$$

and thus the point must be of type (2,0) or (0,0). Consider first a point of type (2,0). Clearly, the stagnation path it lies on is parallel to the x-axis. Now consider a (0,0) point on the axis. First of all, since the x-axis is composed entirely of critical points, the (0,0) point must lie between two stagnation paths along the x-axis, one above it and the other below it. Since all of the eigenvalues of ∇J are zero at such a point, this means that one or both of the partial derivatives $(\partial J_y/\partial z)$ and $(\partial J_z/\partial y)$ is zero, from eqn. (28). If $(\partial J_z/\partial y)$ is zero then there must also exist a pair of stagnation paths meeting at the (0,0) point in the plus and minus y directions since in the xy antiunitary symmetry plane the current density can have only a z component and since the xz plane is also an antiunitary symmetry plane. Similarly, if $(\partial J_y/\partial z)$ is zero then there must exist a pair of stagnation paths meeting at the (0,0) point which are locally directed in the plus and minus z-directions. If both $(\partial J_z/\partial y)$ and $(\partial J_y/\partial z)$ are zero then the (0,0) point serves as the meeting point for six stagnation paths, two along each axis, which is the result predicted by the linear approximation. The essential point is that a (0,0) point lying on the intersection of two antiunitary symmetry planes parallel to the magentic field serves as the meeting point for at least four stagnation paths. If the (0,0) point lies at the meeting point of six

stagnation paths, then one can contruct a "topological sphere" about the (0,0) point, a sphere whose surface is everywhere tangent to the current density and on which the critical points are isolated (on the sphere). One may then apply the Poincare-Hopf index theorem to the sphere using the Euler characteristic of +2. The only critical points which exist on the sphere are saddles and centers, with indices -1 and +1, respectively. The sum of the indices of the six critical points must equal +2 and since each critical point lies on a stagnation path originating or terminating at the (0,0) point, it follows that there must be four center stagnation paths and two saddle stagnation paths meeting at such a (0,0) point.

The notion of the "topological sphere" with regard to the behavior of stagnation paths meeting at a (0,0) critical point was initiated by Gomes.[6] He has stated, without proof, a "branching theorem" for *any* (0,0) critical point of the $\mathbf{J}(\mathbf{r})$ field which appears (since no proof was given) to be based on the assumption that a topological sphere of the type mentioned above can always be contructed about a (0,0) point. The assumption is invalid except in the very special case mentioned above.

Finally, it is important to emphasize that the existence of a (2,0) critical point and its associated stagnation path of (2,0) points is unlikely[21] unless demanded by the symmetry of the total system or by very high local symmetry, such as occurs in the core regions of atoms. The existence of a non-symmetry determined stagnation path, and hence a (2,0) critical point, would be unstable to any small perturbation of the vector current field,[21] as brought about through a change in geometry, for example. Similarly, a symmetry determined stagnation path and its associated (2,0) points is

expected to be unstable with respect to symmetry breaking perturbations.

2-7 Results

Free Atoms

The simplest of induced current distributions is exhibited by the free closed-shell atom, the current density being given by the simple expression

$$\mathbf{J}^{(1)}(\mathbf{r}) = -(e^2/mc)\mathbf{B}\times\mathbf{r}\rho^{(0)}(\mathbf{r}) = \mathbf{J}_d^{(1)}(\mathbf{r}) \qquad (29)$$

where the (gauge) origin of $\mathbf{r}$ is the nucleus of the atom or any other point along the field axis passing through the nucleus. This expression follows from the fact that the paramagnetic part of the current $\mathbf{J}_p^{(1)}(\mathbf{r})$, eqn. (7), vanishes identically for a free atom when such a gauge origin is chosen because $\psi^{(1)}$ is then identically zero. This can be seen from eqn. (19) by recognizing that the free atom energy eigenstates $|n\rangle$ are eigenstates of $\mathbf{B}\cdot\hat{\mathbf{L}}$ when the origin of $\hat{\mathbf{L}}$ lies on the $\mathbf{B}$ axis. From eqn. (29) one sees that the free atom induced current is everywhere perpendicular to $\mathbf{B}$ with the trajectories flowing in circular diamagnetic paths according to the term $\mathbf{B}\times\mathbf{r}$. As an example, the vector current induced in the nuclear plane of the neon atom is shown in figure 2-6a while a three dimensional view of the current is shown in Fig. 2-6b. The same picture applies to any free closed-shell atom. The field axis is coincident with a center stagnation path, a path along which the curl of $\mathbf{J}$ is antiparallel to the field, as shown in Fig 2-4 for the nuclear plane.

From eqn. (29), the induced current density magnitude $|\mathbf{J}|$ in a free atom is given by eqn. (30) for a field applied along the x-axis

$$|\mathbf{J}| = (e^2/mc)\rho^{(0)}(\mathbf{r})(y^2+z^2)^{1/2} \qquad (30)$$

and $|J|$ is thus proportional to the ground state electron density $\rho^{(0)}(\mathbf{r})$ and the distance from the field axis. Fig. 2-7 shows a profile of the induced current magnitude in the Neon atom along an axis lying in the plane shown in Fig. 2-6a and passing through the nucleus. The relatively large magnitude of $J(\mathbf{r})$ in the nuclear region (even though it vanishes right at the position of the nucleus) is a reflection of the fact that the electron density exhibits a maximum at the nucleus. This basic feature of the current density magnitude persists for atoms in molecules, even for protons, and is part of the reason why the nuclear magnetic shielding resulting from an induced molecular current distribution is essentially an atomic property, as will be seen in chapter 3.

H_2

Not surprisingly, the simplest of molecular induced current distributions is exhibited by the H_2 molecule. The current flow in H_2 is homeomorphic with that exhibited by a free atom for the principal orientations of the molecule with respect to the magnetic field. When the magnetic field is parallel to the internuclear axis, the current is everywhere perpendicular to the applied field and flows in closed circular loops about a center stagnation path which is coincident with the internuclear axis, the expression for J being given by eqn. (29) when the gauge origin is taken along the field axis. For a field applied along the internuclear axis of any molecule of $\mathcal{D}_{\infty h}$ symmetry, or for any direction in a free atom, the induced current transforms as does the Σ_g^- irreducible representation of $\mathcal{D}_{\infty h}$, as can be seen from Figs. 2-6a and 2-6b.

For a field applied perpendicular to the internuclear axis in H_2 the current trajectories in the plane of the nuclei are ellipsoidal, as shown in Fig. 2-8a, and all flow about a single center critical point which lies at the

center of the molecule. This critical point lies on a center stagnation path parallel to the magnetic field. The magnetic group for the current field induced by a perpendicular magnetic field in H_2, or any other molecule of $\mathcal{D}_{\infty h}$ symmetry is $\mathcal{D}_{2h}(\mathcal{C}_{2h})$ and the field transforms according to the irreducible representation B_{2g} of the $\mathcal{D}_{2h}$ point group. The antiunitary elements of the group are the two symmetry planes parallel to the field and the two C_2 axes perpendicular to the field. Above and below the unitary symmetry plane (the plane shown in Fig. 2-8a), the current flow is similar to that in Fig. 2-8a, but, with the exception of the antiunitary symmetry planes, is no longer constrained to be perpendicular to the applied field. However, in this relatively simple case the current is nearly planar everywhere. The current density magnitude in H_2 for a perpendicular field is shown in the unitary symmetry plane in Fig. 8-b.

LiH

As a consequence of the extensive transfer of charge from Li to H, the charge distribution of the LiH molecule closely appoximates two localized pairs of electrons,[3] one pair in each of the atomic basins, and new topological features are observed for the current induced by a field perpendicular to the internuclear axis, Fig. 2-9. The induced current distribution in LiH or any other molecule of $C_{\infty v}$ symmetry for a perpendicular applied field belongs to the $C_{2v}(C_s)$ magnetic group and transforms as does the B_1 irreducible representation of the C_{2v} point group. The nuclear plane perpendicular to the applied field is again unitary while the other symmetry plane is antiunitary. The C_2 axis, which coincides with the internuclear axis, is anitunitary. The current density exhibits five critical points in

the unitary symmetry plane: three along the internuclear axis which are center points and a linked pair of off-axis (3,±1) surface critical points. The sum of the indices of these critical points equals one, as required by the Poincare-Hopf Index theorem.[20] In Fig. 2-10 a three-dimensional display of the current trajectories associated with the pair of surface points is shown. The off-axis critical points in LiH have been mistakenly identified by Gomes[6] as saddle points based on the use of a previously published, inaccurate and incomplete display of the current density.[11]

The middle center point shown in Fig. 2-9 lies within the second of the inner-most pair of shells of the curl of $\mathbf{J}^{(1)}$ within the Li basin, and its associated current loops are paramagnetic. Each of the remaining center points in Fig. 2-9 is slightly displaced from either the proton or the Li nucleus, lying within the inner-most shell of vorticity lines, and the associated current loops are therefore diamagnetic. The curl map for LiH in the nuclear plane is displayed in Fig. 2-11a to illustrate how the atomic shell structure of this field persists in a molecule. The Laplacian of the charge density in the same plane is shown in Fig. 2-11b to show that the possibility of the paramagnetic current flow could also have been predicted from the similar shell structure exhibited by the $\nabla^2\rho$ field.

The unique pair of trajectories associated with the pair of surface critical points in LiH, Fig. 2-10, flow in the symmetry plane containing the nuclei and separate the three regions of flow about their respective center points, as well as the region of diamagnetic current which flows about the entire molecule and extends outward to infinity, Fig. 2-9. The closed surface of trajectories associated with this pair of critical points encompasses a

region which lies almost entirely within the Li basin. In the internuclear region, this surface is almost coincident with the interatomic surface defined by the trajectories of the $\nabla\rho(\mathbf{r})$ field which terminate at the bond critical point, Fig. 2-9. The two center points within the Li basin lie on a closed center stagnation path, and what appears in the plane shown in Fig. 2-9 to be two separate flows is in fact a cross-section of a single "doughnut-like" (torus) region of current flow with the center stagnation path as its axis, Fig. 2-12. The center point in the proximity of the proton in Fig. 2-9 lies on an open center stagnation path which extends above and below the plane to infinity and serves as the axis for the diamagnetic flow which encompasses the entire molecule. The stagnation graph for LiH in the perpendicular orientation is shown in Fig. 2-13.

BeH_2

The current distribution induced in the BeH_2 molecule for a perpendicular applied field differs from that in LiH because of the presence of off-axis saddle points in place of the surface pair in the unitary symmetry plane, Fig. 2-14. The current distribution of BeH_2 belongs to the same magnetic group as that for the H_2 molecule, $D_{2h}(C_{2h})$. There are five critical points on the internuclear axis, all of which are center points. The directions of flow about each of these centers is consistent with their positions relative to the shell structure exhibited by the curl of $\mathbf{J}$ and $\nabla^2\rho$, Figs. 2-15a and 2-15b, respectively. The presence of center points in the outer core region of Be along the internuclear axis and their associated paramagnetic current flow appears to be characteristic of systems with extensive interatomic charge transfer for magnetic fields applied perpendicular to the direction of charge

transfer. This effect has already been illustrated for LiH, Fig. 2-9, and for the polar system CO_2, Fig. 2-2. In each case the paramagentic flow is localized within the basin of the electropositive atom.

The regions of flow associated with the three center points in the Be basin shown in Fig. 2-14 are separated from one another and from the outer paramagnetic flow which encompassess all three regions, by the linked pairs of trajectories which originate and terminate at the two innermost saddle points along the C_2 axis perpendicular to the internuclear axis. The pairs of trajectories associated with the two outer saddle critical points along this this axis are linked so as to form boundaries separating the paramagnetic flow in Be from the diamagnetic flows in each hydrogen basin and each of these from the diamagnetic flow encompassing the entire molecule. Each of the saddle points shown in Fig. 2-14 lies on a saddle stagnation path extending above and below the unitary symmetry plane. The saddle points along these paths are linked by unique trajectories just as are those in Fig. 2-14. The union of the saddle trajectories associated with each pair of saddle stagnation paths form closed surfaces separating the different regions of current flow in the molecule.

The stagnation graph shown in Fig. 2-16 for the BeH_2 molecule summarizes the three-dimensional behaviour of the induced current flow. The center stagnation path passing through the beryllium nucleus is parallel to the applied field. The innermost saddle paths approach this center path and merge with it at a distance of 0.548 au on either side of the unitary symmetry plane creating (0,0) critical points, and saddle stagnation paths beyond these points. The new saddle stagnation paths, one above and one below the unitary

symmetry plane, define the trajectories which separate the now smaller inner-shell paramagnetic regions from the encompassing paramagnetic region. At 0.012 au beyond the first (0,0) points, the inner-shell paramagnetic stagnation paths coalesce with the new saddle stagnation paths forming another pair of (0,0) critical points. Beyond these points there is a single pair of paramagnetic center paths in the Be atom lying parallel to the field, one above the unitary plane the other below it. Although not shown in Fig. 2-16, moving further away from the Be nucleus along the field axis, the two outermost saddle stagnation paths coalesce with the remaining paramagnetic centre paths at another pair of (0,0) points to yield a pair of saddle paths whose trajectories separate the remaining regions of diamagnetic flow. At an even greater distance above and below the unitary plane, the hydrogen center paths merge with pair of saddle paths to form a pair of diamagnetic centre paths extending to plus and minus infinity.

The critical points in the plane shown in Fig. 2-2 for the CO_2 molecule and lying within the basin of the carbon atom form a set similar to those in the basin of the beryllium atom, Fig. 2-14, and the stagnation graph they generate is homeomorphic with that shown in Fig. 2-16. Fig. 2-17 shows the stagnation graph generated by the current flow within the basin of an oxygen atom of CO_2 for a perpendicular field. As seen in Fig. 2-2, along the internuclear axis in the oxygen basin there are two diamagnetic and one intervening paramagnetic center points. The associated regions of current flow about these points are separated by the pairs of trajectories originating and terminating at the pair of saddle points which lie on the nonbonded side of the oxygen nucleus. The stagnation paths associated with the saddle point

and center point which lie nearest to the oxygen nucleus merge at (0,0) critical points on either side of the unitary symmetry plane to form a closed loop of critical points. The same behavior occurs for the stagnation path of the other saddle point and the middle center point at a greater height above the unitary plane, leaving a single center stagnation path for the remaining diamagnetic current flow in each oxygen basin. The behavior of the stagnation graph for CO_2 above the second set of (0,0) points in the oxygen basins of CO_2 is then similar to that in BeH_2.

H_2O

The remaining types of critical points possible for a $\mathbf{J}(\mathbf{r})$ field, the (3,+1) spiral points, are illustrated in the current flow of the water molecule in the plane of the nuclei when the applied magnetic field is perpendicular to the plane, Fig. 2-18. Diamagnetic spiral trajectories originating at the (3,+1) critical point along one O-H bond are contiguous with those which terminate at the (3,-1) critical point along the second O-H bond. The unique trajectories linking the spiral critical points are shown in Fig. 2-19. Figure 2-20 illustrates the behavior of a pair of closed current trajectories which spiral around the unique trajectories but don't cross the complex eigenplane of the spiral points. There are two center points and a saddle point on the C_2 axis. The center point which nearly coincident with the oxygen nucleus is diamagnetic while other, whose region of flow is very small in the plane, is paramagnetic. The stagnation paths that the three (2,0) critical points shown in Fig. 2-18 lie on are necessarily confined to the antiunitary symmetry plane and are shown in Fig. 2-21 together with projections of the isolated critical points onto the plane. In addition to

the pair of spiral critical points, there is a pair of surface critical points in the plane of the nuclei whose unique pair of trajectories originate at the (3,-1) on the LHS of Fig. 2-18 and terminate at the (3,+1) on the RHS. These trajectories bound the spiral region. A linked pair of surface trajectories generated by this pair of critical points also lie in this plane and bound the core diamagnetic region of the oxygen atom on the nonbonded side. There are two other surface trajectories in this plane, one of which flows into one of the spiral points, the other flowing out of the second spiral point. The magnetic point group for this induced current distribution of H_2O is $\mathfrak{C}_{2v}(\mathfrak{C}_{2})$ and the field transforms as does the B_2 irreducible representation of the C_{2v} point group.

CH_4

Like H_2O, the current distribution in the methane molecule exhibits all possible types of critical points for a field applied perpendicular to a plane containing two protons and the carbon nucleus, Fig. 2-22. There are two sets of spiral pairs in this plane, one pair again associated with the bonded protons, the second lying closer to the carbon nucleus. There are also two sets of surface points. Fig. 2-23 shows the unique trajectories associated with the two pairs of spiral critical points.

C_2H_4

Figure 2-24 illustrates the current induced by a field perpendicular to the plane of the nuclei in the ethene molecule. There are three center critical points on the C-C axis, two slightly displaced from the C nuclei towards the molecular center, the other at the center of inversion, and all three serving as centers for diamagnetic current flows. There are two sets of

spiral critical points shown in Fig. 2-24. Spiral trajectories originating in one C-H bonded region are contiguous with those which terminate at the critical point in the corresponding region of the second proton bonded to the same carbon. The unique pair of trajectories associated with the single real eigenvalue originate at one critical point and terminate at another, with one trajectory on each side of the symmetry plane. What is interesting is that these out-of-plane trajectories link pairs of spiral critical points associated with different carbon atoms, Fig. 2-25. In Fig. 2-26 the out-of-plane behavior of the closed current trajectories which spiral about the unique trajectories of the spiral points is shown. As stated in section 2-5, this current distribution in ethene belongs to the $D_{2h}(C_{2h})$ magnetic group.

Lazzeretti et al,[14] from a study of a similar current map of ethene calculated using the conventional CPHF method, and thus of lower quality, dismissed the spiral flows in ethene as a "basis set error", concluding, for no apparent reason, that they should be center points. The critical points along the C-H bonds do not lie on a symmetry plane parallel to the field and thus are not constrained to be (2,0) points. As shown in section 2-6, (2,0) critical points are unstable with respect to changes in any parameter, particularly a geometric parameter, and their existence is extremely unlikely except when dictated by the appropriate molecular symmetry and orientation, or by very high local symmetry, as in a core region.

C_2H_2, C_2HF, and C_2F_2

The final examples of induced current distributions to be considered in this chapter are those exhibited by acetylene and its fluoro derivatives for fields applied perpendicular to the internuclear axes. Figure 2-27 shows the

induced current in C_2H_2 in the plane of the nuclei. The internuclear axis, which lies on a symmetry plane parallel to the applied field, posseses nine (2,0) critical points. There is a (2,0) center point along each C-H bond which coincides almost exactly with the corresponding bond critical point in the $\nabla\rho$ field, an interesting result since the positions of the critical points are not symmetry determined. These two critical points serve as centers for diamagnetic current flow. In each carbon basin there are two more center critical points, each of which lies relatively close to the carbon nucleus, one on either side. The one on the bonded hydrogen side lies at the center of a very small region of diamagnetic loops while the center point lying on the carbon side is further from the nucleus and serves as the center for a much larger region of paramagnetic loops which are localized within the carbon basin. The two regions of flow about the center points within the carbon basin are separated by trajectories originating and terminating at a saddle point which lies along the C-H bond very near the diamagnetic center point. There are six off-axis critical points in the plane shown in Fig. 2-24. The two lying along the C_2 axis, which lies in a symmetry plane parallel to the applied field, are center points for diamagnetic current flow. The two corresponding regions are separated from one another by trajectories originating and terminating at the saddle critical point which lies at the centre of symmetry in the molecule. The remaining four off-axis critical points are two linked pairs of surface critical points, one pair for each CH group.

The surface points in C_2H_2 have been mistakenly identified as saddle points by Lazzeretti et al.[15] The surface each pair defines encompasses the C-

H bonded current flow as well as the flow about the two center points within the corresponding carbon basin. The surface separates these regions from the diamagnetic flow about the entire molecule as well as the diamagnetic flows centered on the C_2 axis. The behavior of the current flow contained in the CH group surface is slightly different from the flow within the surface found in the LiH molecule, Figs. 2-9 through 2-13. This can be clearly seen from the stagnation graph for C_2H_2 shown in Fig. 2-28. The stagnation paths of the center and saddle points on the hydrogen bonded side of the carbon nucleus within the carbon basin form a small closed loop of critical points, coalescing above and below the internuclear axis at (0,0) points. As in LiH, the apparently separate paramagnetic and bonded diamagnetic regions of current current flow in the CH group actually flow about a single closed center stagnation path, as in Fig. 2-12 for the LiH molecule. The stagnation paths associated with the two center points lying on the C_2 axis perpendicular to the internuclear axis in Fig. 2-27 are not shown in Fig. 2-28, but they merge, above and below the unitary symmetry plane, with the saddle stagnation path passing through the center of symmetry to form diamagnetic center stagnation paths extending to plus and minus infinity at a distance of 0.64 au. above and below the center of symmetry.

Figure 2-29 shows the induced current distribution in the C_2HF molecule in the nuclear plane while the stagnation graph for this molecule is shown in Fig. 2-30. As in C_2H_2, there are nine (2,0) critical points along the internuclear axis. They occur in the same order as those in C_2H_2 though their positions relative to the nuclei are significantly different. The current flow within the fluorine atom is highly localized and entirely diamagnetic,

resembling that of a free atom. Instead of the bonded center critical point that the hydrogen exhibits, the fluorine possesses a single center critical point which is nearly coincident with its nucleus. Each of the two carbon atoms possesses two center points and a saddle point near the nucleus, just as they do in C_2H_2, but in C_2HF the current flow about these points is significantly different for the two atoms. In particular, and somewhat surprisingly, the current flow in the carbon bonded to fluorine is similar to that in C_2H_2, but the flow in the other carbon is significantly different from that in C_2H_2 in that the diamagnetic flow about the center point on the bonded hydrogen side encompasses a much larger region. This observation is consistent with the larger nuclear magnetic shielding of this carbon than the other carbon in C_2HF or than the carbons of C_2H_2.

The C-H bonded center critical point in C_2HF is not coincident with the interatomic surface as it is in C_2H_2. This is mostly because the C-H interatomic surface is shifted slightly towards the proton due to the perturbation by the fluorine substitution. The most obvious difference between the current flows in C_2HF and C_2H_2 is the "conversion" of the center points lying on the C_2 axis perpendicular to the internuclear axis in C_2H_2 into spiral points in C_2HF. This is a result of the breaking of the symmetry plane perpendicular to the internuclear axis. The flow about these points is still diamagnetic, however. The saddle point lying along the internuclear axis between the the two spiral flows, Fig. 2-29, lies on a saddle stagnation path parallel to the applied field, which is converted into a pair of diamagnetic center paths at a height of 0.58 au above and below the unitary symmetry plane.

In C_2F_2 the symmetry plane perpendicular to the internuclear axis is restored and the corresponding critical points are center points, as in C_2H_2. The current induced in the unitary symmetry plane of C_2F_2 is shown in Fig. 2-31 while the stagnation graph is shown in Fig. 2-32. As with the fluorine in C_2HF, each of the fluorines in C_2F_2 possesses a single center critical point nearly coincident with its nucleus and the current flow in the fluorines is again highly localized and entirely diamagnetic. The set of critical points within the carbon basins are somewhat different than in the carbons of either C_2H_2 or C_2HF. There are three center points lying on the internuclear axis near the carbon nucleus, two paramagnetic points lying on either side of the nucleus and a diamagnetic center point nearly coincident with the nucleus. The diamagnetic center point and the paramagentic center point on the carbon bonded side lie on a closed center stagnation path and the doughnut like current distribution flowing about this path is confined within a surface generated by an extra pair of surface critical points within the carbon basin lying relatively near its nucleus. The outer pair of surface critical points in each of the carbon basins exist as they did in the C_2H_2 and C_2HF and they define a surface which encompasses the localized fluorine current and the relatively large region of paramagnetic current flow in the carbon basin. The center points for these two regions of flow lie on a closed center stagnation path, Fig. 2-32. As in Fig. 2-28 for the C_2H_2 molecule, Fig. 2-32 for the stagnation graph of the C_2F_2 molecule does not show the diamagnetic center stagnation paths lying in the symmetry plane perpendicular to the internuclear axis. Just as in C_2H_2, however, these paths coalesce with the saddle path passing through the center of symmetry at a height of 0.64 au above and below

this point, beyond which exists pair of diamagnetic center paths extending to plus and minus infinity.

2-8 Comments

This study has brought into focus the principal properties of the vector current distributions induced in molecules by an applied magnetic field. This has been achieved through a theoretical, topological analysis of a three-dimensional, divergenceless vector field with magnetic symmetry, together with analyses of several actual induced current distributions made available by the methods introduced in chapter 1. Magnetically induced current distributions in molecules are fully three-dimensional vecto· fields, unlike in a free closed-shell atom, and can exhibit four basic flow patterns about the critical points of the distribution, all of which are commonly observed. The vorticity of a magnetic current distribution has been found to exhibit an atomic-like shell structure analagous to the laplacian of the electron density distribution. It is hoped that this work will inspire further investigations, particularly with regard to correlating the observed topological properties of the $\mathbf{J}^{(1)}(\mathbf{r})$ distributions with other molecular properties.

2-9 References

1. E. Schrödinger, *Ann. d. Physik* **81**, 109 (1926).

2. R. F. W. Bader and P. F. Zou, *Chem. Phys. Letters* **191**, 54 (1992).

3. R. F. W. Bader, *Atoms in Molecules - A Quantum Theory* (Oxford University Press, Oxford, 1990).

4. C. J. Jameson and A. D. Buckingham, *J. Chem. Phys.* **73**, 5684 (1980).

5. J. W. Reyn, *Z. Angew. Math. Phys.* **15**, 540 (1964).

6. J. A. N. F. Gomes, *J. Chem. Phys.* **78**, 4585 (1983). J. A. N. F. Gomes,

Local Density Approximations in Quantum Chemistry and Solid State Physics, Eds. J. P. Dahl and J. Avery, (Plenum Press, New York, 1984), p. 145.8. J.A.N.F. Gomes, *Phys. Rev. A*, **28**, 559 (1983).

7. T. A. Keith and R. F. W. Bader, *Chem. Phys. Letters* **194**, 1 (1992).

8. T. A. Keith and R. F. W. Bader, *Chem. Phys. Letters*, submitted (1993).

9. R. F. W. Bader and T. A. Keith, *J. Chem. Phys.*, submitted. T. A. Keith and R.F.W. Bader, *J. Chem. Phys.*, to be submitted.

10. A. Otto, M. Hesse and K. Schindler, *Topological Fluid Mechanics*, (Cambridge University Press, Cambridge UK), 225 (1990). J.M. Greene, *Topological Fluid Mechanics*, (Cambridge University Press, Cambridge UK), 478 (1990).

11. W. N. Lipscomb, *Adv. Mag. Res.*, **2**, 137 (1966). Lipscomb, W. N., *Theoretical Chemistry*, **1**, *MTP Int Rev. Sci.*, Ed. W. B. Brown, (Butterworths, London, 1972) p. 167. R. M. Stevens, R. M. Pitzer and W. N. Lipscomb, *J. Chem. Phys.* **38**, 550 (1963). R. A. Hagstrom and W. N. Lipscomb, *J. Chem. Phys.* **45**, 2378 (1966). E. A. Laws, R. M. Stevens and W. N. Lipscomb, *ibid*, **54**, 4269 (1971). R. M. Stevens and W. N. Lipscomb, *ibid*, **41**, 3710 (1964).

12. P. Lazzeretti, E. Rossi and R. Zanasi, *J. Chem. Phys.* **77**, 3129 (1982).

13. P. Lazzeretti and R. Zanasi, *Chem. Phys. Letters*, **80**, 533 (1981).

14. P. Lazzeretti, E. Rossi and R. Zanasi, *Int. J. Quantum Chem.* **25**, 929 (1984).

15. P. Lazzeretti, E. Rossi and R. Zanasi, *Int. J. Quant. Chem.*, **25**, 1123 (1984).

16. P. Lazzeretti, E. Rossi and R. Zanasi, *J. Am. Chem. Soc.*, **105**, 12 (1983)

17. P. Morse and H. Feshbach, *Methods of Theoretical Physics*, Part 1, (McGraw-

Hill, New York, 1953).

18. M. Hamermesh, *Group Theory and Its Applications to Physical Problems*, (Dover Pub. Inc., New York, 1962).

19. E.P. Wigner, *Group Theory and Its Applications to the Quantum Mechanics of Atomic Spectra*, (Academic Press Inc., New York, 1959).

20. H. Hopf, *Differential Geometry in the Large*, 2nd Edition, (Springer-Verlag), (1989).

21. J. M. Greene, *J. Geophysical Res.*, **93**, 8583 (1988).

Figure 2-1

a) A contour map of the electron density ρ in CO_2 in a plane containing the nuclei. The nuclei are labeled with crosses. The value of ρ for the outer contour is 0.001 au. while the values for the remaining contours increase inwards in steps of $2x10^{-n}$, $4x10^{-n}$, $8x10^{-n}$, with n increasing in steps of unity from -3. Overlaid upon the contour map is the intersection of each C-O interatomic surface with the plane.

b) A relief map of the electron density ρ in CO_2 in a plane containing the nuclei. The electron density exhibits local maxima only at the nuclei. This results in a partitioning of the gradient vector field $\nabla\rho$ into three non-overlapping atomic domains, as shown in c.

c) The gradient vector field of the electron density ρ in a plane containing the nuclei. Each atom is defined as the region of space traversed by the $\nabla\rho$ trajectories which terminate at its nucleus, or equivalently, as the region of space bounded by the surface of $\nabla\rho$ trajectories generated by the corresponding bond critical point(s), labeled by a dot, linking the atom to the rest of the molecule, a surface of zero-flux in the $\nabla\rho$ field, eqn. (6)

d) A contour map of the laplacian of the electron density $\nabla^2\rho$ in a plane containing the nuclei. Solid contours denote negative values for $\nabla^2\rho$, where the electron charge is locally concentrated. Dashed contours denote positive values of $\nabla^2\rho$, where the electronic charge is locally depleted. Each atom possesses an inner shell of charge concentration and an inner shell of charge depletion, which together correspond to the quantum K shell of electronic structure theory. Due to the extensive electron transfer from C to O, the carbon posseses only a second (valence) shell of charge depletion while the

oxygen atoms possess both a second shell of charge concentration and one of charge depletion. The large "hole" in the valence shell of charge charge concentration in the carbon atom is consistent with its high susceptibility to nucleophilic attack. Each oxygen atom possessess a local maximum of charge concentration in the valence shell on its non-bonded side, a critical point of the $\nabla^2\rho$ field which corresponds to the oxygen lone pairs of the Lewis model.

e) Trajectories of the electronic current density induced in CO_2 by an externally applied magnetic field, one whose direction is perpendicular to the plane shown and coming out of the page. The interatomic surfaces in this plane are also shown to demonstrate the essentially atomic nature of the induced current distribution in this highly polar system. Trajectories flowing counterclockwise are paramagnetic and dominate the flow in the carbon atom. This current is responsible for the extremely large downfield shift of the perpendicular component of the carbon nuclear magnetic shielding tensor.

f) Contour map of the flux, through the plane shown, of the curl of the electronic current density shown if e. Solid contours denote antiparallel flux relative **B** while dashed contours denote parallel flux. The curl of the induced current exhibits a shell structure similar to the laplacian of the charge density shown in d. Using this similarity, together with Stokes' theorem, the possible regions of paramagnetic current flow in CO_2 can be predicted from $\nabla^2\rho$.

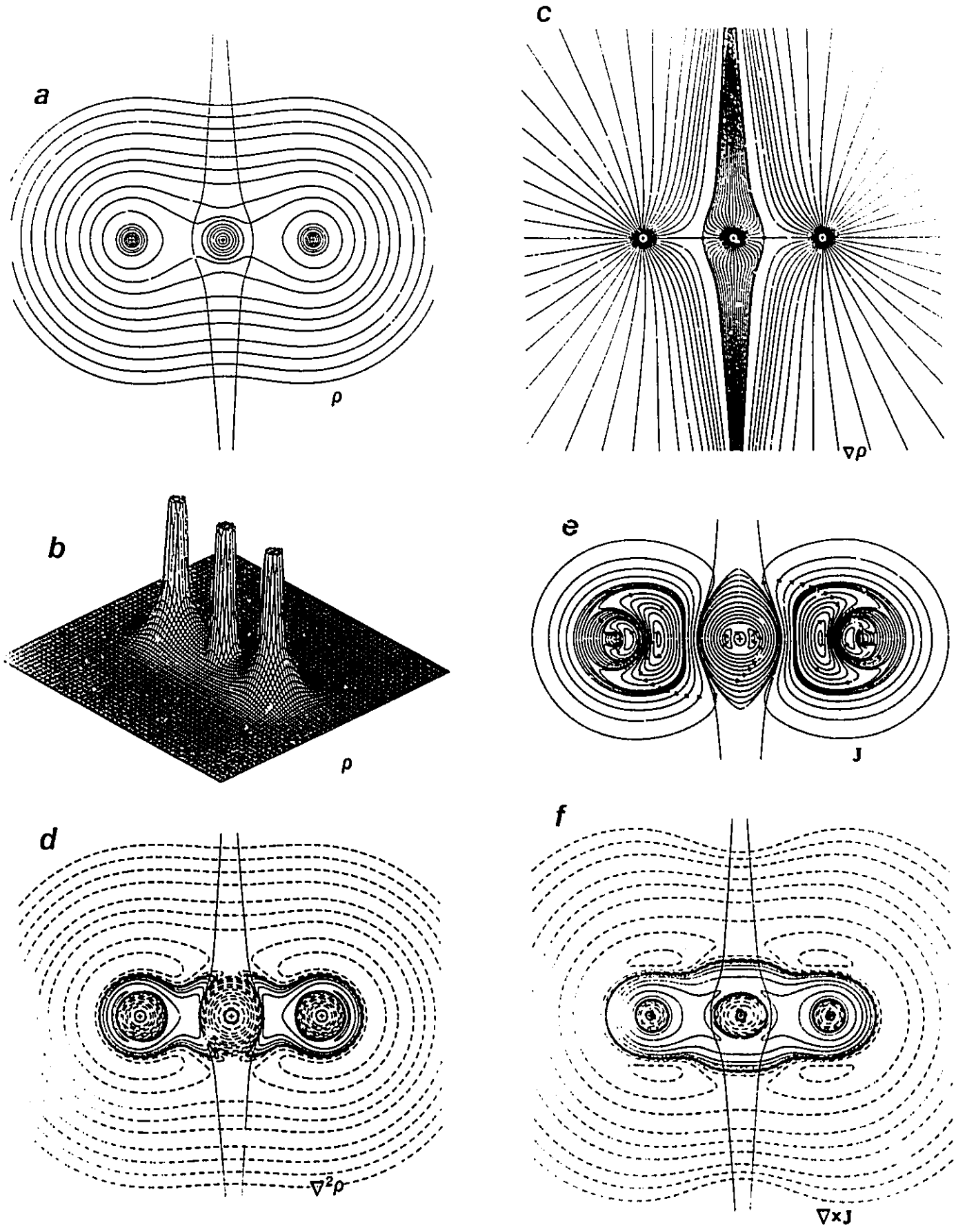
a
ρ
b
ρ
c
∇ρ
d
∇²ρ
e
J
f
∇xJ

Figure 2-2

Display of the first-order induced current density in a plane containing the internuclear axis of the carbon dioxide molecule for a magnetic field directed perpendicular to and coming out of the page. Clockwise directed flow is diamagnetic. Critical points in this and the following displays of $\mathbf{J}^{(1)}(\mathbf{r})$ are denoted as follows: (2,0) center point by a filled circle ; (2,0) saddle point by a cross (X); (3,±1) surface points by filled squares; and (3,±1) spirals by open squares. Nuclei are denoted by plus signs (+). The direction of current flow is not shown about the three center points in the carbon basin (though they can be inferred from the remaining directions of flow). The flow about the center point coincident with the carbon nucleus is diamagnetic (clockwise) while the flow about the other two center points is paramagnetic.

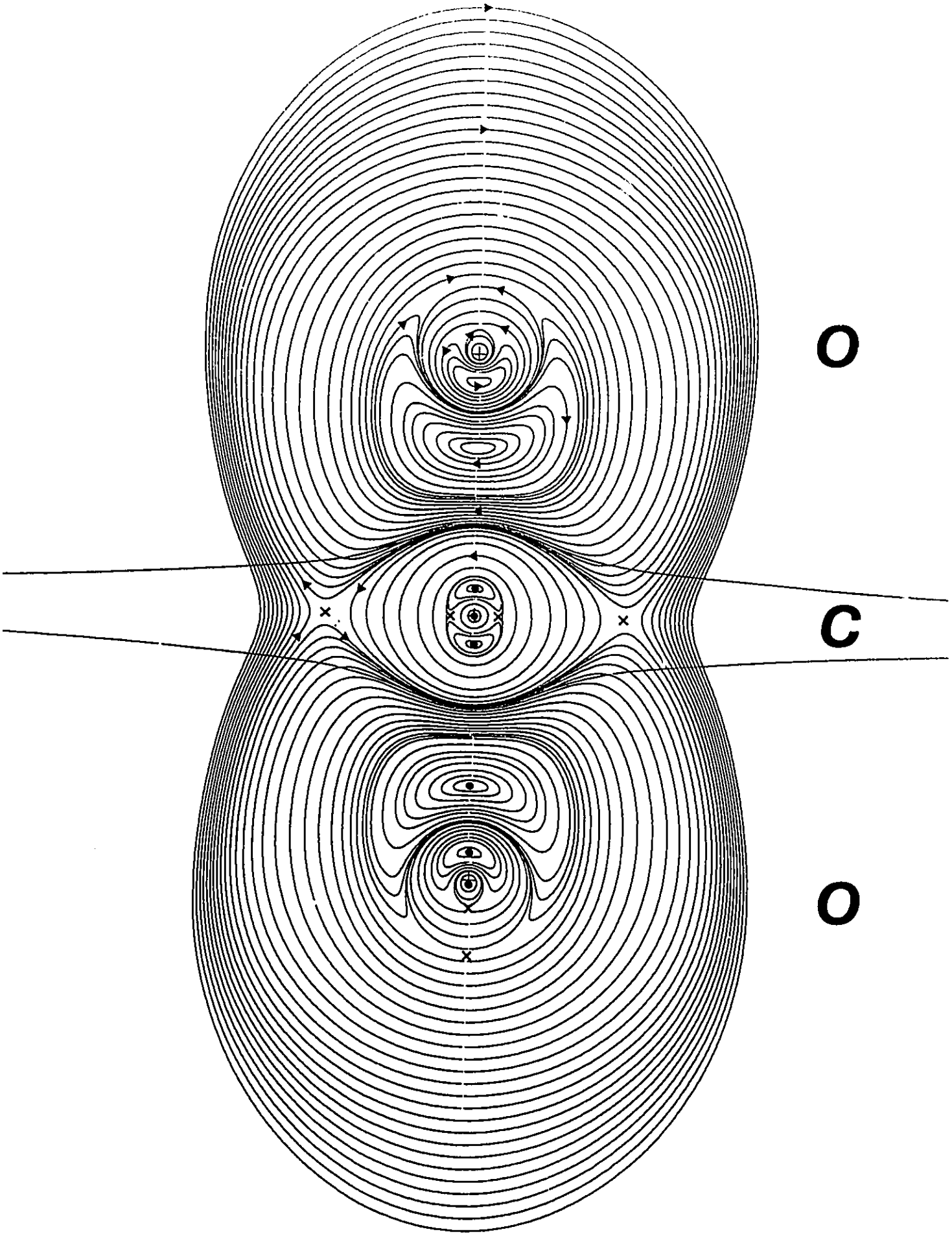
O
C
O

Figure 2-3

Displays of the trajectories of $\mathbf{J}^{(1)}(\mathbf{r})$ in the neighbourhood of a critical point.

a) A (3,+1) surface critical point. Trajectories originating at the critical point lie in a surface. A unique pair of trajectories, locally perpendicular to the surface, terminates at the point. The phase portrait of a (3,-1) surface critical point is obtained by reversing the directions of all trajectories.

b) A (3,+1) spiral critical point. An infinite number of spiral trajectories (only one is shown) originate at the critical point while a unique pair of trajectories, locally perpendicular to the spiral plane, terminates there. The phase portrait of a (3,-1) spiral critical point is obtained by reversing the directions of all trajectories.

c) A (2,0) centre point which serves as the locus for a set of closed, locally planar, current loops.

d) A (2,0) saddle point at which one pair of trajectories originates and another pair terminates. All other trajectories avoid the critical point.

In c and d the critical point is non-isolated and lies on a stagnation path which is locally perpendicular to the two-dimensional manifold of trajectories shown in the diagram. The phase portraits for the other critical points on these paths are identical to those shown in c and d.

c
a
d
b

Figure 2-4

Contour maps illustrating the flux of the curl of $\mathbf{J}^{(1)}$ through a plane containing the nucleus of an atom and perpendicular to the applied field, which is directed out of the plane. Each quantum shell of an atom has associated with it a pair of shells with lines of flow parallel to (dashed lines) and antiparallel to (solid lines) the applied field. There is one such pair of shells in He, two in Ne, Li and N, and three in Ar. The shells within atoms of a given period contract with increasing atomic number whereas they expand within atoms of a given family with increasing atomic number.

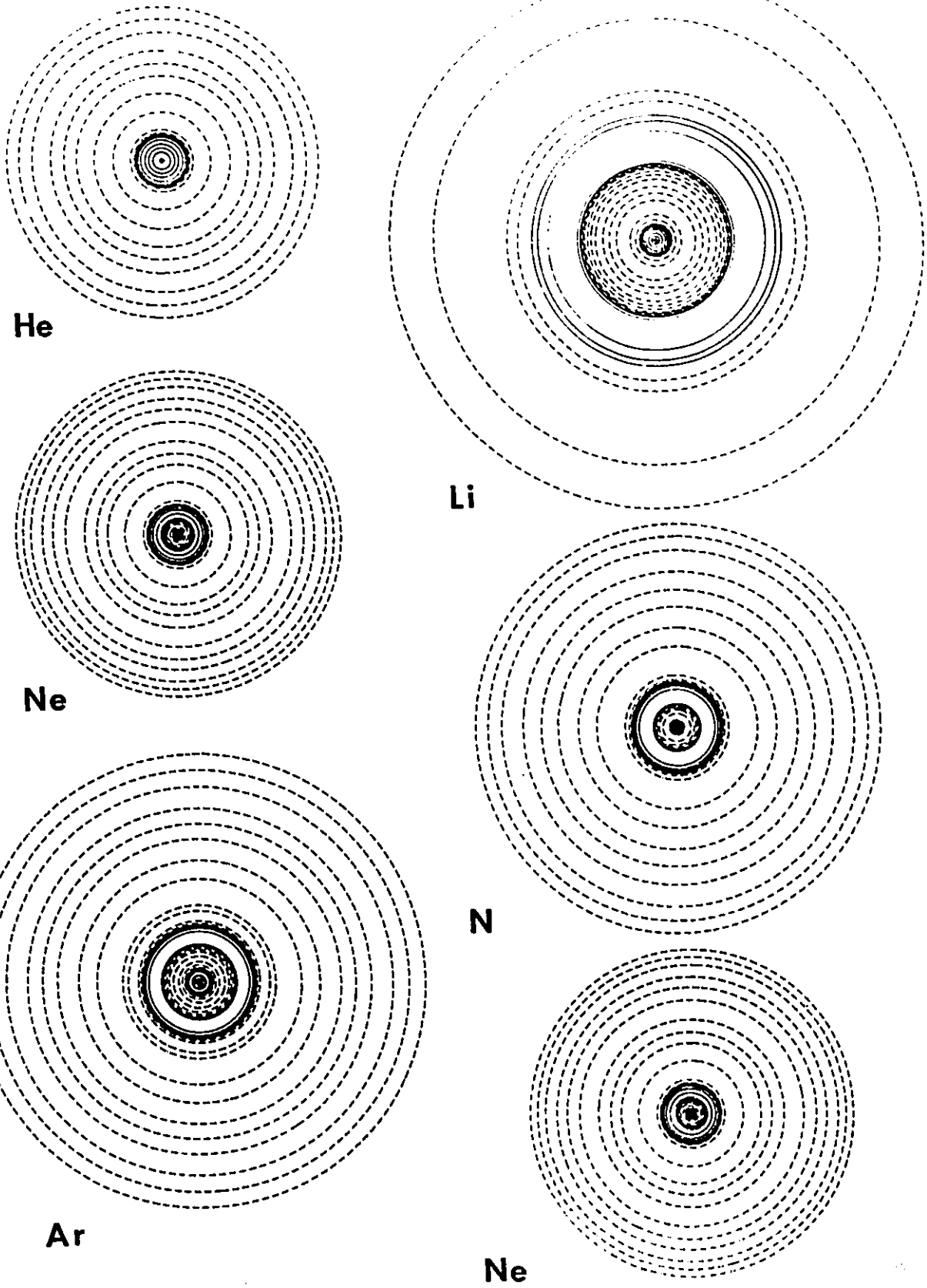
He
Li
Ne
N
Ar
Ne

Figure 2-5

A profile of the curl of $\mathbf{J}^{(1)}$ along a radial axis perpendicular to the applied field for the argon atom. There are three maxima and three minima as required for three quantum shells. The extrema for the inner shells are not shown. The saddle and center critical points of the $\nabla x\mathbf{J}^{(1)}(\mathbf{r})$ field along this axis are labeled by an S and C, respectively. Each of the saddle points lies on a closed saddle stagnation path which generates a surface of $\nabla x\mathbf{J}^{(1)}(\mathbf{r})$ trajectories separating adjacent quantum shells. Each of the center critcal points lies on a closed center stagnation path about which flows a torus of $\nabla x\mathbf{J}^{(1)}(\mathbf{r})$ trajectories contained within the corresponding quantum shell.

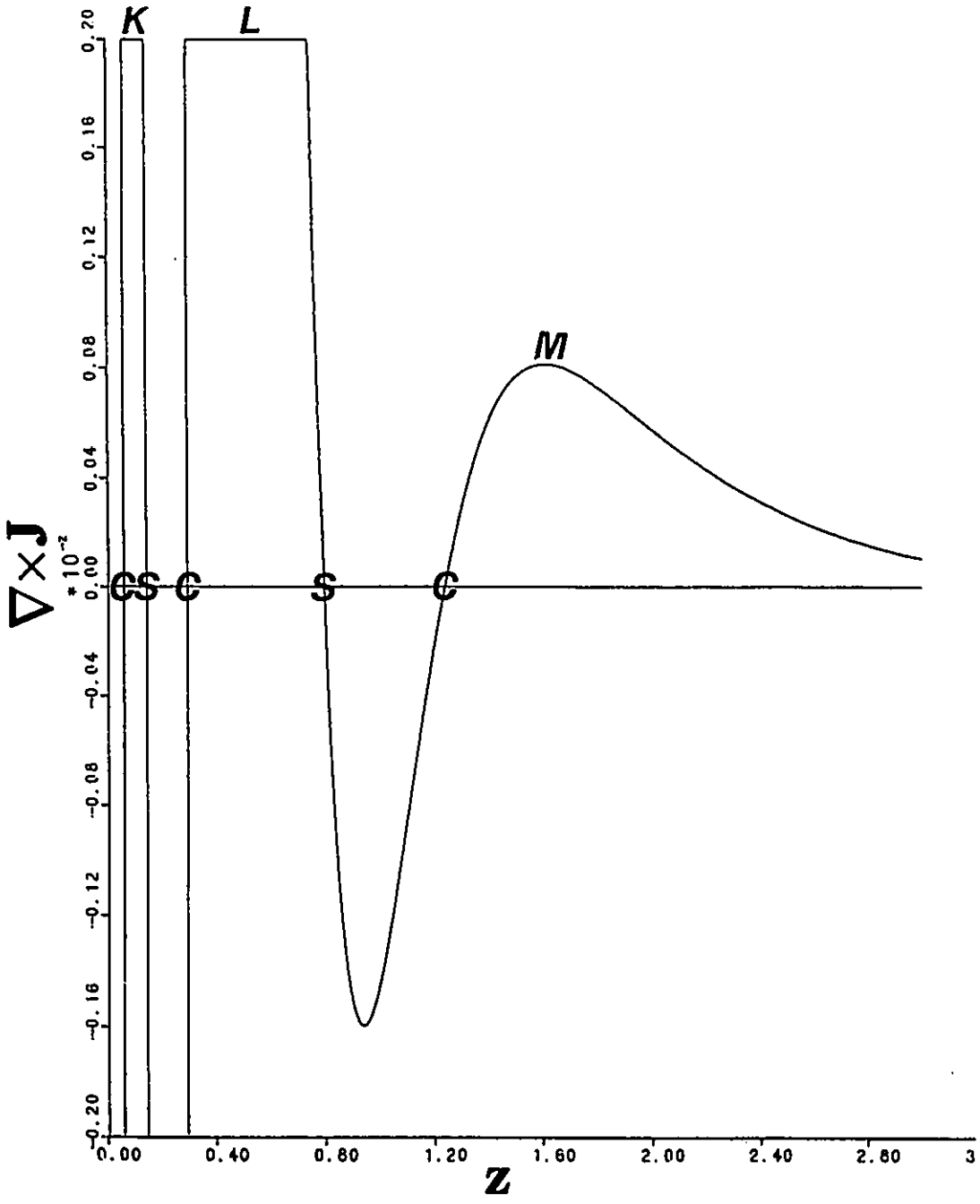
K
L
M
C
S
C
S
C
∇×J
* 10⁻²
0.20
0.16
0.12
0.08
0.04
0.00
-0.04
-0.08
-0.12
-0.16
-0.20
0.00
0.40
0.80
1.20
1.60
2.00
2.40
2.80
3
z

Figure 2-6

a) A display of the trajectories of $\mathbf{J}^{(1)}(\mathbf{r})$ induced in a nuclear plane of the Neon atom with the applied field coming out of the plane. The trajectories are circular and diamagnetic.

b) A three dimensional display of the current induced in a free atom. The current is everywhere circular, perpendicular to the applied field and diamagnetic. The line perpendicular to the current flow is the center stagnation path.

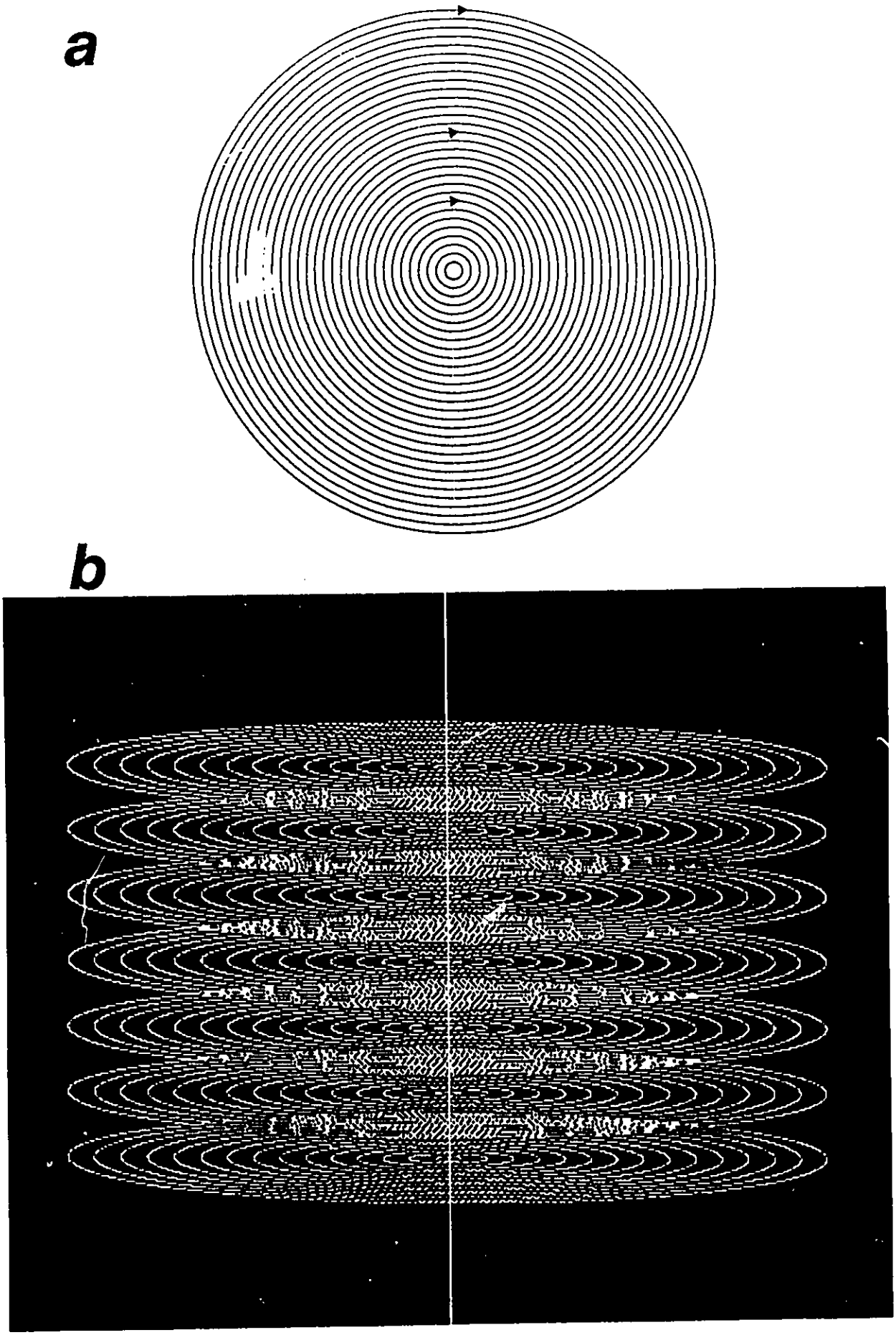
a
b

Figure 2-7

A profile of the current density magnitude along an axis passing through the nucleus in the Neon atom. The applied field is perpendicular to the axis. The current is zero at the nucleus but is very large elsewhere in the core region.

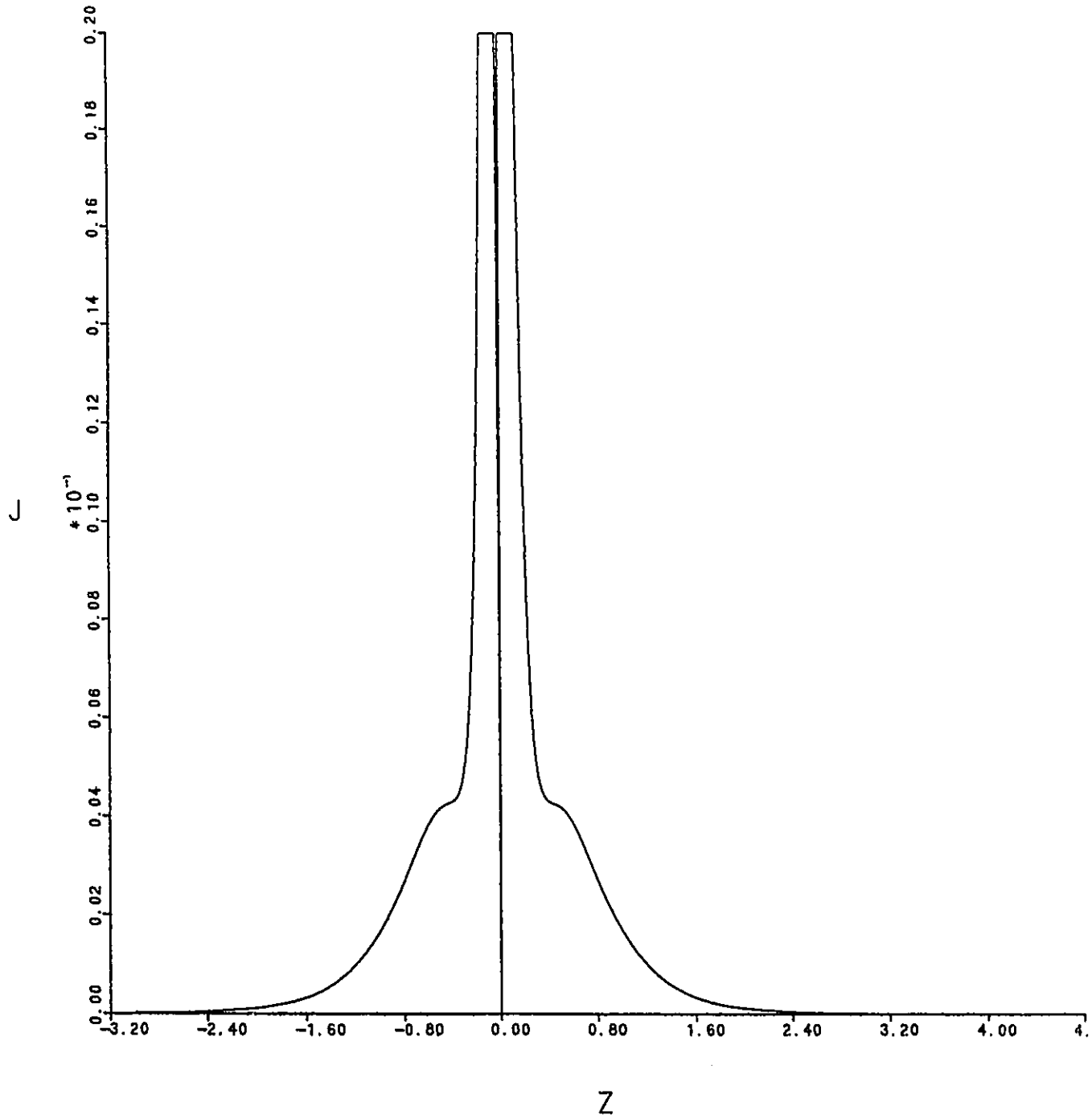
J
* 10⁻¹
0.00
0.02
0.04
0.06
0.08
0.10
0.12
0.14
0.16
0.18
0.20
-3.20
-2.40
-1.60
-0.80
0.00
0.80
1.60
2.40
3.20
4.00
Z

Figure 2-8

a) Induced current density in H_2 in a nuclear plane perpendicular to the applied field, which is directed out of the page. The intersection of the interatomic surface with the plane is also shown. There is a single critical point, a center, lying at the bond midpoint. The flow is diamagnetic.

b) Magnitude of the current density in H_2 along the internuclear axis for a perpendicular applied field.

a

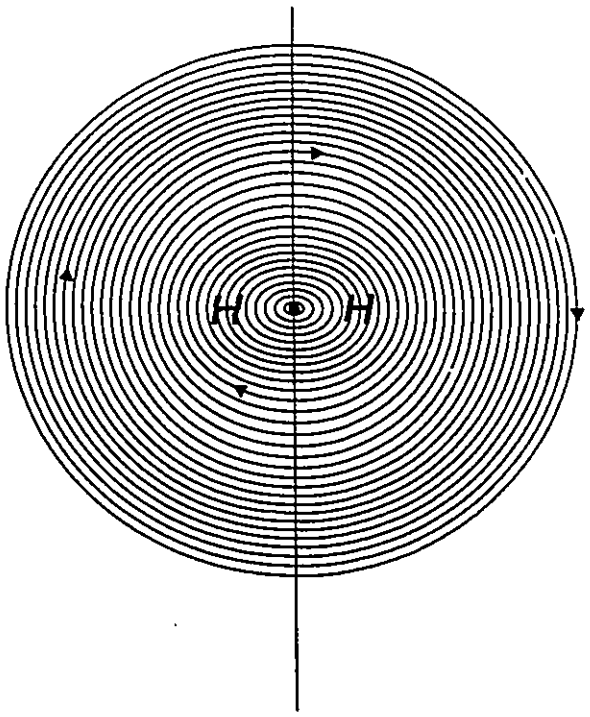
H
H

b

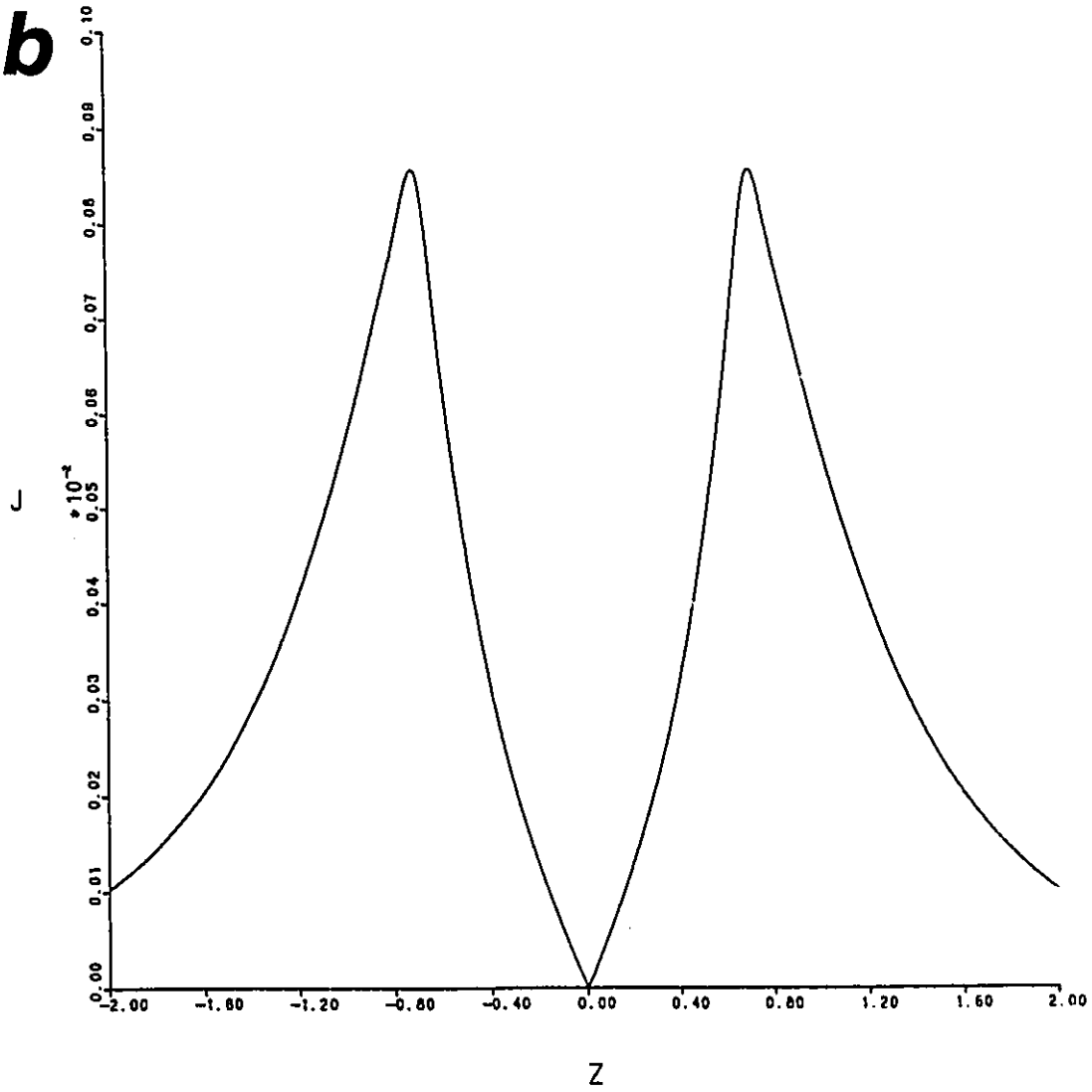
J
* 10⁻²
0.00
0.01
0.02
0.03
0.04
0.05
0.06
0.07
0.08
0.09
0.10
-2.00
-1.60
-1.20
-0.80
-0.40
0.00
0.40
0.80
1.20
1.60
2.00
Z

Figure 2-9

Induced current density in a nuclear plane of the LiH molecule with the applied field coming out of the plane. The intersection of the interatomic surface with the plane is also shown. There are four critical points in the lithium atom: two center points along the internuclear axis; and two surface points off the internuclear axis on either side. The upper surface point is (3,+1) while the lower is (3,-1). The flow about the center point on the bonded side of the lithium nucleus is paramagnetic while the flow about the center point nearly coinident with the lithum nucleus is diamagnetic. There is a single critical point in the hydrogen atom, a diamagnetic center.

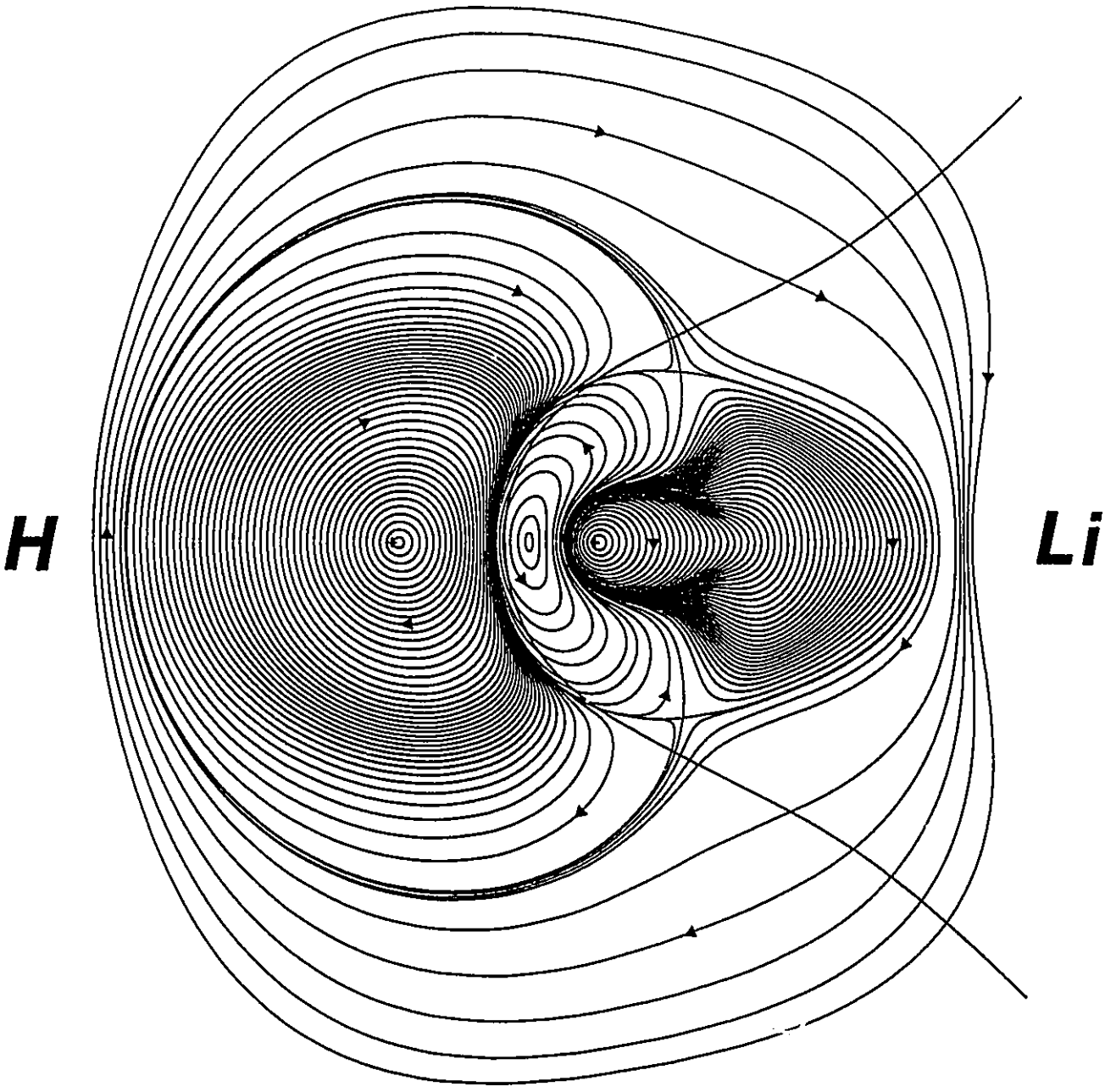
H
Li

Figure 2-10

The trajectories originating and terminating at the pair of surface critical points in LiH for a field applied perpendicular to the internuclear axis. A unique pair of trajectories originates at the closest critical point, a (3,-1) and terminates at the other critical point, a (3,+1). The rest of the trajectories define a *closed* surface originating at the far critical point, the (3,+1), and terminating at the (3,-1). The dot is the proton.

H Li

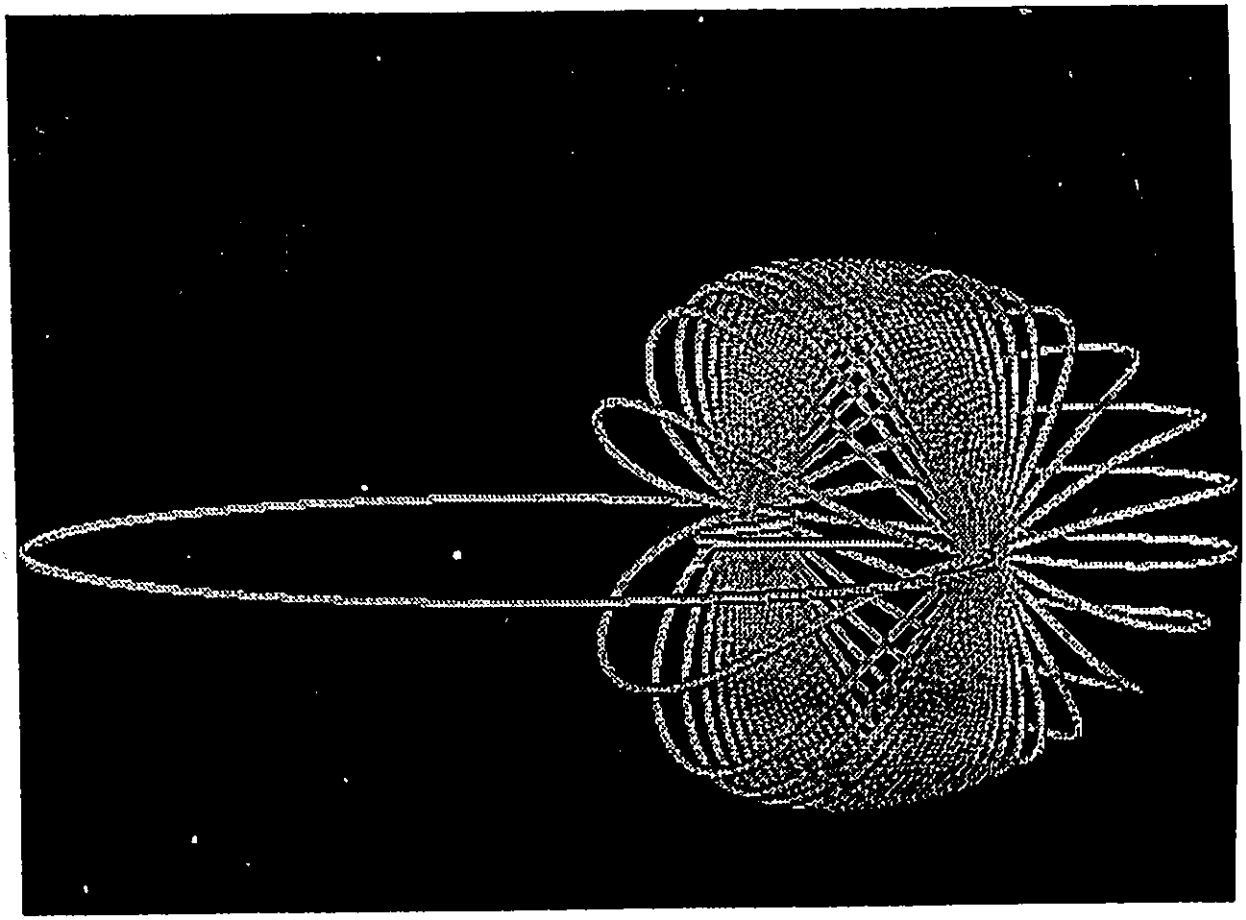

Figure 2-11

a) Contour map of the curl of the current density, the vorticity, induced in the nuclear plane of LiH with the applied field coming out of the plane. Solid contours denote antiparallel vorticity while dashed contours denote parallel vorticity. The intersection of the interatomic surface with the plane is shown.

b) Contour map of the laplacian of the electron density, $\nabla^2\rho$, in a nuclear plane of LiH. Solid contours denote negative values, charge concentration, while dashed contours denote positive values, charge depletion. The intersection of the interatomic surface with the plane is shown.

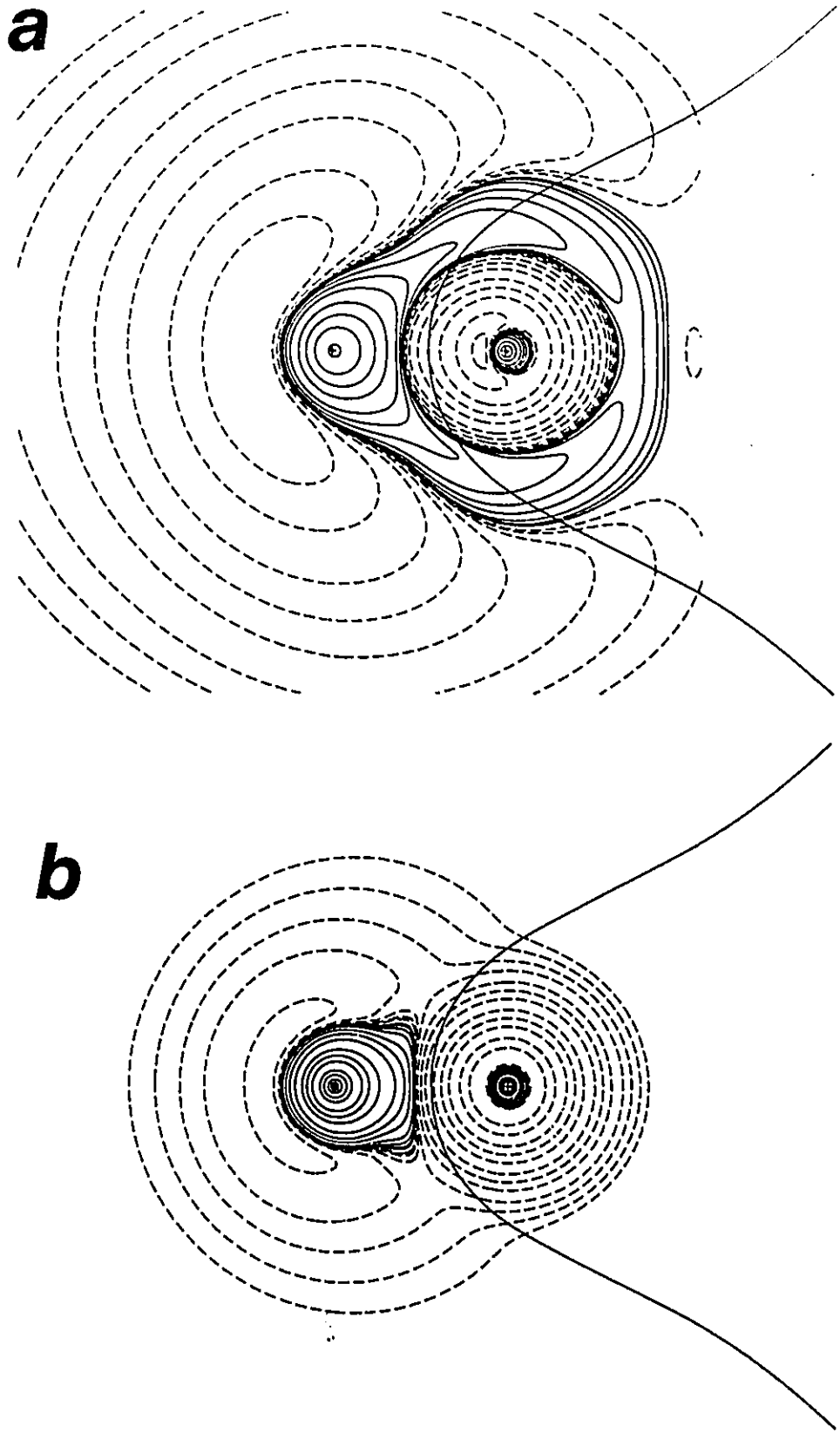
a
b

Figure 2-12

Current flow about the closed center stagnation path in LiH. The flow about the stagnation path is entirely contained within the surface defined by the surface critical points (see Fig. 2-10).

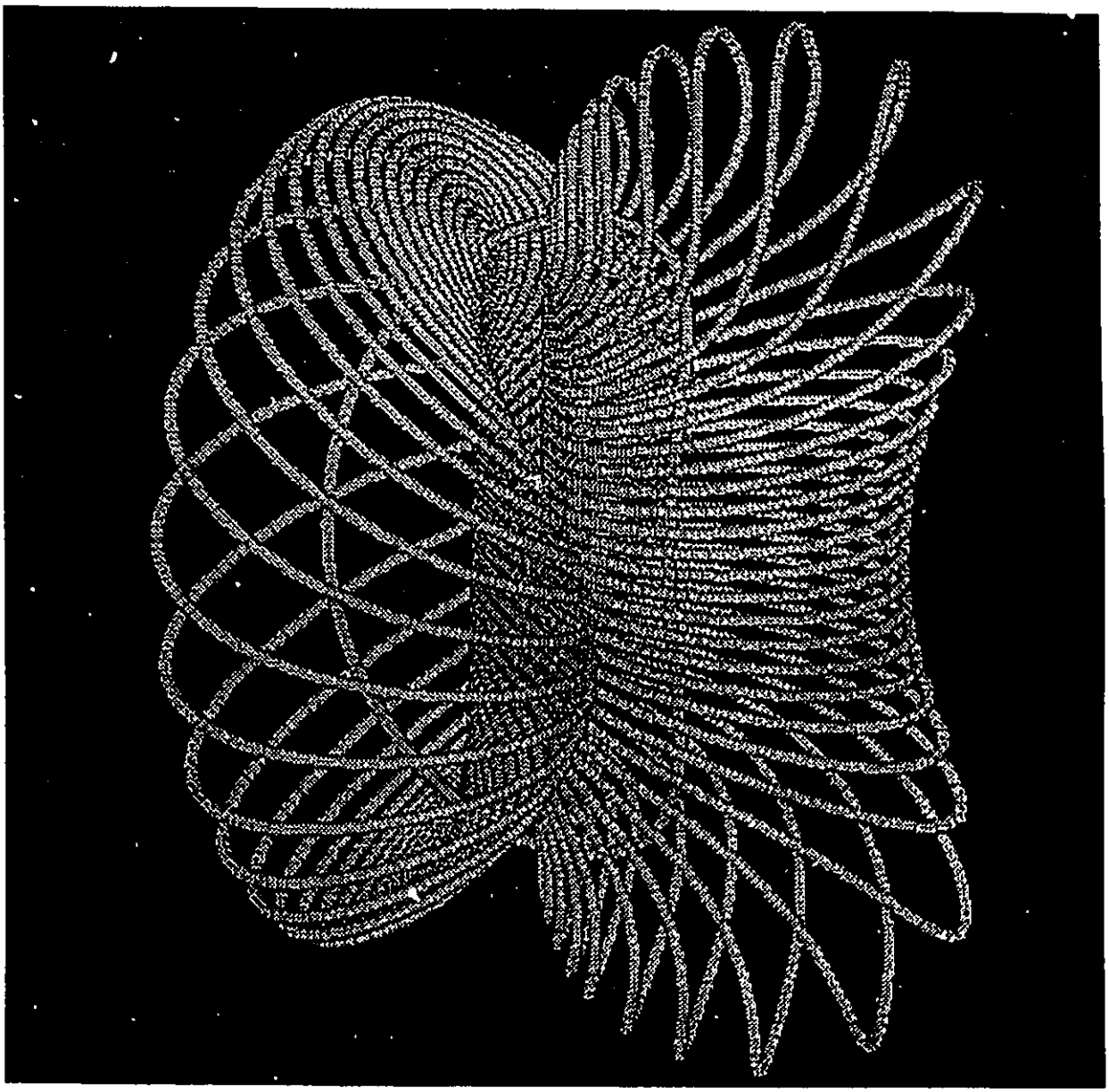

Figure 2-13

Stagnation graph for LiH for a perpendicular field. The view is along an axis perpendicular to the applied field and the internuclear axis. There are two stagnation paths, one in each atom and both centers. The closed center stagnation path (see Fig. 2-12) lies in the lithium atom while the open diamagnetic center stagnation path lies in the hydrogen atom, nearly intersecting the proton. The two spheres on the RHS are the out-of-plane surface critical points, the larger of the two lying in the foreground and representing the (3,-1). The other dots are the nuclei.

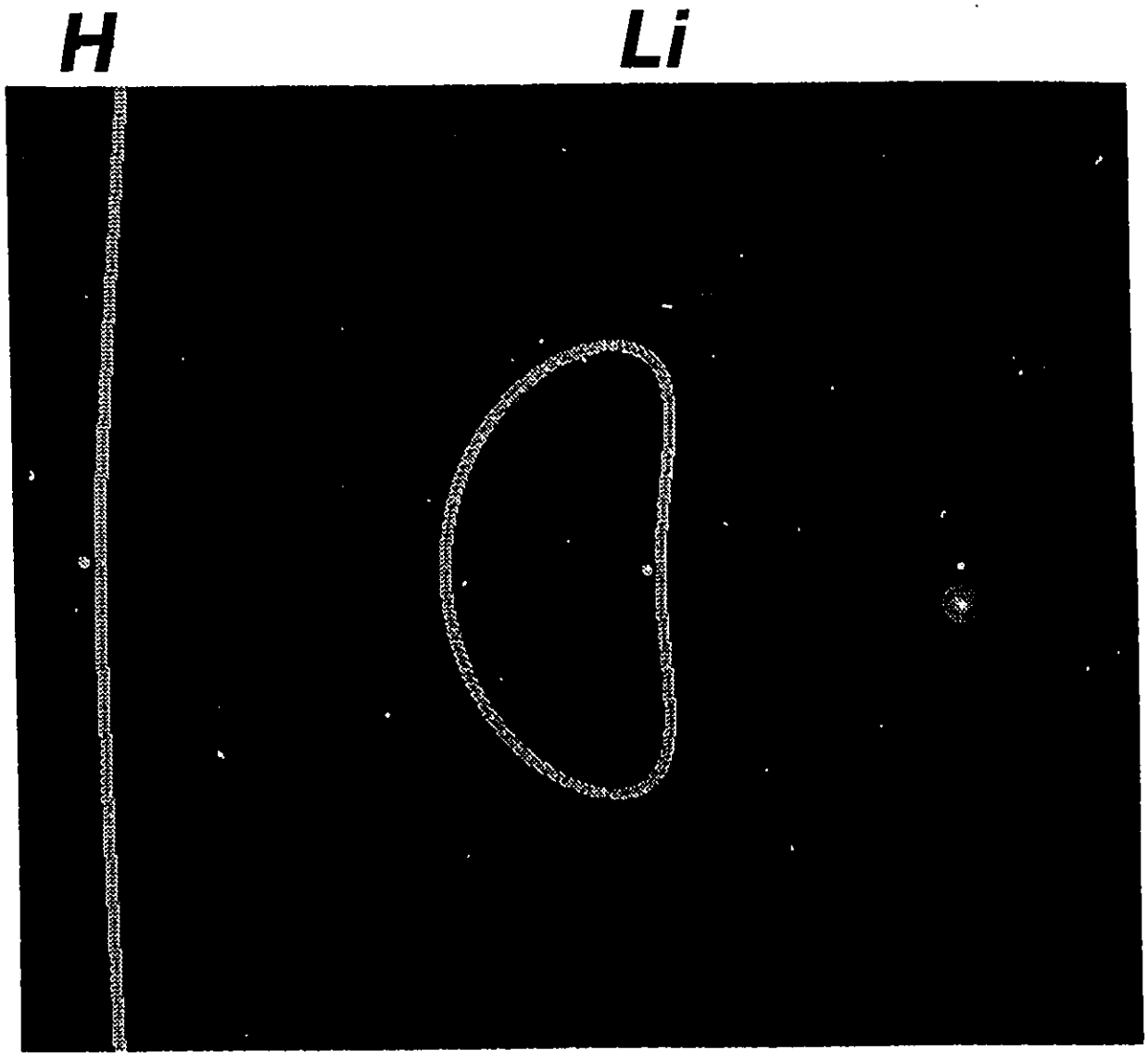
H
Li

Figure 2-14

Current density induced in the nuclear plane of the BeH_2 molecule for an applied magnetic field coming out of the page. Clockwise flow is diamagnetic. X symbols denote saddle points, dots denote center points and plus signs (+) denote the nuclei. The interatomic surfaces are not shown.

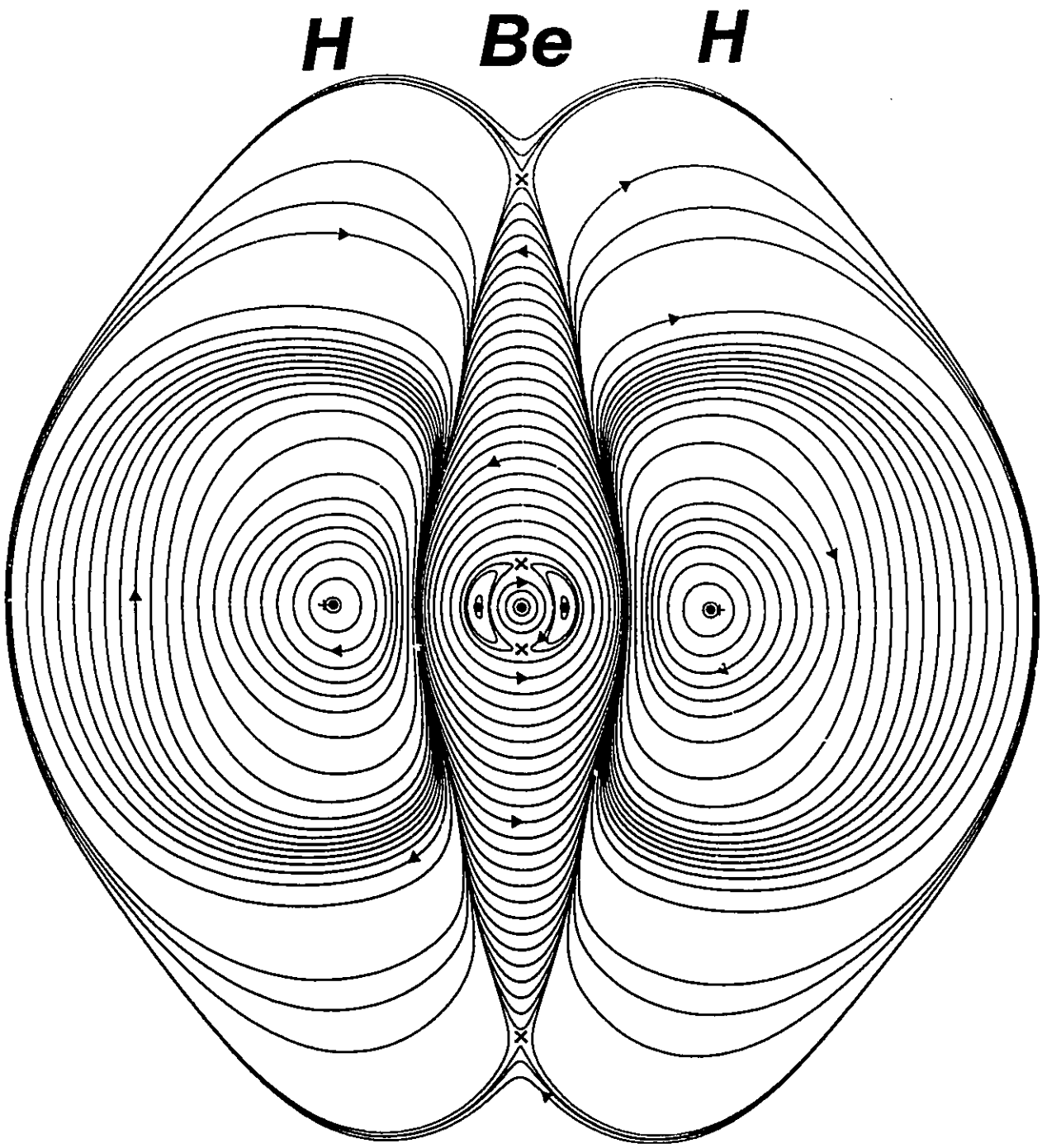
H
Be
H

Figure 2-15

a) Contour map of the curl of the current density, the vorticity, induced in the nuclear plane of BeH_2 with the applied field coming out of the plane. Solid contours denote antiparallel vorticity while dashed contours denote parallel vorticity. The intersection of the interatomic surfaces with the plane is shown.

b) Contour map of the laplacian of the electron density, $\nabla^2\rho$, in a nuclear plane of BeH_2. Solid contours denote negative values, charge concentration, while dashed contours denote positive values, charge depletion. The intersection of the interatomic surfaces with the plane is shown.

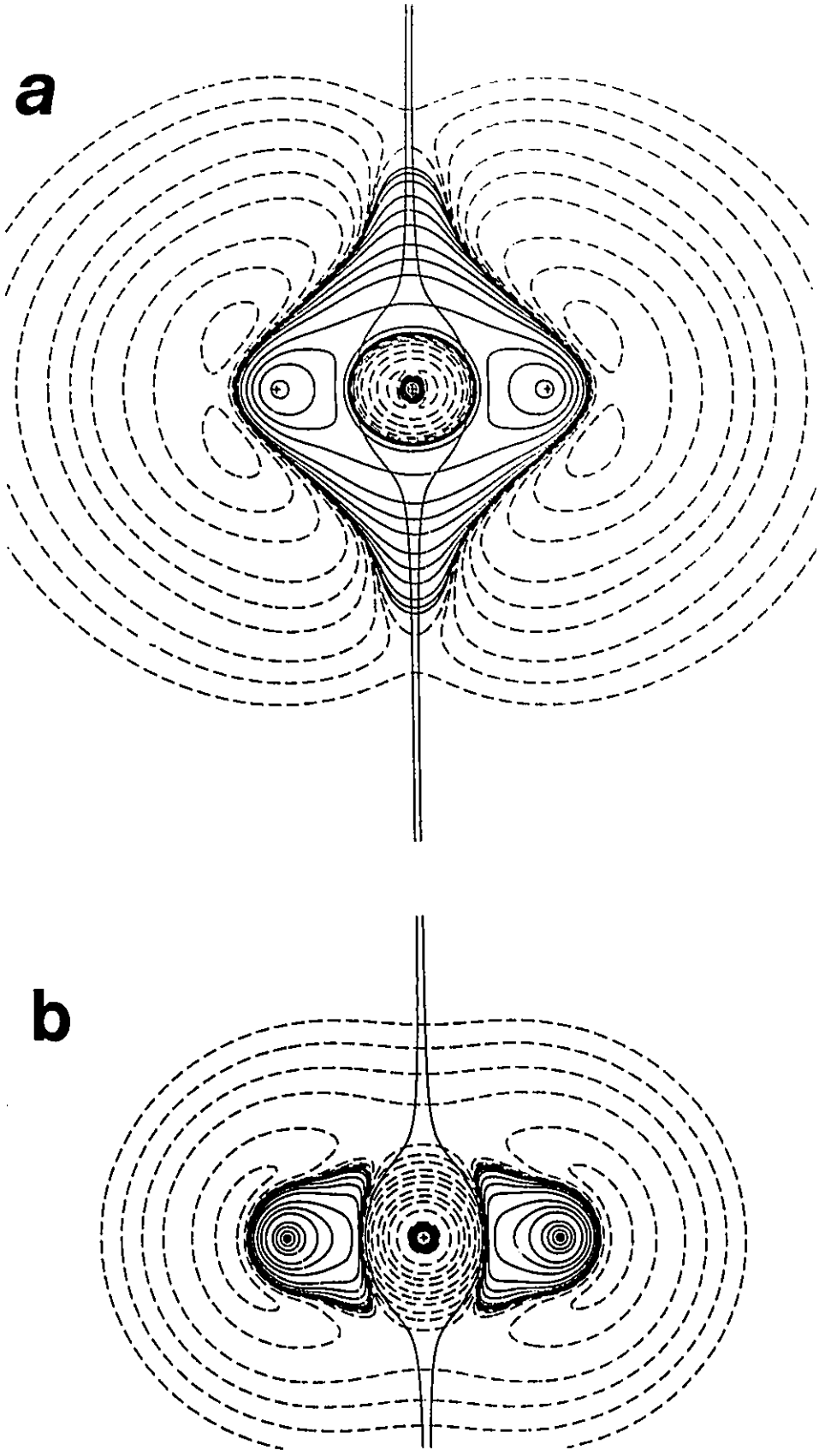
a
b

Figure 2-16

Stagnation graph of BeH_2 for a perpendicular field. The arrow is the internuclear axis. The two outer paths which intersect the internuclear axis are the hydrogen diamagnetic center paths while the two outer paths in the upper LHS and lower RHS of the figure are saddle paths. The stagnation path intersecting the Be nucleus at the center of symmetry is a diamagnetic center path while the two adjacent paths on either side of the Be nucleus and intersecting the internuclear axis are paramagnetic center paths. The other two adjacent paths are saddles which merge with the Be diamagnetic center path above and below the internuclear axis to form (0,0) critical points and then new saddle paths. Not distinguishable from the first mergings in this figure, the two paramagnetic center paths then merge with the newly formed saddle paths above and below the internuclear axis to form two more (0,0) critical points and then a pair of paramagentic center paths. Not shown in this figure, all remaining paths eventually merge along the symmetry axis parallel to the field resulting in two diamagnetic center paths, one extending to plus infinity the other to minus infinity.

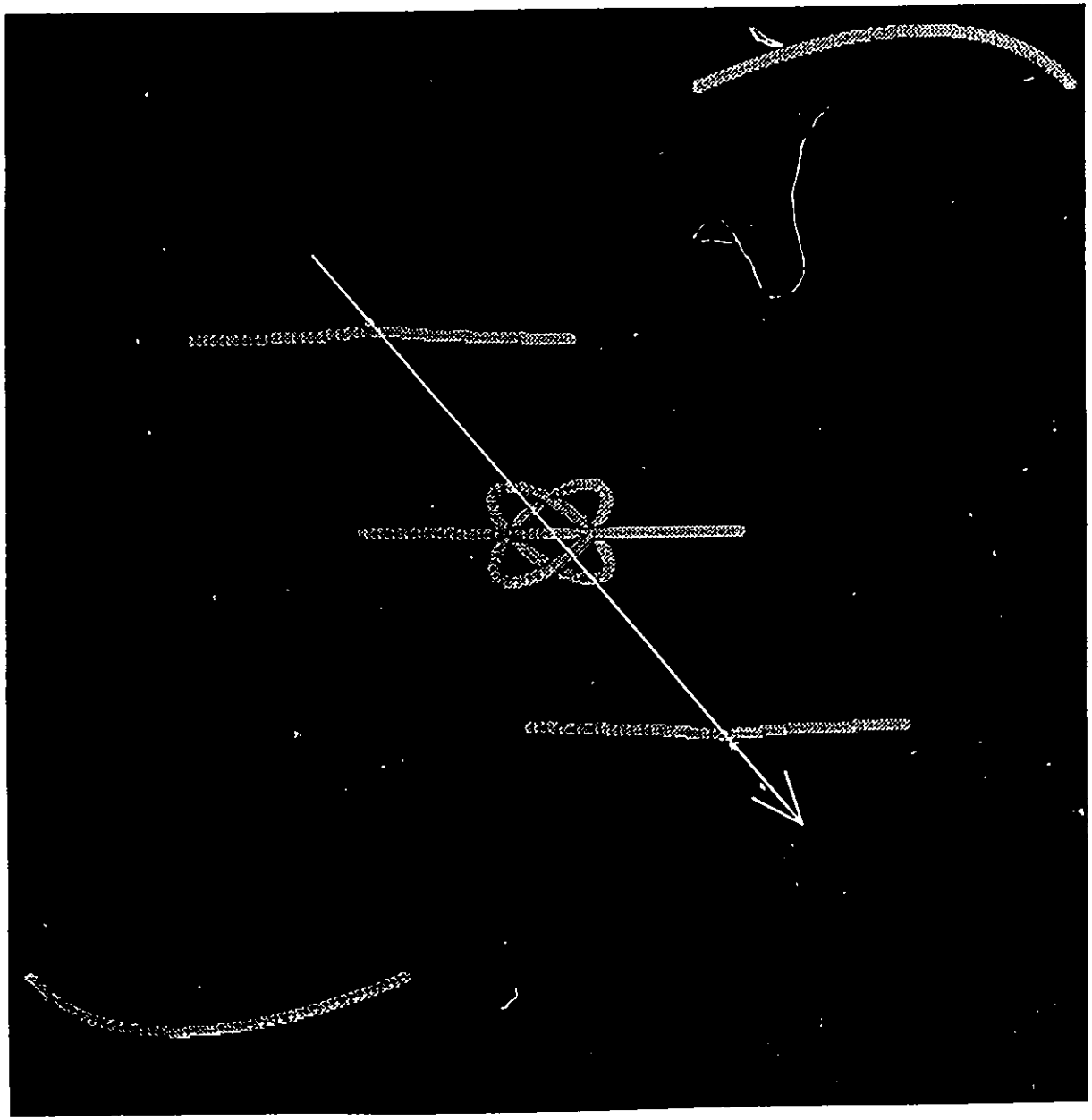

Figure 2-17

Stagnation graph of an oxygen atom of CO_2 for a perpendicular field (see Fig. 2-2). The labels C, S and X denote center stagnation paths, saddle stagnation paths and (0,0) critical points, respectively. The oxygen nucleus is the black plus sign (+).

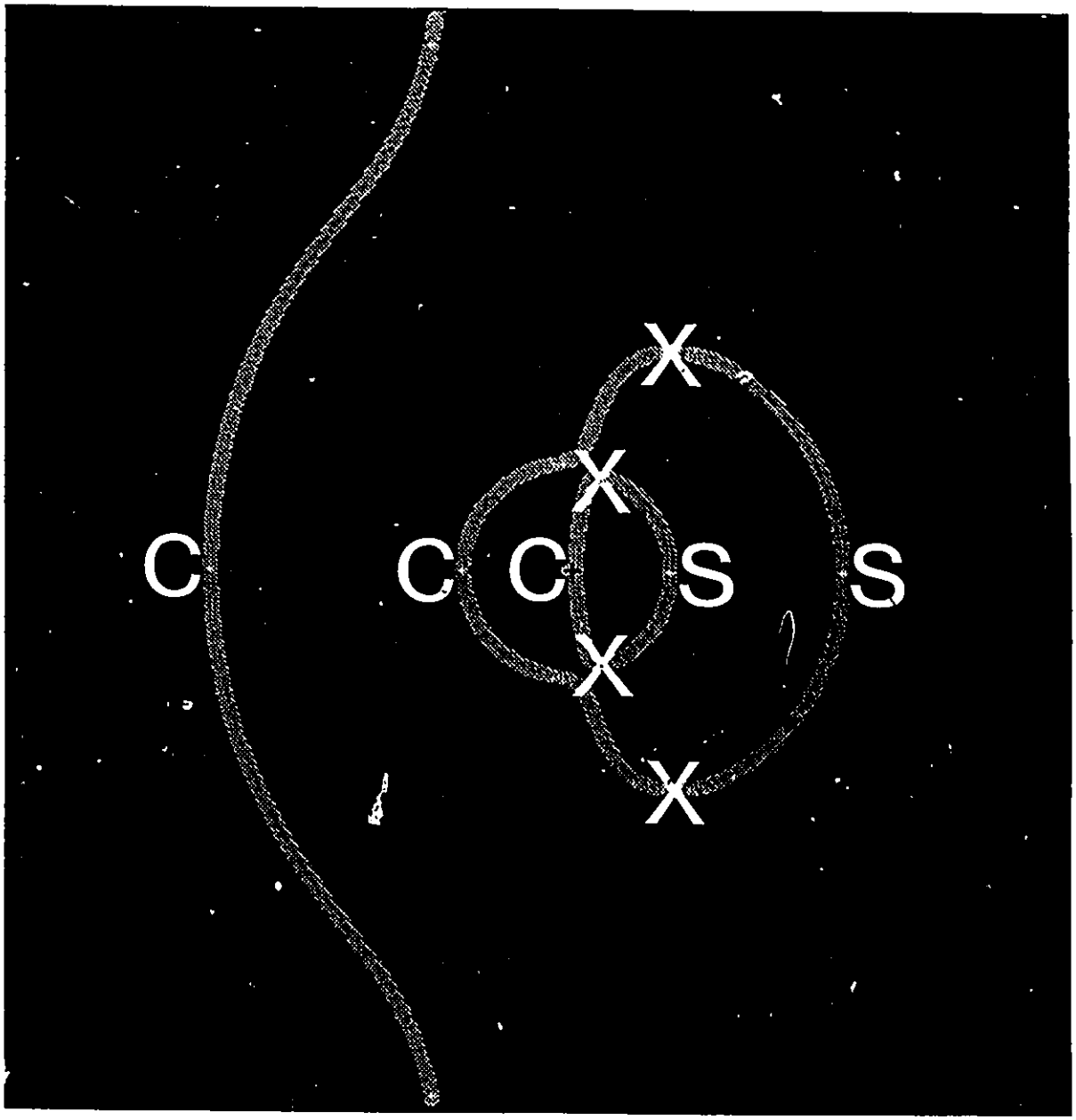
X
X
C
C
C
S
S
X
X

Figure 2-18

Current density induced in the nuclear plane of the H_2O molecule with the applied field coming out of the page. There are two center points and a saddle point on the C_2 axis. The flow about the center point which is nearly coincident with the oxygen nucleus is diamagnetic. The other center point is not distinguishable in this figure, but the small region of flow about it is paramagnetic. There is a (3,-1) diamagnetic spiral point along the O-H bond on the LHS and a corresponding (3,+1) spiral point along the other O-H bond. There is (3,-1) surface point adjacent to the (3,+1) spiral point and a (3,+1) surface point adjacent to the (3,-1) spiral point. The intersection of the interatomic surfaces with the plane is shown.

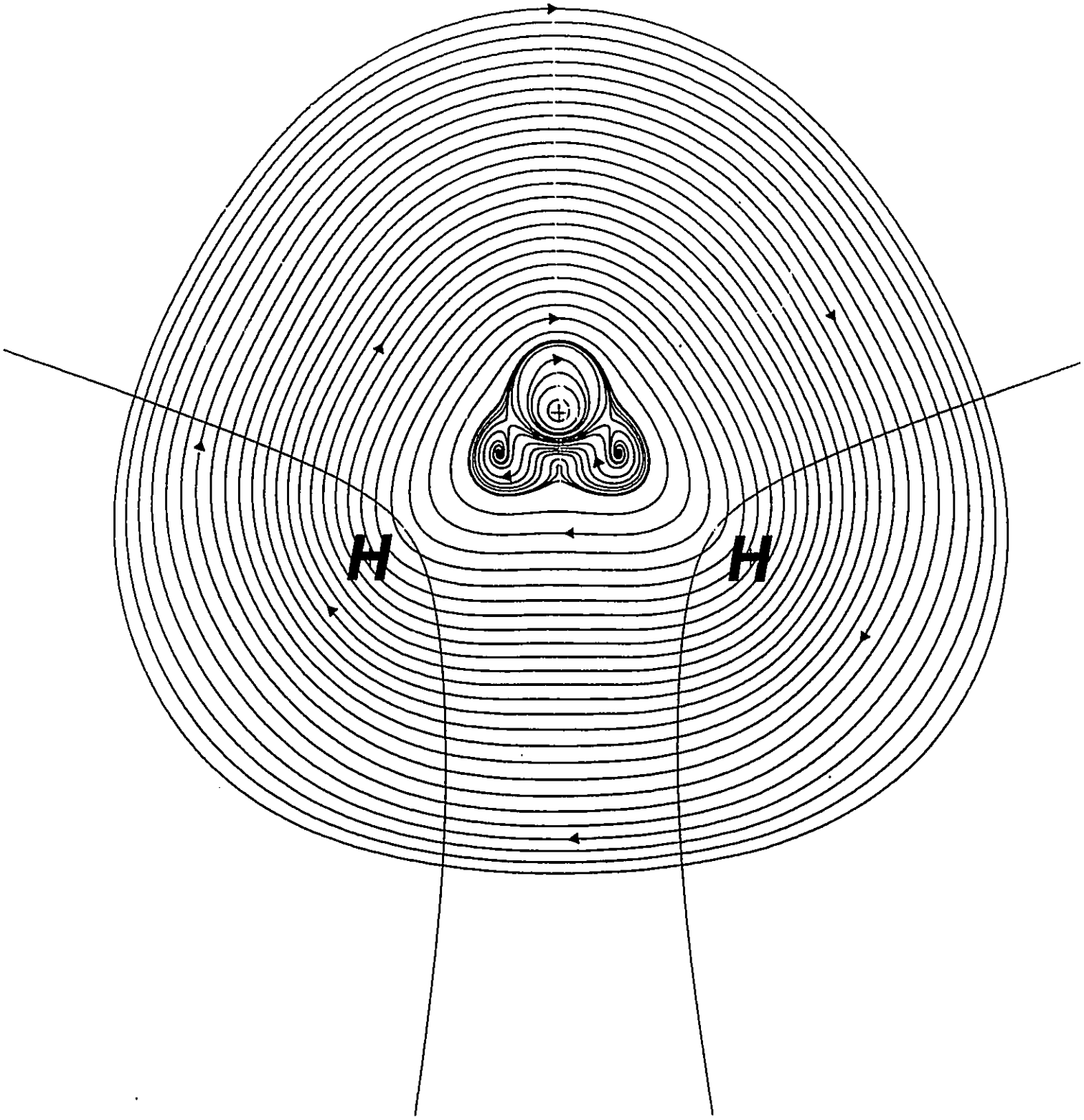
H
H

Figure 2-19

Current density induced in the nuclear plane of H_2O with the applied field perpendicular to the plane. This figure is a blow-up of Fig. 2-18 viewed from slightly above the C_2 axis. The protons lie in the foreground. Also shown is the unique pair of current trajectories linking the spiral points.

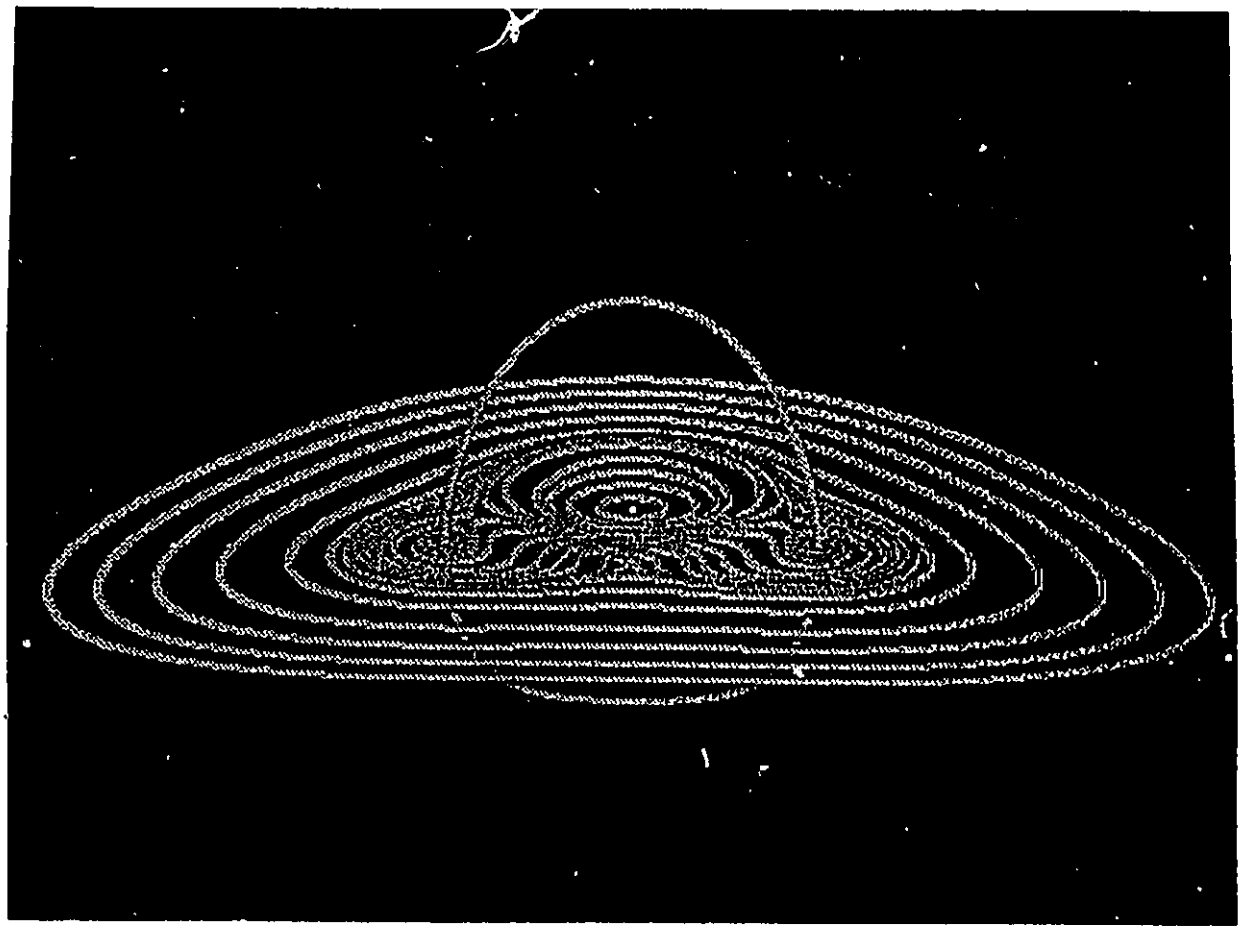

Figure 2-20

View along the C_2 axis of the unique pair of current trajectories linking the spiral points in H_2O, see Fig. 2-19. Also shown are a pair of *closed* trajectories flowing above and below the nuclear plane and wrapping around the unique trajectories.

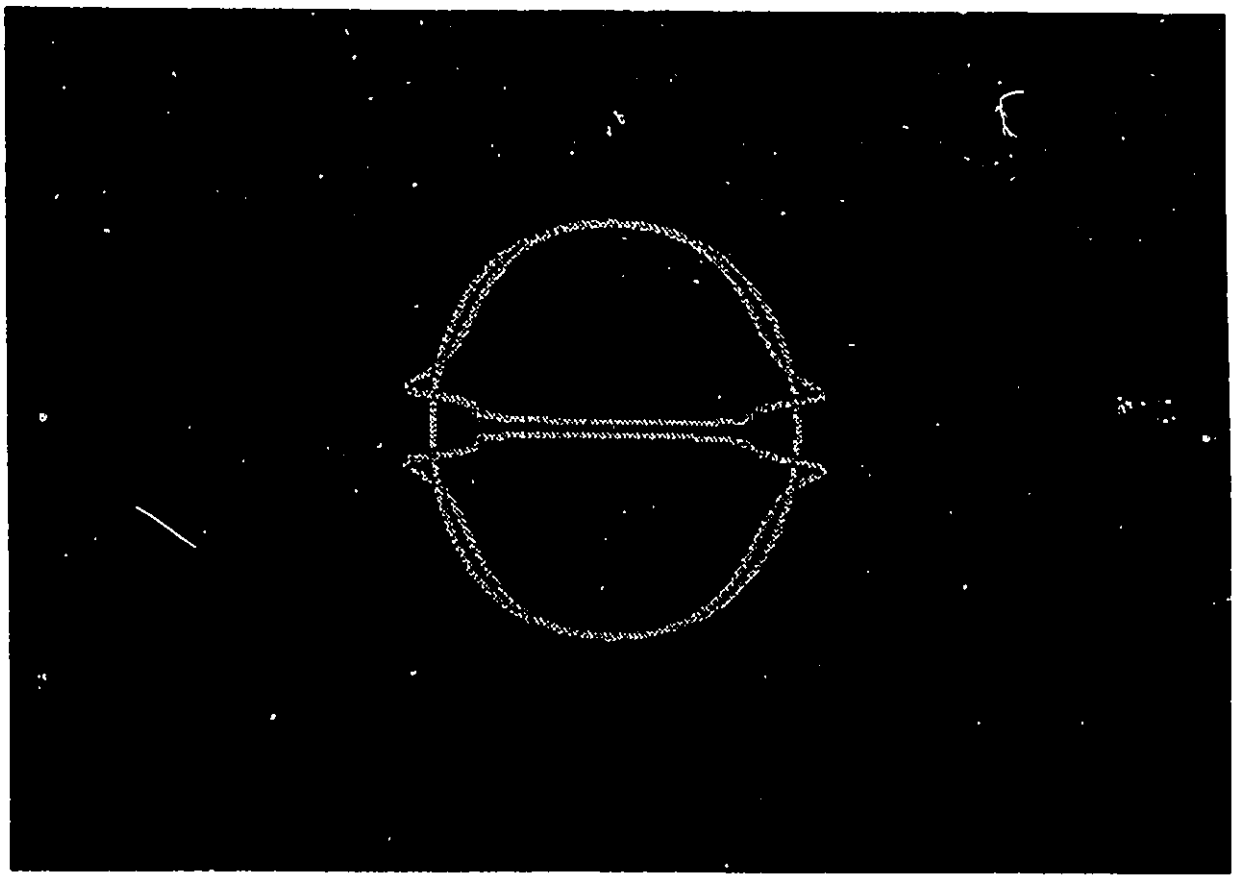

Figure 2-21

Stagnation graph for H_2O viewed perpendicular to the antiunitary symmetry plane for a field applied perpendicular to the nuclear plane. The labels C, S and X denote center stagnation paths, saddle stagnation paths and (0,0) critical points, respectively. The dots apparently lying within the closed center stagnation path are projections of the spiral and surface critical points onto the plane. The protons are on the left, out of the plane shown.

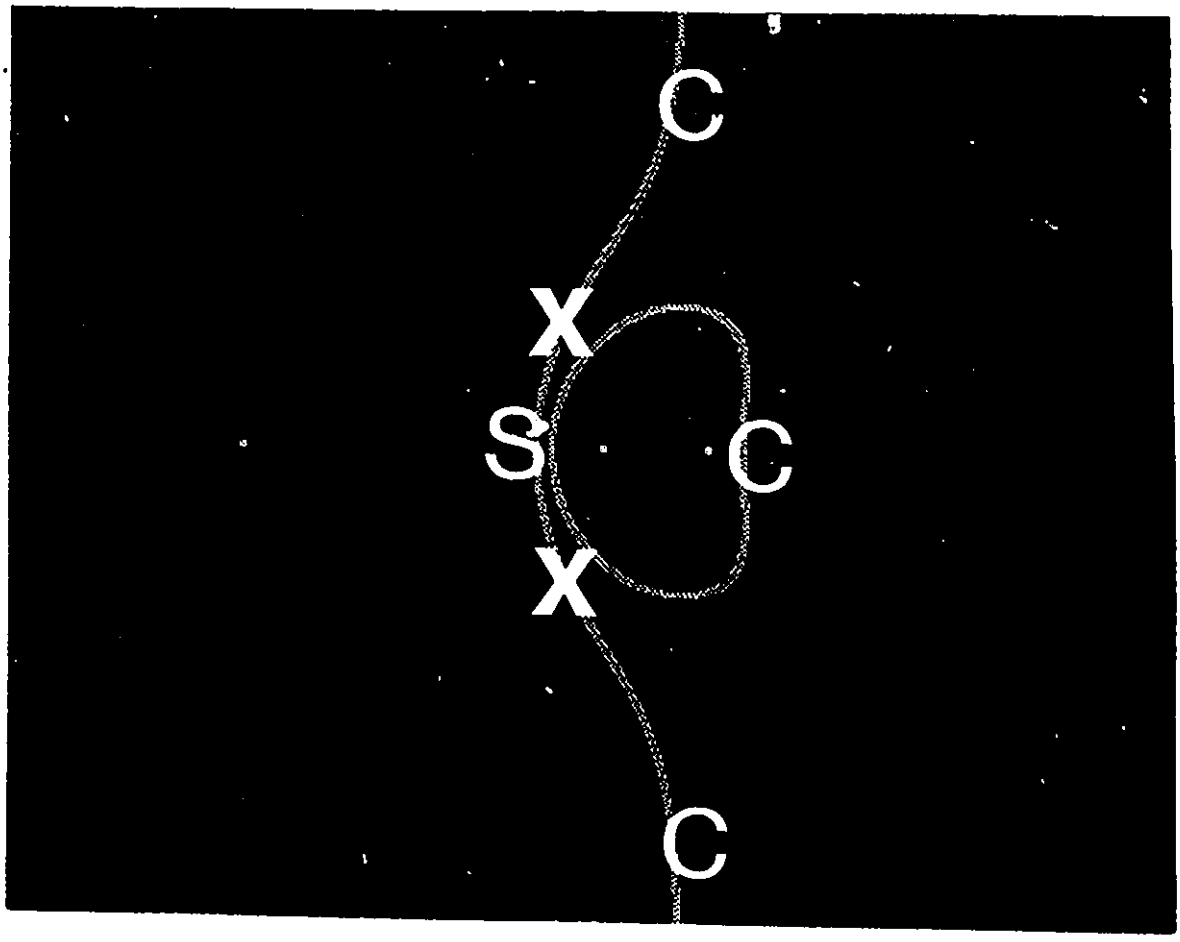
C
X
S
C
X
C

Figure 2-22

Induced current distribution in CH_4 in a plane containing the carbon nucleus and two protons with the applied field coming out of the page. As with the corresponding orientation of H_2O (see Figs. 2-18 and 2-19) there is a diamagnetic spiral critical point along each hydrogen bond, but in CH_4 they lie much closer to the bond midpoint. There are four spiral points, four surface points (filled squares), three center points (dots) and two saddle points (X) in this unitary symmetry plane. The sum of the indices of the critical points equals +1, as required by the Poincare-Hopf index theorem. The intersection of the interatomic surfaces with the plane is shown.

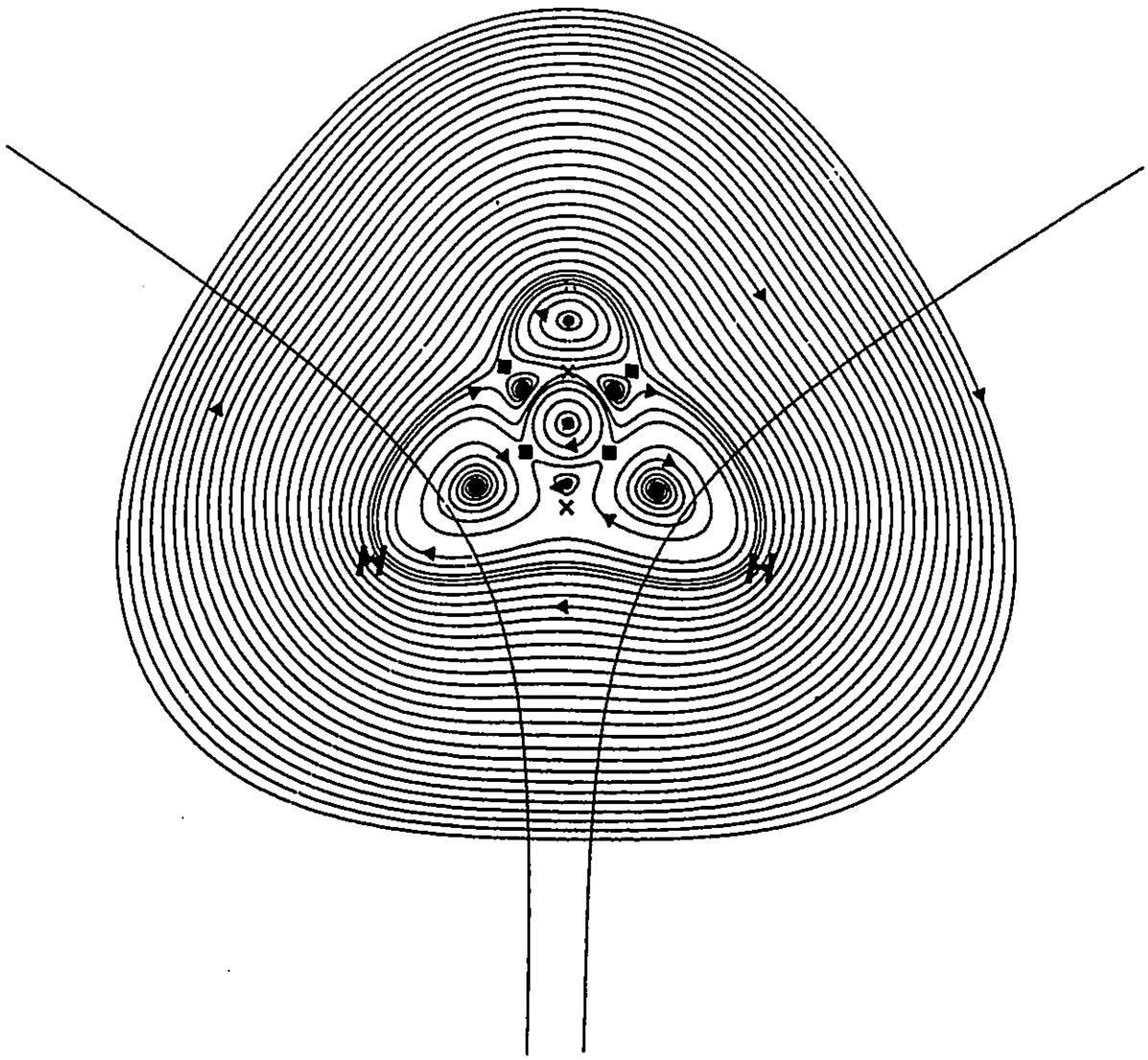

Figure 2-23

Blow up of Fig. 2-22 and viewed slightly above the antiunitary C_2 axis. Unique trajectories linking the two pairs of spiral points are shown on one side of the plane.

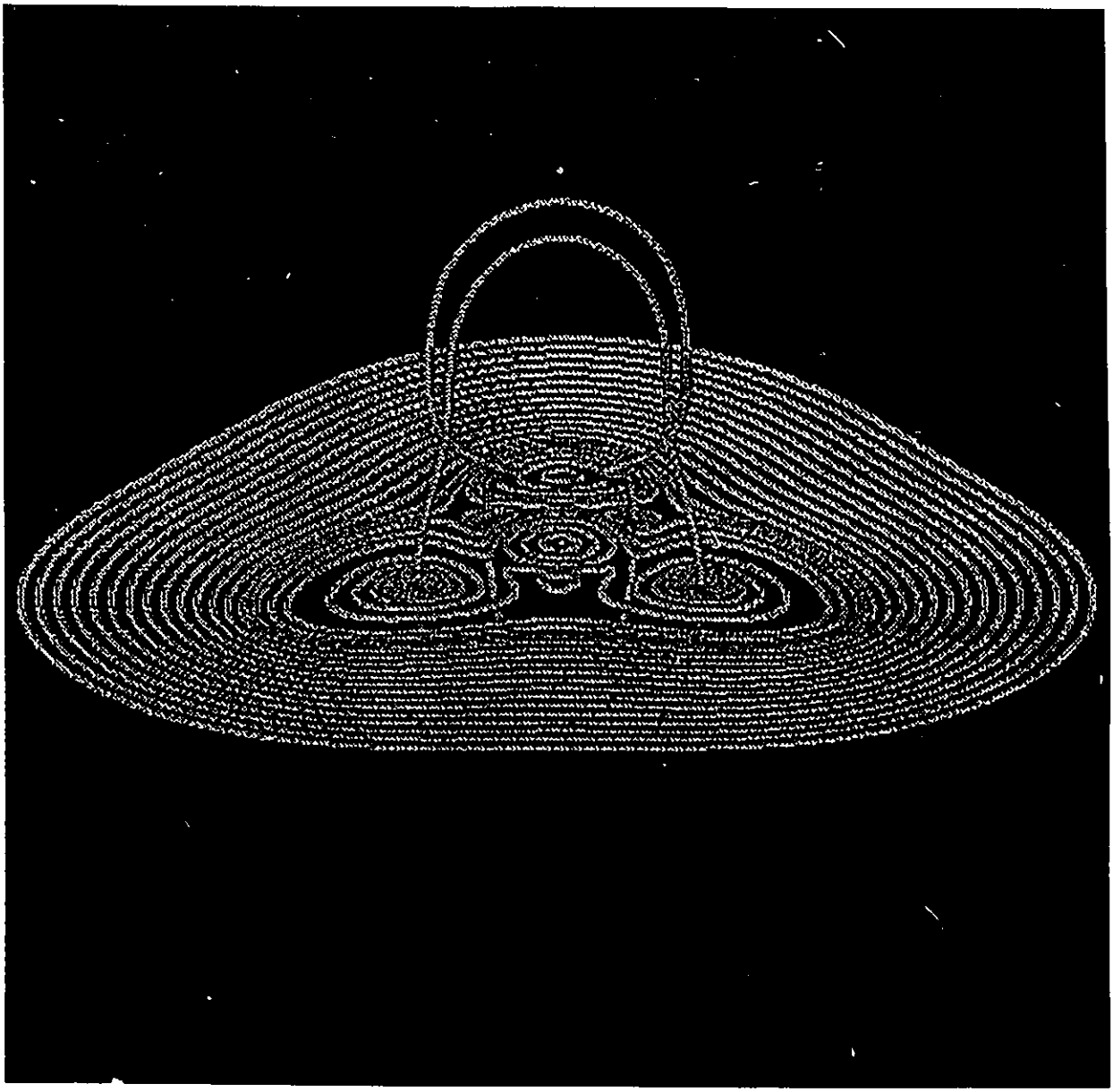

Figure 2-24

Induced current distribution in ethene in the nuclear plane with the magnetic field coming out of the page. The intersection of the interatomic surfaces with the plane is shown. Center critical points are denoted by a dot while saddle critical points are denoted by an X. Surface critical points are denoted by a filled square, while the spiral critical points whose associated trajectories are not shown are denoted by an open square.

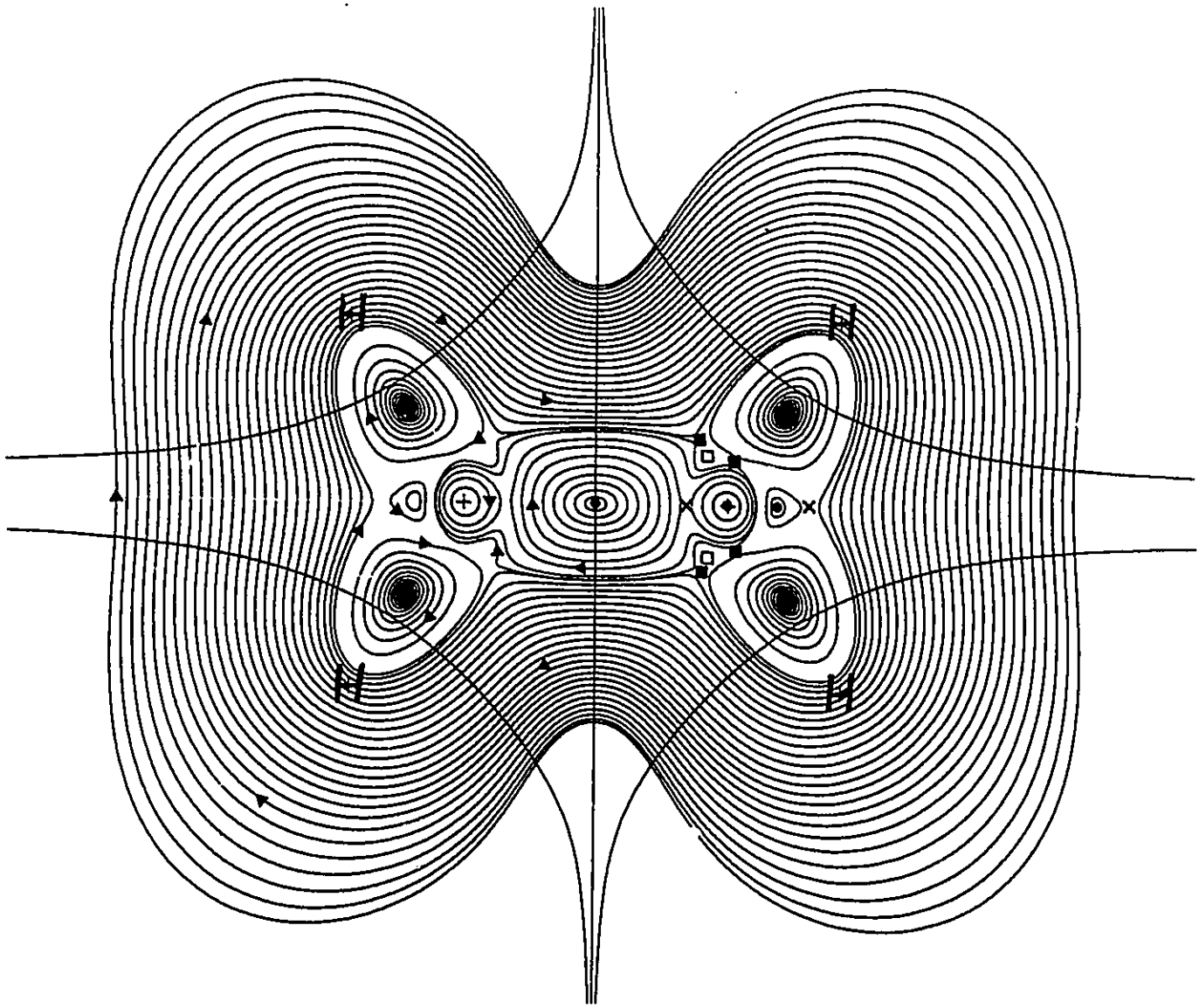

Figure 2-25

Phase portrait of the four C-H bond diamagnetic spiral critical points in ethene for the orientation shown in Fig. 2-24.

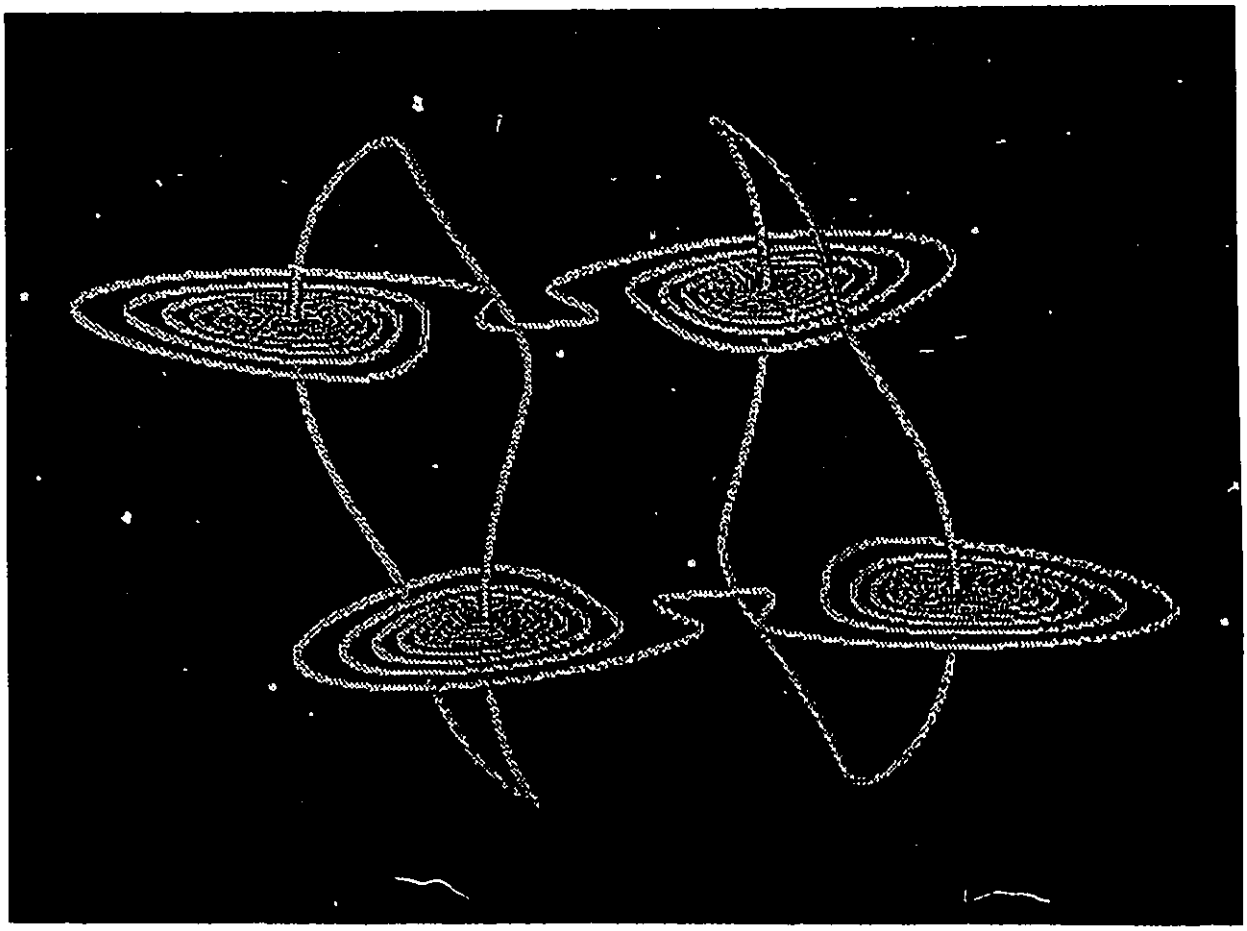

Figure 2-26

The unique trajectories associated with the C-H bond spiral points in ethene together with a single pair of out-of-plane *closed* trajectories which spiral about the unique trajectories and traverse the entire molecule, one above the the nuclear plane, the other below it.

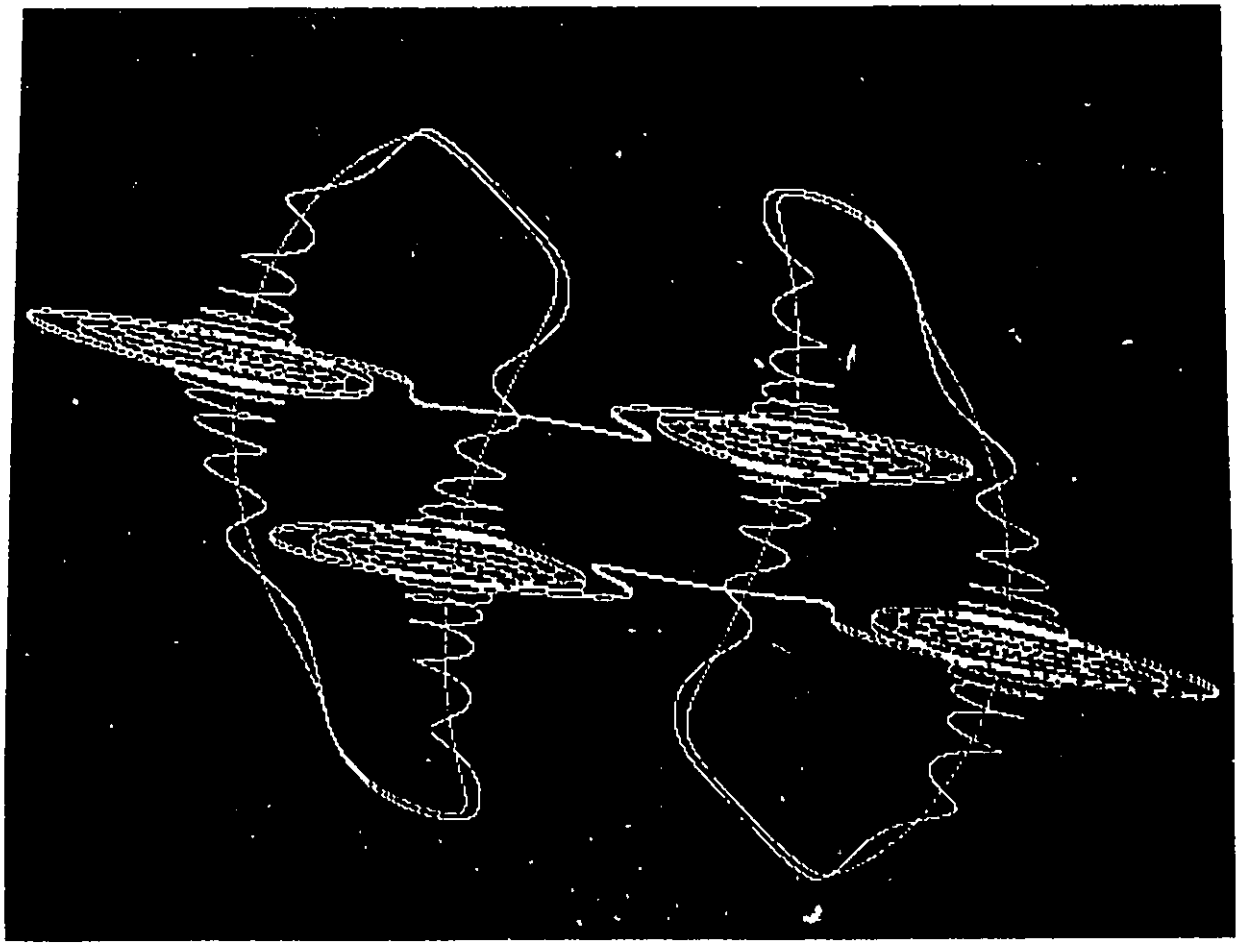

Figure 2-27

Induced current density in C_2H_2 in a plane containing the nuclei with the applied field coming out of the page. The intersection of the interatomic surfaces with the plane is shown. Center critical points are denoted by a dot while saddle critical points are denoted by an X. Each carbon possesses a pair of surface critical points, denoted by a filled square.

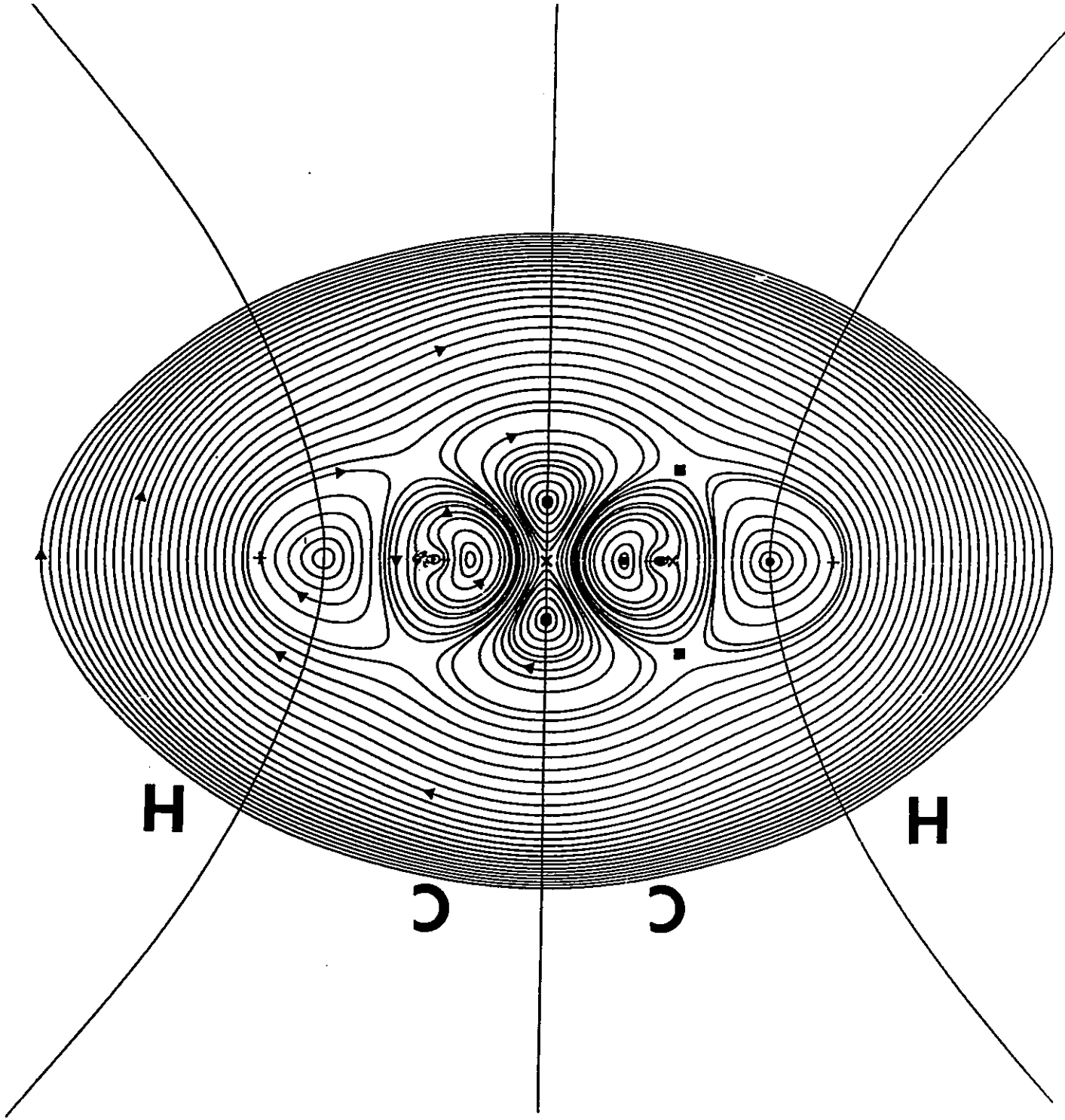
H
H

Figure 2-28

Stagnation graph for C_2H_2 in the symmetry plane parallel to the applied field and containing the internuclear axis. The labels C, S and X correspond to center stagnation paths, saddle stagnation paths and (0,0) critical points respectively. The two out-of-plane center stagnation paths are not shown.

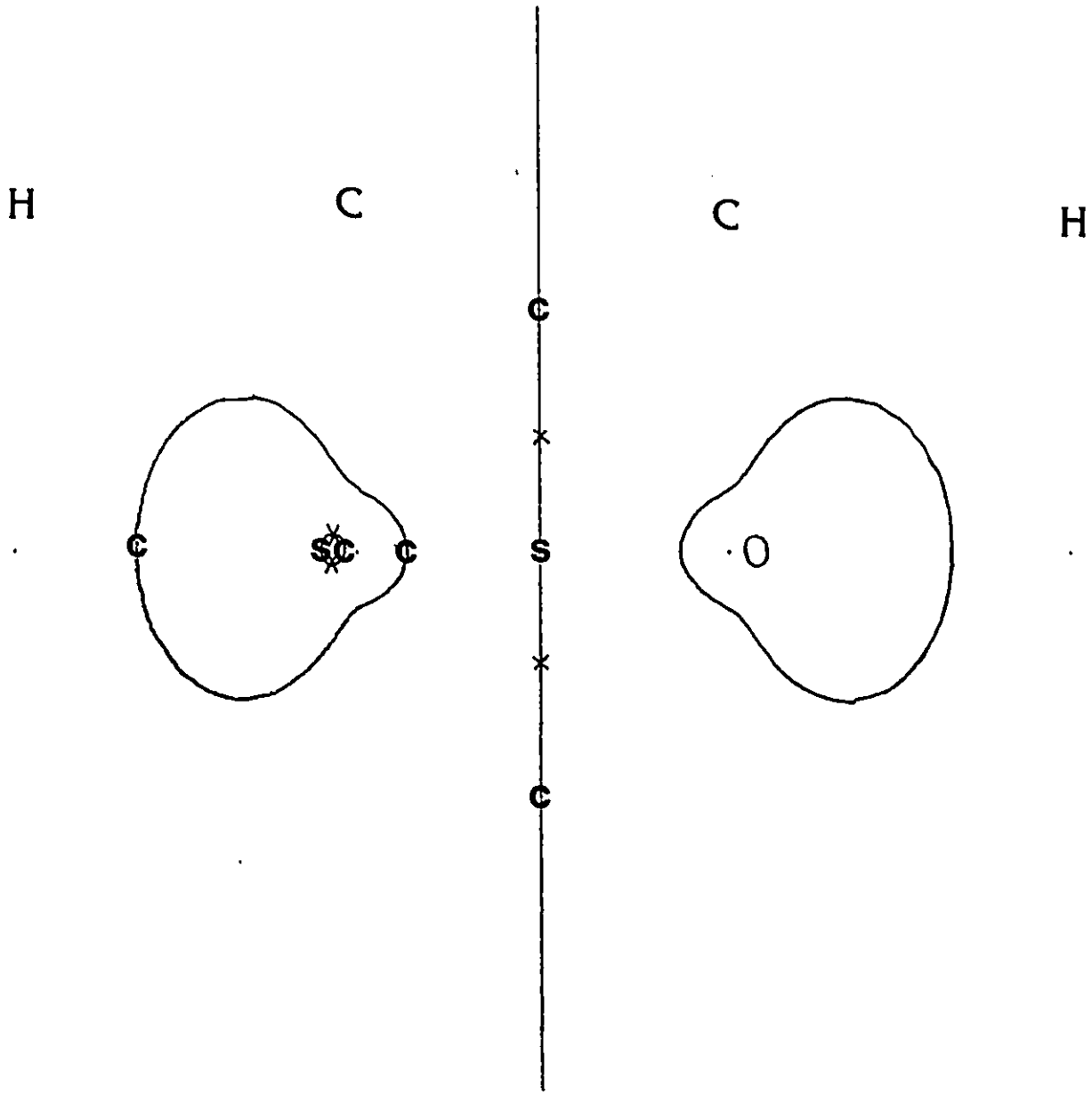
H
C
C
H
O

Figure 2-29

Induced current density in C_2HF in a plane containing the nuclei with the applied field coming out of the page. The intersection of the interatomic surfaces with the plane are also shown. Center critical points are denoted by a dot. There are three saddle critical points in this plane, each denoted by an X. Each carbon possesses a pair of surface critical points, denoted by a filled square.

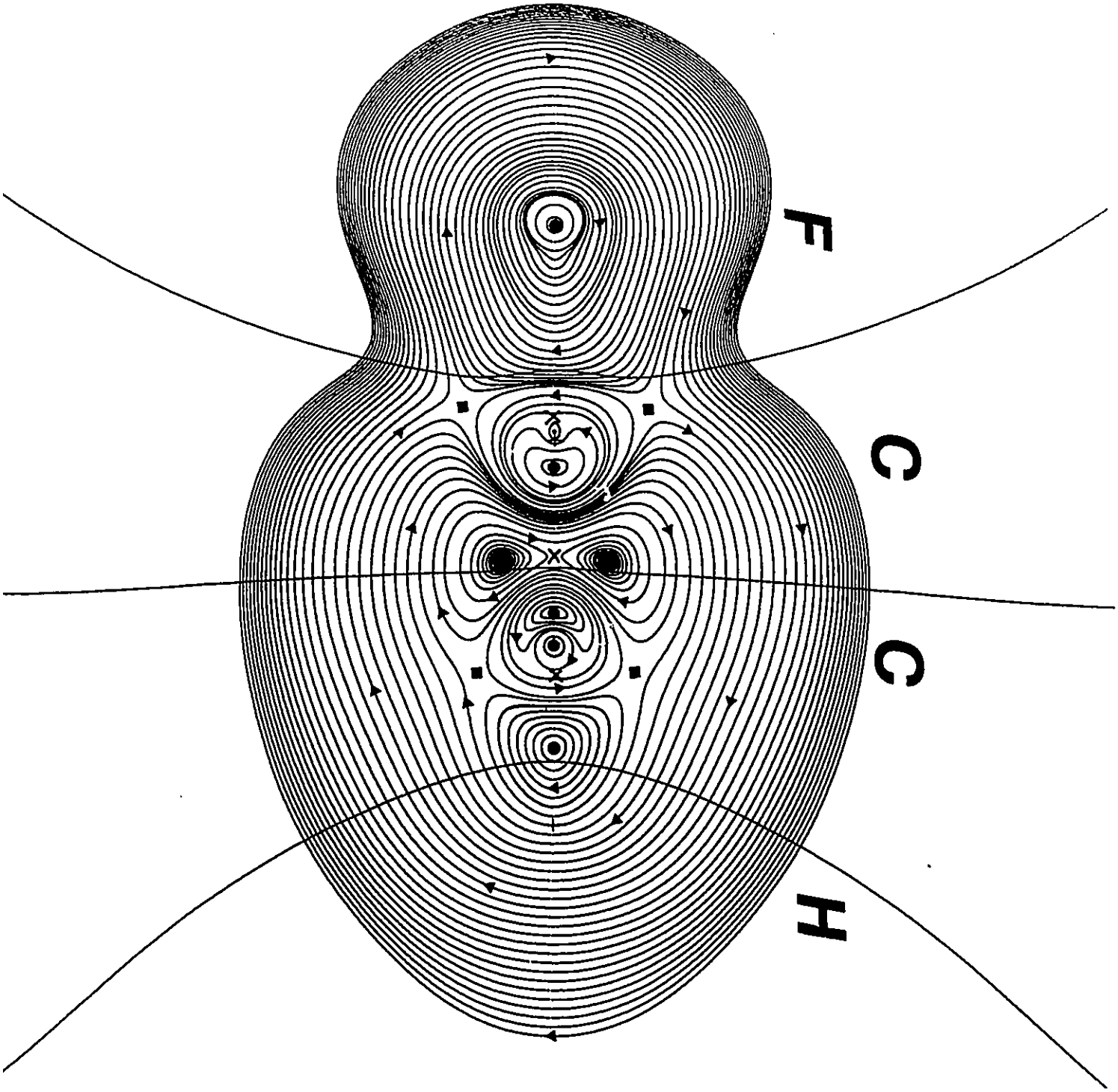
F
C
C
H

Figure 2-30

Stagnation graph for C_2HF in the symmetry plane parallel to the applied field and containing the internuclear axis. The labels C, S and X correspond to center stagnation paths, saddle stagnation paths and (0,0) critical points respectively.

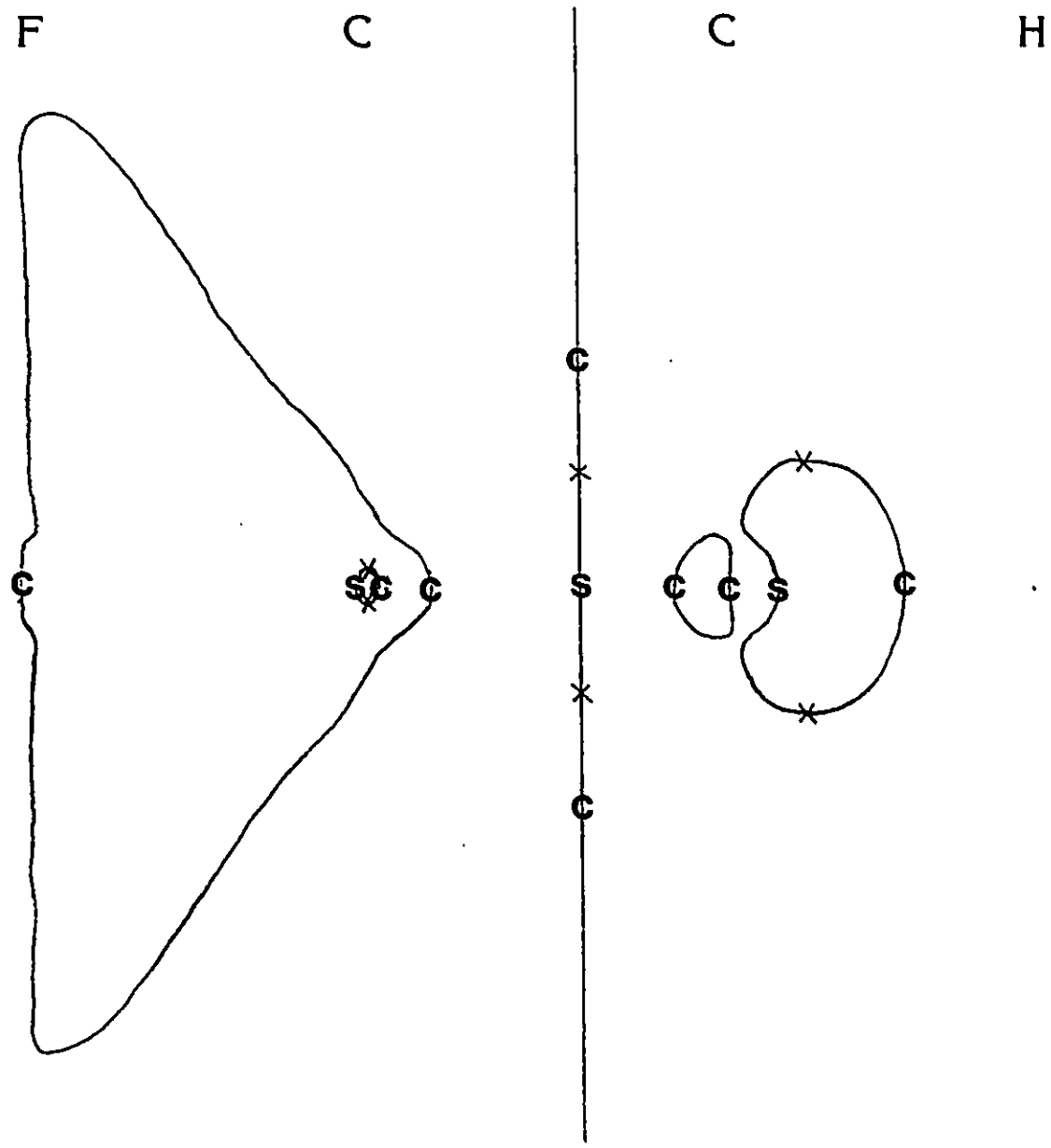
F
C
C
H

Figure 2-31

Induced current density in C_2F_2 in a plane containing the nuclei with the applied field coming out of the page. The intersection of the interatomic surfaces with the plane are also shown. Center critical points are denoted by a dot. There is a single saddle point in this plane at the center of symmetry, denoted by an X. There are four surface critical points in each carbon, each denoted by a filled square.

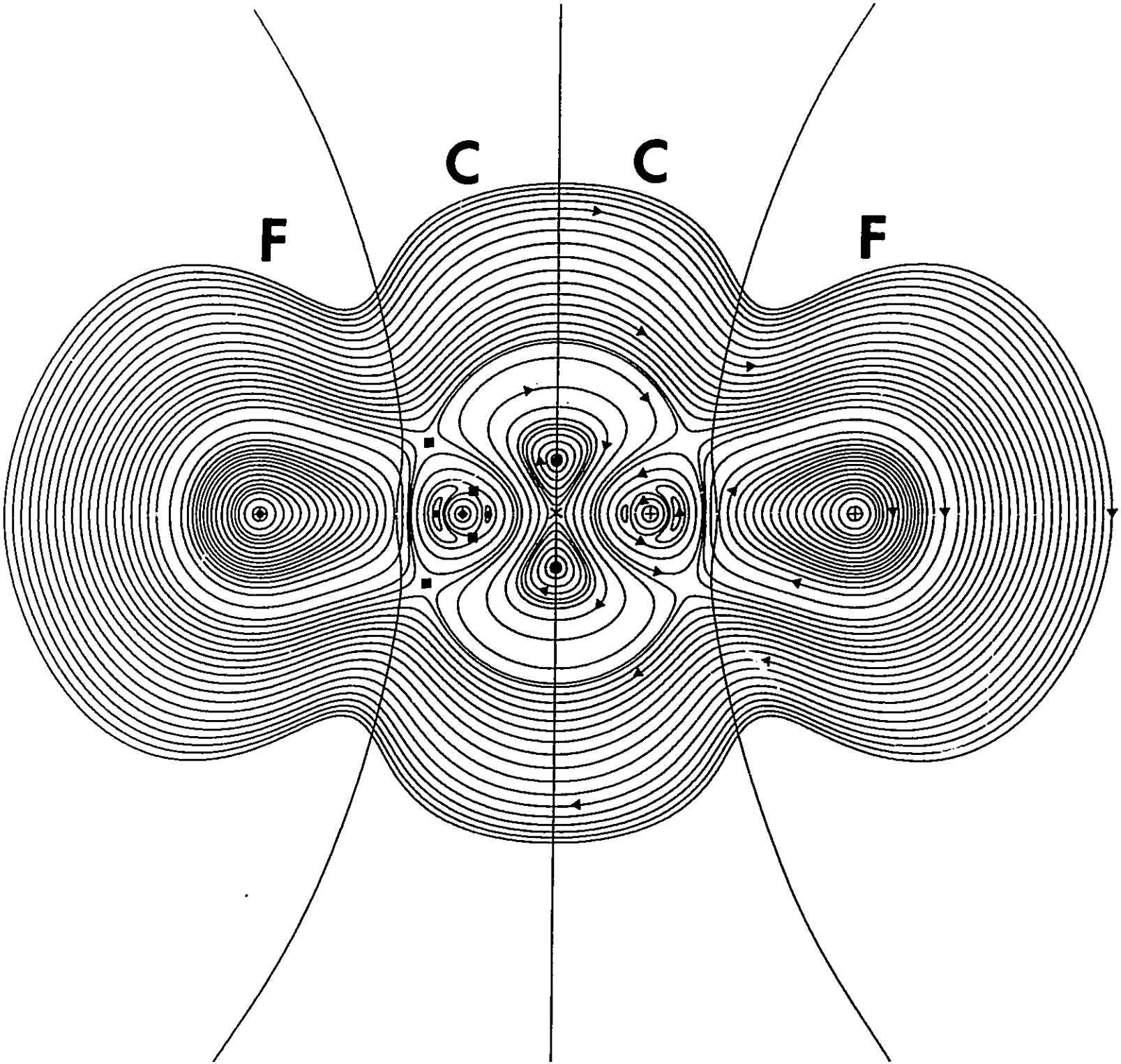
C
C
F
F

Figure 2-32

Stagnation graph for C_2F_2 in the symmetry plane parallel to the applied field and containing the internuclear axis. The labels C, S and X correspond to center stagnation paths, saddle stagnation paths and (0,0) critical points, respectively. The two out of plane center stagnation paths are not shown.

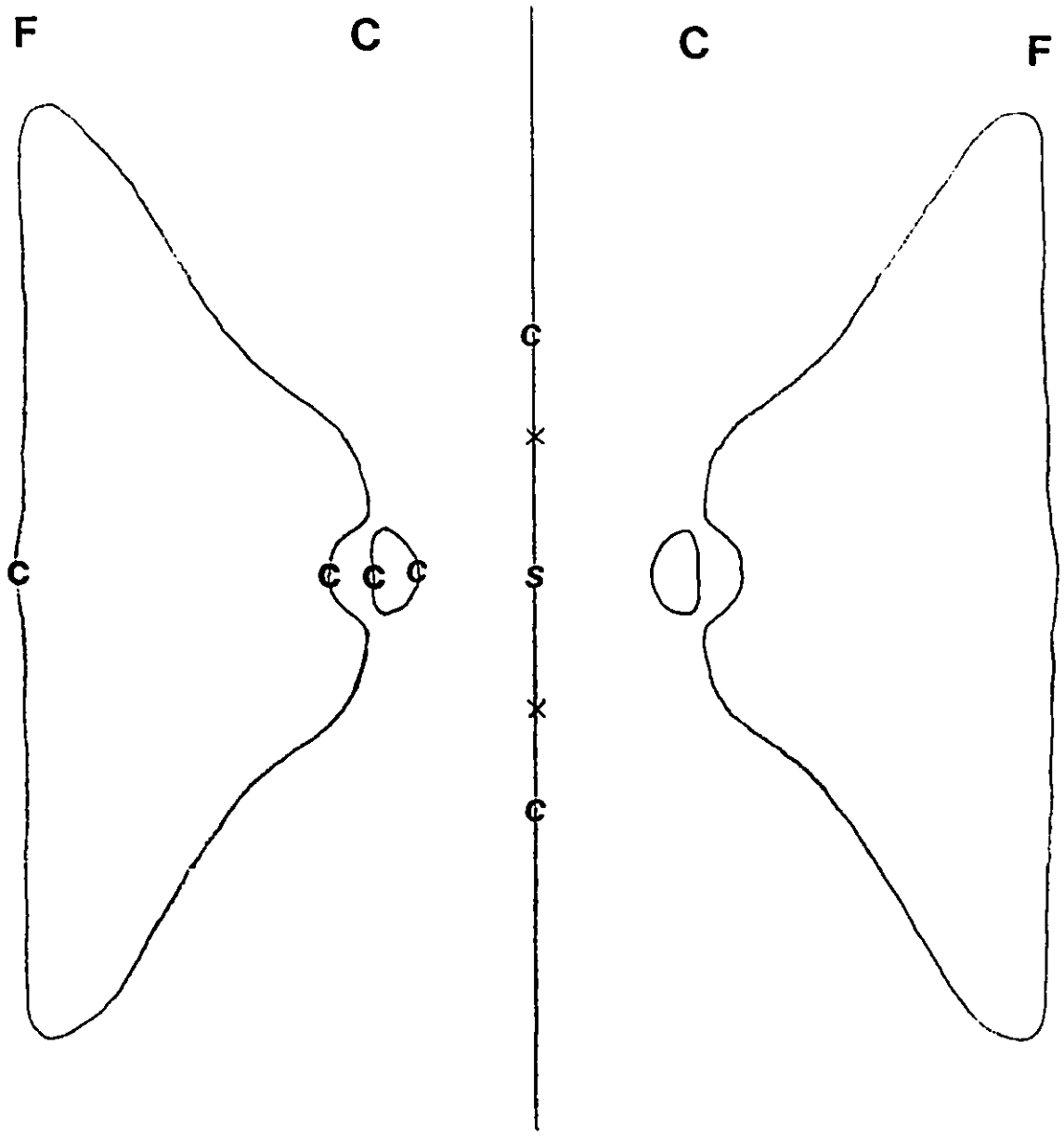
F
C
C
F
C
C
C
C
C
C
S
C

3. Magnetic Susceptibility and Nuclear Magnetic Shielding Tensors

3-1 Introduction

In this chapter magnetic susceptibility and nuclear magnetic shielding tensors of diamagnetic molecules are investigated. Following a basic review of the classical understanding of magnetic susceptibilities, the quantum mechanical perturbation theory approach to defining this property for closed-shell molecules is described. Exploiting the relationship between the magnetic field induced current density distribution and the corresponding magnetic moment, it is shown that the magnetic susceptibility tensor of a molecular system can be expressed as a sum of atomic contributions. An atomic contribution is totally determined by two fundamental properties of the atom: the electronic charge and current density distributions within its basin and on its surface. The computed, isotropically averaged atomic and group

magnetic susceptibilites are shown to be transferable between molecules in a manner which is consistent with the empirical atomic and group increment schemes of Pascal. The transferability is a result of the corresponding transferability of the charge and current density distributions of the atoms. In the case of the normal alkanes, a homologous series in which the methylene group increment can be defined without an arbitrary reference, the theoretical group value is shown to be in excellent agreement with the experimentally derived increment. The elements of an atomic magnetic susceptibility tensor each consist of two distinct contributions: a basin contribution, which measures the magnetic moment of the induced current density distribution within the basin of the atom relative to its nucleus; and a surface contribution, which measures the magnetic moment produced by the net position-weighted flux of the induced current density through each of the interatomic surfaces bounding the atom. The partitioning of the atomic contributions in this way provides a means for further understanding magnetic susceptibility tensors. For example, the unusually large anisotropy of the magnetic susceptibility tensor of benzene is found to be almost entirely a result of the corresponding anisotropy of the surface contributions of the carbon atoms, a result which is consistent with the "ring-current" models that have been developed to explain the anisotropy.

Nuclear magnetic shielding tensors are also determined by the first-order magnetically induced current distributions and, as a result, can also be expressed in terms of atomic contributions. Like an atomic magnetic susceptibility tensor, an atomic NMR shielding tensor is determined entirely by the electronic charge and current density distributions of the atom. With

the exception of protons, the shielding tensor for a particular nucleus is always dominated by the atom containing the nucleus. The contributions from the other atoms in the molecule are relatively small and the total exterior contribution to the shielding of a particular type of non-proton nucleus is nearly constant in different molecules. Thus, the observed substituent effects in carbon NMR spectroscopy are indirect effects arising from the perturbation of the atom containing the shielded nucleus. Since the hydrogen atom does not possess core electrons, the range of proton shielding is much smaller than that for other nuclei and the exterior contributions to the proton shielding tensor are more significant. For example, the observed 2 ppm downfield shift of the proton resonance in benzene relative to ethene and the large 5 ppm anisotropy of the proton shielding in benzene arises almost entirely from the contribution of the benzene ring to the proton shielding tensor rather than from the hydrogen atom containing the proton.

3-2 Background of the Magnetic Susceptibility[1-5]

Experimentally, it is observed that most substances, if placed in a non-uniform magnetic field, will move from their initial position. If the field posesses a gradient only along the x-axis, for example, then such substances will translate along the x-axis, some moving in the direction of the field gradient, toward higher field strength, others in the opposite direction.

This observed behavior is explained classically by defining a magnetic dipole moment **m** for a given substance and expressing the energy of interaction E(**B**) between the substance and the magnetic field **B** field as in eqn. (1)

$$E(\mathbf{B}) = -\mathbf{m}\cdot\mathbf{B} \qquad (1)$$

It follows from this relationship that the classical force acting on the substance is expressed as in eqn. (2), for a field directed along the x-axis

$$\mathbf{F} = -\nabla E(\mathbf{B}) = \mathbf{m}\cdot\nabla\mathbf{B} = \mathbf{i}m(\partial B/\partial x) \qquad (2)$$

This force explains the motion of the substance when the **B** field is not uniform, and it can often be quantitatively measured. If the field strength B is increased and the field gradient is kept constant, it is observed that the force is linearly proportional to the field strength, at least up to moderate field strengths. This observation implies that the magnetic dipole moment of substances in a magnetic field is proportional to the field strength, as expressed in eqn. (3)

$$\mathbf{m} = \chi\mathbf{B} \qquad (3)$$

The proportionality constant χ between **m** and B in eqn. (3), which is found to be a characteristic of the substance, is called the magnetic susceptibility. It is possible to measure the force in eqn. (2) for different orientations of the substance with respect to **B**. If the arrangement of the molecules in the substance is ordered, such as in a crystal, then it is generally observed that both the magnitude and direction of the force, and hence **m**, are dependent on this orientation. These observations, together with an initial torque (**m** x **B**) on such a substance (assumed spherically shaped for simplicity) which rotates it to a specific orientation with respect to **B**, indicate that the magnetic susceptibility is actually a symmetric second-rank tensor χ. Thus, the magnetic dipole moment of the substance is expressed more generally as in eqn. (4)

$$\mathbf{m} = \chi\cdot\mathbf{B} \qquad (4)$$

The relationship in eqn. (4) states that the magnetic dipole moment of the substance in the presence of the field **B** is linearly proportional to the field strength B but is not necessarily directed along the same axis as the **B** field. The elements of the tensor χ are not unique but depend on the chosen coordinate system. However, since χ is real and symmetric, there exists a unique coordinate system in which it is diagonal. When the magnetic field is applied along one of the axes of this coordinate system, the magnetic dipole moment direction for the substance is coincident with the field direction. These unique axes are called the principal magnetic axes of the substance and the corresponding components of χ are called the principal magnetic susceptibilities. If the substance is a molecular crystal, the principal magnetic axes of the crystal do not necessarily coincide with the principal magnetic axes of the molecules in the crystal. However, if the orientation of the molecules in the crystal is known, then the molecular principal susceptibilities can be determined from the crystal's principal susceptibilities if the interactions between molecules is negligible. From a macroscopically disordered solid or a liquid or gas the individual components of the susceptibility tensors of the constituent molecules cannot be determined using this approach, in general, but only the average, $\bar{\chi}$, of the diagonal components of χ can be determined. This is because the molecules are randomly oriented in the bulk substance. Since $\bar{\chi}$ is proportional to the trace of χ, it is an invariant quantity equal to the average of the principal susceptibilities.

The "force" method is by no means the only technique for gathering information about the χ tensor, though it is perhaps conceptually the

simplest. There now exist a variety of experimental techniques,[6,7] primarily spectroscopic, for measuring differences in the principal susceptibilities, ie. the anisotropies of the principal χ tensor. These anisotropies, together with $\bar{\chi}$, often allow the determination of the principal components of χ.

From eqns. (1) and (4), the relationship between χ and the interaction energy E(B) is expressed as in eqn. (5)

$$E(B) = -B \cdot \chi \cdot B \qquad (5)$$

This classical formula, relating the magnetic susceptibility tensor to the interaction energy, is the key to defining and calculating χ within the framework of quantum mechanics, as will be shown in the following section.

Generally, molecular substances can be divided into two classes (ferromagnetic and related materials are excluded from this entire discussion) according to the sign and magnitude of their average susceptibility $\bar{\chi}$ as well as the variation of this quantity with respect to temperature. *Paramagnetic* substances are those with relatively large *positive* susceptibilities which, in general, vary linearly with the field strength and inversely with temperature. They are now known to be composed of molecules with permanent magnetic moments which, in the absence of the field, are randomly oriented giving the bulk substance, even if crystalline, a magnetic dipole moment of zero. In the presence of the field the individual moments of the molecules become partially aligned with the field giving the bulk substance a nonzero magnetic moment, the alignment increasing with decreasing temperature and increasing field strength. The magnetic moment of a paramagnetic substance approaches a finite maximum value at low temperature and/or high field strength, corresponding to perfect alignment of the molecular moments with the field.

Since the magnetic moment of a paramagnetic substance is always at least partially aligned with the field, the interaction energy is always negative (stabilizing), eqn. (5), and a paramagnetic substance translates in the direction of a field gradient, eqn. (2).

Diamagnetic substances are composed of molecules without permanent magnetic moments. Instead, the applied magnetic field *induces* a magnetic dipole moment in each of the molecules making up the substance, and thus in the bulk substance as a whole. Diamagnetic substances, usually, but not necessarily, possess *negative* susceptibilities, ie. the induced moment is at least partially anti-parallel to the **B** field, with the interaction energy being positive (destabilizing), eqn. (5). Such diamagnetic substances translate in opposition to the direction of a field gradient, eqn. (4), ie. they are repelled from high field regions. Unlike bulk paramagnetic susceptibilities, bulk diamagnetic susceptibilities are essentially temperature independent.

The mechanism responsible for diamagnetism (and paramagnetism) is entirely quantum mechanical in origin[5] and, as will be shown below, is actually present in all substances. In paramagnetic substances the diamagnetism is not directly measurable because the magnitude of the paramagnetism is usually much larger. Nonetheless, diamagnetism is a universal property of matter, and it is thus the physics of diamagnetism that is addressed in this work.

From a chemist's viewpoint, perhaps the most well known results associated with diamagnetism are those initiated by Pascal et al,[1-4,8-9] who devised simple but powerful schemes for predicting the diamagnetic

susceptibilities of complex compounds based on a set of transferable atomic and group contributions defined from the measured susceptibilities of relatively simple compounds. Prior to the development of NMR (primarily) measured diamagnetic susceptibilities together with the empirical increment schemes were significant tools in determining molecular structure as well as chemical composition.

Another well known result associated with diamagnetism is the very large magnetic susceptibility anisotropy that certain cyclic, aromatic compounds such as benzene exhibit.[1-7] The principal susceptibility of benzene corresponding to a field applied perpendicular to the plane of the ring is nearly three times as large in magnitude as the principal susceptibilities corresponding to fields applied parallel to the plane of the ring. This observation prompted the proposition of various "ring-current" models[1-7] in order to explain it, whereby the enhanced magnetic moment resulting from a field applied perpendicular to the conjugated ring is attributed to an enhanced, delocalized electronic current flowing about the ring, as opposed to the localized, "atomic-like" currents which were inferred from the successful atomic increment schemes.

This work is an attempt to understand the physical basis of the observations mentioned above as well as other aspects of molecular diamagnetism.

3-3 Quantum Theory of the Diamagnetic Susceptibility Tensor χ[10-16]

A quantum theory of the diamagnetic susceptibility tensor most easily begins with eqn. (5), which relates χ to an energy, a well-defined property in

quantum mechanics. Following this approach, in order to define χ for a quantum molecular system one needs to define the energy of the molecule in the presence of a magnetic field, E(**B**). In accordance with the experimental conditions under which χ is usually measured, the theoretical magnetic field is static (time-independent), and uniform throughout the molecule (field gradients present in the experiment refer to macroscopic dimensions). The electronic Schrodinger equation in this case is given in eqn. (6) for an N-electron molecule with no net electron spin (S=0), where the Born-Oppenheimer approximation is assumed and all non-coulombic internal interactions are neglected.

$$\hat{H}\psi = (1/2m)\sum_{i=1}^{N}(\hat{\pi}_i)^2\psi + \hat{V}\psi = (1/2m)\sum_{i=1}^{N}(\hat{\mathbf{p}}_i+(e/c)\hat{\mathbf{A}}_i)^2\psi + \hat{V}\psi$$

$$= \hat{H}^{(0)}\psi + \sum_{i=1}^{N}((e/mc)\hat{\mathbf{A}}_i\cdot\hat{\mathbf{p}}_i + (e^2/2mc^2)\hat{\mathbf{A}}_i^2)\psi$$

$$= \hat{H}^{(0)}\psi + \sum_{i=1}^{N}((e/2mc)\mathbf{B}\cdot\hat{\mathbf{L}}_i + (e^2/8mc^2)\mathbf{B}\cdot[\mathbf{I}r_i^2 - \mathbf{r}_i\mathbf{r}_i]\cdot\mathbf{B})\psi$$

$$= \hat{H}^{(0)}\psi + \hat{H}^{(1)}\psi + \hat{H}^{(2)}\psi = E(\mathbf{B})\psi \qquad (6)$$

In this equation, $\hat{\pi}_i$ is the canonical momentum operator for the i^{th} electron which is defined, according to Hamilton's principle, from the Lagrangian equation of motion for the electron in the presence of **B**. The operator $\hat{\mathbf{L}}_i$ is the angular momentum operator for the i^{th} electron, equal to $(\hat{\mathbf{r}}_i \times \hat{\mathbf{p}}_i)$, while **I** is the unit tensor.

The quantity $\mathbf{A}_i$ in eqn. (6) is a vector potential for the i^{th} electron which is defined to yield the magnetic field **B** through Maxwell's equation, given in eqns. (7)

$$\nabla \cdot \mathbf{B} = 0$$

$$\therefore \mathbf{B} = \nabla_i \times \mathbf{A}_i$$

$$\nabla_i \times \nabla_i f(\mathbf{r}_i) = 0$$

$$\therefore \mathbf{B} = \nabla_i \times [\mathbf{A}_i + \nabla_i f(\mathbf{r})] \qquad (7)$$

but it is not unique because the addition of the gradient of any scalar function $f(\mathbf{r}_i)$ to $\mathbf{A}_i$ leaves **B**, and therefore properties determined through interactions involving **B**, unchanged. For a uniform magnetic field the potential $\mathbf{A}_i$ can be expressed as

$$\hat{\mathbf{A}}_i = (1/2)(\mathbf{B} \times (\mathbf{r}_i - \mathbf{r}_0) \qquad (8)$$

which is the form used in eqn. (6). Choosing this form for $\mathbf{A}_i$ is simply based on convenience: because $\mathbf{A}_i$ in eqn. (8) is divergenceless ($\nabla_i \cdot \mathbf{A}_i = 0$), Schrodinger's equation, eqn. (6), is simplified. Nonetheless, even this form of the vector potential is arbitrary with respect to an origin $\mathbf{r}_0$ for the electronic position vectors $\mathbf{r}_i$. A shift in the origin of $\mathbf{A}_i$ by an amount **d** corresponds to $f(\mathbf{r}_i) = (1/2)(\mathbf{B} \times \mathbf{d}) \cdot \mathbf{r}_i$ in eqn. (7) and does not affect the simplifying relation $\nabla_i \cdot \mathbf{A}_i = 0$ or the energy E(B) calculated from eqn.(6).

In exact treatments of eqn. (6) the arbitrariness of $\mathbf{A}_i$ is unimportant, but in approximate methods it becomes very important. This is the "gauge problem",[13] commonly encountered in calculating magnetic properties of electronic systems. Chapter 1 describes the methods[17,18] used in this work to overcome the gauge problem, so it will not be considered further here.

To obtain a diamagnetic susceptibility tensor from the energy E(B), one

can expand $E(\mathbf{B})$ in a Taylor series about $\mathbf{B}=0$, as in eqn. (9)

$$E(\mathbf{B}) = E^{(0)} + E(\mathbf{B})^{(1)} + E(\mathbf{B})^{(2)} + \ldots$$

$$= E^{(0)} + (\nabla E(\mathbf{B}))_{B=0}\cdot\mathbf{B} + (1/2)\mathbf{B}\cdot\nabla\nabla(E(\mathbf{B}))_{B=0}\cdot\mathbf{B} + \ldots \qquad (9)$$

and identify the Hessian of $E(\mathbf{B})$ evaluated at zero field strength, $\nabla\nabla(E(\mathbf{B}))_{B=0}$, with -2χ in accordance with classical expression for $E(\mathbf{B})$ given in eqn. (5). With this identification, to calculate χ completely for a molecule it is necessary to determine the energy $E(\mathbf{B})$ to second-order $E(\mathbf{B})^{(2)}$ in a general uniform magnetic field $\mathbf{B}(B_x,B_y,B_z)$. Standard perturbation theory can be used to obtain $E(\mathbf{B})^{(2)}$ from eqn. (6) if the unperturbed molecular problem has been solved.

Following the perturbative approach, the *first*-order correction to the energy, $E(\mathbf{B})^{(1)}$, of the molecule perturbed from the ground state $\psi_0^{(0)}$ is given as in eqn. (10)

$$E(\mathbf{B})^{(1)} = \langle\psi_0^{(0)}|\hat{H}^{(1)}|\psi_0^{(0)}\rangle = (e/2mc)\mathbf{B}\cdot\sum_{i=1}^{n}\langle\psi_0^{(0)}|\hat{\mathbf{L}}_i|\psi_0^{(0)}\rangle \qquad (10)$$

Defining the field-free *orbital* magnetic moment operator $\hat{\mathbf{m}}^{(0)}$ as in eqn. (11)

$$\hat{\mathbf{m}}^{(0)} = -(e/2mc)\sum_{i=1}^{N}\mathbf{r}_i\times\hat{\mathbf{p}}_i = -(e/2mc)\sum_{i=1}^{N}\hat{\mathbf{L}}_i \qquad (11)$$

the first-order energy can be written in analogy with the classical expression of eqn. (1) as

$$E(\mathbf{B})^{(1)} = -\langle\psi_0^{(0)}|\hat{\mathbf{m}}^{(0)}|\psi_0^{(0)}\rangle\cdot\mathbf{B} \qquad (12)$$

where $\langle\psi_0^{(0)}|\hat{\mathbf{m}}^{(0)}|\psi_0^{(0)}\rangle$ is the orbital magnetic moment of the unperturbed molecule, ie. the permanent orbital magnetic moment. For closed-shell molecules, the only molecules of concern in this work, $\psi_0^{(0)}$ can always be chosen real. Since $E(\mathbf{B})$, and therefore $E(\mathbf{B})^{(1)}$, must be real, and since

$E(B)^{(1)}$ is an expectation value of the imaginary operator $\hat{m}^{(0)}$, $E(B)^{(1)}$ must be zero in these molecules, ie. closed-shell molecules possess no permanent orbital magnetic dipole moment. In open-shell molecules $\langle\hat{m}\rangle^{(0)}$ can be non-zero and, in addition to this orbital magnetic moment, a molecule can possess a permanent magnetic moment arising from the net spin of the electrons if the molecule is in a non-singlet state. Since open-shell molecules have permanent magnetic moments, they are paramagnetic.

It is important to recall at this point that the classical linear relationship between magnetic moment and field strength refers to bulk substances whereas eqn. (12) refers to a single molecule whose magnetic moment is independent of field strength. A statistical mechanical treatment[1-4] of an ensemble of such molecules shows that the moment of the bulk substance, which is the sum of the molecular moments, is linear in the field strength and inversely proportional to the temperature of the substance as long as the ratio B/T is not too small.

Since open-shell molecules also have non-vanishing second-order energies, they, like the closed-shell molecules of interest here, also possess a diamagnetic contribution to the total susceptibility, as will become clear below.

The second-order correction to the energy of the molecule in the B field, $E(B)^{(2)}$, is given in eqn. (13)

$$E(B)^{(2)} = (1/2)\{\langle\psi_0^{(0)}|\hat{H}^{(1)}|\psi^{(1)}(B)\rangle+\langle\psi^{(1)}(B)|\hat{H}^{(1)}|\psi_0^{(0)}\rangle\}+\langle\psi_0^{(0)}|\hat{H}^{(2)}|\psi_0^{(0)}\rangle \quad (13)$$

where $\psi(B)^{(1)}$ is the first-order correction to the wavefunction due to the magnetic field perturbation, as given in eqn. (14)

$$\psi(\mathbf{B})^{(1)} = \sum_{n=1}^{\infty} (E_0^{(0)} - E_n^{(0)})^{-1} \langle \psi_n^{(0)} | \hat{H}^{(1)} | \psi_0^{(0)} \rangle \psi_n^{(0)} \qquad (14)$$

In this equation, $\psi_n^{(0)}$ and $E_n^{(0)}$ represent the n^{th} eigenstate and eigenvalue, respectively of the unperturbed electronic Hamiltonian $\hat{H}^{(0)}$.

Explicitly, $E(\mathbf{B})^{(2)}$ is expressed as in eqn. (15)

$$E(\mathbf{B})^{(2)} = \sum_{n=1}^{\infty} \{ (E_0^{(0)} - E_n^{(0)})^{-1} \langle \psi_0^{(0)} | \hat{H}^{(1)} | \psi_n^{(0)} \rangle \langle \psi_n^{(0)} | \hat{H}^{(1)} | \psi_0^{(0)} \rangle \} + \langle \psi_0^{(0)} | \hat{H}^{(2)} | \psi_0^{(0)} \rangle$$

$$= (e^2/8m^2c^2) \sum_{n=1}^{\infty} \{ (E_0^{(0)} - E_n^{(0)})^{-1} \mathbf{B} \cdot \langle \psi_0^{(0)} | \sum_{i=1}^{N} (\mathbf{r}_i \times \hat{\mathbf{p}}_i) | \psi_n^{(0)} \rangle \langle \psi_n^{(0)} | \sum_{i=1}^{N} (\mathbf{r}_i \times \hat{\mathbf{p}}_i) | \psi_0^{(0)} \rangle \cdot \mathbf{B} \}$$

$$+ (e^2/8mc^2) \mathbf{B} \cdot \langle \psi_0^{(0)} | [\mathbf{I} r_i^2 - \mathbf{r}_i \mathbf{r}_i] | \psi_0^{(0)} \rangle \cdot \mathbf{B} \qquad (15)$$

Using eqns. (5) and (9), the $\alpha\beta$ component of the diamagnetic susceptibility tensor, $\chi_{\alpha\beta}$, can be obtained from $E(\mathbf{B})$ as in eqn. (16)

$$\chi_{\alpha\beta} = (-1/2)(\partial^2 E(\mathbf{B})/\partial B_\alpha \partial B_\beta)_{B=0} = (-1/2)(\partial^2 E(\mathbf{B})^{(2)}/\partial B_\alpha \partial B_\beta) \qquad (16)$$

Using eqn. (15), $\chi_{\alpha\beta}$ is expressed explicitly as in eqn. (17)

$$\chi_{\alpha\beta} = (e^2/4m^2c^2) \sum_{n=1}^{\infty} (E_0^{(0)} - E_n^{(0)})^{-1} \langle \psi_0^{(0)} | \sum_{i=1}^{N} (\mathbf{r}_i \times \hat{\mathbf{p}}_i)_\alpha | \psi_n^{(0)} \rangle \langle \psi_n^{(0)} | \sum_{i=1}^{N} (\mathbf{r}_i \times \hat{\mathbf{p}}_i)_\beta | \psi_0^{(0)} \rangle$$

$$+ (e^2/4mc^2) \langle \psi_0^{(0)} | [\delta_{\alpha\beta} r_i^2 - \mathbf{r}_{i\alpha} \mathbf{r}_{i\beta}] | \psi_0^{(0)} \rangle \qquad (17)$$

Eqn. (17) is the Rayleigh-Schrodinger perturbation theory expression for the diamagnetic susceptibility tensor χ of any molecule.[10]

Alternatively, one can obtain the same expression for χ from eqn. (4) and the Hellmann-Feynman[12] theorem by defining the magnetic dipole moment operator $\hat{\mathbf{m}}(\mathbf{B})$ in the presence of the B field, in analogy with the field-free case, as in eqn. (18)

$$\hat{\boldsymbol{\pi}}_i = [\hat{\mathbf{p}}_i + (e/c)\mathbf{A}_i]$$

$$\therefore \hat{\mathbf{m}}(\mathbf{B}) = -(e/2mc)\mathbf{r}_i \times \hat{\boldsymbol{\pi}}_i \qquad (18)$$

Expanding the expectation value of this operator $\langle\hat{\mathbf{m}}(\mathbf{B})\rangle$ in terms of B, as in eqn. (19)

$$\langle\mathbf{m}(\mathbf{B})\rangle = \langle\hat{\mathbf{m}}(\mathbf{B})\rangle^{(0)} + \langle\hat{\mathbf{m}}(\mathbf{B})\rangle^{(1)} + \ldots$$

$$= \langle\hat{\mathbf{m}}^{(0)}\rangle + \chi\cdot\mathbf{B} + \ldots \tag{19}$$

leads to the following expression for χ

$$\chi_{\alpha\beta} = (\partial\langle\hat{\mathbf{m}}(\mathbf{B})\rangle_{\alpha}/\partial B_{\beta})_{B=0} \tag{20}$$

Noting, from the Hellmann-Feynman theorem, that

$$(\partial E(\mathbf{B})/\partial B_{\alpha}) = \langle(\partial\hat{H}/\partial B_{\alpha})\rangle = -\langle\hat{\mathbf{m}}(\mathbf{B})\rangle_{\alpha} \tag{21}$$

it follows from eqns. (20) and (21) that the expression for $\chi_{\alpha\beta}$ given in eqn. (16) is again obtained. It is repeated here as eqn. (22)

$$\chi_{\alpha\beta} = -(1/2)(\partial^2 E(\mathbf{B})/\partial B_{\alpha}\partial B_{\beta})_{B=0} \tag{22}$$

Because of the indistinguishability of electrons, the explicit expression for $\chi_{\alpha\beta}$ given in eqn. (17) can be usefully written in terms of the operators $\mathbf{r}$ and $\hat{\mathbf{p}}$ for a single electron, as in eqn. (23)

$$\chi_{\alpha\beta} = (Ne^2/4m^2c^2)\sum_{n=1}^{\infty}(E_0^{(0)}-E_n^{(0)})^{-1}\langle\psi_0^{(0)}|(\mathbf{r}\times\hat{\mathbf{p}})_{\alpha}|\psi_n^{(0)}\rangle\langle\psi_n^{(0)}|(\mathbf{r}\times\hat{\mathbf{p}})_{\beta}|\psi_0^{(0)}\rangle$$

$$+ (e^2/4mc^2)\int d\tau'\rho^{(0)}(\mathbf{r})[\delta_{\alpha\beta}r^2 - r_{\alpha}r_{\beta}] \tag{23}$$

where $\rho^{(0)}(\mathbf{r})$ is the ground-state electron density and the integration in the second term is over all electronic spin coordinates and the spatial coordinates of all electrons but one.

3-4 Relationship of χ to the Magnetically Induced Current Density $\mathbf{J}^{(1)}(\mathbf{r})$

It is possible and useful to express χ in terms of a more fundamental, and independently observable quantity, the electronic current density $\mathbf{J}(\mathbf{r})$

induced by **B**, which is given in general form in eqn. (24)

$$\mathbf{J}(\mathbf{r}) = (-e/2m) \sum_{i=1}^{N} \int d\tau' \, [\psi^* \hat{\pi}_i \psi + (\hat{\pi}_i \psi)^* \psi] \tag{24}$$

where $d\tau'$ again refers to the integration over the coordinates of all N electrons but one. Using Rayleigh-Schrodinger perturbation theory, the induced current density to first-order in **B**, $\mathbf{J}^{(1)}(\mathbf{r})$, is as follows

$$\mathbf{j}^{(1)}(\mathbf{r}) = (-e/2m) \sum_{i=1}^{N} \int d\tau' \, [\psi_0^{(0)*} \hat{\mathbf{p}}_i \psi^{(1)} + \psi^{(1)*} \hat{\mathbf{p}}_i \psi_0^{(0)} - (\hat{\mathbf{p}}_i \psi_0^{(0)*}) \psi^{(1)} - (\hat{\mathbf{p}}_i \psi^{(1)*}) \psi_0^{(0)}]$$

$$- (e^2/mc) \sum_{i=1}^{N} \int d\tau' \, \psi_0^{(0)} \psi_0^{(0)} \mathbf{A}_i$$

$$= (-e/m) \sum_{i=1}^{N} \int d\tau' \, [\psi_0^{(0)} \hat{\mathbf{p}}_i \psi^{(1)} - \psi^{(1)} \hat{\mathbf{p}}_i \psi_0^{(0)}] - (e^2/mc) \sum_{i=1}^{N} \int d\tau' \, \psi_0^{(0)} \psi_0^{(0)} \mathbf{A}_i$$

$$= (-Ne/m) \int d\tau' \, [\psi_0^{(0)} \hat{\mathbf{p}} \psi^{(1)} - \psi^{(1)} \hat{\mathbf{p}} \psi_0^{(0)}] - (e^2/mc) \rho^{(0)}(\mathbf{r}) \mathbf{A}$$

$$= (-Ne/m) \sum_{n=1}^{\infty} (E_0^{(0)} - E_n^{(0)})^{-1} \langle \psi_0^{(0)} | (\mathbf{r} \times \hat{\mathbf{p}}) | \psi_n^{(0)} \rangle \int d\tau' \, [\psi_0^{(0)} \hat{\mathbf{p}} \psi_n^{(0)} - \psi_n^{(0)} \hat{\mathbf{p}} \psi_0^{(0)}]$$

$$- (e^2/mc) \rho^{(0)}(\mathbf{r}) \mathbf{A}] \tag{25}$$

The topology and other properties of the $\mathbf{J}^{(1)}(\mathbf{r})$ vector field are analyzed in detail in Chapter 2.

From the expression for $\mathbf{J}^{(1)}(\mathbf{r})$ in eqn. (25) and the expression for χ given in eqn. (20), the following relationship between χ and $\mathbf{J}^{(1)}(\mathbf{r})$ is obtained[19]

$$\chi_{\alpha\beta} = -(1/2Bc) \int d\mathbf{r} [\mathbf{r} \times \mathbf{J}_\beta^{(1)}(\mathbf{r})]_\alpha \tag{26}$$

where $\mathbf{J}_\beta^{(1)}(\mathbf{r})$ is the first-order vector current density induced by the β

component of the magnetic field, and the origin of $\mathbf{r}$ is arbitrary since the total induced current of the molecule is zero. From the relationship between χ and the first-order magnetic dipole moment $\mathbf{m}(\mathbf{B})^{(1)}$ given in eqn. (19), the well known classical relationship between a current density distribution and a magnetic dipole moment is seen to hold for quantum molecular systems.[19]

$$\mathbf{m}(\mathbf{B})^{(1)} = -\mathbf{B}\cdot\chi = (1/2c)\int d\mathbf{r}[\mathbf{r} \times \mathbf{J}_{\beta}^{(1)}(\mathbf{r})] \tag{27}$$

3-5 Atomic Contributions to Magnetic Susceptibility Tensors

Eqn. (26) is the starting point for defining a diamagnetic susceptibility tensor $\chi_{\alpha\beta}(\Omega)$ for an atom Ω in a molecule.[20] The aspects of the theory of atoms in molecules relevant to this work are summarized in the Appendix. The most obvious definition for $\chi_{\alpha\beta}(\Omega)$ would simply be to restrict the integration in equation (26) to the basin of the atom, a definition which will be labeled $\chi'_{\alpha\beta}(\Omega)$ and is given in eqn. (28)

$$\chi'_{\alpha\beta}(\Omega) = -(1/2Bc)\int_{\Omega} d\mathbf{r}[\mathbf{r} \times \mathbf{J}_{\beta}^{(1)}(\mathbf{r})]_{\alpha} \tag{28}$$

Since the partitioning of molecules into atoms is disjoint and complete, such a definition satisfies the physical requirement that the atomic contributions $\chi_{\alpha\beta}(\Omega)$ sum to the molecular value $\chi_{\alpha\beta}$, as in eqn. (29)

$$\chi_{\alpha\beta} = \sum_{\Omega} \chi'_{\alpha\beta}(\Omega) \tag{29}$$

However, $\chi'_{\alpha\beta}(\Omega)$, as defined in eqn. (28), is origin dependent, and therefore of little use, since the total induced current within an atom is not necessarily zero as it is in the molecule as a whole. A useful definition of

$\chi_{\alpha\beta}(\Omega)$ must be origin independent and be determined only by other properties of the atom so that it can be compared among different environments. Such a definition is possible by first expressing the electronic position vector $\mathbf{r}$ as in eqn. (30)

$$\mathbf{r} = \mathbf{r}_\Omega + \mathbf{R}_\Omega \tag{30}$$

where $\mathbf{R}_\Omega$ is the position vector of the nucleus of atom Ω relative to an arbitrary origin and $\mathbf{r}_\Omega$ is the electronic position vector relative to the nucleus. With this substitution $\chi'_{\alpha\beta}(\Omega)$ becomes

$$\chi'_{\alpha\beta}(\Omega) = -(1/2Bc)\{\int_\Omega d\mathbf{r}_\Omega[\mathbf{r}_\Omega \times J^{(1)}_\beta(\mathbf{r}_\Omega)]_\alpha + \mathbf{R}_\Omega \times \int_\Omega d\mathbf{r} J^{(1)}_\beta(\mathbf{r})\}$$

$$= -(1/2Bc)\{\int_\Omega d\mathbf{r}_\Omega[\mathbf{r}_\Omega \times J^{(1)}_\beta(\mathbf{r}_\Omega)]_\alpha + \mathbf{R}_\Omega \times J^{(1)}_\beta(\Omega)\} \tag{31}$$

where $J^{(1)}_\beta(\Omega)$ is the average vector current induced in atom Ω by a magnetic field applied in the β direction. In eqn. (31) the origin dependence of $\chi'_{\alpha\beta}(\Omega)$ is contained in the second term only, through the nuclear position vector $\mathbf{R}_\Omega$.

Since the average induced current of the molecule is zero, $J^{(1)}_\beta(\Omega)$ can be replaced by the minus the average induced current of the remainder of the molecule Ω', $J^{(1)}_\beta(\Omega')$, resulting in eqn. (32)

$$\chi'_{\alpha\beta}(\Omega) = -(1/2Bc)\{\int_\Omega d\mathbf{r}_\Omega[\mathbf{r}_\Omega \times J^{(1)}_\beta(\mathbf{r}_\Omega)]_\alpha - \mathbf{R}_\Omega \times J^{(1)}_\beta(\Omega')\} \tag{32}$$

The region Ω' of the remainder of the molecule is naturally partitioned into atoms or groups of atoms Ω'', each of which is separated from atom Ω by an interatomic surface $S(\Omega,\Omega'')$, a portion of the total surface $S(\Omega)$ of atom Ω which is defined by a critical point in the charge density distribution

embedded within $S(\Omega)$ (see Appendix). In the ethanol molecule for example, the methylol carbon is linked to the four groups: H_a, H_b, CH_3 and OH separately through the four (3,-1) bond critical points in its surface. With this partitioning of Ω' the expression for $\chi'_{\alpha\beta}(\Omega)$ becomes

$$\chi'_{\alpha\beta}(\Omega) = -(1/2Bc)\{\int_{\Omega} dr_{\Omega}[r_{\Omega} \times J^{(1)}_{\beta}(r_{\Omega})]_{\alpha} + \sum_{\Omega''}[-R_{\Omega} \times J^{(1)}_{\beta}(\Omega,\Omega'')]\} \quad (33)$$

The origin dependence of this expression is completely removed by the substitution

$$-R_{\Omega} \rightarrow (R^{cp}_{\Omega,\Omega''} - R_{\Omega}) \quad (34)$$

for each term in the summation over Ω'', where $R^{cp}_{\Omega,\Omega''}$ is the position vector of the critical point linking group Ω'' to atom Ω. With this substitution, one obtains the following origin independent expression for the diamagnetic susceptibility tensor of atom Ω

$$\chi_{\alpha\beta}(\Omega) =$$

$$-(1/2Bc)\{\int_{\Omega} dr_{\Omega}[r_{\Omega} \times J^{(1)}_{\beta}(r_{\Omega})]_{\alpha} + \sum_{\Omega''}[(R^{cp}_{\Omega,\Omega''} - R_{\Omega}) \times J^{(1)}_{\beta}(\Omega,\Omega'')]\} \quad (35)$$

With a similar expression for each atom in the molecule, the physical requirement that the atomic contributions $\chi_{\alpha\beta}(\Omega)$ sum to the molecular value $\chi_{\alpha\beta}$ is preserved, as shown in eqn. (36)

$$\sum_{\Omega} \chi_{\alpha\beta}(\Omega) = (-1/2Bc) \sum_{\Omega} \{\int_{\Omega} dr_{\Omega}[r_{\Omega} \times J^{(1)}_{\beta}(r_{\Omega})]_{\alpha} + \sum_{\Omega''}[(R^{cp}_{\Omega,\Omega''} - R_{\Omega}) \times J^{(1)}_{\beta}(\Omega,\Omega'')]\}$$

$$= \sum_{\Omega} \chi'_{\alpha\beta}(\Omega) + \sum_{i=1} R^{cp}_{i} \times J^{(1)}_{\beta}(MOL)$$

$$= \sum_{\Omega} \chi'_{\alpha\beta}(\Omega) = \chi_{\alpha\beta} \tag{36}$$

In the second line of this equation, each term in the summation over the critical points i vanishes due to the conservation of current in the molecule, $J_{\beta}^{(1)}(MOL) = 0$.

The expression for $\chi_{\alpha\beta}(\Omega)$ in equation (36) can be recast in a more physically revealing form with the use of the following identity,

$$J_{\beta}^{(1)}(\mathbf{r}) = \nabla\cdot(J_{\beta}^{(1)}(\mathbf{r})\mathbf{r}) - \mathbf{r}\nabla\cdot J_{\beta}^{(1)}(\mathbf{r}) = \nabla\cdot(J_{\beta}^{(1)}(\mathbf{r})\mathbf{r}) \tag{37}$$

which is valid for the stationary states considered here since $\nabla\cdot J_{\beta}^{(1)}(\mathbf{r}) = 0$, ie. the first-order current density satisfies the continuity equation,[12] as was shown in chapter 1. Substituting eqn. (37) into eqn. (35) one obtains

$$\chi_{\alpha\beta}(\Omega) = -(1/2Bc)\{\int_{\Omega} d\mathbf{r}_{\Omega}[\mathbf{r}_{\Omega} \times J_{\beta}^{(1)}(\mathbf{r}_{\Omega})]_{\alpha} +$$

$$\sum_{\Omega''} [(\mathbf{R}^{cp}_{\Omega,\Omega''} - \mathbf{R}_{\Omega}) \times \int_{\Omega''} d\mathbf{r}\nabla\cdot(J_{\beta}^{(1)}(\mathbf{r})\mathbf{r})]\} \tag{38}$$

which, upon application of Gauss' theorem, becomes

$$\chi_{\alpha\beta}(\Omega) =$$

$$-(1/2Bc)\{\int_{\Omega} d\mathbf{r}_{\Omega}[\mathbf{r}_{\Omega} \times J_{\beta}^{(1)}(\mathbf{r}_{\Omega})]_{\alpha} + \sum_{\Omega''} [(\mathbf{R}^{cp}_{\Omega,\Omega''} - \mathbf{R}_{\Omega}) \times \int d\mathbf{s}(\Omega,\Omega')\cdot J_{\beta}^{(1)}(\mathbf{r})\mathbf{r}]\}$$

$$= \chi^{b}_{\alpha\beta}(\Omega) + \chi^{s}_{\alpha\beta}(\Omega) \tag{39}$$

Thus, the atomic magnetic susceptibility tensor, $\chi_{\alpha\beta}(\Omega)$, consists of two distinct contributions: a basin contribution $\chi^{b}_{\alpha\beta}(\Omega)$ which measures the magnetic moment, per unit applied field, of the induced current density distribution within the basin of atom Ω relative to its nucleus; and a surface contribution $\chi^{s}_{\alpha\beta}(\Omega)$ which measures the magnetic moment per unit

applied field arising from the position-weighted inward flux of current $J_\beta^{(1)}(\mathbf{r})$ through each of the interatomic surfaces $S(\Omega,\Omega'')$ bounding atom Ω. Eqn. (39) is the final expression for the contribution of atom Ω to the molecular magnetic susceptibility tensor χ.

3-6 Computational Methods and Units

The results reported in this work were obtained using coupled-perturbed Hartree-Fock theory (more precisely SCF perturbation theory)[15] together with the IGAIM[17] and continuous gauge transformation methods[18] described in chapter 1. None of the *relationships* between observable properties or *definitions* of atomic quantities given in the previous section are changed by using the perturbed SCF approximation, though the results for the individual properties certainly can be. The perturbed SCF first-order wavefunctions were obtained using a locally modified version of CADPAC.[21] All of the magnetic susceptibility results are reported in cgs units multiplied by 10^6, ie. cgs-ppm. Negative values are diamagnetic while positive values are paramagnetic.

3-7 Results for Magnetic Susceptibility Tensors

3-7-1 First-Row Hydrides

Shown in Table 3-1 are the calculated principal components, $\chi_\perp$ and $\chi_\parallel$, of the magnetic susceptibility tensors for a set of closed-shell first-row hydrides AH_n, where A is either H or one of the atoms of the first period, Li -> F. The parallel component $\chi_\parallel$ refers to a field applied parallel to the principal rotation axis of the molecule while the perpendicular component $\chi_\perp$ actually refers to the average of the susceptibilities for two mutually

orthogonal fields applied perpendicular to the principal axis. Table 3-1 also shows the average of the principal components, $\bar{\chi} = (1/3)[2\chi_{\perp} + \chi_{\parallel}]$, as well as the corresponding experimental gas phase values, when available. Finally, the total basin χ^{b} and surface χ^{s} contributions to $\chi_{\perp}$, $\chi_{\parallel}$ and $\bar{\chi}$ are shown in Table 3-1. The calculated values for $\bar{\chi}$ are in good agreement with experiment in those cases where comparison is possible.

Table 3-2 shows the contributions of the hydrogen atoms to the quantities given in Table 3-1, along with their net charges $q(\Omega)$. The corresponding results for the A atoms can be obtained by difference from these two tables. In Figs. 3-1 through 3-8 maps of the non-trivial current density distributions induced in this series of molecules are shown for at least one of the principal orientations while in Fig. 3-9 the sizes and shapes of the atoms, as determined by the charge density distribution, are shown.

The trends in the atomic contributions to $\bar{\chi}$ are as anticipated on the basis of the variations in the charge and current distributions. The magnitude of the basin contribution to $\chi(H)$ decreases through the series from its maximum value found in LiH, paralleling the decreases in its electron population and atomic volume. The value of $\bar{\chi}(H)$ for H_2 falls between CH_4 and NH_3, as does its net charge. The basin contributions to $\bar{\chi}(A)$ are positive for Be and B, their values being dominated by the paramagnetic currents induced in these atoms by the $\perp$ fields. The increasing extent of the paramagnetic current centered within the basin of the A atom, and its associated positive contribution to $\chi_{\perp}$, accounts for the decrease in the magnitude of $\bar{\chi}$ in the ionic systems LiH, BeH_2 and BH_3 despite a steady increase in the magnitude of the diamagnetic $\chi_{\parallel}$. These paramagentic currents for a perpendicular field are

so large in BH_3 that the molecular value $\chi_\perp$ is actually slightly positive due to a near cancellation of the much reduced diamagnetic basin contributions with the paramagnetic surface contributions. The molecules BeH_2 and BH_3 are therefore predicted to possess large negative anisotropies, $\chi_\parallel - \chi_\perp$, equal to -7.35 and -17.55, respectively. The anisotropies of the basin contributions to $\bar{\chi}(A)$ and in $\bar{\chi}$ itself become increasingly smaller for N, O and F reflecting the increasing dominance of the central nucleus in determining the form of the charge and current distributions. The contributions from the current fluxes through the interatomic surfaces are smallest for the ionic systems and for the most polar molecule, HF. They are largest for methane where the valence charge distribution is nearly equally shared between the C and H atoms. While the basin contribution to $\bar{\chi}$ in methane is somewhat less in magnitude than the maximum value for $\bar{\chi}^b$ attained in ammonia, the significantly larger surface contributions in the non-polar CH_4 give this hydride the largest magnetic susceptibility.

3-7-2 First-Row Methane Derivatives

Consideration of the magnetic susceptibilities of the compounds obtained by replacing one H in AH_n by a methyl group enables one to determine the extent of transferability of the contribution of the AH_{n-1} group between the two sets of compounds and determine as well the variation in the values of $\bar{\chi}(CH_3)$. Shown in Tables 3-3 and 3-4 for the first-row methane derivatives are the quantities analagous to those listed in Tables 3-1 and 3-2 for the hydride series. The experimental gas phase values for $\bar{\chi}$ are listed in Table 3-3 when available and are again in good agreement with the calculated results.

The net charge on the methyl group in CH_3AH_{n-1} is almost the same as the charge on H in HAH_{n-1} and thus the charge on the AH_{n-1} group is correspondingly similar for the two sets of compounds. Paralleling the net charges, the values of the basin and surface flux contributions to $\bar{\chi}(AH_{n-1})$ exhibit nearly identical variations throughout both series of molecules, as does, therefore, $\bar{\chi}(AH_{n-1})$ itself. They are remarkably similar for the ionic members in the two series, A = Li to B. This result is consistent with the localized nature of the electronic charge and current distributions with respect to the $H|AH_{n-1}$ and $CH_3|AH_{n-1}$ interactions for these ionic systems, as reflected in their small surface flux contributions, $\bar{\chi}^s(AH_{n-1})$. The largest changes in $\bar{\chi}(AH_{n-1})$, $\approx$ 9%, are found for the methyl and amino derivatives, those systems with a shared interaction across the interatomic surface with the A atom and for which the surface flux contributions are maximal. While the changes to the surface flux contributions themselves are relatively small, their large magnitude indicates a strong interaction between the two groups sharing the surface, and the basin contributions reflect the change in the interacting partner. The changes in $\bar{\chi}(AH_{n-1})$ and its basin and surface contributions are somewhat less for the most polar compounds, those containing O and F, but the charge and current distributions are not localized within the individual atomic basins here as they are for the ionic systems. The magnitude of $\bar{\chi}(CH_3)$ and its basin and surface contributions all decrease substantially through the series, paralleling the flow of electronic charge from methyl to its bonded partner, as is also observed for the H atom. The spread in the value of $q(CH_3)$ is indicative of the substantial changes that

occur within this group as its bonded neighbour changes from Li to F.

It is possible to observe an almost constant transferable contribution to $\bar{\chi}$ even from a very electronegative group such as |OH or |F if the group is buffered by one or more methylene groups. This is illustrated by the data in Table 3-5 which lists a number of properties of the OH and F groups in H|OH and H|F along with the values of ρ and $\nabla^2\rho$ at the bond critical point which generates the surface bounding the group. Succeeding entries in Table 3-5 give the changes in the values of the properties, relative to the values for the preceding compound, upon the addition of a CH_2 group. The values of all properties change considerably when a methylene group is interspaced between H and the electronegative group X to transform HX into the methyl derivative. The addition of a second methylene group causes only small changes, changes which become smaller still for the addition of the third methylene group to give the propyl derivative. Even with three methylene groups interspaced between the original point of substitution, however, there are small but significant perturbations transmitted to the surface and basin of the X group, perturbations which are responsible for the NMR chemical shifts. Experimentally, the X group would appear to contribute a fixed amount to the magnetic susceptibility of the normal alcohols following ethanol, with even the field-free total energy of the group changing by only 2 kcal/mol. Contributions from a given group to a molecular system's properties can assume constant values when the group is sufficiently isolated from the point of substitution.

3-7-3 Hydrocarbons

The first set of compounds for which measurements indicated an incremental behavior of the diamagnetic susceptibility were the normal hydrocarbons.[1] Initially Henrichson,[2,2] and later Pascal[3,4] and others,[5,6] observed that the isotropically averaged diamagnetic susceptibilities $\bar{\chi}$ of the normal hydrocarbon series obeyed the following additivity relationship to within experimental accuracy,

$$\bar{\chi}[CH_3(CH_2)_nCH_3] = 2\bar{\chi}(CH_3) + n\bar{\chi}(CH_2) \quad n=1, \ldots \tag{40}$$

a relationship which implies constant methyl and methylene group diamagnetic susceptibility contributions within a given molecule as well as their transferability between different molecules. While the many workers who have investigated the normal hydrocarbons disagree (primarily based on the experimental data) somewhat on the best values for $\bar{\chi}(CH_3)$ and $\bar{\chi}(CH_2)$, virtually all agree that the "best" value for $\bar{\chi}(CH_3)$ is about -14.2 ± 0.3 while that for $\bar{\chi}(CH_2)$ is -11.5 ± 0.3 In particular, Pascal's values are $\bar{\chi}(CH_3) = -14.3$ and $\bar{\chi}(CH_2) = -11.3$.[1-3] The normal hydrocarbons are unique in that they are probably as close as one can come to *experimentally* determining an atomic or group property within a molecule, without the use of symmetry. These molecules are therefore useful for theoretically investigating the additivity and transferability of atomic and group contributions to the diamagnetic susceptibility.

Table 3-6 shows the calculated principal values of the χ tensor for the molecules methane through pentane. The longitudinal component $\chi_{\parallel}$ refers to a field applied along the carbon chain while the components $\chi_{\perp 1}$ and $\chi_{\perp 2}$ refer to fields applied perpendicular to the carbon chain. The field for $\chi_{\perp 1}$ is parallel to the plane defined by the carbon nuclei, while the field for $\chi_{\perp 2}$ is

averages $\bar{\chi}$ are also given in Table 3-6 to indicate the accuracy of the results and the reliability of the interpretation given below.

None of the molecules in the series shows a large anisotropy in the magnetic susceptibility tensor but the longitudinal susceptibility $\chi_{\parallel}$ is slightly larger than the perpendicular susceptibilities $\chi_{\perp i}$ and $\chi_{\perp o}$ for all of the molecules (except methane). Unlike the electric polarizabilities[25] where the anisotropy $\alpha_{\parallel} - \alpha_{\perp}$ increases nearly five-fold from ethane to pentane due to a field-induced transfer of charge across the length of the carbon chain, the anisotropy of the χ tensor remains roughly constant through the series. Each entry in the column labeled $\delta\bar{\chi}$ in Table 3-6 is the difference between the isotropic susceptibility of the corresponding molecule in the table and that of the previous member of the series, ie. the change in $\bar{\chi}$ upon the addition of a CH_2 group to the previous member of the series. Based upon experimental results for the higher members of the series, the increment is expected to level off near the value in pentane.

Table 3-7 lists the contributions from the methyl and methylene groups to $\bar{\chi}$, together with the separate basin and surface contributions, $\bar{\chi}^b$ and $\bar{\chi}^s$. The group contributions to $\bar{\chi}$ exhibit the same pattern of transferability as do the corresponding group contributions to the volume, energy, first moments and mean polarizability.[20,25] Reference 25 provides a full discussion of this point. Briefly, a methyl group in molecules following ethane in the series is bonded to a methylene group from which it withdraws a small fixed amount of charge, -0.018e, an amount independent of chain length. The decrease in energy of the methyl group resulting from this charge transfer is equal to the increase in energy of the methylene group and consequently, energy as well as

increase in energy of the methylene group and consequently, energy as well as charge is conserved. The value of $\bar{\chi}(CH_3)$ in ethane is therefore somewhat less than its value for the methyl groups in the remaining molecules, for which it remains essentially constant. The value of $\bar{\chi}(CH_2)$ for the methylene group in propane, since it contributes charge and energy to two methyl groups, is slightly less than the value of $\bar{\chi}(CH_2)$ for the other molecules wherein two methylene groups are each bonded to but a single methyl and the middle methylene is pentane is bonded only to other methylenes.

The transfer of charge and energy from CH_2 to CH_3 is damped by a single intervening CH_2 group and thus the central methylene group in pentane should exhibit a zero net charge and possess the energy of the repeating transferable methylene group, labelled CH_2°. The difference in $\bar{\chi}(CH_2)$ for this methylene group and those bonded to a single methyl is so small for the magnetic susceptibility, that the value $\bar{\chi}(CH_2^\circ)$ for the central group in pentane falls within the average value of those obtained for the methylene groups bonded to a single methyl.

The value of $\bar{\chi}(CH_3)$ for the transferable methyl group is -14.50 with a mean deviation of $\pm$ 0.02. The same degree of transferability is found for the methylene groups, with $\bar{\chi}(CH_2)$ equal to -11.54. The value assigned to the central methylene group in pentane is equal to the incremental difference in the values of $\bar{\chi}$ for the butane and pentane molecules, to within 2%. Thus, theory defines the transferable methyl and methylene groups in this series of molecules.

The underlying basis for the transferable nature of the susceptibilities for these groups is illustrated by the displays of the magnitude and the curl

of J for the butane and pentane molecules shown in Fig. 3-10.

The central transferable methylene group can be represented symbolically by $|CH_2^c|$, with the vertical bars denoting the two interatomic surfaces linking the group to the remainder of the molecule, and graphically through a display of the two interatomic surfaces and their intersection with the 0.001 au isosurface of the electronic charge density, Fig. 3-11. This envelope determines the van der Waals shape of the group and replaces those portions of the atomic surfaces which occur infinitely far from the nuclei.[20] This distribution of charge in real space, up to and including the interatomic surfaces, is transferable without detectable change from pentane on, in the succeeding members of the homologous series. Thus, as demanded by the atomic force theorem,[20] the transferable group contributes a constant amount to the average value of each property in every molecule in which it occurs. As shown above, these properties include those induced by externally applied magnetic fields, and it is therefore an *observation* that *if the charge density distribution of an atom is transferable between systems, then so is the field induced current density distribution and its dependent properties*.

The theoretical CH_2 and CH_3 group values are close to the corresponding contributions quoted by Pascal and Pacault,[8,9,23] equal to -14.3 for methyl and -11.3 for methylene, values obtained by fitting experimental values of $\bar{\chi}$ for a wide range of homologous series. Taking into account the spread displayed by the experimentally determined group values which can be as large as 1, it is clear that the methyl and methylene groups of theory explain the experimentally observed additivity of the magnetic susceptibility for the normal hydrocarbon molecules.

The same pattern of transferability is exhibited by the separate basin and surface flux contributions to the group values. The surface flux contributions to $\bar{\chi}$ are comparable to those from the atomic basins, a reflection of the shared nature of the valence electron density and current in these molecules, as illustrated by the map of the current density shown for ethane in Fig. 3-12. There are internal flux contributions from each of the C-H surfaces of the group as well as a contribution from the external C-C surface which is -1.27 for a transferable methyl group. A methylene group has two external C|C interatomic surfaces, Fig. 3-11. The corresponding contribution to $\bar{\chi}^{s}(CH_2)$ for the flux through each C|C surface is -1.31, close to the corresponding value for the methyl group. The individual atomic contributions to the group values exhibit the same degree of constancy as found for the complete group, the value of $\bar{\chi}^{b}(H)$ for one of the two equivalent hydrogens of methyl, for example, exhibiting a variation of ±0.01 about a mean value of -1.47. Because of the constancy in the charge distributions of the methyl and methylene groups in this series, all properties are similarly transferable.

The group susceptibilities in isobutane and neopentane have also been calculated at the same level. These results, together with both the calculated and experimental values for $\bar{\chi}$ are summarized in Table 3-8. The value for $\bar{\chi}(CH_3)$ in both of these molecules differs by less than 0.2 from the transferable value defined by the normal hydrocarbons. In isobutane the surface contribution to the methine group susceptibility $\bar{\chi}(CH)$ is slightly larger than the basin contribution while in neopentane the surface contribution to the quaternary carbon susceptibility $\bar{\chi}(C)$ is twice as large as

the basin contribution due to the four C-C interatomic surfaces bounding the group, each of which contributes -1.42 to the total value of $\bar{\chi}^{s}(C)$. The closeness between the $\bar{\chi}(CH_3)$ values in neopentane and isobutane with that of the transferable value defined by the normal hydrocarbons suggests that a simple *theoretical* group increment scheme based on the values of $\bar{\chi}(CH_3)$ and $\bar{\chi}(CH_2)$ obtained from the hydrocarbons together with the $\bar{\chi}(CH)$ and $\bar{\chi}(C)$ values obtained from isobutane and neopentane should predict reasonable values of $\bar{\chi}$ for any saturated hydrocarbon, branched or unbranched. This is indeed the case as the data in Table 3-9 shows. The slight but consistent overestimates of the predicted susceptibility magnitudes are consistent with the slight overestimates calculated for the molecules from which the group values were derived.

It is not the purpose of Table 3-9 to suggest that a group increment scheme for hydrocarbons based on theoretical group susceptibilities could supplant the powerful empirical schemes, at least not yet. The purpose of Table 3-9 is to demonstrate that the empirical additivity relationships have a basis in physical theory. The theoretical group susceptibilities are defined and calculated, without adjustment, entirely in terms of quantum mechanical observables, the charge density and current density distributions, together with the quantum mechanical definition of a subsystem.[20]

3-7-4 Benzene

Benzene exhibits an unusual and historically significant magnetic susceptibility tensor in that it possesses an unusually large anisotropy for an organic molecule with a full valence shell.[1-4] The experimentally measured

susceptibility[6,7] for a field applied perpendicular to the plane of the ring, -94.5, is nearly three times that for a field applied in the plane of the ring, -34.5. This observation has prompted the development of various "ring-current" models to explain it,[1-4] models which are still being used for various purposes today. The physical basis for the ring current models has been addressed by many researchers,[1-4] but, in the opinion of the author, no satisfactory analysis of the situation yet exists. To investigate the physical basis for the ring-current model, or more importantly the observed anisotropy, one must first and foremost study the current distribution responsible for the magnetic susceptibility. Assuming a means for determining this distribution reasonably accurately is available,[17,18] one then requires a definition of an atom in a molecule,[20] for the ring-current models (as applied to benzene) are explicitly based on the *interatomic* flow of electronic current in the molecule. Finally, one needs a measure of the contribution of this interatomic current flow to the total magnetic susceptibility.

In Table 3-10 the calculated values of the principal magnetic susceptibilities of benzene are shown together with their atomic contributions. Both the parallel $\chi_{\parallel}$ and perpendicular $\chi_{\perp}$ components of χ are calculated to be about 10% larger than the experimentally measured components. The calculated anisotropy, $\Delta\chi$ = -67.7, is also about 10% larger than the experimental value. Lazzeretti et al[26,27] and Augspurger and Dykstra[28] have recently reported calculations of the magnetic properties of benzene using a single gauge origin at the charge centroid. Lazzeretti et al[27] use basis sets of increasing size, up to a very large one consisting of 474 primitives, contracted to 396 basis functions, the latter yielding values for $\bar{\chi}$ and its

anisotropy of -62.7 and -68.2, respectively. Augspurger and Dykstra use a basis set comparable to the one employed here and obtain values for $\bar{\chi}$ and $\Delta\chi$ of -89.62 and -48.59, respectively. Both sets of results are in poorer agreement with the experimental values[6,7] of -54.8 for $\bar{\chi}$ and -59.7 for $\Delta\chi$ than are the results given in Table 3-10, which were calculated using the IGAIM method.[17] In any case, the molecular values reported in Table 3-10 are certainly sufficiently close to experiment to allow a more detailed analysis, one whose results will be at least qualitatively accurate.

Shown in Fig. 3-13a is the current induced in the nuclear plane of the benzene molecule for a field applied parallel to the principal axis. A set of diamagnetic current loops is found in each of the C-C and C-H bonded regions, with the center points for the former lying in the C-C interatomic surface. Bonded sets of current loops are characteristic of a *shared* atomic interaction, one for which the Laplacian of electron density, $\nabla^2\rho$, exhibits a corresponding shared charge concentration in the bonded region.[20] A map of the laplacian of the charge density is shown in Fig. 3-13d to illustrate this point. Shown in Fig. 3-13c is the $\nabla x\mathbf{J}$ map in the same plane. This map mimics not only the shell structure of $\nabla^2\rho$, but also its bonded features, the flux antiparallel to **B** in the valence shell of $\nabla x\mathbf{J}^{(1)}$ for a carbon atom forming three shared regions with its bonded neighbours. There are two more center points in the basin of each carbon atom, Fig. 3-13a. One is slightly displaced off the nucleus toward the ring side and serves as a centre for a diamagnetic flow. The other is found in the core shell where the flux in the curl of **J** is parallel to **B** and thus serves as the center for a paramagnetic flow. Both regions are relatively small and contribute little to the magnetic

susceptibility.

The outermost valence shell in the $\nabla \times \mathbf{J}$ field for the carbon atoms overlap one another in the ring's interior, Fig. 3-13c. Since the flux in this shell is parallel to **B**, the (2,0) center point at the ring center and its associated stagnation path serve as the axis for a set of paramagnetic current loops. Thus the shell structure of the curl of **J** provides a simple explanation of the origin of the central paramagentic current in benzene. This behaviour is also to be predicted on the basis of the analogous shell structure exhibited by $\nabla^2\rho$, which is positive in the ring interior, as a result of the overlap of the corresponding valence shells of charge depletion of the atoms forming the ring.

Outer diamagnetic current loops encompass the entire molecule in the plane of the nuclei. For planes sufficiently displaced from the symmetry plane along the parallel field axis only the central stagnation line remains for a diamagnetic current flow encompassing the entire molecule. For a plane displaced by 0.8 au, Fig. 3-13b, the current map exhibits an outer diamagnetic flow bounding an inner paramagnetic flow. The diamagnetic current flow about the ring contributes substantially to the position weighted flux of $\mathbf{J}^{(1)}$ through the interatomic surfaces of the atoms forming the ring.

The carbon basin contributions to χ exhibit a relatively small anisotropy but the surface terms are three times the magnitude of the basin term for a parallel field. The largest of the surface terms arise from the flux in the current induced by a parallel field through the interatomic surfaces separating the atomic basins in the ring of bonded carbon atoms. These C|C surface terms exhibit a large anisotropy, equal to -8.7 for a single carbon

atom. This is the origin of the large anisotropy in χ observed for benzene and it is a direct result of the delocalized nature of the current induced by a parallel field shown in Fig. 3-13a,b. The contributions to $\bar{\chi}$ from current fluxes through the C-H interatomic surface are relatively small for both C and H and the basin contributions to χ(H) exhibit no anisotropy. Ninety-six percent of the value of $\Delta\chi$ comes from the carbon atom contributions, 77% having its origin in a current flowing from the basin of one carbon atom into that of its neighbour. The current plot in Fig. 3-13a,b and the relative values of the basin to surface contributions to $\bar{\chi}$ (C) confirm the existence of a significant diamagnetic current encompassing the ring of the benzene molecule.

3-8 Nuclear Magnetic Shielding

The first-order induced current density distributions $\mathbf{J}^{(1)}(\mathbf{r})$ in a molecule also determine the nuclear magnetic shielding tensors σ^N. Using an approach similar to that for the magnetic susceptibility tensor, it can be shown that the shielding tensor of a nucleus N with a magnetic dipole moment μ^N is expressed in terms of $\mathbf{J}^{(1)}(\mathbf{r})$ according to the following expression[16,19]

$$\mu^N \cdot \sigma^N \cdot \mathbf{B} = (-\mu^N/c) \cdot \int d\mathbf{r}(1/r_N^3)[\mathbf{r}_N \times \mathbf{J}^{(1)}(\mathbf{r})] \qquad (41)$$

where $\mathbf{r}_N$ is the real space position vector relative to the nucleus N. A similar expression applies to all nuclei in a molecule with the result that in order to calculate a complete nuclear magnetic shielding tensor for any nucleus in a given molecule, it is sufficient to know the first-order current density distributions induced by an external magnetic field **B** for three

perpendicular field directions. Eqn. (41) is essentially a statement of the classical Biot-Savart law for current distributions in terms of a current distribution for a quantum system.

Eqn. (41) can be used to advantage in understanding shielding tensors in terms of local or regional contributions in a molecule. One can unambiguously define a shielding tensor **density** $\sigma^N(\mathbf{r})$ in real space as the integrand of eqn. (41)[19]

$$\mu^N \cdot \sigma^N(\mathbf{r}) \cdot \mathbf{B} = (-\mu^N/c) \cdot (1/r_N^3)[\mathbf{r}_N \times \mathbf{J}^{(1)}(\mathbf{r})] \tag{42}$$

where the α,β component of $\sigma^N(\mathbf{r})$ is

$$\sigma^N_{\alpha\beta}(\mathbf{r}) = (-1/Bcr_N^3)[\mathbf{r}_N \times \mathbf{J}^{(1)}_\beta(\mathbf{r})]_\alpha \tag{43}$$

with $\mathbf{J}^{(1)}_\beta(\mathbf{r})$ again being the first-order current density induced by an external magnetic field in the β direction and where α refers to the corresponding component of μ^N. Using the density $\sigma^N_{\alpha\beta}(\mathbf{r})$ one can interpret $\sigma^N_{\alpha\beta}$ in terms of contributions from each point in the real space of the molecule.[19] Similarly, the average contribution to $\sigma^N_{\alpha\beta}$ from an atom Ω in a molecule $\sigma^N_{\alpha\beta}(\Omega)$ can be determined by integrating $\sigma^N_{\alpha\beta}(\mathbf{r})$ over the basin of the atom[17,20]

$$\sigma^N_{\alpha\beta}(\Omega) = (-1/cB)\int_\Omega d\mathbf{r}_N (1/r_N^3)[\mathbf{r}_N \times \mathbf{J}^{(1)}_\beta(\mathbf{r})]_\alpha \tag{44}$$

Since atoms in molecules are non-overlapping and exhaust all of molecular space,[20] the contributions $\sigma^N_{\alpha\beta}(\Omega)$ sum to yield the total shielding $\sigma^N_{\alpha\beta}$

$$\sigma^N_{\alpha\beta} = \sum_\Omega \sigma^N_{\alpha\beta}(\Omega) \tag{45}$$

Given the form of the shielding density ($\sigma^N_{\alpha\beta} \sim r_N^{-3}$) one expects that the dominant contribution to the shielding tensor of a particular nucleus will come from the atom containing the nucleus. With the exception of protons this

molecule shows. All three principal components of the carbon shielding tensor in ethylene are quite different, with the largest anisotropy ($\sigma^C_{xx} - \sigma^C_{yy}$) equalling 253.1 ppm. The corresponding anisotropy of the exterior contribution to σ^C (the contribution from all atoms except the carbon containing the shielded nucleus) is only 3.9 ppm, however. For the proton shielding tensor the largest anisotropy is $\sigma_{zz} - \sigma_{yy}$ = 6.4 ppm with the corresponding anisotropy of the exterior contribution equal to 5.9 ppm. These are typical results. For atoms with core electrons the shielding tensor of the atom's nucleus is determined almost entirely by the current distributions within the atom, with the relative contibution of the other atoms decreasing with increasing atomic number of the shielded nucleus. For protons, which possess no core electrons, the shielding range is very small and thus the exterior contributions are more significant.

The shielding tensor is thus largely an atomic property for nuclei other than protons, reflecting the current distributions within the atom containing the shielded nucleus. This is illustrated in Fig. 2-2 for the carbon dioxide molecule where the current induced in a plane containing the internuclear axis by a perpendicular field is shown. The current in the carbon basin is mostly paramagnetic while that in the oxygen basins is mostly diamagnetic. The corresponding carbon shielding component $\sigma^C_\perp$ is -55.6 with the contribution from the carbon atom being -50.8 ppm. Since the carbon nucleus is significantly off-center with respect to the diamagnetic current in the oxygen atoms, the oxygen atoms further deshield the carbon nucleus slightly.

The isotropic carbon shieldings $\bar{\sigma}^C$ in the normal hydrocarbons are shown in Table 3-11 for the molecules methane through pentane. Also shown in each

in Table 3-11 for the molecules methane through pentane. Also shown in each case is the contribution to $\bar{\sigma}^C$ from the carbon atom containing the shielded nucleus, $\bar{\sigma}^C_{int}$, the contribution from each of the hydrogen atoms directly bonded to the shielded carbon atom, $\bar{\sigma}^C(H_\alpha)$, as well as the contributions from the other groups, $\bar{\sigma}^C(G)$, in the molecule. The relative shieldings are in good agreement with experiment.[13] The essential feature of these results is that the total exterior contribution $\bar{\sigma}^C_{ext}$ to the isotropic carbon shielding is essentially constant at about 17.5 ppm with the relative shifts in $\bar{\sigma}^C$ being determined entirely by the interior contributions $\bar{\sigma}^C_{int}$. The results in Table 3-11 also show that the individual, exterior atomic and group contributions are essentially constant. Thus, in the molecules ethane through pentane, the bonded hydrogens contribute an almost constant amount of 4.1 $\pm$ 0.1 ppm, while the bonded methyl groups contribute the constant amount of 4.9 $\pm$ 0.0 ppm and the bonded methylenes an amount 3.7 $\pm$ 0.1 ppm, etc. Substitution of a methyl group for a proton in ethane to yield propane, for example, results in a deshielding of the methyl carbons and this deshielding is entirely a result of the perturbation of the induced current distributions within the methyl carbon atom rather than the altered current distributions of its environment. This basic result is certainly not restricted to hydrocarbons, as the isotropic carbon shielding data in Table 3-12 for the normal alcohols makes clear.

The differing proton shielding in the series of molecules C_2H_2, C_2H_4, C_2H_6 and benzene has been the subject of much discussion.[6,7,13] In Tables 3-13, 3-14 and 3-15 the atomic contributions to the proton shielding tensors in this series of molecules are given for the orientations defined by the corresponding principal magnetic susceptibility tensors. The calculated,

experimental gas phase results.[13] From Table 3-13 one sees that the interior contribution $\bar{\sigma}^{H}_{int}$ to the total isotropic proton shielding $\bar{\sigma}^{H}$ exhibits a much smaller variation than does the exterior contribution $\bar{\sigma}^{H}_{ext}$. Thus, the isotropic shielding of the acetylene proton is 4 ppm larger than the ethylene proton due primarily to the differing shielding contributions from the atoms in the two molecules other the hydrogen atom containing the shielded proton. Similarly, the 2 ppm downfield shift of the benzene proton resonance relative to the ethylene proton is due entirely to the differing exterior contributions. From Tables 3-14 and 3-15 one sees that the largest anisotropy, $^{\parallel}\sigma^{H} - {}^{\perp}\sigma^{H}$, is exhibited by the acetylene proton, equal to 16.5 ppm. This large anisotropy is primarily due to the large diamagnetic shielding from the current induced within the bonded carbon atom for a parallel field. The benzene proton exhibits an appreciable negative anisotropy, equal to about -5 ppm. The negative anisotropy arises primarily from the deshielding of the proton by the ipso carbon of the benzene ring for a parallel field, with the the interior contribution to σ^{H} being nearly isotropic. The deshielding of the benzene proton by the ipso carbon for a parallel field is also the basis for the 2 ppm downfield isotropic shift relative to ethylene.

3-9 Comments

This work has demonstrated that the understanding of the observed magnetic properties of molecules is to be found in the magnetically induced molecular current density distributions together with atoms in molecules whose surfaces are defined by the molecular electron density distribution. Every atom in a molecule makes an additive contribution to the magnetic properties of the molecule of which it is a part. Like atomic contributions to other properties, the extent to which the atomic magnetization is transferable from one molecule to another parallels

the corresponding transferability of the atom's electron density distribution. Examples have been given of group mean magnetic susceptibilities that are predicted to be transferable without change within experimental error. The physical significance of the atoms of theory is reiterated through the recovery of Pascal's group mean magnetic susceptibility increments for the normal hydrocarbons. The importance of the magnetization within an atomic basin relative to the fluxes of induced current through the interatomic surfaces parallels the extent to which the electron density is localized within the individual atomic basins. In the case of benzene, the large position-weighted flux of induced current through the carbon-carbon interatomic surfaces for a magnetic field perpendicular to the ring is found to be responsible for the large anisotropy of the magnetic susceptibility, a result which is consistent with the ring-current model. Future work should focus on more detailed correlations of the atomic magnetic susceptibility and nuclear magnetic shielding tensors with other atomic properties, as well as the topological properties of the induced current distributions described in Chapter 2.

3-10 References

1. L.N. Mulay and E.A. Bordeaux, *Theory and Applications of Molecular Diamagnetism*, (John Wiley and Sons, Inc., 1976)

2. L.F. Bates, *Modern Magnetism*, 4th Edition, (Cambridge University Press,, Cambridge, 1961)

3. P.W. Selwood, *Magnetochemistry*, 2nd Edition, (Interscience Publishers, Inc., 1956)

4. E.G. Stoner, *Magnetism and Matter*, (Methuen and Co. Ltd., London, 1934)

5. R.P. Feynman, R.B. Leighton and M. Sands, *The Feynman Lectures on Physics*,

(Addison-Wesley Publishing Co., Reading, Mass., 1965)

6. R. Ditchfield, *Mol. Phys.*, **27**, 789 (1974)

7. B.R. Appleman and B.P. Dailey, *Adv. Mag. Res.*, **7**, 231 (1974).

8. P. Pascal, *Ann. Chim. Phys.* **19**, 5 (1910).

9. P. Pascal, F. Gallais, and S. F. Labarre, *C. R. hebd. Seances Acad. Sci.* **252**, 2644 (1961).

10. J.H. Van Vleck, *The Theory of Electric and Magnetic Susceptibilities*, (Oxford University Press, Oxford 1932)

11. P.W. Atkins, *Molecular Quantum Mechanics*, 2nd Edition, (Oxford Univerisity Press, Oxford) 1987.

12. S.T. Epstein, *The Variation Method in Quantum Chemistry*, (Academic Press, New York 1974).

13. W. Kutzelnigg, U. Fleischer, M. Schindler, *NMR Basic Principles and Progress*, **23**, 165 (1990).

14. D.W. Davies, *The Theory of the Electric and Magnetic Properties of Molecules*, (Wiley and Sons, Inc. 1990).

15. W.N. Lipscomb, *Adv. Mag. Res.*, **2**, 137 (1966).

16. W.N. Lipscomb, *MTP Int. Rev. Sci.*, **1**, 167 (1972).

17. T. A. Keith and R. F. W. Bader, *Chem. Phys. Letters*, **194**, 1 (1992).

18. T. A. Keith and R. F. W. Bader, *Chem. Phys. Letters*, submitted (1993).

19. C. J. Jameson, and A. D. Buckingham, *J. Chem. Phys.*, **73**, 5684 (1980).

20. R. F. W. Bader, *Atoms in Molecules - A Quantum Theory* (Oxford University Press, Oxford, 1990).

21. R.D. Amos and J.E. Rice, CADPAC - *The Cambridge Analytic Derivatives Package*, Version 4.0 (1987).

22. G. Henrichsen, *Wied. Ann.* **34**, 186 (1888).

23. A. Pacault, *Rev. Sci.* **86**, 38 (1948);

24. *Handbook of Chemistry and Physics*, Ed. D.R. Lide, (CRC Press, Cleveland) 72nd edition, 1991-92, 938.

25. R. F. W. Bader, T. A. Keith, K. M. Gough and K. E. Laidig, *Mol. Phys.*, **75**, 1167 (1992).

26. P. Lazzeretti, E. Rossi and R. Zanasi, *J. Chem. Phys.* **77**, 3129 (1982).

27. P. Lazzeretti, M. Malagoli and R. Zanasi, *J. Mol. Struct. (Theocham)* **234**, 127 (1991).

28. J. D. Augspurger and C. E. Dykstra, *Mol. Phys.*, **76**, 229 (1992).

PAGINATION ERROR.

TEXT COMPLETE.

ERREUR DE PAGINATION.

LE TEXTE EST COMPLET.

NATIONAL LIBRARY OF CANADA.

CANADIAN THESES SERVICE.

BIBLIOTHEQUE NATIONALE DU CANADA.

SERVICE DES THESES CANADIENNES.

Figures 3-1 through 3-8

Trajectories of the first-order current density induced in the first row hydrides. Clockwise flow is diamagnetic. Intersections of the interatomic surfaces with the plane are shown when present. The applied field is directed out of the plane of the paper.

3-1) The H_2 molecule in a plane containing the nuclei.

3-2) The LiH molecule in a plane containing the nuclei.

3-3) The BeH_2 molecule in a plane containing the nuclei.

3-4a) The BH_3 molecule in the plane containing all four nuclei.

3-4b) The BH_3 molecule in a σ_v symmetry plane.

3-5) The CH_4 molecule in a plane containing the carbon nucleus and two protons.

3-6a) and b) A comparison of the localized current flow in LiH with the delocalized flow in CH_4 in an alternating plane of symmetry.

3-7a) The H_2O molecule in a plane containing all three nuclei.

3-7b) The H_2O molecule in the σ_v symmetry plane.

3-8) The HF molecule in a plane containing the two nuclei.

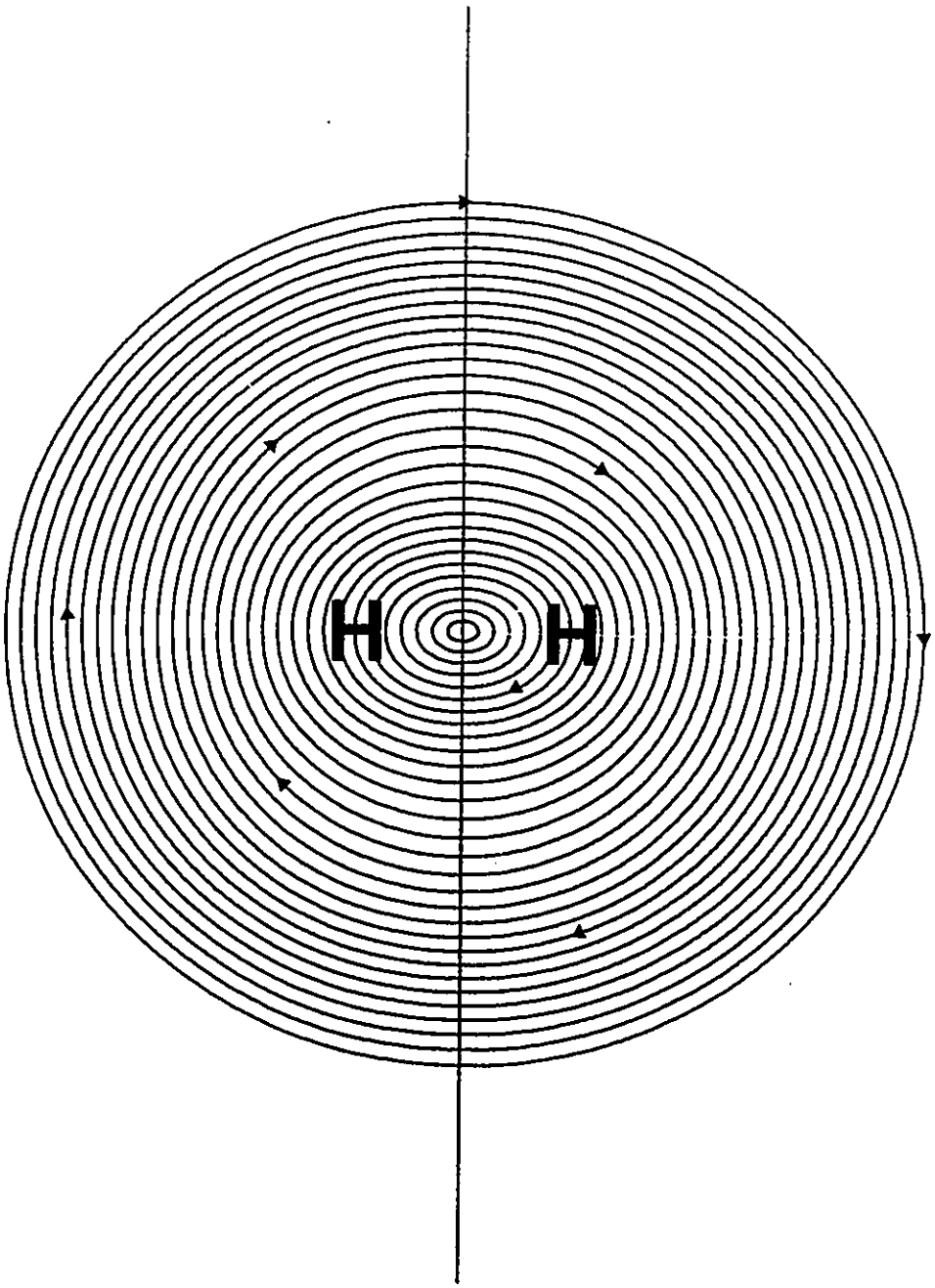
H
H

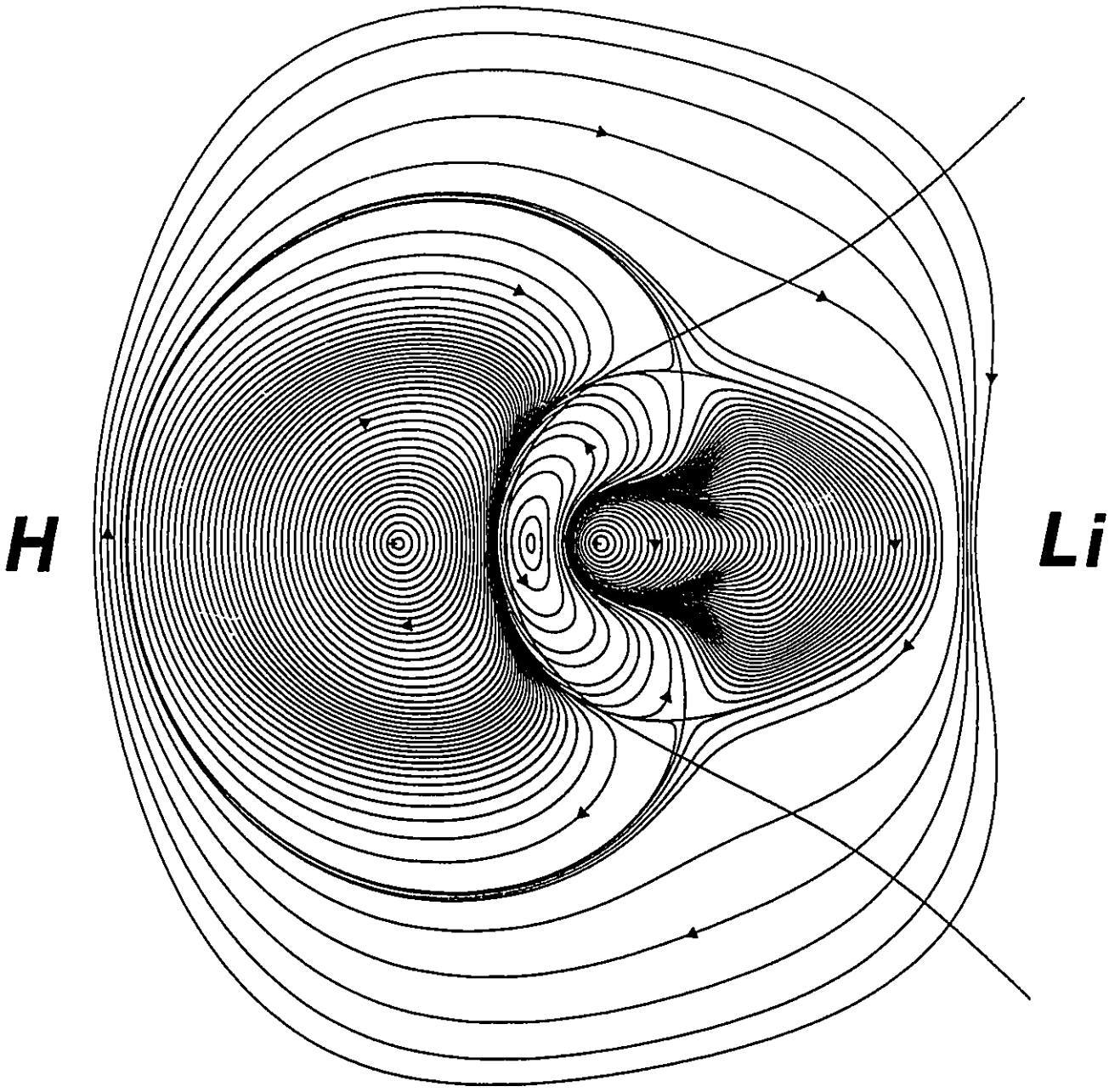
H
Li

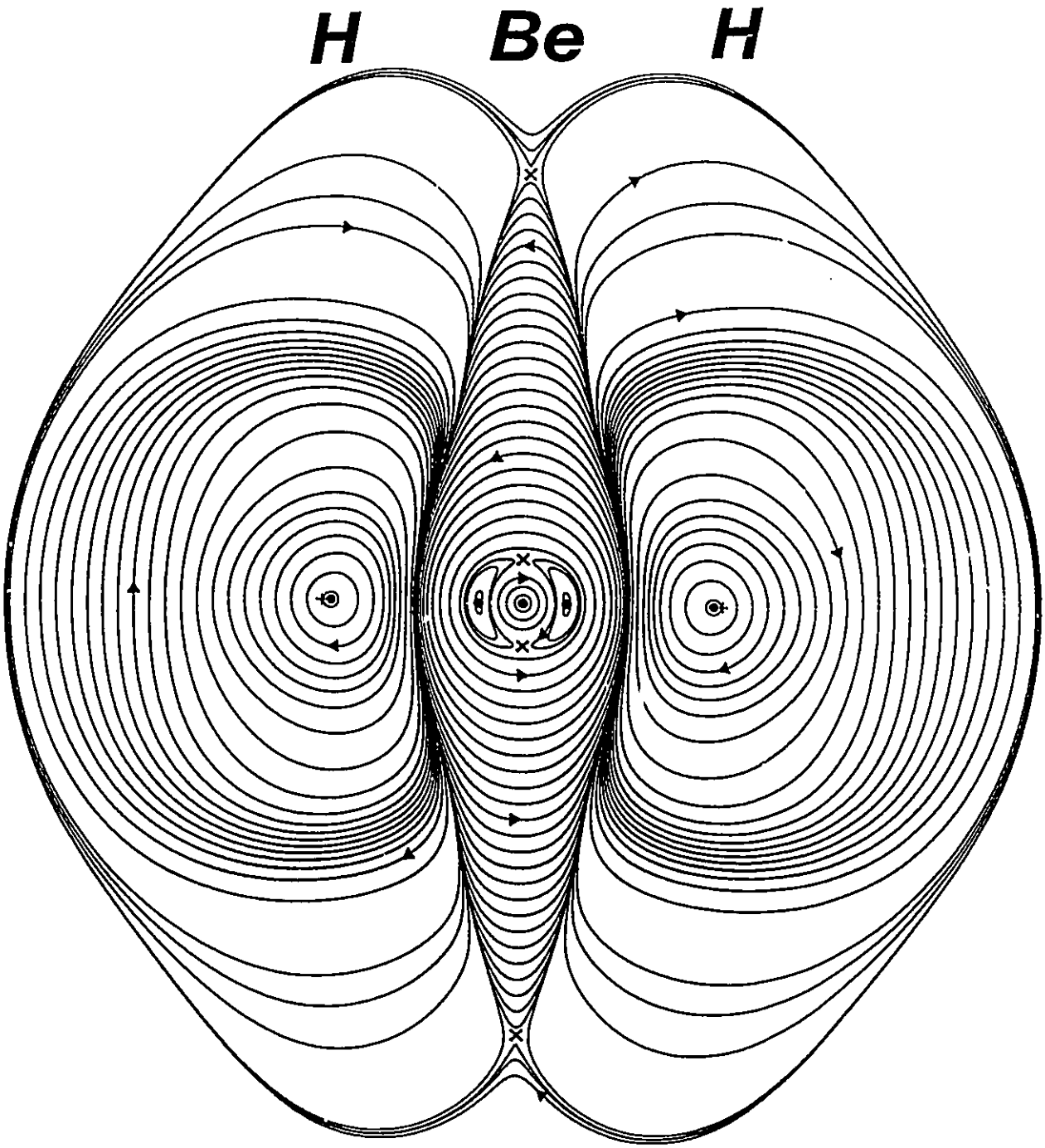
H
Be
H

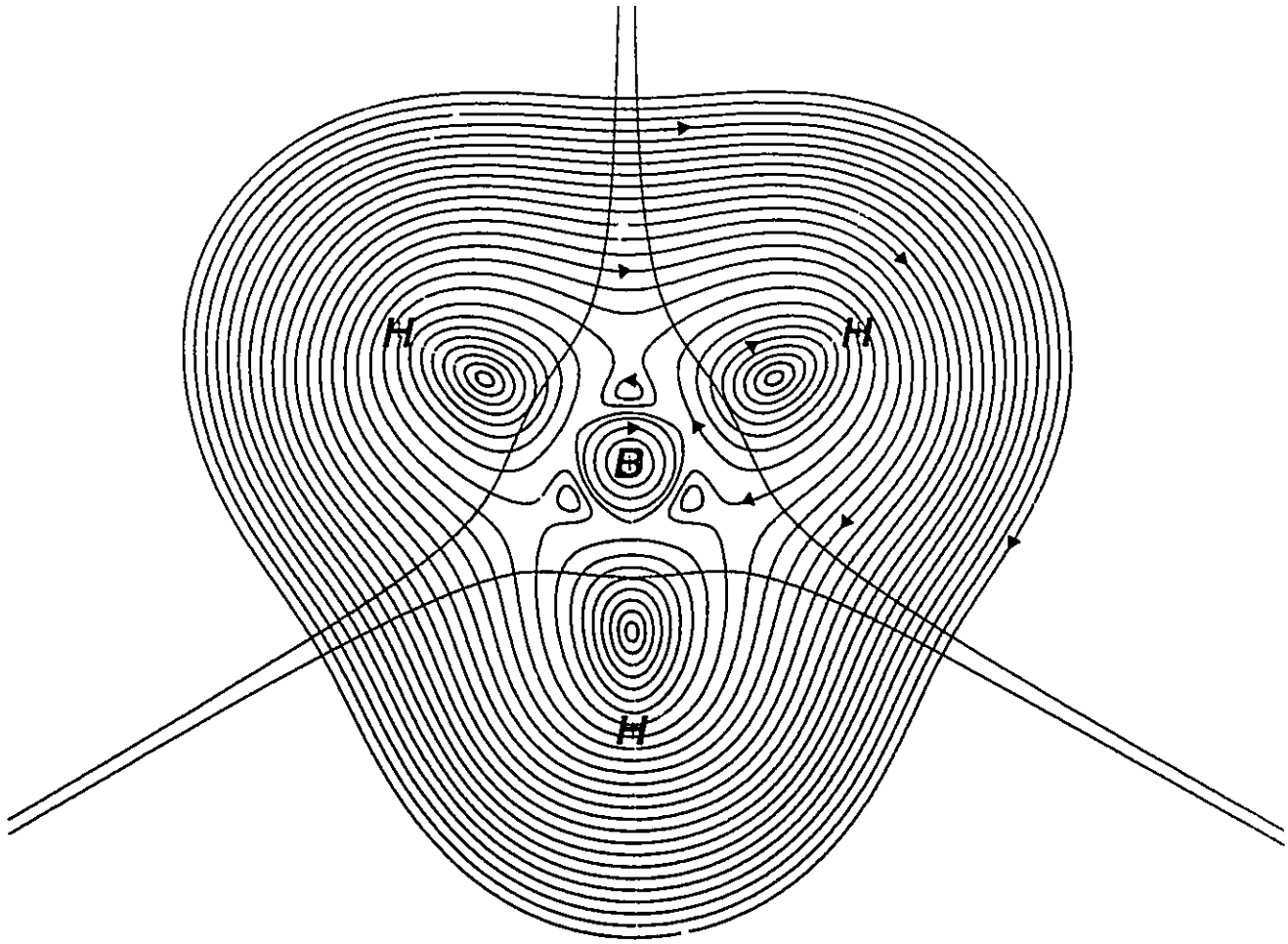
H
H
B
H

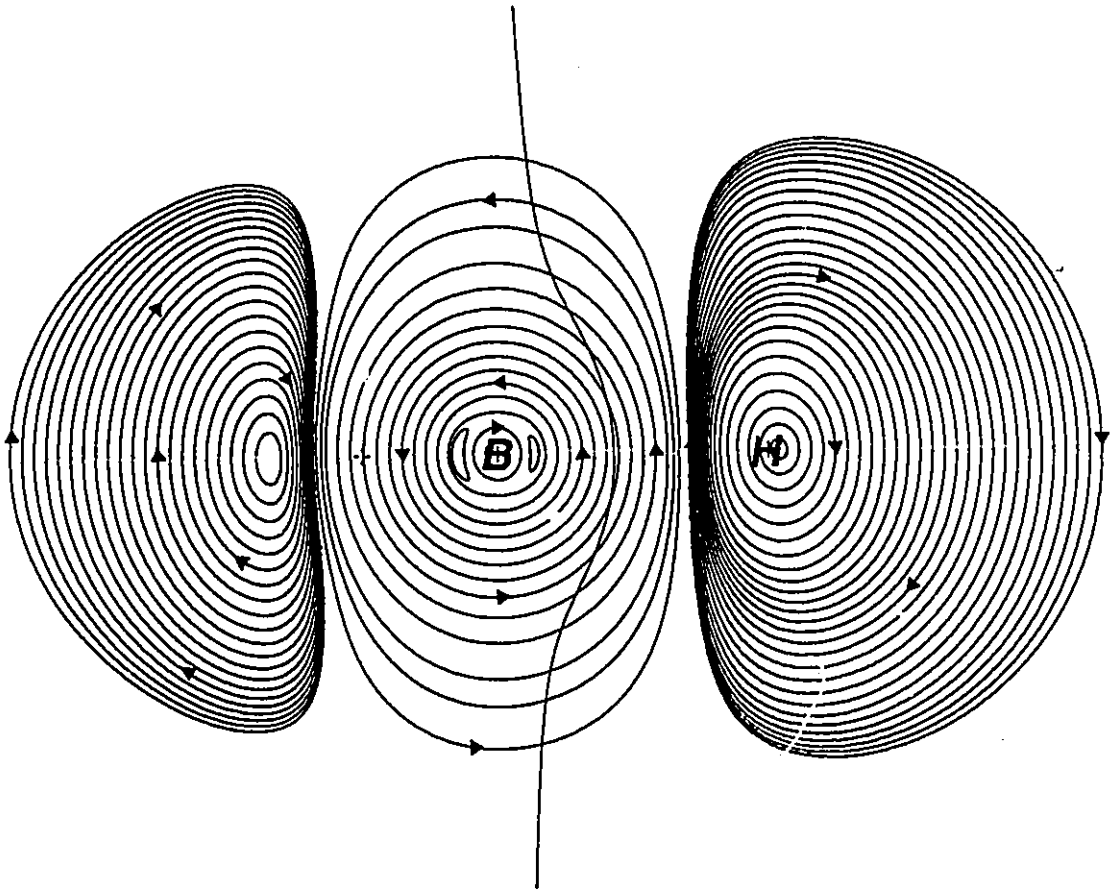
B
H

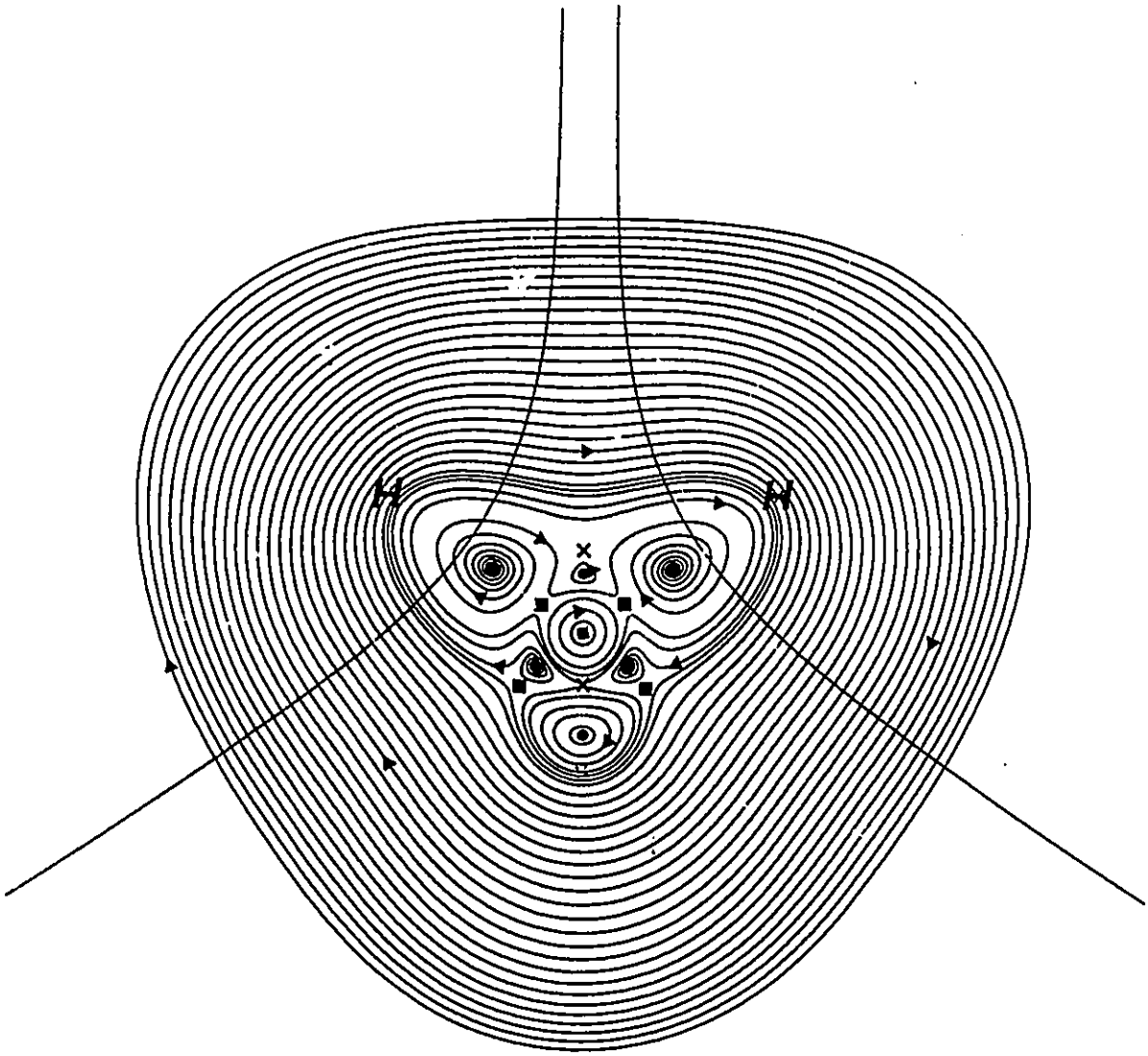
H
H

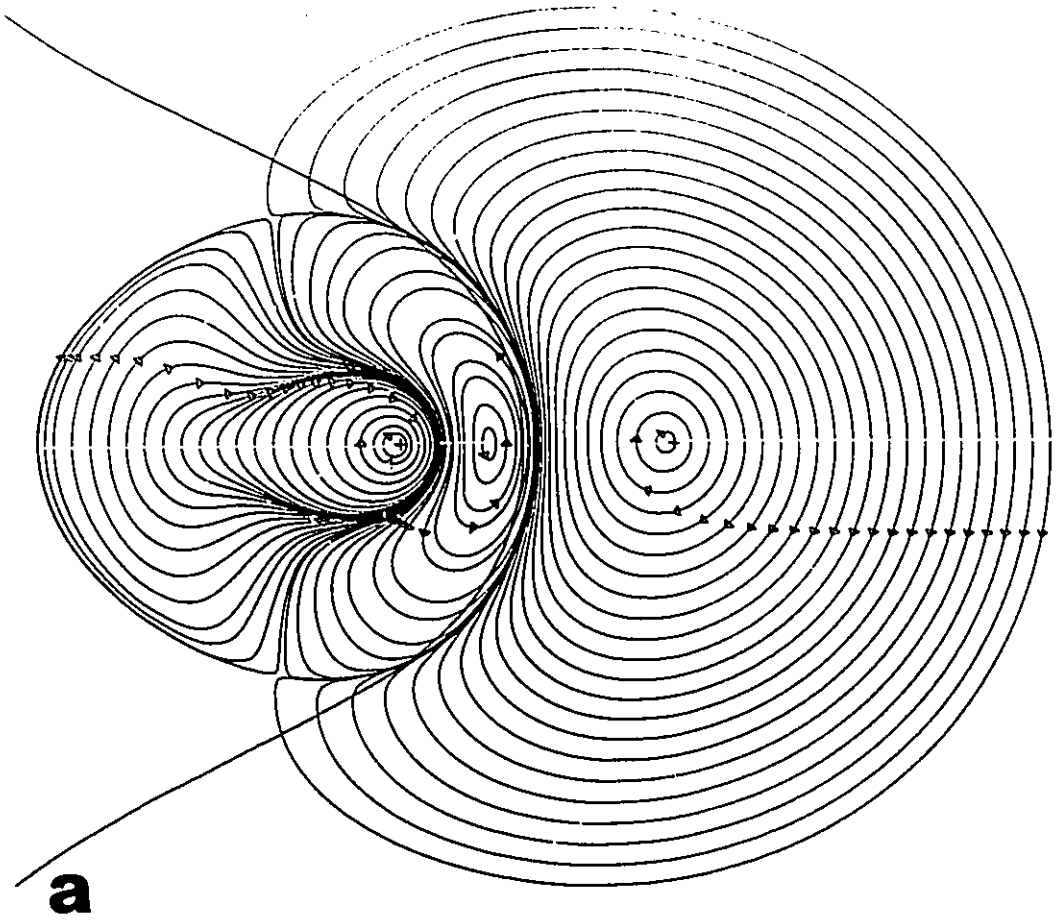

a

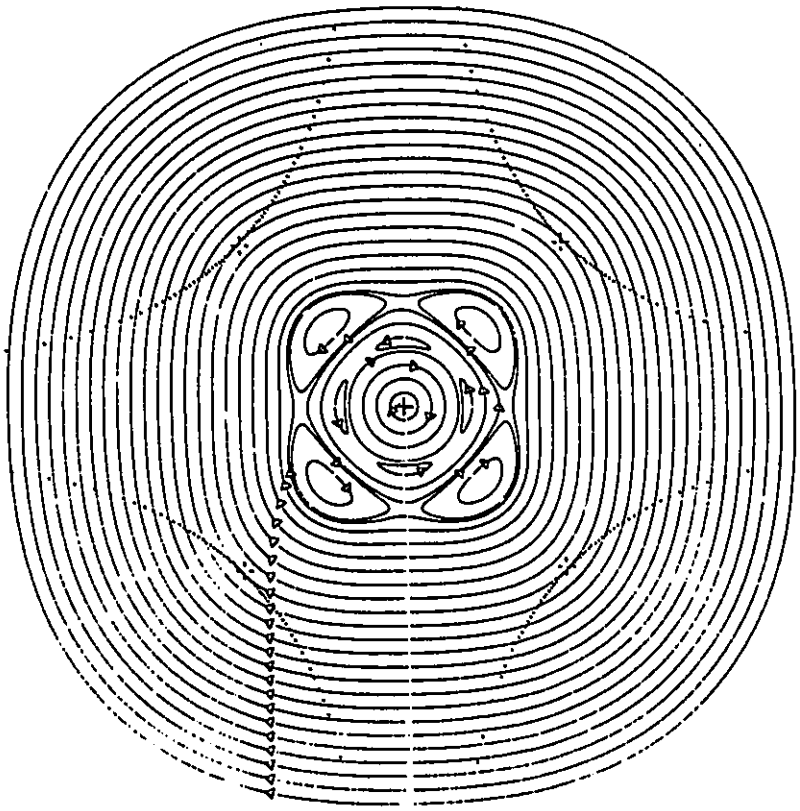

b

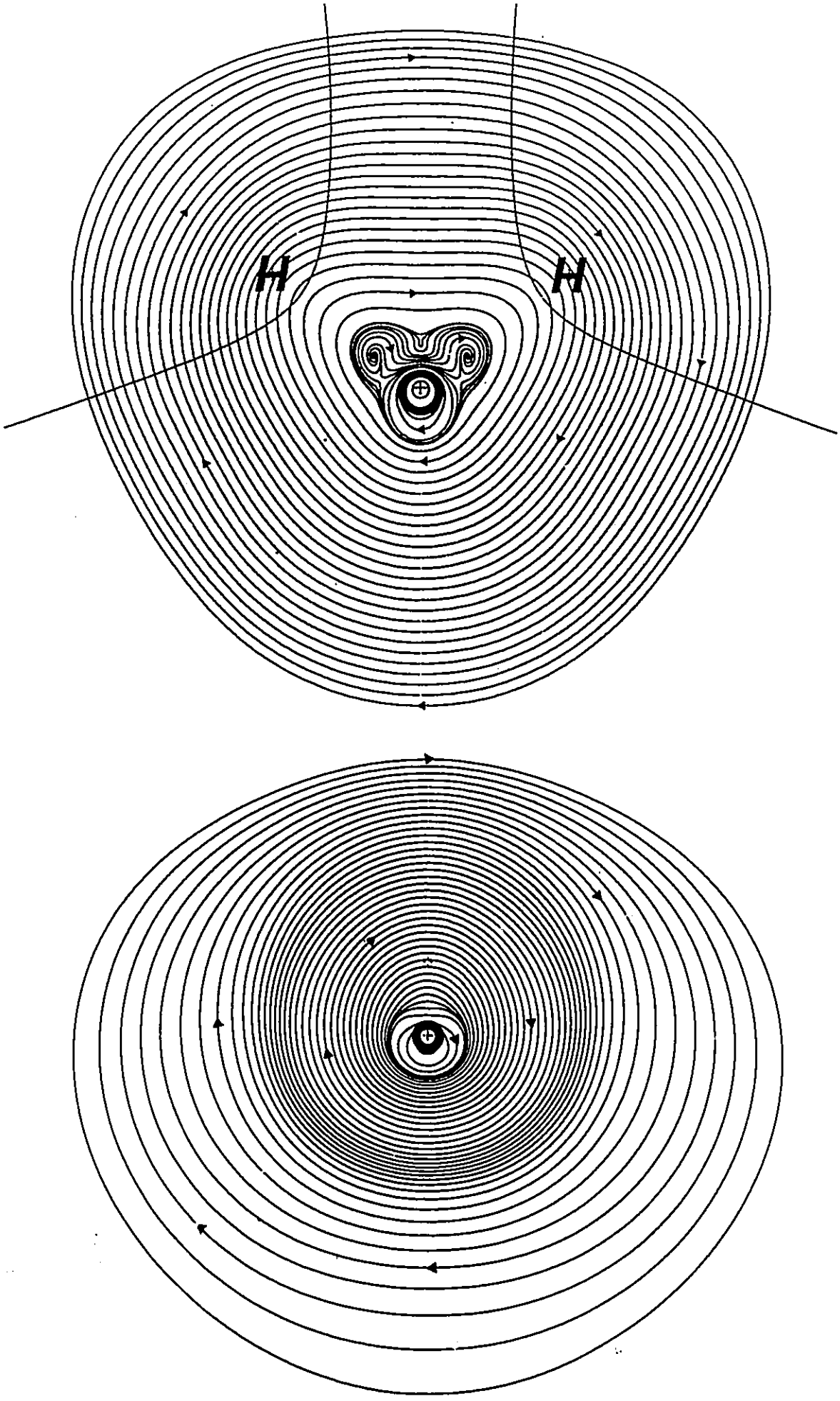
H
H

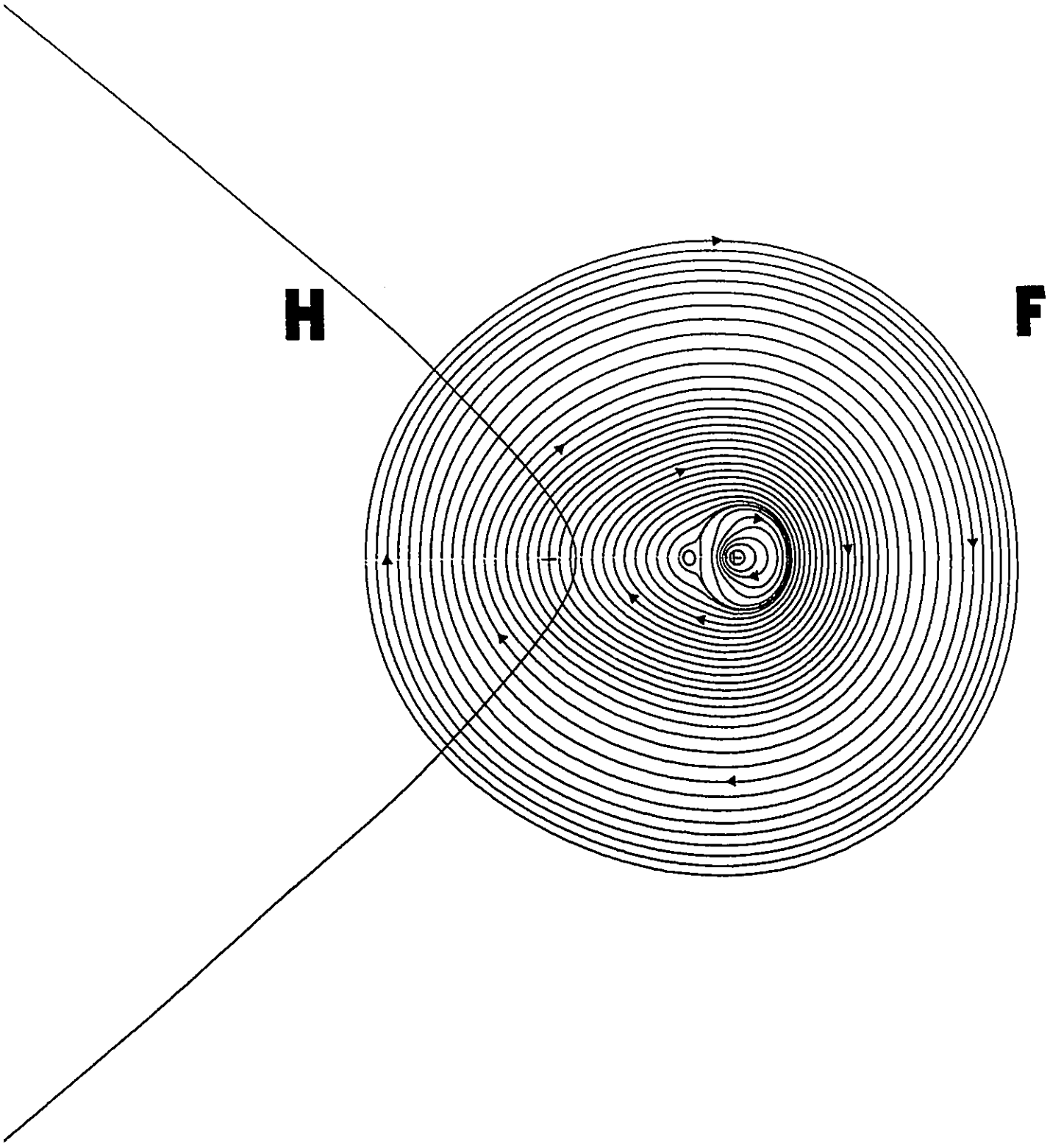
H
F

Figure 3-9

Representations of the atoms in the first row hydrides AH_n. In the hydridic members, LiH, BeH_2 and BH_3, the A atom consists primarily of a core of decreasing radius, dressed with some residual valence density. The form and properties of the atoms undergo a marked change at methane, a nonpolar molecule. No core is visible on the C atom and the H atoms, considerably reduced in size and population, now possess the convex side of the interatomic surface. The increasing polarity of the remaining members is reflected in the decreasing size of the H atom and the increasing convexity of its interatomic surface.

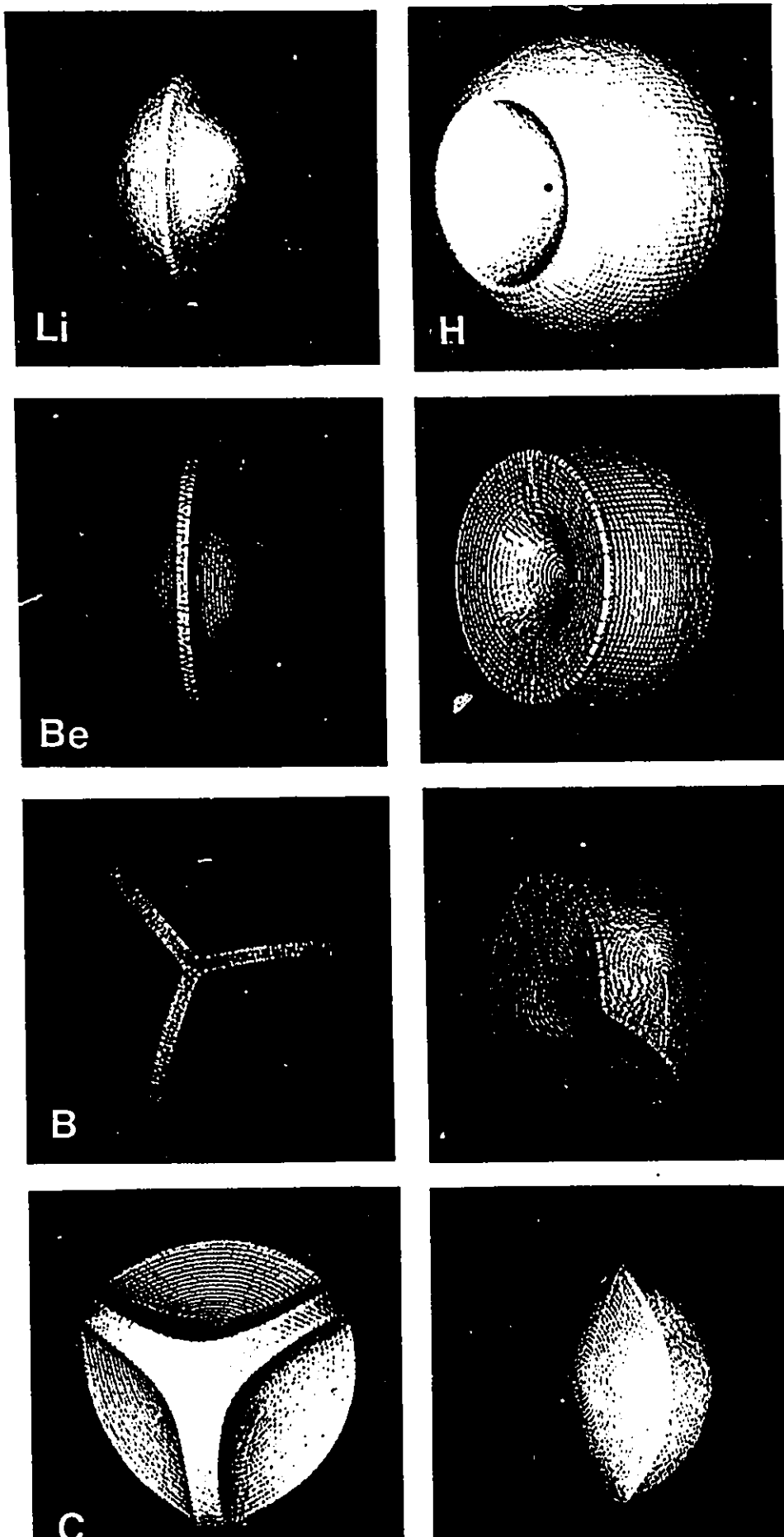
Li
H
Be
B
C

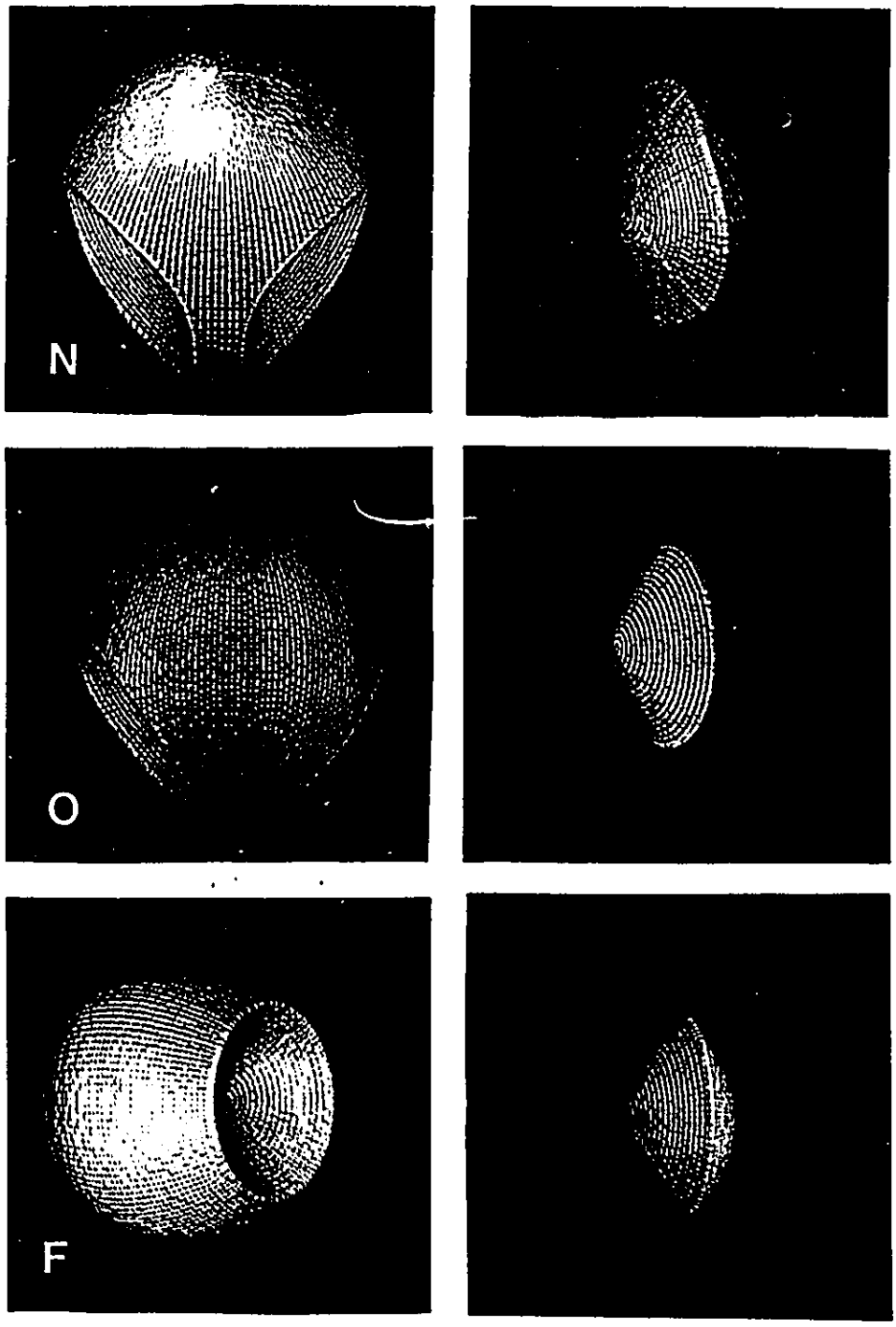
N
O
F

Figure 3-10

Contour maps of the magnitude (a and b) and curl (c and d) of the current density for butane (a and c) and pentane (b and d) in a plane containing the carbon nuclei. The intersections of the interatomic surfaces with the plane are also shown.

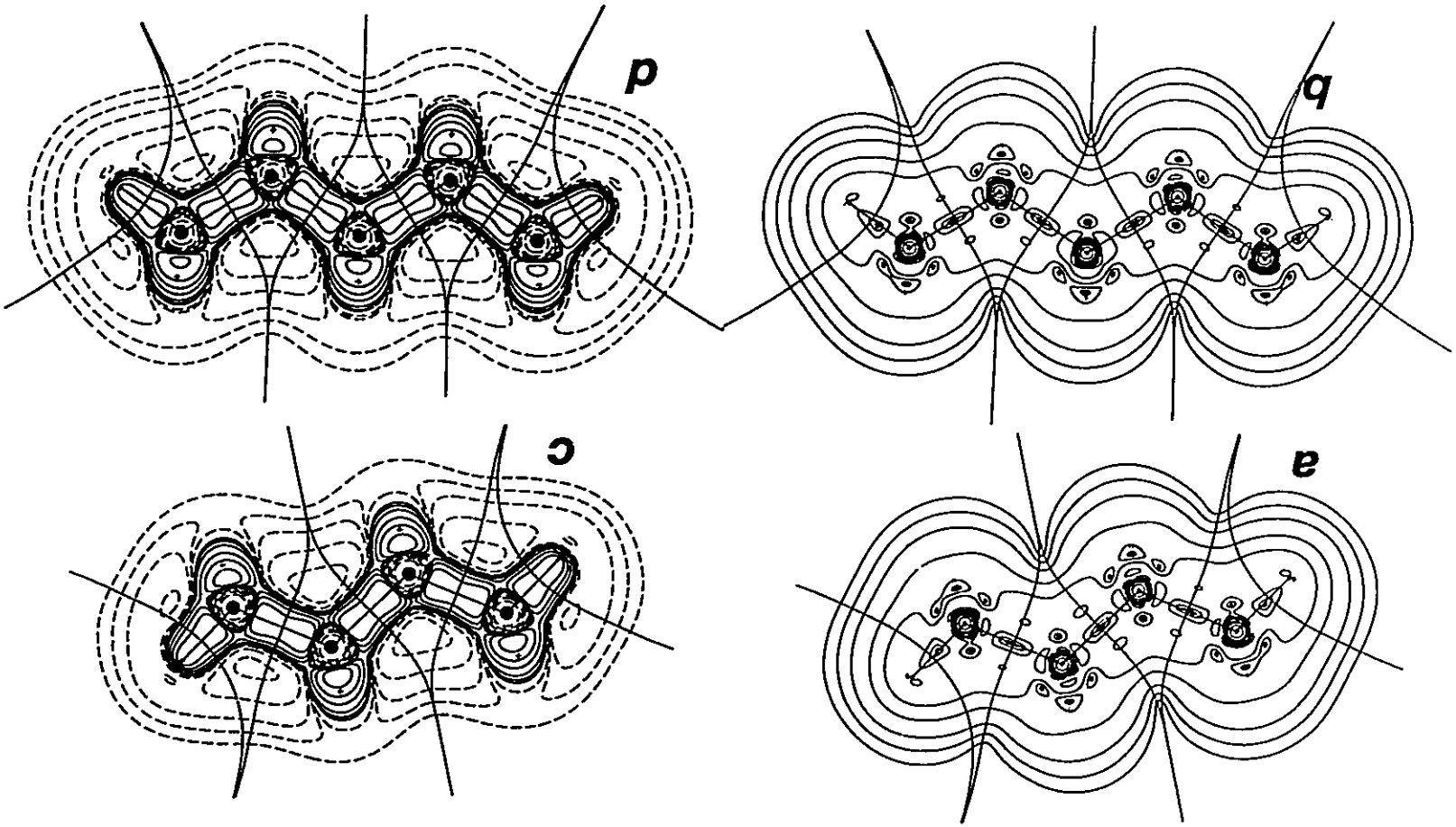
p
q
c
e

Figure 3-11

View of the transferable methylene group of the normal hydrocarbons with the van der Waals surface of two hydrogen atoms in the foreground in a and with the two C|C interatomic surfaces in the foreground in b. The bond critical point is denoted by a dot in one such surface. c) is the set of bond paths of the methylene group together with the associated (3,-1) bond critical points (black dots). d) is an interatomic surface separating the transferable methylene group from a neighboring methylene group. Also shown is the pair of bond paths originating at the associated bond critical point.

a
b
c
d

Figure 3-12

The current density in the ethane molecule in a plane perpendicular to a σ_d symmetry plane which is parallel to the applied field is shown in a). This is not a symmetry plane and the current density is non-planar. The critical point at the centre lies in the σ_d symmetry plane and it is a (2,0) centre point. Each carbon basin contains two centre points and two saddle points on the C-C axis. There are also surface points and spirals associated with the protons. Their out-of-plane behaviour is made evident in b) which shows the same induced current viewed along the C-C axis. This current distribution in ethane is similar to that induced in the ethene molecule by a field applied perpendicular to the σ_h plane (compare Fig. 2-24 of chapter 2) and this accounts for the nearly identical values for the corresponding components of the carbon shielding tensor.

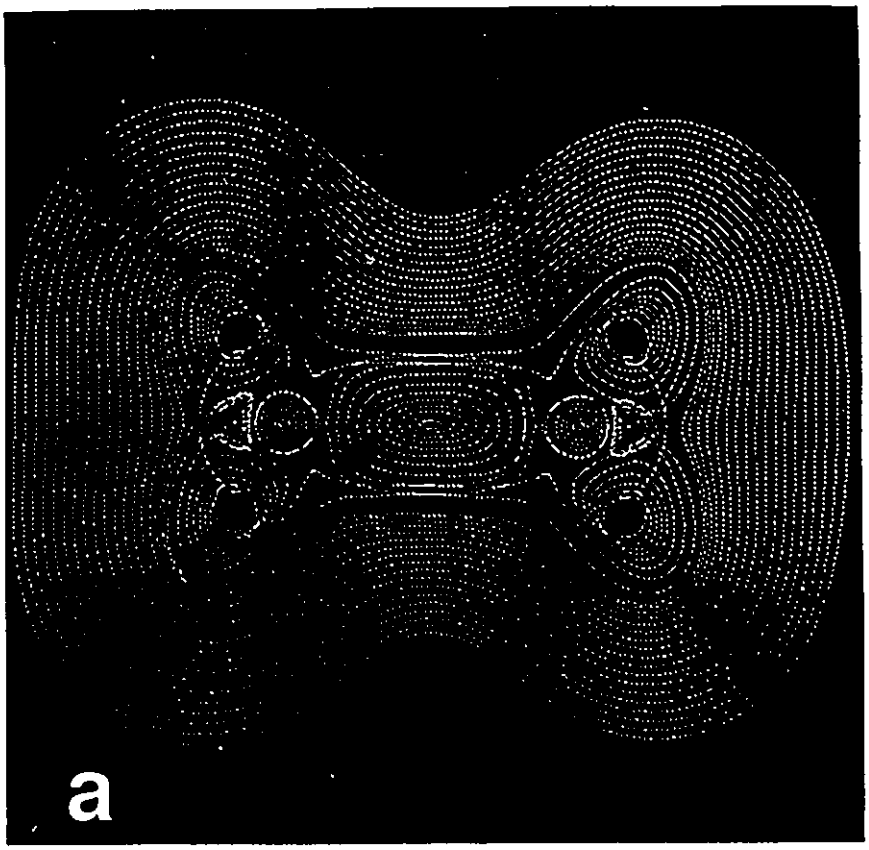
a

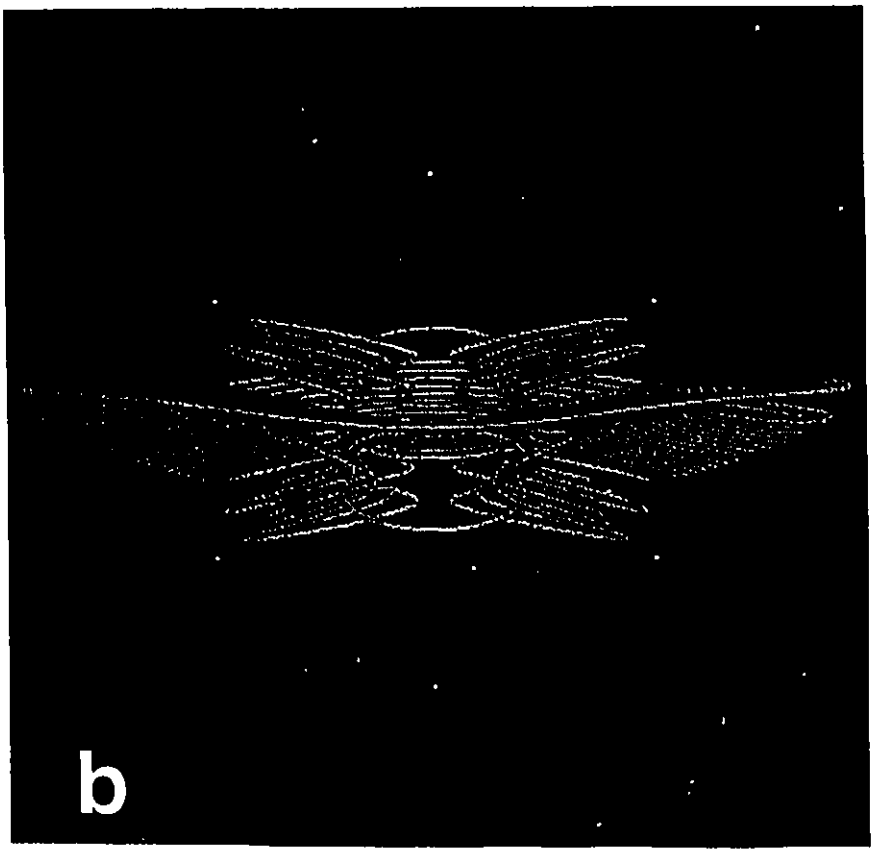
b

Figure 3-13

Displays of the current density, its curl and the Laplacian of ρ for the benzene molecule. The maps for $\mathbf{J}^{(1)}$ and its curl are for a field directed out of and perpendicular to the ring plane. In a) the current density is shown in the ring plane. b) is a projection of onto a plane 0.8 au above the symmetry plane, of current trajectories which intersect it. In addition to the outer diamagnetic and inner paramagnetic flows, there is a vestige of each bonded set of diamagnetic current flows present. The shell structure and regions of charge concentration/depletion defined by $\nabla^2\rho$ in d) are similar to the shell structure and regions of outwardly/inwardly directed flux in the $\nabla\times\mathbf{J}^{(1)}$ field in c).

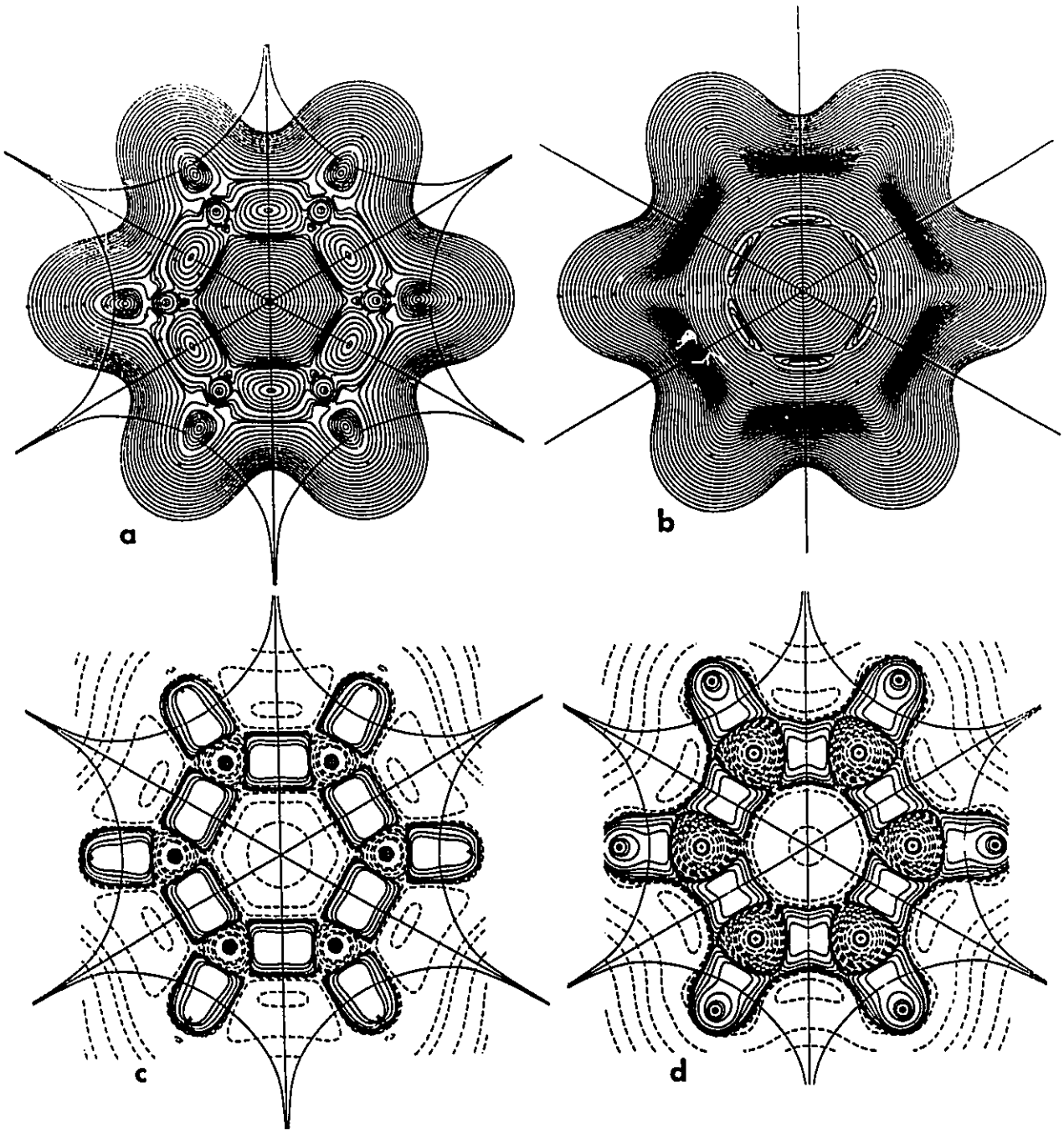
a
b
c
d

Figure 3-14

The atomic contributions to the principal components of the carbon shielding tensor in ethene. The star denotes the shielded nucleus. Units are ppm.

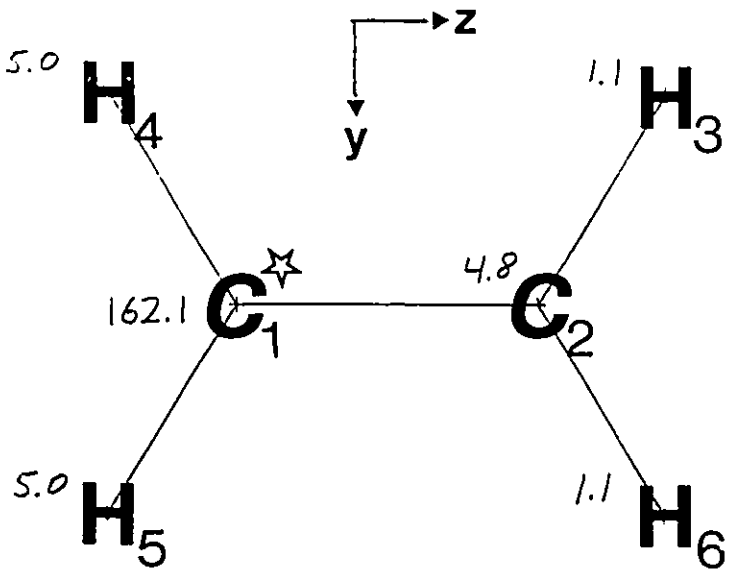

$\sigma^c = 179.1$

$B\perp$

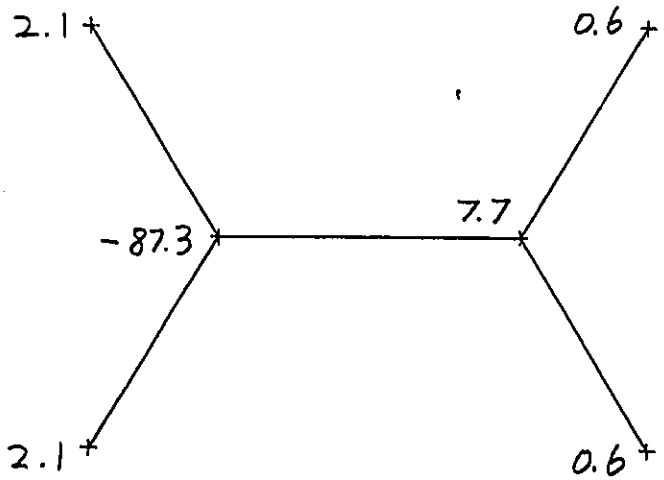

$\sigma^c = -74.2$

B

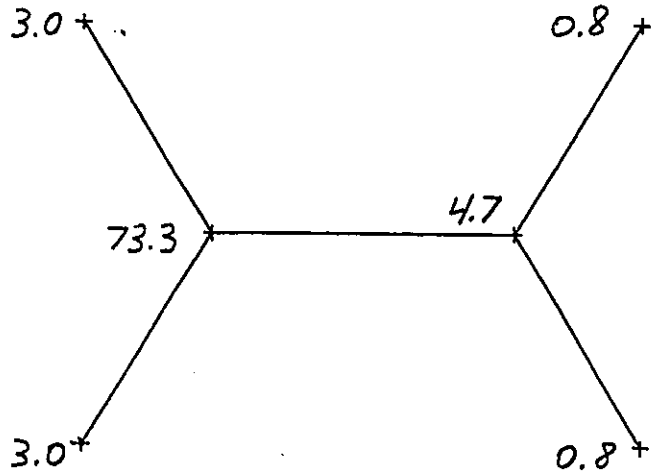

$\sigma^c = 85.6$

$\leftarrow B$

Figure 3-15

The atomic contributions to the proton shielding tensor for the same field directions as in Fig. 3-14. The star denotes the shielded nucleus. Units are ppm.

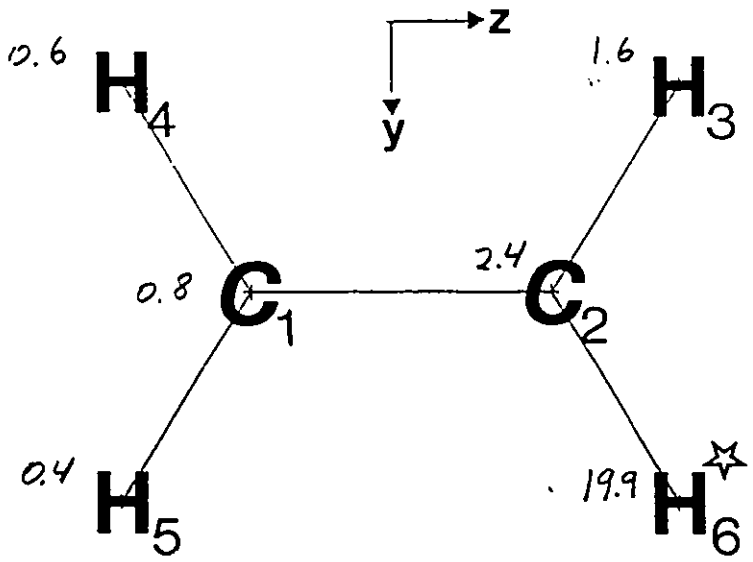

$\sigma^H = 25.7$

B⊥

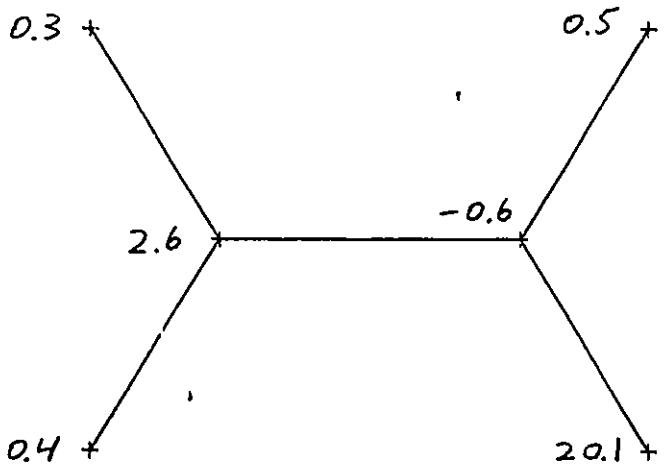

$\sigma^H = 23.3$

B

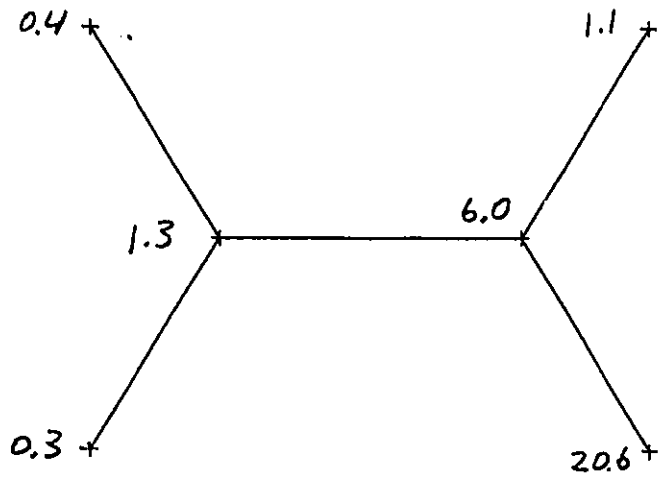

$\sigma^H = 29.7$

B

Table 3-1[a]

Total Contributions to Magnetic Susceptibility Tensor χ in First Row Hydrides.

Units are cgs-ppm.

Mol	$\chi_{\perp}^{b}$	$\chi_{\parallel}^{b}$	$\bar{\chi}^{b}$	$\chi_{\perp}^{s}$	$\chi_{\parallel}^{s}$	$\bar{\chi}^{s}$	$\chi_{\perp}$	$\chi_{\parallel}$	$\bar{\chi}$	$\bar{\chi}^{*}_{exp}$
H_2	-3.01	-3.67	-3.23	-0.93	0.00	-0.62	-3.94	-3.67	-3.85	-3.9
LiH	-6.77	-9.32	-7.62	0.04	0.00	0.03	-6.72	-9.32	-7.59	-7.6
BeH_2	-6.01	-11.61	-7.88	1.75	0.00	1.17	-4.26	-11.61	-6.71	
BH_3	-3.23	-8.29	-4.92	3.40	-9.09	-0.76	0.17	-17.38	-5.68	
CH_4			-11.34			-6.87			-18.20	-18.7
NH_3	-13.93	-11.51	-13.12	-3.43	-4.48	-3.78	-17.35	-15.99	-16.90	-16
H_2O	-12.17	-12.27	-12.21	-1.67	-1.58	-1.64	-13.84	-13.86	-13.85	-13.1
HF	-9.84	-10.02	-9.90	-0.92	0.00	-0.61	-10.76	-10.02	-10.51	-10.3

[a]The symbol $\perp$ refers to axes perpendicular to the principal rotation axis.
The symbol $\parallel$ refers to the principal rotation axis.
All calculations were done using the IGAIM method with the 6-311++G(2d,2p) basis set at the corresponding theoretical equilibrium geometries.

*References 6 and 7.

Table 3-2[a]

Hydrogen Atom (H) Contributions to Magnetic Susceptibility Tensor χ in First Row Hydrides. Units are cgs-ppm.

Mol	$\chi_{\perp}^{b}(H)$	$\chi_{\parallel}^{b}(H)$	$\bar{\chi}^{b}(H)$	$\chi_{\perp}^{s}(H)$	$\chi_{\parallel}^{s}(H)$	$\bar{\chi}^{s}(H)$	$\chi_{\perp}(H)$	$\chi_{\parallel}(H)$	$\bar{\chi}(H)$	q(H)*
H_2	-1.51	-1.83	-1.62	-0.47	0.00	-0.31	-1.97	-1.83	-1.93	0.00
LiH	-6.49	-8.40	-7.13	0.04	0.00	0.03	-6.45	-8.40	-7.10	-0.92
BeH_2	-3.57	-5.42	-4.19	0.50	0.00	0.33	-3.07	-5.42	-3.85	-0.86
BH_3	-1.92	-2.56	-2.14	0.65	-1.74	-0.15	-1.27	-4.30	-2.28	-0.70
CH_4			-1.53			-0.65			-2.18	-0.04
NH_3	-0.88	-0.90	-0.89	-0.31	-0.40	-0.34	-1.20	-1.30	-1.23	0.35
H_2O	-0.48	-0.48	-0.48	-0.21	-0.15	-0.19	-0.69	-0.63	-0.67	0.63
HF	-0.34	-0.13	-0.27	-0.32	0.00	-0.21	-0.65	-0.13	-0.48	0.78

[a]The symbol $\perp$ refers to axes perpendicular to the principal rotation axis. The symbol $\parallel$ refers to the principal rotation axis. All calculations were done using the IGAIM method with the 6-311++G(2d,2p) basis set at the corresponding theoretical equilibrium geometries.

*q(H) is the net charge of the hydrogen atom.

Table 3-3[a]

Total Contributions to Magnetic Susceptibility Tensor (χ) in First Row Mono-substituted Methane Molecules. Units are cgs-ppm.

Mol	$\chi_{\perp}^{b}$	$\chi_{\parallel}^{b}$	$\bar{\chi}^{b}$	$\chi_{\perp}^{s}$	$\chi_{\parallel}^{s}$	$\bar{\chi}^{s}$	$\chi_{\perp}$	$\chi_{\parallel}$	$\bar{\chi}$	$\bar{\chi}^{*}_{exp}$
CH_4			-11.34			-6.87			-18.20	-18
CH_3Li	-16.74	-15.64	-16.37	-5.86	-7.60	-6.44	-22.60	-23.24	-22.81	
CH_3BeH	-16.90	-19.29	-17.70	-4.29	-7.35	-5.31	-21.19	-26.64	-23.01	
CH_3BH_2	-13.01	-13.97	-13.65	-1.43	-8.57	-13.65	-14.44	-22.54	-19.84	
CH_3CH_3	-16.09	-18.51	-10.85	-13.12	-13.12	-11.61	-26.94	-31.63	-28.50	-27
CH_3NH_2	-16.44	-17.84	-17.37	-6.39	-8.69	-7.93	-22.83	-26.53	-25.30	
CH_3OH	-14.25	-17.31	-16.29	-5.50	-5.83	-5.72	-19.75	-23.14	-22.01	-22
CH_3F	-12.70	-17.36	-14.25	-3.49	-6.54	-4.51	-16.19	-23.90	-18.76	-18

[a]The symbol $\perp$ refers to axes perpendicular to the principal rotation axis in the molecules with at least C_{3v} symmetry: CH_3Li, CH_3BeH, CH_3CH_3 and CH_3F and and the axis perpendicular to the reflection plane in the molecules with C_s symmetry: CH_3BH_2, CH_3NH_2 and CH_3OH. The symbol $\parallel$ refers to the principal rotation axis in CH_3Li, CH_3BeH, CH_3CH_3, CH_3F and axes in the reflection plane for CH_3BH_2, CH_3NH_2 and CH_3OH.

All calculations were done using the IGAIM method with the 6-311++G(2d,2p) basis set at the corresponding theoretical equilibrium geometries.

*References 6 and 7.

TABLE 3-4[a]

Methyl Group (M) Contributions to Magnetic Susceptibility Tensor in First Row Mono-substituted Methane Molecules. Units are cgs-ppm.

Mol	$\chi_{\perp}^{b}(M)$	$\chi_{\parallel}^{b}(M)$	$\bar{\chi}^{b}(M)$	$\chi_{\perp}^{s}(M)$	$\chi_{\parallel}^{s}(M)$	$\bar{\chi}^{s}(M)$	$\chi_{\perp}(M)$	$\chi_{\parallel}(M)$	$\bar{\chi}(M)$	q(M)*
CH_4			-9.81			-6.22			-16.03	0.04
CH_3Li	-16.60	-14.76	-15.99	-5.86	-7.60	-6.44	-22.48	-22.37	-22.43	-0.92
CH_3BeH	-14.51	-13.13	-14.05	-4.73	-7.35	-5.60	-19.24	-20.48	-19.65	-0.87
CH_3BH_2	-11.58	-10.49	-10.85	-2.90	-6.88	-5.58	-14.55	-17.37	-16.43	-0.72
CH_3CH_3	-8.04	-9.25	-8.45	-5.42	-6.56	-5.80	-13.47	-15.82	-14.25	0.00
CH_3NH_2	-5.92	-7.56	-7.01	-3.47	-5.16	-4.60	-9.39	-12.72	-11.61	0.38
CH_3OH	-5.39	-6.68	-6.25	-2.91	-4.57	-4.02	-8.30	-11.25	-10.27	0.64
CH_3F	-4.58	-8.18	-5.78	-2.51	-6.54	-3.85	-7.09	-14.73	-9.63	0.74

[a]The symbol ⊥ refers to axes perpendicular to the principal rotation axis in the molecules with at least C_{3v} symmetry: CH_3Li, CH_3BeH, CH_3CH_3 and CH_3F and and the axis perpendicular to the reflection plane in the molecules with C_s symmetry: CH_3BH_2, CH_3NH_2 and CH_3OH. The symbol ∥ refers to the principal rotation axis in CH_3Li, CH_3BeH, CH_3CH_3, CH_3F and axes in the reflection plane for CH_3BH_2, CH_3NH_2 and CH_3OH.

All calculations were done using the IGAIM method with the 6-311++G(2d,2p) basis set at the corresponding theoretical equilibrium geometries.

*q(M) is the net charge of the methyl group.

Table 3-5[a]

Incremental Changes in Properties* for Group X=(OH or F)

Property	H|X	HCH_2|X	HCH_2CH_2|X	$HCH_2CH_2CH_2$|X
X = OH				
$\bar{\chi}$	-13.11	+1.63	-0.10	+0.04
$\bar{\chi}^b$	-11.73	+1.69	+0.12	+0.02
$\bar{\chi}^s$	-1.39	-0.06	-0.22	+0.03
q	-0.627	-0.016	-0.007	-0.004
E	-75.7147	-0.0888	-0.004	+0.003
v	168.80	-13.69	-0.69	+0.65
ρ_b	0.3964	-0.1309	-0.0031	+0.0001
$\nabla^2\rho_b$	-3.1057	+2.7639	+0.0116	+0.0074
X = F				
$\bar{\chi}$	-10.03	+0.92	+0.02	+0.02
$\bar{\chi}^b$	-9.63	+1.16	+0.16	+0.02
$\bar{\chi}^s$	-0.40	-0.24	-0.14	0.00
q	-0.779	0.044	-0.006	-0.001
E	-99.8149	-0.0220	+0.0082	+0.0061
v	130.44	-22.84	-2.91	+3.26
ρ_b	0.4042	-0.1632	-0.0051	+0.0002
$\nabla^2\rho_b$	-4.0047	+4.3951	-0.0150	+0.0102

[a]All calculations were done with SCF 6-311++G(2d,2p) wavefunctions obtained at

the corresponding theoretical equilibrium geometries. Magnetic susceptibilities were calculated using IGAIM with the same basis set.

*All quantities in atomic units except for $\bar{\chi}$, which is in cgs-ppm.

$\bar{\chi}$ = total mean magnetic susceptibility

$\bar{\chi}^{(1)}$ = basin contribution to total mean magnetic susceptibility

$\bar{\chi}^{(2)}$ = surface contribution to total mean magnetic susceptibility

q = net charge

E = energy

v = volume of the group enclosed by the 0.001 au isosurface.

ρ_b = electron density at bond critical point linking the group to the remainder of the molecule.

$\nabla^2\rho_b$ = Laplacian of electron density at bond critical point linking the group to the remainder of the molecule.

Table 3-6[a]

Calculated Magnetic Susceptibility Tensors χ of Normal Hydrocarbons.

Units are cgs-ppm.

Molecule	$\chi_{\perp 1}$	$\chi_{\perp 0}$	$\chi_{\parallel}$	$\bar{\chi}$	$\delta\bar{\chi}$	$\bar{\chi}^{*}_{exp}$
CH_4	-18.20	-18.20	-18.20	-18.20		(-18.7,-17.4)
C_2H_6	-26.94	-26.94	-31.63	-28.50	-10.30	(-27.4,-26.8)
C_3H_8	-40.08	-38.79	-42.35	-40.41	-11.91	(-40.5,-38.6)
C_4H_{10}	-51.00	-50.41	-55.19	-52.20	-11.79	(-50.0)
C_5H_{12}	-62.93	-61.75	-65.95	-63.54	-11.34	(-63.1)

[a]All calculations were done using the IGAIM method with the 6-311++G(2d,2p) basis set at the corresponding theoretical equilibrium geometries.

*Experimental values are from reference 24.

Table 3-7[a]

Group Contributions to Magnetic Susceptibility Tensor in Normal Hydrocarbons. Units are cgs-ppm.

Molecule	Methyl group			Methylene group		
	$\bar{\chi}_b(\Omega)$	$\bar{\chi}_f(\Omega)$	$\bar{\chi}(\Omega)$	$\bar{\chi}_b(\Omega)$	$\bar{\chi}_f(\Omega)$	$\bar{\chi}(\Omega)$
CH_4	-9.81	-6.22	-16.03			
C_2H_6	-8.45	-5.80	-14.25			
C_3H_8	-8.37	-6.11	-14.48	-6.06	-5.39	-11.45
C_4H_{10}	-8.38	-6.15	-14.53	-5.96	-5.61	-11.57
C_5H_{12}	-8.37	-6.12	-14.49	-5.96	-5.55	-11.51
C_5H_{12}	(unique methylene)			-5.83	-5.71	-11.54

[a]All calculations were done using the IGAIM method with the 6-311++G(2d,2p) basis set at the corresponding theoretical equilibrium geometries.

Table 3-8[a]

Mean Magnetic Suceptibilities in Isobutane and Neopentane. Units are cgs-ppm.

Isobutane		Neopentane	
$\bar{\chi}^{b}(CH_3)$	-8.23	$\bar{\chi}^{b}(CH_3)$	-8.04
$\bar{\chi}^{s}(CH_3)$	-6.29	$\bar{\chi}^{s}(CH_3)$	-6.33
$\bar{\chi}(CH_3)$	-14.52	$\bar{\chi}(CH_3)$	-14.37
$\bar{\chi}^{b}(CH)$	-4.16	$\bar{\chi}^{b}(C)$	-2.61
$\bar{\chi}^{s}(CH)$	-5.45	$\bar{\chi}^{s}(C)$	-5.67
$\bar{\chi}(CH)$	-9.61	$\bar{\chi}(C)$	-8.28
$\bar{\chi}$	-53.17	$\bar{\chi}$	-65.76
$\bar{\chi}(expt)^{*}$	-51.7	$\bar{\chi}(expt)^{*}$	-63.1

[a]All calculations were done using the IGAIM method with the 6-311++G(2d,2p) basis set at the corresponding theoretical equilibrium geometries.

*Reference 24.

Table 3-9[a]

Predicted and Experimental Mean Magnetic Susceptibilities for Branched Hydrocarbons.

Molecule	$\bar{\chi}$(pred)	$\bar{\chi}$(expt)*
2-methyl pentane	-76.1	-75.3
3-methyl pentane	-76.1	-75.5
2-methyl hexane	-87.6	-86.2
2,2-dimethyl butane	-77.8	-76.2
2,3-dimethyl butane	-77.2	-76.2
2,3-dimethyl pentane	-88.7	-87.5
2,4-dimethyl pentane	-88.7	-87.5
2,2,3-trimethyl butane	-90.4	-88.4
2,2,4-trimethyl pentane	-101.9	-99.1

[a] $\bar{\chi}(CH_3) = -14.5$; $\bar{\chi}(CH_2) = -11.5$; $\bar{\chi}(CH) = -9.6$; $\bar{\chi}(C) = -8.3$

*Reference 24.

Table 3-10[a]

Atomic Contributions to Magnetic Susceptibility Tensor of Benzene.

Units are cgs-ppm.

Atom	Ω	$\chi_{\perp}^{b}(\Omega)$	$\chi_{\parallel}^{b}(\Omega)$	$\bar{\chi}^{b}(\Omega)$	$\chi_{\perp}^{s}(\Omega)$	$\chi_{\parallel}^{s}(\Omega)$	$\bar{\chi}^{s}(\Omega)$	$\chi_{\perp}$	$\chi_{\parallel}$	$\bar{\chi}$
C		-2.23	-3.56	-2.67	-0.56^{H}	-1.35^{H}	-0.82^{H}	-4.57	-15.39	-8.18
					-1.79^{R}	-10.48^{R}	-4.68^{R}			
					-2.35^{T}	-11.83^{T}	-5.51^{T}			
H		-1.29	-1.29	-1.29	-0.33	-0.79	-0.48	-1.62	-2.08	-1.77
C_6H_6		-21.10	-29.11	-23.77	-16.08	-75.72	-35.96	-37.18	-104.83	-59.73

$\Delta\chi$	= -67.65	$6\Delta\chi(C)$	= -64.92	$6\Delta\chi(H)$	= -2.76
$\Delta\chi^{s}$	= -59.64	$6\Delta\chi^{s}(C)$	= -56.88	$6\Delta\chi^{s}(H)$	= -2.76
$\Delta\chi^{b}$	= -8.01	$6\Delta\chi^{b}(C)$	= -7.98	$6\Delta\chi^{b}(H)$	= 0.00

[a]The calculations were done using the IGAIM method with the 6-311++G(2d,2p) basis set at the corresponding theoretical equilibrium geometry.

The symbol ⊥ refers to axes perpendicular to the principal rotation axis and corresponding atomic values are averaged over both ⊥ field directions. The symbol ∥ refers to the principal rotation axis. [H]Refers to current flux through the C|H surface. [R]Refers to current flux through C|C surfaces in ring. [T]Refers to total current flux contribution.

Table 3-11[a]

Atomic and Group Contributions to Isotropic Carbon Shielding in Normal Hydrocarbons. Units are ppm.

Mol/Atom	$\bar{\sigma}^{C}_{int}$	$\bar{\sigma}^{C}(H_{\alpha})$	$\bar{\sigma}^{C}(G_{\alpha})$	$\bar{\sigma}^{C}(G_{\beta})$	$\bar{\sigma}^{C}(G_{\lambda})$	$\bar{\sigma}^{C}(G_{\delta})$	$\bar{\sigma}^{C}_{ext}$	$\bar{\sigma}^{C}$
CH_4–C	179.4	4.5					18.0	197.4
C_2H_6–C	168.9	4.2	4.8				17.4	186.3
C_3H_8–C1	161.2	4.2	3.8	1.1			17.5	178.8
C_3H_8–C2	159.6	4.0	4.9				17.7	177.3
C_4H_{10}–C1	162.4	4.2	3.7	0.7	0.5		17.5	179.9
C_4H_{10}–C2	151.8	4.0	4.9,3.8	1.1			17.7	169.5
C_5H_{12}–C1	163.4	4.2	3.7	0.6	0.3	0.2	17.6	180.8
C_5H_{12}–C2	154.5	4.0	4.9,3.7	0.7	0.5		17.8	172.3
C_5H_{12}–C3	145.1	4.0	3.7	0.9			17.7	162.8

[a]All calculations were done using the IGAIM method with the 6-311++G(2d,2p) basis set at the corresponding theoretical equilibrium geometries.

Table 3-12[a]

Atomic and Group Contributions to Isotropic Carbon Shielding $\bar{\sigma}^{C}$ in Normal Alcohols. Units are ppm.

Mol/Atom	$\bar{\sigma}^{C}_{int}$	$\bar{\sigma}^{C}(H_{\alpha})$	$\bar{\sigma}^{C}(G_{\alpha})$	$\bar{\sigma}^{C}(G_{\beta})$	$\bar{\sigma}^{C}(G_{\lambda})$	$\bar{\sigma}^{C}_{ext}$	$\bar{\sigma}^{C}$
CH_3OH	133.1	3.4	4.6			14.9	148.0
$CH_3\underline{C}H_2OH$	125.3	3.2	4.7(OH),4.6(CH_3)			15.7	141.0
$\underline{C}H_3CH_2OH$	160.9	4.2	3.7	0.8		17.0	177.9
$CH_3CH_2\underline{C}H_2OH$	119.4	3.2	4.6(OH),3.4(CH_2)	1.1		15.5	134.9
$CH_3\underline{C}H_2CH_2OH$	153.1	3.9	3.6(CH_2),4.9(CH_3)	0.8		17.2	170.3
$\underline{C}H_3CH_2CH_2OH$	166.9	4.3	3.9	0.8	0.3	17.8	184.6

[a]All calculations were done using the IGAIM method with the 6-311++G(2d,2p) basis set at the corresponding theoretical equilibrium geometries.

Table 3-13[a]

Isotropic Proton Shielding $\bar{\sigma}^{H}$ Ethane, Ethene, Acetylene and Benzene. Units are ppm.

Mol	$\bar{\sigma}^{H}_{int}$	$\bar{\sigma}^{H}(C_{\alpha})$	$\bar{\sigma}^{H}(C_{\beta})$	$\bar{\sigma}^{H}(H_{\alpha})$	$\bar{\sigma}^{H}(H_{\beta})$	$\bar{\sigma}^{H}_{ext}$	$\bar{\sigma}^{H}$
C_2H_6	21.6	4.9	0.5	1.4	0.5(i) 0.4(o)	9.4	31.0
C_2H_4	20.2	2.8	1.5	1.1	0.3(cis) 0.4(tr)	6.1	26.3
C_2H_2	19.0	8.0	2.9		0.4	11.3	30.3
C_6H_6	20.1		0.0(C_{ipso}) 0.7(C_{ortho}) 0.6(C_{meta}) 0.5(C_{para})		0.3(H_{ortho}) 0.2(H_{meta}) 0.2(H_{para})	4.1	24.2

[a]All calculations were done using the IGAIM method with the 6-311++G(2d,2p) basis set at the corresponding theoretical equilibrium geometries.

Table 3-14[a]

Proton Shielding in Ethane, Ethene, Acetylyene and Benzene - ∥ Field. Units are ppm.

Mol	σ^{H}_{int}	$\sigma^{H}(C_{\alpha})$	$\sigma^{H}(C_{\beta})$	$\sigma^{H}(H_{\alpha})$	$\sigma^{H}(H_{\beta})$	σ^{H}_{ext}	σ^{H}
CH_4	21.4	5.6		1.5		10.1	31.4
C_2H_6	21.2	4.3	1.0	1.8	0.6(i)	10.5	31.7
					0.4(o)		
C_2H_4	19.9	2.6	0.7	1.6	0.3(cis)	5.8	25.7
					0.6(tr)		
C_2H_2	21.9	16.8	2.5		0.1	19.4	41.3
C_6H_6	19.9		$-4.2(C_{ipso})$			0.6	20.5
			$0.0(C_{ortho})$	$0.4(H_{ortho})$			
			$1.1(C_{meta})$	$0.3(H_{meta})$			
			$1.1(C_{para})$	$0.3(H_{para})$			

[a]All calculations were done using the IGAIM method with the 6-311++G(2d,2p) basis set at the corresponding theoretical equilibrium geometries.

Table 3-15[a]

Proton Shielding in Ethane, Ethene, Acetylyene and Benzene - ⊥ Field. Units are ppm.

Mol	$^{\perp}\sigma^{H}_{int}$	$^{\perp}\sigma^{H}(C_{\alpha})$	$^{\perp}\sigma^{H}(C_{\beta})$	$^{\perp}\sigma^{H}(H_{\alpha})$	$^{\perp}\sigma^{H}(H_{\beta})$	$^{\perp}\sigma^{H}_{ext}$	$^{\perp}\sigma^{H}$
CH_4	21.4	5.6		1.5		10.1	31.4
C_2H_6	21.8	5.1	0.2	1.2	0.4(i)	4.2	30.6
					0.3(o)		
C_2H_4	20.4	2.8	2.0	0.8	0.3(cis)	6.2	26.6
					0.3(tr)		
C_2H_2	17.5	3.7	3.0		0.5	7.2	24.8
C_6H_6	20.2		$2.1(C_{ipso})$			5.9	26.1
			$1.0(C_{ortho})$		$0.3(H_{ortho})$		
			$0.3(C_{meta})$		$0.1(H_{meta})$		
			$0.1(C_{para})$		$0.1(H_{para})$		

[a]All calculations were done using the IGAIM method with the 6-311++G(2d,2p) basis set at the corresponding theoretical equilibrium geometries.

4. COMPUTATIONAL IMPROVEMENTS FOR THE THEORY OF ATOMS IN MOLECULES

4-1 Introduction

The calculation of properties of atoms in molecules[1] from ab-initio molecular wavefunctions is currently realized with PROAIM (PROperties of Atoms In Molecules),[2] a program written by F.W. Biegler-Konig which is becoming widely used in the scientific community. With the increasing use of PROAIM two practical problems have become apparent: a) it is a slow program; and b) the accurate determination of properties of atoms in molecules with complicated charge density topologies is often not possible. The first problem (a) arises primarily for the following three reasons: i) PROAIM uses relatively high-order (ie., many points), three-dimensional, Gaussian quadrature numerical integration throughout the atom in order to obtain accurate results; ii) PROAIM was written for low memory, scalar processing computers; and iii) PROAIM retains much unnecessary *molecular* information from the wavefunction in order to calculate *atomic* properties, and thus performs much unnecessary computation. The second problem (b) arises from the *non-local* method used to approximate the often complex surfaces bounding atoms in molecules, surfaces which must be determined accurately prior to the numerical integration in order to obtain accurate atomic properties. Both of PROAIM's difficulties have been

separately addressed and the methods to overcome them will be described in this chapter. Section 4-2 describes PROAIMV, a much more efficient version of PROAIM. Section 4-3 describes PROMEGA, a program which employs a new, *local* method of approximating atomic surfaces, one which allows accurate calculation of atomic properties in any system, however complex.

4-2 PROAIMV

4-2-1 Introduction to PROAIMV

It is the purpose of this section to describe a new program, PROAIMV (PROperties of Atoms In Molecules - Vectorized), which eliminates the problem of CPU time associated with PROAIM. The success of PROAIMV is achieved, without loss of the accuracy of PROAIM, by employing the following three strategies: i) significantly reducing the number of numerical integration points necessary to achieve a given level of accuracy; ii) vectorizing the numerical integration over large batches of integration points; and iii) employing an efficient, pre-integration cutoff algorithm to determine those primitive basis functions appearing in the expansion of the molecular wavefunction which can be neglected during the numerical integration. As an example of the efficiency and accuracy of the new program, CPU times and integration results obtained on an IBM RS6000 model 350 are given for the symmetrically unique atoms of 18,6 crown ether in its D_{3d} conformation, with and without the primitive cutoff algorithm. These CPU times are compared with those of the original PROAIM program, obtained on the same machine. Without the primitive cutoff algorithm, PROAIMV is between ten and twenty-five times faster than the original PROAIM. With the primitive cutoff algorithm, PROAIMV

is between twenty and fifty times faster.

With the primitive cutoff algorithm, CPU times using PROAIMV will rarely exceed one hour on any modern workstation, even for the largest molecular wavefunctions likely to be used in theoretical studies. This leads to the important result that the calculation of the properties of the atoms in a molecule is now competitive with the determination of the molecular wavefunction itself and the direct calculation of molecular properties.

4-2-2 Background

An atom Ω in a molecule is, by definition,[1] a region of real molecular space $\mathbb{R}^3$ with a surface $S(\mathbf{r},\Omega)$ defined by the quantum boundary condition

$$\nabla\rho(\mathbf{r})\cdot\hat{\mathbf{n}}(\mathbf{r}) = 0, \quad \forall \mathbf{r} \in S(\mathbf{r},\Omega) \tag{1}$$

where $\nabla\rho(\mathbf{r})$ is the gradient of the electron density $\rho(\mathbf{r})$ at a point $\mathbf{r}$ on the surface and $\hat{\mathbf{n}}(\mathbf{r})$ is the unit vector normal to the surface at $\mathbf{r}$. A pictorial example is given in Fig. 4-1, where the atomic surface of the carbon atom in methane is shown. Since this molecule is isolated the carbon atomic surface extends to infinity, but in Fig. 4-1 the surface is only shown out to its intersection with the 10^{-5} au. iso-surface of $\rho(\mathbf{r})$, beyond which the electron density is neglibly small. As can be clearly seen in Fig. 4-1, the carbon atomic surface in methane is itself composed of four *interatomic* surfaces, one for each C-H bond, each of which is defined by the set of $\nabla\rho(\mathbf{r})$ trajectories which terminate at the corresponding (3,-1) "bond" critical point in the $\nabla\rho(\mathbf{r})$ field. In fact, the atomic surface shown in Fig. 4-1 was calculated in just this manner - by traversing a subset of the $\nabla\rho(\mathbf{r})$ trajectories backward from the four (3,-1) critical points. Since an atomic surface is always defined by

interatomic surfaces of $\nabla\rho(\mathbf{r})$ trajectories, eqn. (1) is identically satisfied.

An equivalent definition of an atom is a molecule is given as that region of molecular space traversed by the complete set of trajectories of $\nabla\rho(\mathbf{r})$ which terminate at the nucleus of the atom, the trajectories being paths of steepest ascent in $\rho(\mathbf{r})$, a function which possesses local maxima at the nuclei.[1] This is seen in Fig. 4-2 for the same methane carbon atom, where a subset of the $\nabla\rho(\mathbf{r})$ trajectories terminating at the carbon nucleus are shown out to their intersection with the same 10^{-5} au. iso-surface in $\rho(\mathbf{r})$. The important point to be noted is that the region traversed by the trajectories in Fig. 4-2, the carbon atomic basin, is equivalent to the region enclosed by the interatomic surfaces in Fig. 4-1.

The calculation of any property F of an atom Ω in a molecule from a molecular wavefunction proceeds by defining a corresponding *property density* $F(\mathbf{r})$ in real space whose integration over the whole molecule MOL yields the molecular property F(MOL).[1,2] The integration of $F(\mathbf{r})$ over the basin of an atom in a molecule then yields the atomic value for that property, $F(\Omega)$.

$$F(\Omega) = \int_{\Omega} d\mathbf{r}F(\mathbf{r}) \tag{2}$$

The simplest example of a property density is the electron density $\rho(\mathbf{r})$, whose integration over Ω yields the atomic electron population $N(\Omega)$.

$$N(\Omega) = \int_{\Omega} d\mathbf{r}\rho(\mathbf{r}) \tag{3}$$

Two particularly important property densities are the kinetic energy densities $G(\mathbf{r})$ and $K(\mathbf{r})$, defined as follows in terms of the first-order density matrix $\Gamma^{(1)}(\mathbf{r},\mathbf{r}')$.

$$G(\mathbf{r}) = (1/2)[\nabla\cdot\nabla' \Gamma^{(1)}(\mathbf{r},\mathbf{r}')]_{\mathbf{r}=\mathbf{r}'} \quad (4)$$

$$K(\mathbf{r}) = (-1/2)[\nabla^2 \Gamma^{(1)}(\mathbf{r},\mathbf{r}')]_{\mathbf{r}=\mathbf{r}'} \quad (5)$$

Either of these two densities, when integrated over an atom in a molecule, yields the same value for the atomic kinetic energy, $T(\Omega)$.

$$T(\Omega) = G(\Omega) = \int_{\Omega} d\mathbf{r} G(\mathbf{r}) = K(\Omega) = \int_{\Omega} d\mathbf{r} K(\mathbf{r}) \quad (6)$$

This equivalence is unique to an atom in a molecule[1] because the difference between $G(\mathbf{r})$ and $K(\mathbf{r})$ is proportional to the laplacian of the charge density $\nabla^2\rho(\mathbf{r})$, whose integral over an atom in a molecule vanishes identically according to Gauss' theorem and the definition of an atomic surface, eqn. (1)

$$L(\Omega) = \int_{\Omega} d\mathbf{r} L(\mathbf{r}) = (-1/4)\int_{\Omega} d\mathbf{r} \nabla^2\rho(\mathbf{r}) = (-1/4)\int_{\Omega} dS(\Omega) \nabla\rho(\mathbf{r})\cdot\hat{\mathbf{n}} = 0 \quad (7)$$

The value of $L(\Omega)$ provides a measure of the accuracy of an approximate calculation of atomic properties.

Since molecules are disjointly and completely partitioned into atoms[1] the sum of all atomic values $F(\Omega)$ of any given property F equals the molecular value F(MOL).

$$F(MOL) = \int_{MOL} d\mathbf{r} F(\mathbf{r}) = \sum_{\Omega} \int_{\Omega} d\mathbf{r} F(\mathbf{r}) = \sum_{\Omega} F(\Omega) \quad (8)$$

The extent to which this additivity relationship is obeyed for a set of approximate atomic integrations provides another measure of the accuracy of the results.

4-2-3 Proaim

In a spherical polar coordinate system centered on the nucleus of atom Ω,

the integral expression for an atomic property can be usefully written as in eqn. (9)[2]

$$F(\Omega) = \int_0^{2\pi} d\phi \int_0^{\pi} d\theta \sin\theta \; x$$

$$\left(\int_0^{beta} dr r^2 F(r,\phi,\theta) + \int_{beta}^{R1(\phi,\theta)} dr r^2 F(r,\phi,\theta) + \int_{R2(\phi,\theta)}^{R3(\phi,\theta)} dr r^2 F(r,\phi,\theta) \right) \qquad (6\text{-}9)$$

where *beta* is the radius of a sphere centered on the nucleus and contained within the atom and $R1(\phi,\theta)$ is the length from the nucleus to the first intersection with the atomic surface $S(\mathbf{r},\Omega)$ of a ray whose orientation is defined by the angles ϕ and θ. Similarly, $R2(\phi,\theta)$ and $R3(\phi,\theta)$ are the distances from the nucleus to the second and third intersections, if they exist, of the same ray with the atomic surface. A ray with more than three intersections has not been observed and such rays will not be considered here.

In general, atoms in molecules do not have simple shapes and the property densities $F(r,\phi,\theta)$ do not have simple functional forms so the integration of the property densities cannot be done (fully) analytically as in the molecular case, but must be done (at least partially) numerically. The program PROAIM employs three dimensional gaussian quadrature integration[3] to approximate the triple integral in eqn. (9)[2]

$$F(\Omega) = \sum_{\theta=0}^{2\pi} W(\phi) \sum_{\phi=0}^{2\pi} W(\theta)\sin\theta \left(\sum_{r=0}^{BETA} W(r) r^2 F(r,\phi,\theta) + \right.$$

$$\left. \sum_{r=BETA}^{R1(\phi,\theta)} W(r) r^2 F(r,\phi,\theta) + \sum_{r=R2(\phi,\theta)}^{R3(\phi,\theta)} W(r) r^2 F(r,\phi,\theta) \right) \qquad (10)$$

where $W(\phi)$, $W(\theta)$ and $W(r)$ are gaussian quadrature weights for the particular values of ϕ, θ and r, respectively.

In practice, the property densities $F(r,\phi,\theta)$ are calculated from the natural orbitals of the molecular single-particle density matrix for any one-electron property with the corresponding operator $\hat{F}$ as follows

$$F(r,\phi,\theta) = \sum_{i=1}^{NMO} \lambda_i \psi_i(r,\phi,\theta) \hat{F} \psi_i(r,\phi,\theta) \qquad (11)$$

where $\psi_i(r,\phi,\theta)$ is the i^{th} natural orbital evaluated at the point $\mathbf{r} = (r,\phi,\theta)$, λ_i is the corresponding occupation number and NMO is the total number of natural orbitals.

The determination of $F(\Omega)$ by PROAIM thus involves the following steps:

i) Specify the number of ϕ and θ values to be used in the numerical integration and load the corresponding weighting coefficients $W(\phi)$ and $W(\theta)$. 64 ϕ values and 64 θ values uniformly distributed between 0 and 2π and 0 and π, respectively, are usually more than adequate. In principle, the more ϕ and θ values used, the greater the accuracy, but in fact, at this order of (angular) numerical integration the accuracy of the results is often determined by how closely the interatomic surface $S(\mathbf{r},\Omega)$ can be approximated using the method outlined in step ii), assuming a sufficiently high order of radial integration.

ii) Specify *beta* as the distance from the nucleus to the nearest critical point in the $\nabla\rho$ field which lies in the atomic surface and determine all of the distances $R1(\phi,\theta)$, $R2(\phi,\theta)$ and $R3(\phi,\theta)$. The latter are determined in PROAIM by first approximating the atomic surface $S(\mathbf{r},\Omega)$ by a relatively large set of trajectories of $\nabla\rho(\mathbf{r})$ which terminate at each of the (3,-1) critical points of the $\nabla\rho$ field which lie in the atomic surface, as in Fig. 4-1 for the methane carbon atom. A (3,-1) critical point in $\nabla\rho(\mathbf{r})$ is a point between two

bonded nuclei where $\nabla\rho(\mathbf{r})$ vanishes, $\rho(\mathbf{r})$ is a minimum along the corresponding bond and a local maximum in all perpendicular directions. The area between adjacent $\nabla\rho(\mathbf{r})$ trajectories in the surface is completely partitioned into triangles and each integration ray is checked to determine which, if any, of the surface triangles it intersects and at what distance(s) $R(\phi,\theta)$. For moderate to large sytems this step is usually, but not always, negligible in time relative to the integration in PROAIM. However, as stated above, this step can limit the accuracy of the results if the charge distribution defining the surface is topologically complex.

iii) For a particular pair of ϕ and θ values determine the number and position of integration points to be used in the radial integration(s) according to the values of *beta*, $R1(\phi,\theta)$, $R2(\phi,\theta)$ and $R3(\phi,\theta)$ and load the corresponding radial integration weights W(r). In PROAIM, the numerical integration is done one integration ray at a time, each in two or three parts. The first part involves the integration from the nucleus of the atom to the surface of a sphere contained in the atom, the *beta* sphere. This part of the radial integration requires many integration points, typically 96, as the property densities are largest and least smooth, radially, in the neighborhood of the nucleus. The second part involves the integration from the surface of the *beta* sphere to the first intersection $R1(\phi,\theta)$, which is sometimes infinity, of the given ray with the atomic surface. The number of integration points in this part of the integration depends, of course, on the distance integrated, but can be small relative to the *beta* sphere integration because the property densities are smoother, radially, in the non-nuclear regions of an atom. Occasionally, integration rays intersect the atomic surface more

than once. In this case, a third radial integration along the ray from the second intersection R2(ϕ,θ) to the third is performed. If the first or third intersection occurs at infinity, then the radial integration is carried out to a distance where the property densities are negligibly small, usually a distance of 8-10 au.

iiia) For each ϕ, θ and r(ϕ,θ) the values of ψ_i, $\nabla\psi_i$ and $\nabla^2\psi_i$ are required to determine the set of property densities F(r,ϕ,θ) calculated in PROAIM. The evaluation of ψ_i, $\nabla\psi_i$ and $\nabla^2\psi_i$ is accomplished by first determining the corresponding values of the primitive functions ϕ_j, $\nabla\phi_j$ and $\nabla^2\phi_j$ used in the expansion of the natural orbitals. The primitives are then summed into the natural orbitals and their derivatives weighted by the corresponding expansion coefficients C_{ij}. The loop structure used by PROAIM to evaluate the ψ_i, $\nabla\psi_i$ and $\nabla^2\psi_i$ at a given point ϕ, θ and r(ϕ,θ) is shown in Fig. 4-3. Naturally, the evaluation of the ϕ_j and the ψ_i is done in cartesian coordinates.

Once the values of the natural orbitals and their derivatives are calculated at the given point $\mathbf{r}$ (= r,ϕ,θ), the property densities F($\mathbf{r}$) are formed according to eqn. (11) and summed into the atomic value F(Ω) according to eqn. (10). Step iiia) is then repeated for all ϕ, θ used in the numerical integration.

For wavefunctions with many natural orbitals and primitives the CPU time required to calculate atomic properties with PROAIM becomes *prohibitive* on any computer, given the structure of the program and the large number of integration points used to obtain accurate results. The most time-consuming part of the integration is, of course, in step iiia), the calculation of the primitives and their derivatives and their contraction into the natural

orbitals. In PROAIM this step is carried out many of thousands of times in any given atomic calculation, one integration point at a time.

4-2-4 Recent Advances

Two proposals have recently appeared in the literature to decrease the CPU time required by PROAIM. The first of these[4] reduces the number of primitives NPRIMS to be calculated and contracted into the natural orbitals by neglecting, throughout the whole numerical integration, those which are centered on a nucleus sufficiently far removed from the nucleus of the integrated atom, taking into account the exponent and type of each primitive function. In order to be completely general and accurate, however, this method must necessarily be overly cautious in its cutoff criterion. Another approach is that given by Cioslowski,[5] in which the order of operations in the calculation and contraction of the primitives is rearranged to allow a "vectorization" of the primitives calculation at each integration point and a "dynamic" (pointwise) determination of which primitives can be neglected in the contraction into the natural orbitals. For very large systems with many natural orbitals, many long contraction loops are avoided and a significant savings in time results. Both of these methods are somewhat successful in significantly reducing atomic integration times for large systems.

4-2-5 Description of PROAIMV

In the approach developed here, several unique steps are taken to dramatically increase the efficiency of PROAIM. The first involves the vectorization of the whole numerical integration process, whereby the property

densities are calculated at many integration points at once. In this vectorized integration, the time-consuming part of step iiia) appears as in Fig. 4-4.

In the approach depicted in Fig. 4-4, the values of the primitives and their derivatives are first evaluated at many (NPTS) integration points and stored in core memory. The primitives are then contracted into the natural orbitals at the NPTS points with the long NPTS loop being the inner one. Aside from the explicit vectorization over the large number of integration points, this arrangement allows a significant decrease in the number of floating point operations and CPU time for either of two reasons. First, for a given number of primitives NPRIMS many of the primitive contributions to the natural orbitals are effectively zero *throughout the atom* so the long inner loop over the NPTS points can be skipped if this information is predetermined and encoded within the coefficients C_{ij}. Of course, if the contribution of a given primitive to all of the natural orbitals is effectively zero within the atom, then the primitive can be removed entirely from the calculation, thus saving even more time. Second, the contraction of the primitives into the natural orbitals at many points is a matrix-matrix multiplication process and is ideally suited for the machine optimized matrix multiplication routines which exist on most computers today.

It is important to emphasize that in the method employed by PROAIMV the vectorized loops are over the integration points, which are always large in number, and thus PROAIMV yields significantly faster results than PROAIM for *any* sized system, even without the primitive cutoff algorithm.

A problem is to efficiently pre-determine which primitives cannot be

neglected entirely in the numerical integration and, of these, which expansion coefficients C_{ij} can be safely set to zero.

The primitive cutoff algorithm employed in PROAIMV proceeds in two stages, in parallel with the numerical integration itself. The first stage determines which of the primitives (and their derivatives) make negligible contributions to all of the natural orbitals' property densities within the *beta* sphere and may thus be neglected throughout the *beta* sphere part of the integration. Of the primitives which are not neglected entirely within the *beta* sphere, the first stage also determines those which make negligible contributions to a given natural orbital and the corresponding expansion coefficients C_{ij} are then set to zero so that the inner points loop is skipped in the contraction step for the corresponding primitives and natural orbitals. The primitive cutoff determination for the *beta* sphere is done simply by an explicit, but sparse, sampling of the *beta* sphere for each of the primitives.

The second stage of the primitive cutoff algorithm determines which primitive contributions are negligibly small within the atom but outside of the *beta* sphere. This is achieved in an *atom-specific* manner by taking advantage of the definition of an atom in a molecule as that region of molecular space traversed by $\nabla\rho$ trajectories which terminate at the nucleus of the atom (see Fig. 4-2). By sampling the basin of the atom outside of the *beta* sphere along a set of such $\nabla\rho$ trajectories, those primitives which may be neglected throughout the integration, entirely or within a given natural orbital, can be quickly and easily accomplished. In effect, by employing this primitive cutoff approach, one is eliminating all of the unnecessary information in the molecular wavefunction and creating a "wavefunction" for an

atom in a molecule in order to determine the atomic properties.

The final step taken in PROAIMV to reduce atomic integration times is simply to reduce the number of numerical integration points necessary to obtain results equivalent to those of PROAIM. This is achieved by a *complete* separation of the *beta* sphere integration from the integration outside of the *beta* sphere. Within the *beta* sphere of an atom, the property densities vary rapidly radially but are smooth with respect to variation of the angles ϕ and θ. Just the opposite is true in the region of the atom which lies outside of the *beta* sphere. In PROAIMV only a fraction of the integration rays used outside of the *beta* sphere are actually used within the *beta* sphere. In other words, the spherical polar numerical integration in PROAIMV is *completely* separated into two parts as follows,

$$
\begin{aligned}
F(\Omega) = & \sum_{\phi^b=0}^{2\pi} W(\phi^b) \sum_{\theta^b=0}^{\pi} W(\theta^b)\sin\theta^b \sum_{r=0}^{BETA} W(r)r^2F(r,\phi^b,\theta^b) \\
& + \sum_{\phi=0}^{2\pi} W(\phi) \sum_{\theta=0}^{\pi} W(\theta)\sin\theta \left(\sum_{r=BETA}^{R1(\phi,\theta)} W(r)r^2F(r,\phi,\theta) \right. \\
& \left. + \sum_{r=R2(\phi,\theta)}^{R3(\phi,\theta)} W(r)r^2F(r,\phi,\theta) \right) \qquad (12)
\end{aligned}
$$

The number of angles ϕ^b and θ^b used within the *beta* sphere is, of course, dependent on the radius of the sphere but is always much less than the number needed outside of the *beta* sphere. Thus, in PROAIMV far fewer integration points are used to achieve the same level of accuracy as PROAIM.

4-2-6 PROAIMV Results

Table 4-1 shows a set of CPU times for the calculation of the properties of the four symmetrically unique atoms of 18,6 crown ether ($C_{12}H_{24}O_6$) at its D_{3d} 6-31g** optimized geometry using PROAIMV. The molecular wavefunction used is that from a standard Gaussian 90[6] SCF calculation with the same 6-31g** basis set. This wavefunction contains 672 primitive gaussian functions and 72 canonical orbitals and approaches the size limit of most ab-initio SCF studies today. Given the enormous amount of CPU time required by the original PROAIM for large systems such as this one, only one of the crown atoms (hydrogen b), that expected to require the least amount of CPU time, was actually integrated with the original PROAIM for comparison. The integration results obtained with PROAIMV for this atom, both with and without the cutoff algorithm, are in agreement with those of the original PROAIM to at least 10^{-5} au. for all of the properties calculated by PROAIM, which is more than adequate since the PROAIM results are accurate to 10^{-4} au. at best. PROAIMV has been tested on a large number of systems of varying complexity and consistently gives results in agreement with the original PROAIM program to at least 10^{-5} atomic units.

The timing results in Table 4-1 need little explanation. Without the primitive cutoff algorithm, PROAIMV is faster than the original PROAIM by at least a factor of 10 for all of the crown atoms, and with the cutoff algorithm by at least a factor of 20.

To demonstrate the accuracy of PROAIMV, the $L(\Omega)$ values, net charges and energies of the symmetrically unique crown atoms, as determined by PROAIMV, are shown in Table 4-2.

4-3 PROMEGA

4-3-1 Introduction to PROMEGA

The second problem with PROAIM is more serious than the timing problem addressed in section 4-2 because it involves the accuracy of the calculated atomic properties. For atoms in molecules bounded by surfaces with many critical points or "near-critical" points in the $\nabla\rho$ field, PROAIM (as well as PROAIMV and any other modified versions of PROAIM) sometimes fails to yield accurate results because of the method used to approximate the surface which defines the atomic region of numerical integration. It is the purpose of this section to describe a new program, PROMEGA, which employs a more general and accurate method to approximate atomic surfaces, however complex, while maintaining the efficient numerical integration procedure used in PROAIMV. With PROMEGA, the properties of an atom in any system can be determined accurately.

4-3-2 Background

The first general program[7] developed to calculate properties of atoms in molecules utilized fully the topological definition of an atom in molecule as the union of a three dimensional attractor of the gradient vector field of the charge density $\nabla\rho(\mathbf{r})$ and its associated basin: i.e., that part of molecular space containing the nucleus of the atom (attractor) and the region (basin) traversed by the complete set of $\nabla\rho(\mathbf{r})$ trajectories which terminate at the nucleus (see Fig. 4-2). This original program has since been slightly modified and is now called OMEGA.[8] In principle, by integrating property densities along the set of $\nabla\rho$ trajectories which traverse the atomic basin, from their termination point at the nucleus to their origination points

(usually infinity) in the atomic surface, one necessarily covers the volume of the atom, exclusively and completely, and thus obtains the atomic values for the properties. This is the basis for the OMEGA program. While straightforward in principle, the algorithm of OMEGA is unreliable in practice because it is necessary, of course, to employ numerical integration with a finite number of $\nabla\rho$ trajectories. Poor sampling of the atomic basins by the $\nabla\rho$ trajectories in the bonding regions, regions of nearly constant charge density, often leads to inaccurate results.

The second general atomic integration program, PROAIM,[2] is much more reliable than OMEGA and it, or more efficient versions of it such as PROAIMV, is the one currently used by most researchers. As described in section 6-2, PROAIM avoids the basin sampling problems associated with OMEGA by simply using gaussian quadrature numerical integration over the basin of the atom in a spherical polar coordinate system centered on the nucleus. The property densities are integrated along a set of *uniformly distributed* rays originating at the nucleus of the atom, neglecting the segments of the rays which lie outside of the atomic basin. Unlike OMEGA, PROAIM requires that the complete atomic surface be approximated prior to the numerical integration so that the points of intersection of the integration rays with the surface can be determined.

As mentioned in section 4-2, the method used in PROAIM to approximate an atomic surface is based on the fact that an atomic surface consists of a set of interatomic surfaces, each of which is defined by the union of a two-dimensional attractor of the gradient vector field of the charge density, a "bond" critical point in the $\nabla\rho$ field, and the surface defined by the complete

set of $\nabla\rho$ trajectories which terminate at this attractor (see Fig. 4-1). In principle, the entire atomic surface can be mapped out with the complete set of trajectories which define the interatomic surfaces and the intersections of the integration rays found by determining the intersections of the rays with the set. This is, essentially, the basis for the PROAIM program. In practice, for each interatomic surface a finite set of $\nabla\rho(\mathbf{r})$ trajectories which terminate at the corresponding (3,-1) critical point is calculated and the areas between adjacent trajectories are completely partitioned into triangles to yield an approximation to the complete interatomic surface. The points of intersection of each integration ray with the atomic surface are then determined by calculating which of the surface triangles it intersects and assigning the centers of the corresponding triangles as the points of intersection.

While much more reliable than OMEGA, PROAIM is also beset with a few difficulties. First, in order to proceed a complete knowledge of the critical points which lie in the atomic surface is required. For complex systems without symmetry, this can be a non-trivial task. Second, just as OMEGA suffers from the problem of nonuniform sampling of the atomic basin by the basin $\nabla\rho(\mathbf{r})$ trajectories, a difficulty with PROAIM is the nonuniform sampling of the interatomic surfaces by the finite number of $\nabla\rho(\mathbf{r})$ trajectories used to approximate them. This latter problem is part of the more general problem with PROAIM that the surface determination algorithm is a non-local one: ie., how well a particular region of an interatomic surface is approximated depends on the chosen starting points for the $\nabla\rho$ trajectories from the corresponding (3,-1) critical points as well as the (sometimes pathological) behavior of the

$\nabla\rho(\mathbf{r})$ surface trajectories leading to the given region. In many cases, the non-local calculation of the interatomic surfaces in PROAIM results in very large areas between adjacent $\nabla\rho$ trajectories and therefore large errors in the intersection points of the integration rays with the atomic surface. This is seen, for example, in Fig. 4-5 where the atomic surface of a boron atom in $B_6H_6^{2-}$, as approximated using the method of PROAIM, is shown.

4-3-3 Description of PROMEGA

A new method for calculating atomic properties has been developed, one which incorporates the positive aspects of both OMEGA and PROAIM while avoiding the negative aspects. Because of this, the program employing this algorithm is called PROMEGA. As stated above, the main problem with PROAIM is the method by which the atomic surface is approximated prior to the determination of the points of intersection of the uniformly distributed integration rays with the surface and the subsequent numerical integration. PROMEGA also uses uniformly distributed integration rays, but the method used to calculate the corresponding intersections is, like OMEGA, based on the definition of an atom in a molecule as the union of the corresponding nuclear attractor of the $\nabla\rho$ field and its associated basin. PROMEGA does not require an approximation of the *complete* atomic surface prior to the numerical integration, or a knowledge of the critical points of the charge density which lie in the atomic surface.

The finite points of intersection of a given integration ray with the atomic surface satisfy the *local* condition that the nuclear attractor of the $\nabla\rho(\mathbf{r})$ trajectories intersecting the ray changes, from the nucleus of the atom

to another nucleus or vice versa, as the ray passes through these intersections. At a point of intersection with the surface, the attractor of the $\nabla\rho(\mathbf{r})$ trajectory is not a nucleus but a "bond" critical point which lies in the atomic surface. This simple but important point is demonstrated in Fig. 4-6, which shows a set of $\nabla\rho(\mathbf{r})$ trajectories of the symmetry plane of the CH_3Li molecule. The essential feature of Fig. 4-6 is that all of the $\nabla\rho(\mathbf{r})$ trajectories terminate at one of the nuclei, except the pairs which lie in the interatomic surfaces and terminate at the corresponding (3,-1) bond critical points. Also shown in Fig. 4-6 are six integration rays for the carbon atom to illustrate the point that near the finite intersections of a given ray with the interatomic surface, the attractor of the $\nabla\rho(\mathbf{r})$ trajectories which intersect the ray changes from the carbon nucleus to a bond critical point and then to another nucleus, or vice versa. Thus, the intersections of a given ray with the interatomic surface can, in principle, be determined by calculating the attractors of the complete set of $\nabla\rho$ trajectories which intersect the ray and assigning the points on the ray whose attractor is a "bond" critical point as the points of intersection. If all points on the ray intersect $\nabla\rho$ trajectories which terminate at the nucleus of the integrated atom then the ray only intersects the atomic surface at infinity.

In general, an atomic integration ray may be classified as n^{th} order where n is the number of finite intersections of the ray with the atomic surface. In the carbon atom of CH_3Li, for example, there are three types of integration rays: 0^{th} order, where the first and only intersection with the interatomic surface is at infinity so that the attractor along the ray never changes, all $\nabla\rho(\mathbf{r})$ trajectories which intersect the ray terminating at the

carbon nucleus. The rays labeled 2 and 3 in Fig 4-6 are of this type. In this case the ray would be integrated from the nucleus to infinity; 1^{st} order, where the first and only intersection is finite indicating that the nuclear attractor changes only once along the ray, from the carbon nucleus to the another nucleus as the ray passes through the point of intersection with the carbon atomic surface. The rays labeled 1 and 5 in Fig. 4-6 are of this type. In this case the ray is only integrated from the nucleus to this first intersection; 2^{nd} order, where the ray intersects the atomic surface three times, the first and second intersections being finite and the third at infinity. For a 2^{nd} order integration ray, the attractor changes from the carbon nucleus to another nucleus as the ray passes through the first intersection with the carbon surface, changes back to the carbon nucleus as it passes through the second intersection and then the remains outside the carbon atom all the way to infinity. The rays labeled 4 and 6 in Fig. 4-6 are of this type. In this case the ray is integrated in two parts, from the nucleus to the first intersection and from the second intersection to infinity. Third order integration rays, which are not present in CH_3Li, differ from second order rays only in that the third intersection is finite. Integration rays of fourth order and higher are rarely observed. Indeed most atoms will possess only 0^{th} and 1^{st} order integration rays. The lithium and hydrogen atoms in CH_3Li, for example, are of this type.

In practice, of course, the complete set of trajectories which intersect an integration ray cannot be determined, in general. Thus, it is not possible to determine the points of intersection of the integration rays with the atomic surface exactly by searching for those points along the ray whose

attractor is a bond critical point. The points of intersection may be approximated to any level of accuracy, however, by searching for very small segments along the ray in which the attractor changes from the nucleus of the integrated atom to another nucleus, or vice versa. The acccuracy with which the true intersection is approximated using this procedure is proportional the length of the segment. This method of approximating the atomic surfaces is the basis for the PROMEGA program. The success of this approach is seen explicitly in Fig. 4-7 where the surface of the same boron atom in $B_6H_6^{2-}$ is again shown (see Fig. 4-5), but now with no large gaps.

Thus, PROMEGA retains PROAIM's advantage of using a uniform distribution of integration rays, but the determination of the integration boundaries for these rays is, like OMEGA, based on the fact that each point within an atomic basin lies on a $\nabla\rho$ trajectory which terminates at the nucleus of the atom (see Fig. 4-2).

The implementation of the algorithm of PROMEGA is straightforward. The objective is essentially to efficiently determine those segments of the integration rays which intersect $\nabla\rho$ trajectories terminating at the nucleus of the atom. A $\nabla\rho(\mathbf{r})$ trajectory satisfies a differential equation of the form

$$d\mathbf{r}(s)/ds = \nabla\rho(\mathbf{r}(s))/|\nabla\rho(\mathbf{r}(s))| \qquad (13)$$

where s is the path length along the trajectory from a given starting point. In PROMEGA, the $\nabla\rho(\mathbf{r})$ trajectories are calculated starting from points along the integration rays to their termination points (the nuclear attractors) by solving equation (4-13) numerically.

The procedure for calculating the first intersection of a given integration ray of atom Ω with its atomic surface is essentially as follows.

(i) Starting at a user specified distance *beta* along the ray, calculate the $\nabla\rho(\mathbf{r})$ trajectory from the corresponding point to its termination point, a nuclear attractor.

(ii) If the nuclear attractor from (i) is that of atom Ω, step outward a user specified distance FSTP along the ray. If the nuclear attractor from (i) is that of another atom step backward a distance FSTP along the ray.

(iii) Calculate the $\nabla\rho(\mathbf{r})$ trajectory from the new point along the ray to its nuclear attractor.

(iv) If the nuclear attractor from (iii) is that of atom Ω step forward a distance FSTP if the nuclear attractor from (i) was also that of atom Ω, but step forward a distance FSTP/2 if the nuclear attractor from (ii) was that of another atom. If the nuclear attractor from (iii) is that of another atom then step backward a distance FSTP along the ray if the nuclear attractor from (i) was also that of another atom, but step backwards a distance FSTP/2 if the nuclear attractor from (i) was that of atom Ω.

(v) Repeat step (iii) and move forward or backward along the ray according to the criteria in step (iv) except that once a point is reached at which the attractor differs from the initial point in (i) then the step size along the ray from that point and all subsequent points is half of the previous point.

Step (v) is repeated until the step size along the ray is less than a user specified value THRESH, signifying the current point is within this distance along the ray from the true first intersection with surface. If the distance along the ray reaches a user specified distance TINF without changing attractors, then the ray intersects the atomic surface at infinity only and the search is terminated.

PROMEGA is also structured to search for the less common second and third intersections of the integration rays with the atomic surface. The procedure for searching for these intersections is similar to the search for the first intersection except that the starting point for the second intersection search is the first intersection while the starting point for the third intersection search is the second intersection. Only those rays with a finite first intersection need be searched for second and third intersections. To avoid stepping over intersections completely when second and third intersections are present, it is necessary that the initial step size along the rays be much smaller than if only first intersections are present. For this reason, the search for second and third intersections in addition to first intersections is more time consuming. Fortunately, most atoms will not contain a significant number of integration rays with second and third intersections and their search can usually be avoided without sacrificing the accuracy of the results.

Once all of the integration ray intersections with the atomic surface are found, the atomic properties are calculated by numerically integrating the corresponding property densities along the segments of the rays which lie in the atomic basin, just as in PROAIMV.

The process of seaching for the integration ray intersections in the above manner is time consuming because for each sampled point along a given ray the $\nabla\rho(\mathbf{r})$ trajectory which intersects the point must be numerically calculated to its nuclear attractor. To speed up this process without affecting the accuracy of the results, PROMEGA employs several strategies. Firstly, the search for the intersections is "vectorized" in the sense that

the searching process is carried out for a large number of rays simultaneously rather than one ray at a time. This approach allows the simultaneous evaluation of $\nabla\rho(\mathbf{r})$ at a large number of points using a procedure similar to that of the numerical integration in PROAIMV. Secondly, a $\nabla\rho(\mathbf{r})$ trajectory need not be calculated all the way to its nuclear attractor but rather only to the surface of a sphere centered on the attractor and known to be contained within the corresponding atom, a sphere which acts to capture the trajectory for the attractor. Thus, as input, PROMEGA requires a "capture sphere" size for each of the atoms in the molecule. The size of an atom's capture sphere is restricted only in that it be contained within the atom, but the larger the better. Thirdly, PROMEGA employs an Adams-Bashforth-Moulton predictor corrector method of order 6 for numerically solving equation (13) for the $\nabla\rho(\mathbf{r})$ trajectories. This method allows relatively large step sizes (0.05 au) to be taken in the accurate solution of eqn. (13) in comparison with a simple single-step Euler method. Fourthly, the starting point along the rays to begin the search is an important consideration. Thus, PROMEGA first determines the first intersections of a small, uniformly distributed, subset of integration rays and uses these intersections to provide good starting points in the search for the remaining integration rays' intersections.

Using only the four strategies mentioned above, PROMEGA would still be too time-consuming for wavefunctions with many natural orbitals and primitives due to the large number of evaluations of $\nabla\rho(\mathbf{r})$ required. To avoid prohibitive computation times for large wavefunctions, it is necessary to take advantage of the fact that most of the primitives used in the expansion of a large wavefunction make negligible contributions to the charge density in any

given region. PROMEGA thus employs a "dynamic" primitive cutoff algorithm in calculating the $\nabla\rho(\mathbf{r})$ trajectories. The approach used is similar to that described by Cioslowski,[5] except that the cutoff criterion for a primitive must be met for a batch of points being evaluated rather than a single point. With the implementation of this procedure, the calculation of the $\nabla\rho(\mathbf{r})$ trajectories becomes much more efficient, without loss of accuracy, and the computation times for large molecular wavefunctions do not become prohibitive.

4-3-4 PROMEGA Results

Table 4-3 shows some integration results for the symmetrically unique atoms of a set of molecules of varying complexity. Results calculated using both PROMEGA and PROAIM are given in this table, along with the analytically calculated molecular values, to demonstrate that the integration results of PROMEGA are, in nearly all cases, equal to or better than those of PROAIM. The numerical integration quadrature used in each case was identical for both programs so that the results reflect the accuracy with which the surface of the atomic basin is approximated. For the last four systems, SiF_4-NH_3, CH_4-NO_2^+, K^+-18-crown-6 ether and tetra-glycine helix, PROAIM fails to yield accurate results for at least of one of the corresponding atoms whereas PROMEGA yields results of quantitative accuracy in all cases. The potassium crown ether and tetraglycine calculations illustrate that PROMEGA is not restricted to small systems. In particular, tetraglycine which possesses no useable symmetry required 27 separate integrations, the individual results for which are not shown to save space. In this particular molecule PROAIM failed to yield results of even qualitative accuracy for over half of the atoms. It

is likely that better accuracy still could be attained with PROMEGA for this complex system by employing higher-order numerical integration. PROMEGA has been used for a large number of other molecules as well and almost always yields results accurate to better than 10^{-3} atomic units for all calculated properties, regardless of the topological complexity of the charge density distribution.

4-4 References

1. R.F.W. Bader, *Atoms in Molecules - A Quantum Theory*, (Oxford University Press, Toronto, 1990).

2. F.W. Biegler-Konig, R.F.W. Bader, and T.H. Tang, *J. Comput. Chem.*, **13**, 317 (1982).

3. B. Carnahan, H.A. Luther and J.O. Wilkes, *Applied Numerical Methods*, (John Wiley and Sons, Inc., New York, 1969).

4. R. Glaser and B.L. Harris, *J. Mol. Struct. (THEOCHEM)*, **255**, 45 (1992)

5. J. Cioslowski, *Chem. Phys. Lett.*, **194**, 73 (1992)

6. *Gaussian 90*; M.J. Frisch, M. Head-Gordon, G.W. Trucks, J.B. Foresman, H.B. Schlegel, K. Raghavachari, M.A. Robb, J.S. Binkley, C. Gonzalez, D.J. Defrees, D.J. Fox, R.A. Whiteside, R. Seeger, C.F. Melius, J. Baker, R.L. Martin, L.R. Kahn, J.J.P. Stewart, S. Topiol and J. A. Pople (Gaussian Inc, Pittsburgh, 1990)

7. F.W. Biegler Konig, T.T. Nguyen-Dang, Y. Tal, R.F.W. Bader, and A.J. Duke, *J. Phys. B: At. Mol. Phys.*, **14**, 2739 (1981)

8. K.E. Laidig, McMaster University (1989)

Figure 4-1

Atomic surface of carbon atom in methane in terms of its four C-H interatomic surfaces, each of which is defined in terms of the trajectories of the gradient vector field of the charge density which terminate at the corresponding (3,-1) bond critical point. View is along a C_3 axis. The surface is shown out to the intersection with the 10^{-4} au isosurface of the charge density.

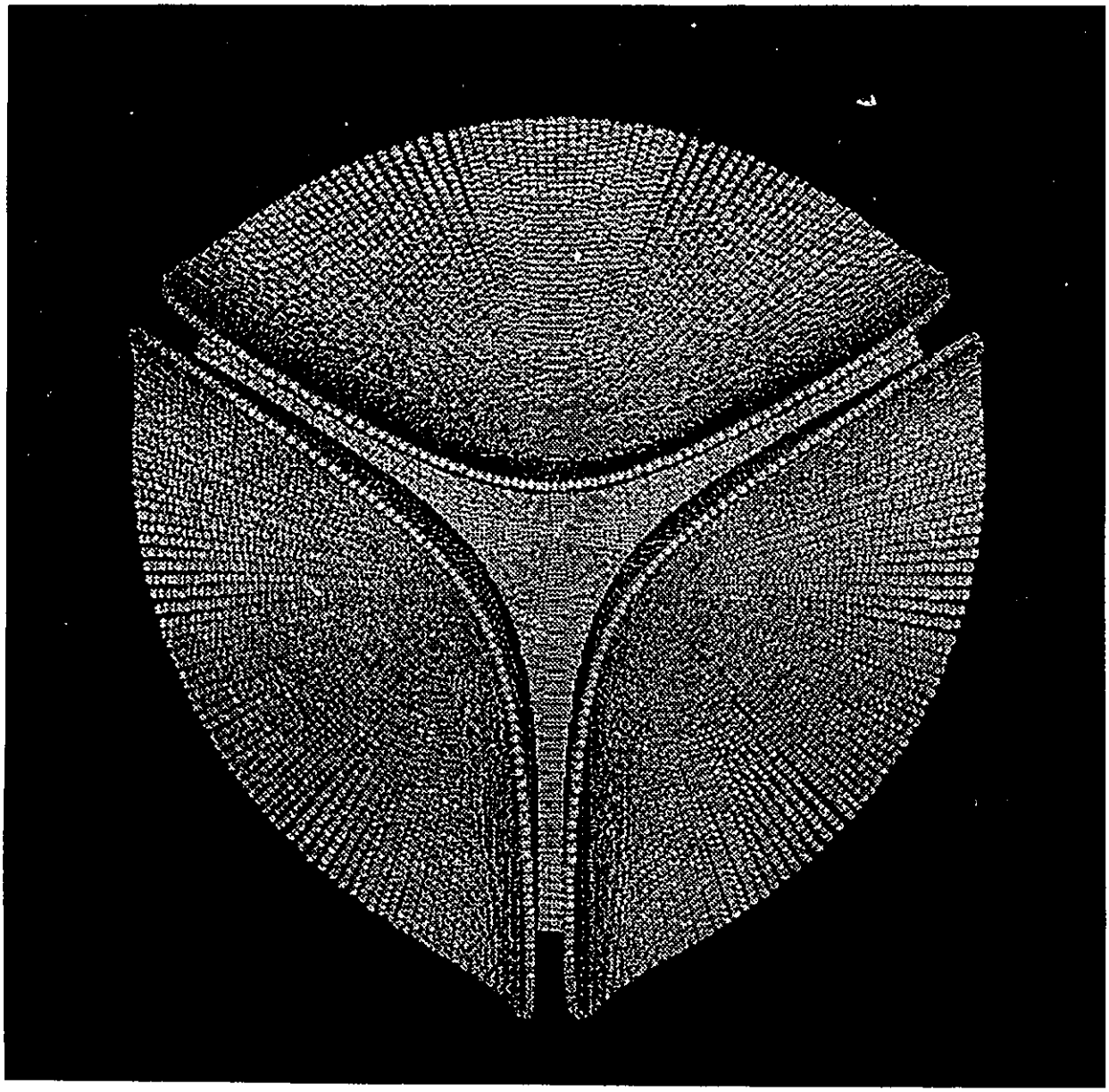

Figure 4-2

Atomic basin of carbon atom in methane defined in terms of trajectories of the gradient vector field of the charge density which terminate at the carbon nucleus. Trajectories are shown out to their intersection with the 10^{-5} au isosurface of the charge density. View is along a C_3 axis.

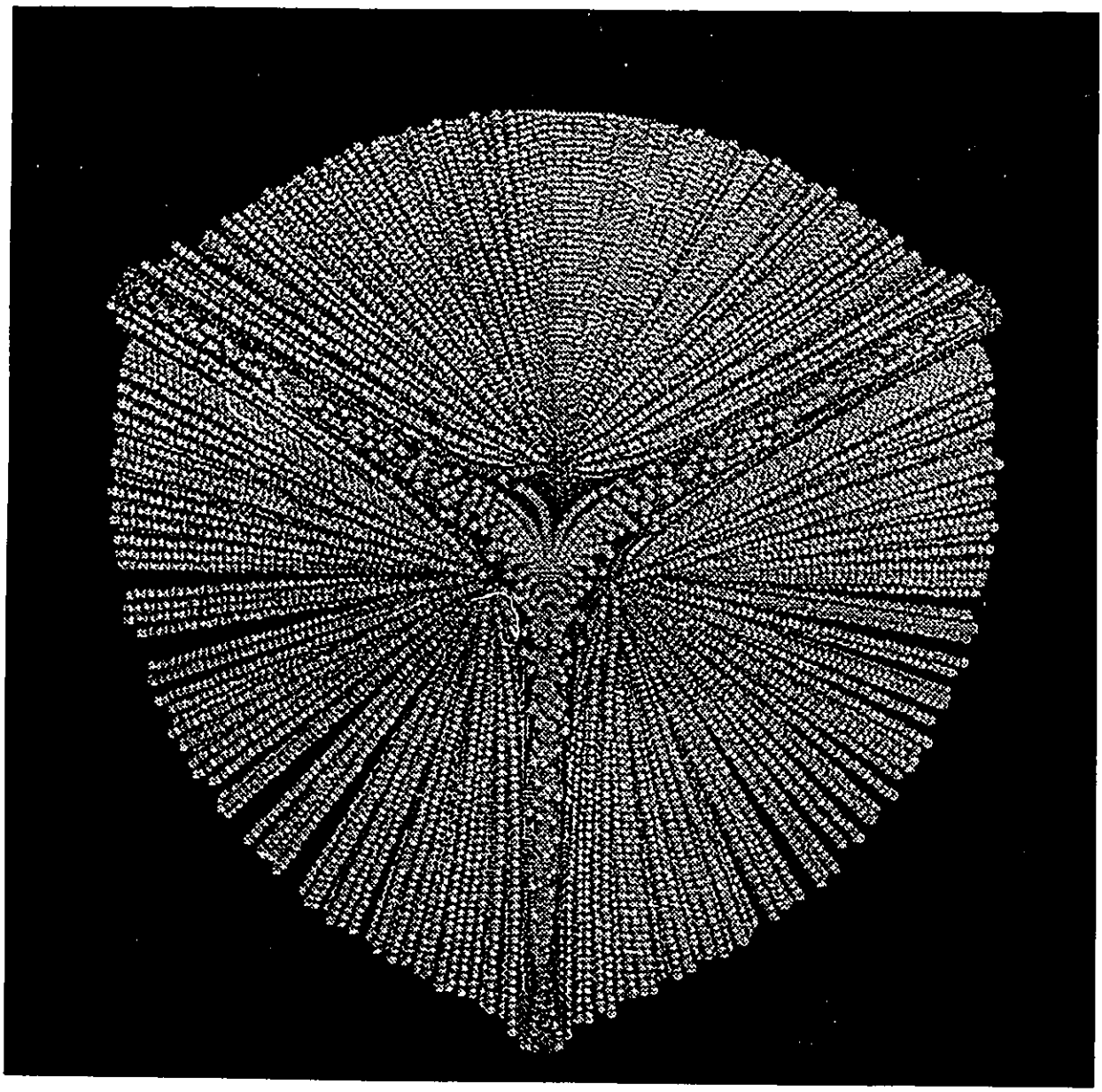

Figure 4-3

Loop Structure Used in PROAIM for the evaluation of the primitive functions and their contraction into the molecular orbitals.

```
      DO 50 i=1,NMO
      ψ_i = ZERO
      dψ_i/dx = ZERO
      dψ_i/dy = ZERO
      dψ_i/dz = ZERO
      ∇²ψ_i = ZERO
50    CONTINUE
      DO 100 j=1,NPRIMS
      φ_j = expression
      dφ_j/dx = expression
      dφ_j/dy = expression
      dφ_j/dz = expression
      ∇²φ_j = expression
      DO 200 i=1,NMO
      ψ_i = ψ_i + C_ij φ_j
      dψ_i/dx = dψ_i/dx + C_ij (dφ_j/dx)
      dψ_i/dy = dψ_i/dy + C_ij (dφ_j/dy)
      dψ_i/dz = dψ_i/dz + C_ij (dφ_j/dz)
      ∇²ψ_i = ∇²ψ_i + C_ij ∇²φ_j
200   CONTINUE
100   CONTINUE
```

Figure 4-4

Loop structure used in PROAIMV for the evaluation of the primitive functions and their contraction inot the molecular orbitals.

```
      DO 100 j=1,NPRIMS
      DO 150 k=1,NPTS
      φ_kj = expression
      dφ_kj/dx = expression
      dφ_kj/dy = expression
      dφ_kj/dz = expression
      ∇²φ_kj = expression
150   CONTINUE
100   CONTINUE
      DO 200 i=1,NMO
      DO 250 j=1,NPRIMS
      IF(C_ij.NE.ZERO) THEN
      DO 300 k=1,NPTS
      ψ_ki = ψ_ki + C_ij φ_j
      dψ_ki/dx = dψ_ki/dx + C_ij (dφ_kj/dx)
      dψ_ki/dy = dψ_ki/dy + C_ij (dφ_kj/dy)
      dψ_ki/dz = dψ_ki/dz + C_ij (dφ_kj/dz)
      ∇²ψ_ki = ∇²ψ_ki + C_ij ∇²φ_kj
300   CONTINUE
      ENDIF
250   CONTINUE
200   CONTINUE
```

Figure 4-5

Four B-B interatomic surfaces of a boron atom in $B_6H_6^{2-}$ as calculated by PROAIM. The large gaps result in inaccurate intersection coordinates for the Boron integration rays and poor integration results for the Boron properties.

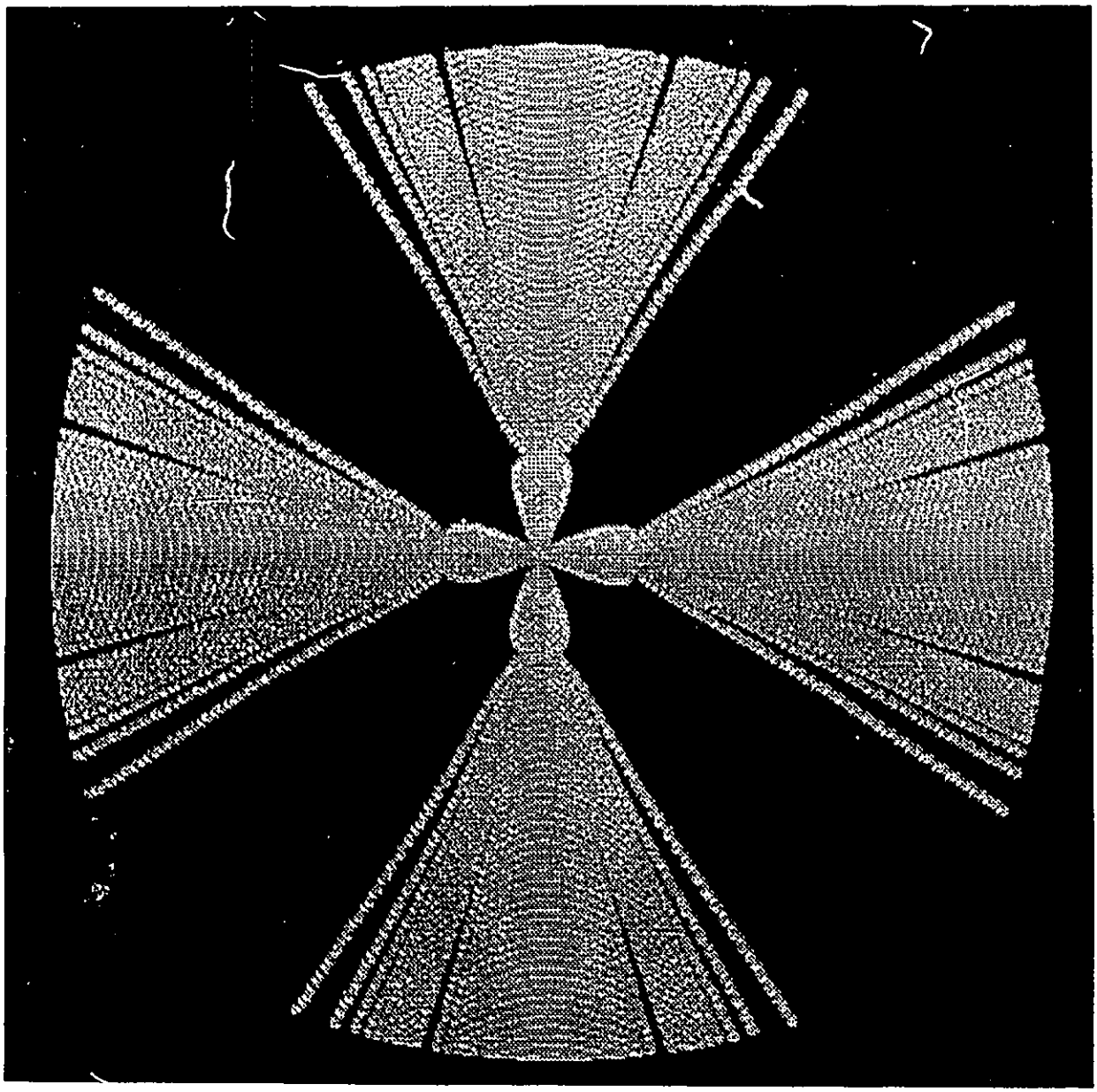

Figure 4-6

Display of the gradient vector field of the charge density in the symmetry plane of CH_3Li. Bond critical points are labeled by dots. Also shown are some integration rays, labeled 1 through 6, for the carbon atom. The intersections of the integration rays with the surface are labeled by closed squares. Rays 2 and 3 intersect the carbon surface only at infinity. Ray 5 intersects the C-Li interatomic surface once while ray 4 intersects the same surface twice. Ray 1 intersects the C-H interatomic surface once while ray 6 intersects it twice.

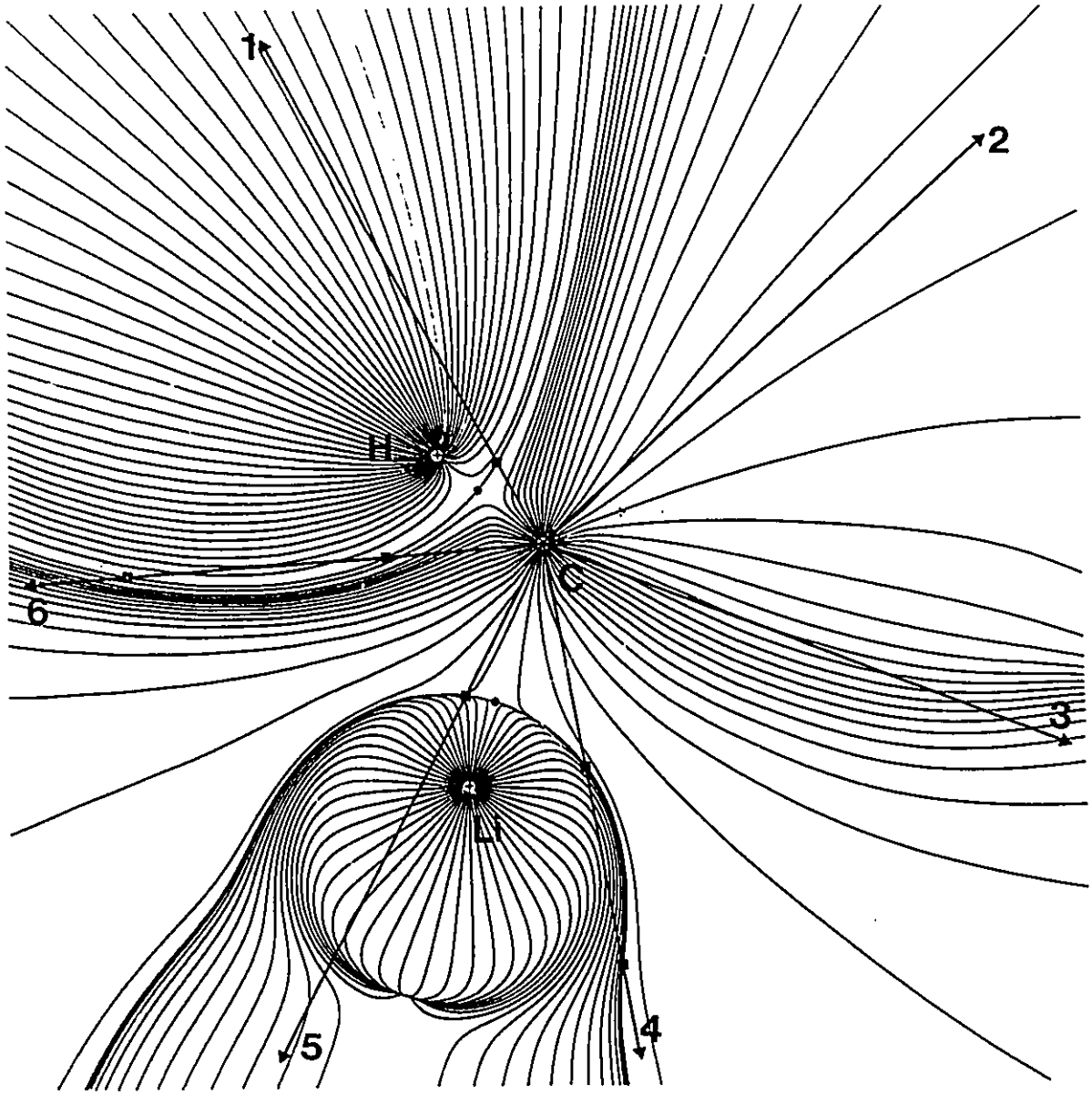
1
2
H
C
6
3
Li
5
4

Figure 4-7

Intersections of Boron atom integration rays with the four B-B interatomic surfaces in a Boron atom of $B_6H_6^{2-}$ as calculated using PROMEGA.

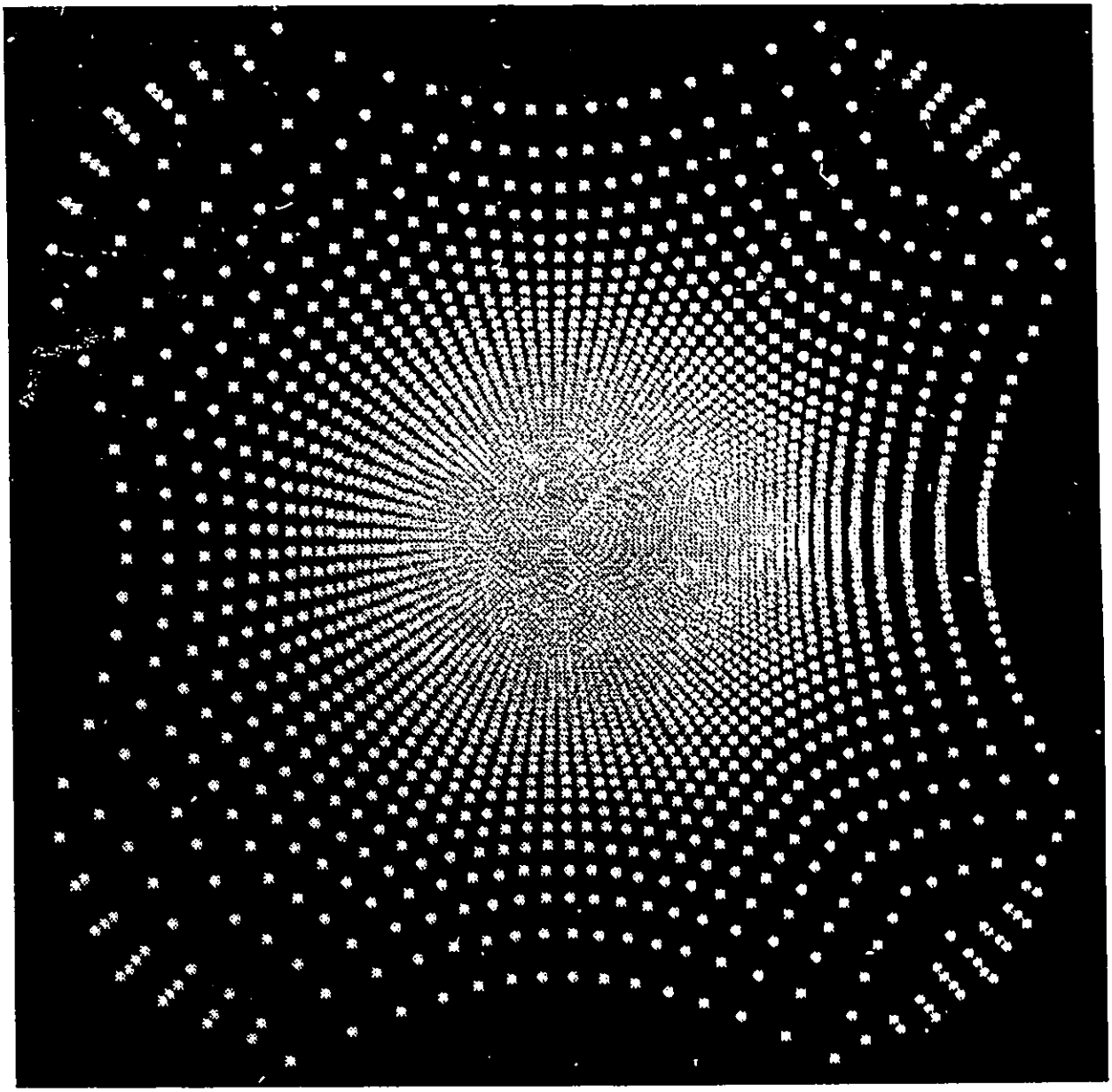

Table 4-1

CPU Times for Atomic Property Calculations in 18,6 Crown Ether on an IBM RS6000 Model 350.

Atom	PROAIMV(cutoffs)	PROAIMV(no cutoffs)	PROAIM(Original)
Carbon	40.7 minutes	88.2 minutes	> 1000 minutes
Oxygen	45.7 minutes	93.9 minutes	> 1000 minutes
Hydrogen a	17.4 minutes	43.8 minutes	> 1000 minutes
Hydrogen b	19.6 minutes	42.1 minutes	1028.8 minutes

Table 4-2

Some Atomic Properties of 18,6 Crown Ether Calculated Using PROAIMV.

Atom(Ω)	L(Ω)	Net Charge	Energy
Carbon	0.001 au	0.806	-37.349 au
Oxygen	0.001 au	-1.309	-75.529 au
Hydrogen a	0.0001 au	-0.093	-0.679 au
Hydrogen b	0.0001 au	-0.059	-0.667 au

Sum of atomic charges = -0.001

Sum of atomic energies = -917.511 au

Molecular SCF energy = -917.511 au

Table 4-3[1]

Calculated Atomic Properties of Some Molecules using PROMEGA and PROAIM

	--------PROMEGA---------			---------PROAIMV--------			
Mol_Atom(Ω)	q(Ω)	E(Ω)	L(Ω)	q(Ω)	E(Ω)	L(Ω)	E(SCF)
LiH_Li	+0.91159	-7.36622	-7.4E-6	+0.91171	-7.36621	+7.3E-5	
LiH_H	-0.91093	-0.61998	1.7E-4	-0.91634	-0.61982	-3.0E-5	
LiH	+0.00066	-7.98620		-0.00463	-7.98603		-7.98616
CH_4_C	+0.17480	-37.66023	+1.3E-4	+0.17462	-37.66007	-2.3E-4	
CH_4_H	-0.04368	-0.63803	-7.1E-6	-0.04357	-0.63804	+8.4E-5	
CH_4	-0.00008	-40.21235		-0.00034	-40.21223		-40.21232
C_3H_6_C(ring)	0.06149	-37.74559	2.4E-4	0.06156	-37.74552	1.6E-4	
C_3H_6_H(ring)	-0.03067	-0.64312	-2.4E-5	-0.03064	-0.64317	7.7E-5	
C_3H_6(ring)	0.00045	-117.09549		0.00084	-117.09558		-117.09538
C_4H_4_C(cage)	-0.07167	-37.82241	8.0E-5	-0.07199	-37.82246	-1.3E-4	
C_4H_4_H(cage)	0.07189	-0.58793	-4.2E-5	0.07191	-0.58798	4.9E-5	
C_4H_4(cage)	0.00086	-153.64136		-0.00032	-153.64176		-153.64163
Propene_Ha	-0.03006	-0.63634	-8.2E-7				
Propene_Hb	-0.02382	-0.63482	-2.0E-5				
Propene_Hc	-0.03260	-0.64311	-2.0E-05				
Propene_Hd	-0.04345	-0.64508	7.6E-6				
Propene_He	-0.041597	-0.64236	8.2E-6				
Propene_C1	0.03627	-37.76054	3.5E-4				

Propene_C2	0.002104	-37.81664	-5.0E-5	
Propene_C3	0.17464	-37.69119	-4.9E-4	
Propene	-0.00011	-117.11244		-117.11242
CH_4-NO_2^+_C	-0.04724	-38.12339	5.5E-04	
CH_4-NO_2^+_H_a	0.31768	-0.46136	8.4E-06	
CH_4-NO_2^+_H_b	0.29532	-0.47571	-2.1E-05	
CH_4-NO_2^+_N	0.49174	-54.23082	4.2E-04	
CH_4-NO_2^+_Oa	-0.35586	-75.14514	-1.3E-06	
CH_4-NO_2^+_Ob	-0.31331	-75.12458	3.6E-04	
CH_4-NO_2^+	1.00133	-244.49807		-244.49771
SiF_4-NH_3_Si	3.42216	-287.54911	-4.9E-04	
SiF_4-NH_3_F_{eq}	-0.87774	-99.87040	-1.9E-04	
SiF_4-NH_3_F_{ax}	-0.87084	-99.86245	-1.6E-04	
SiF_4-NH_3_N	-1.12390	-54.92378	6.9E-04	
SiF_4-NH_3_H	0.40170	-0.46579	6.2E-05	
SiF_4-NH_3	-0.00070	-743.34391		-743.34371
Crown-K^+_K	0.95896	-599.61913	-2.6E-5	
Crown-K^+_C	0.76185	-37.36209	4.2E-4	
Crown-K^+_O	-1.32470	-75.46623	-1.5E-3	
Crown-K^+_H_a	-0.04777	-0.66160	1.1E-4	
Crown-K^+_H_b	-0.04830	-0.66162	1.1E-4	
Crown-K^+	+1.00012	-1516.64023		-1516.64064
Helix	-0.00756	-789.60894		-789.61012

[a]All results were calculated from single determinant SCF molecular

wavefunctions at the corresponding theoretical equilibrium molecular geometry. The basis set used for LiH was an uncontracted gaussian basis set consisting of 11s7p3d for lithium and 9s5p2d for hydrogen. The basis set for CH_4, C_3H_6, C_4H_4, Propene and SiF_4-NH_3 was the standard 6-311++g(2d,2p) set as incorporated into Gaussian 90,[b] the program with which all of the SCF calculations were performed. The basis set for the Crown-K^+ complex was the standard 6-31G** as incorporated into Gaussian 90. The basis set for the helix was 6-311++G** as incorporated into Gaussian 90.

$q(\Omega)$ is the net charge of atom Ω

$E(\Omega)$ is the total energy of atom Ω

$L(\Omega)$ is -(1/4) times the integral of the laplacian of the charge density over atom Ω, a quantity which is equal to zero for a perfect integration.

E(SCF) is the SCF total energy.

APPENDIX: THE THEORY OF ATOMS IN MOLECULES

Central to much of the original research presented in this thesis is the theory of atoms in molecules.[1-9] A complete development of this theory is given in the comprehensive book of reference 1. The theory of atoms in molecules has also been reviewed a number of times recently. For example, in review articles[2-5], or theses[6-9]. For the sake of completeness, however, those aspects of the theory which are directly relevant to the original work of this thesis are reviewed here.

An atom Ω in a molecule is defined to be a region of a molecule in real space $\mathbb{R}^3$ that is completely bounded by a surface $S(\Omega,\mathbf{r})$ which satisfies the following condition

$$\nabla\rho(\mathbf{r})\cdot\hat{\mathbf{n}}(\mathbf{r}) = 0 \quad \forall\mathbf{r} \in S(\Omega,\mathbf{r}) \tag{1}$$

where $\rho(\mathbf{r})$ is the electron density at the point $\mathbf{r}$ in $\mathbb{R}^3$ and where $\hat{\mathbf{n}}(\mathbf{r})$ is a unit vector normal to the surface $S(\Omega,\mathbf{r})$ at $\mathbf{r}$. In words, an atom in a molecule is defined as a region of a molecule that is bounded by a surface through which the flux of the gradient of the electron density $\nabla\rho(\mathbf{r})$ is zero at *every* point $\mathbf{r}$ on the surface.

The reasons for identifying a region of a molecule which satisfies eqn. (1) with the atom of empirical chemistry are many in number. First of all, *observations* of a large number of experimentally and theoretically determined electron density distributions show that the electron density almost always exhibits local maxima only at the nuclear positions in molecules. As a consequence, the nuclei in molecules are the only three-dimensional *attractors* of the trajectories of the $\nabla\rho(\mathbf{r})$ field and molecules are thus observed to be

completely and naturally partitioned by the $\nabla\rho(\mathbf{r})$ field into mononuclear regions which satisfy eqn. (1). A $\nabla\rho(\mathbf{r})$ trajectory is a path of steepest ascent in the electron density distribution. As an example, some representative trajectories of the $\nabla\rho(\mathbf{r})$ field in the nuclear plane of the ethene molecule are shown in Figure A-1a. In this figure one sees that with each nucleus is associated a connected region of the ethene molecule that is traversed by $\nabla\rho(\mathbf{r})$ trajectories which originate at infinity and terminate at nuclei, which are topologically equivalent to critical points of the $\nabla\rho(\mathbf{r})$ field. The nuclei are classified as (3,-3) critical points to indicate that the Hessian of the electron density at the points, $\nabla\nabla\rho$, possesses three negative eigenvalues, ie. the nuclei are local maxima in the $\rho(\mathbf{r})$ distribution. In three dimensions, the region traversed by the complete set of $\nabla\rho(\mathbf{r})$ trajectories which terminate at a given nucleus is the *basin* associated with the corresponding nuclear attractor.

Not shown in Fig. A-1a is the set of unique $\nabla\rho(\mathbf{r})$ trajectories in the plane which do not both originate at infinity and terminate at the nuclei, but rather either originate or terminate at certain points lying between certain pairs of nuclei. These unique trajectories are overlaid upon the map of Fig. A-1a and are shown in Fig. A-1b. The points at which these unique trajectories originate or terminate are also critical points of the $\nabla\rho(\mathbf{r})$ field and are labelled by black dots in Fig. A-1b. Unlike the nuclear critical points, however, the internuclear critical points are not local maxima of the electron density. Instead, they are *surface* critical points, each serving as the terminus for a surface of $\nabla\rho(\mathbf{r})$ trajectories which originate at infinity, with the electron density being a maximum in the

surface. These surfaces separate the basins of the nuclear attractors and show explicitly that the boundaries of the basins satisfy eqn. (1) identically. Each of the internuclear critical points also serves as the origin for a pair of $\nabla\rho(\mathbf{r})$ trajectories, each of which terminates at one of the two nuclei which the critical point lies between, with the electron density at the internuclear critical point being a minimum along the axis connecting the two corresponding nuclei. Such critical points are classified as (3,-1) to indicate that the Hessian of the electron density at such points posseses three nonzero eigenvalues, two of which are negative and whose eigenvectors are locally tangent to the surface of $\nabla\rho(\mathbf{r})$ trajectories terminating at the point, and one of which is positive and whose associated eigenvector is locally parallel to the pair of trajectories originating at the point. It is to be noted that there is an internuclear critical point only between those nuclei which are considered, chemically, to be bonded to one another and thus the internuclear critical points are called *bond critical points*. In Fig. A-1c the $\nabla\rho(\mathbf{r})$ trajectories originating and terminating at the bond critical points in the nuclear plane of the ethene molecule are shown overlaid upon a contour map of the electron density, a map which also shows that the electron density is a local maximum at the nuclear positions. From this figure one sees that the primary chemical concepts of atoms and bonds are defined by the gradient vector field of the electron density. An atom in a molecule is the union of a three-dimensional attractor of the $\nabla\rho(\mathbf{r})$ field together with its associated basin and is bounded by interatomic surfaces which are defined by the trajectories of $\nabla\rho(\mathbf{r})$ which terminate at the bond critical points connecting the atom to its neighbors. The union of the pair

of trajectories originating at a given bond critical point defines a *bond path* explicitly linking the corresponding atoms. The set of all bond paths in a given molecule defines the *molecular graph*. Thus, in the ethene molecule, for example, each carbon atom possesses three bond critical points and therefore three interatomic surfaces, one each separating it from the two bonded hydrogens and one separating it from the other CH_2 group. The results observed in ethene are a general property of matter having now been observed in literally thousands of theoretically and experimentally determined electron distributions.

Having observed that molecules are naturally partitioned into atomic-like pieces in terms of an observable property of the molecule, the electron density distribution, the second reason for identifying these regions with the chemical atom lies in the generalization of quantum mechanics from a total molecular system to a subsystem, ie. a generalization which defines subsystem properties and equations of motion in complete analogy with the total system. Such a generalization of molecular quantum mechanics is possible *only* for a subsystem which satisfies eqn. (1), and thus it is an observation that molecules (indeed all forms of electronic matter) are observed to be naturally partitioned into *quantum subsystems*.

The most important basis for identifying the topologically observed quantum subsystems with the atoms of chemistry lies in a consideration of their properties. It was shown in Chapter 4 how the properties of an atom in a molecule are calculated. For a single-particle observable $\hat{A}$ and a molecule in the state ψ one defines a property density in real space $A(\mathbf{r})$ whose integral over the real space of the whole molecule yields the expectation

value of the observable for the molecule. Since quantum subsystems are defined in real space, the expectation value of the observable for an atom Ω in a molecule $A(\Omega)$ is obtained by the integration of $A(\mathbf{r})$ over the basin of the atom, as in eqn. (2)

$$A(\Omega) = (N/2)\int_{\Omega} d\mathbf{r} \int d\tau' \, [\psi^* \hat{A}\psi + (\hat{A}\psi)^* \psi] \qquad (2)$$

where N is the number of electrons and $d\tau'$ denotes integration over the spin coordinates of all electrons (the observable is assumed here to be independent of spin) and the spatial coordinates of all electrons but one. Since molecules are disjointly and completely partitioned into atoms the important property that the atomic values be additive to yield the molecular value A(MOL) is satisfied, as in eqn. (3)

$$A(\mathrm{MOL}) = \sum_{\Omega} A(\Omega) \qquad (3)$$

Properties such as the total energy, volume, net charge, dipole polarization and polarizability have been calculated for atoms and groups of atoms in many molecules in order to better understand molecular properties. An essential observation is that all atomic properties are transferable between different molecular systems in a manner which is consistent with the empirical chemical atom and this is, ultimately, the basis for their identification with atoms in molecules.

References

1. R.F.W. Bader, *Atoms in Molecules - A Quantum Theory*, (Oxford University Press, Oxford, 1990).

2. R.F.W. Bader, *Chem. Rev.*, **91**, 893 (1991).

3. R.F.W. Bader, *Accts. Chem. Res.*, **18**, 9 (1985).

4. R.F.W. Bader and T.T. Nguyen-Dang, *Adv. Quant. Chem.*, **14**, 63 (1981).

5. R.F.W. Bader, T.T. Nguyen-Dang and Y. Tal, *Rep. Prog. Phys.*, **44**, 893 (1981).

6. J.R. Cheeseman, Ph.D. Thesis (1992).

7. C. Cheng, Ph.D. Thesis (1990).

8. M. Carroll, Ph.D. Thesis (1989).

9. P.J. MacDougall, Ph.D. Thesis (1989).

Figure A-1

Maps of the gradient vector field of the electron density in the plane containing the nuclei in the ethene molecule. Each line is a trajectory of $\nabla\rho$. In a) only those trajectories which terminate at the positions of the nuclei and originate at infinity are shown. Each trajectory is arbitrarily terminated at the surface of a small circle about a nucleus. The set of trajectories which terminate at a given nucleus define the basin of the nuclear attractor. b) is the same as a) but also includes those trajectories which originate and terminate at the (3,-1) bond critical points of the electron distribution. The position of a (3,-1) bond critical point is denoted by a black dot. The pairs of trajectories which, in this plane, terminate at the (3,-1) bond critical points mark the intersection of the interatomic surfaces with the plane shown. The $\nabla\rho$ trajectories which originate at the (3,-1) critical points and terminate nuclei are denoted by heavier lines. In c) the $\nabla\rho$ trajectories associated with the (3,-1) critical points are superimposed on a contour map of the electron density in the same plane as a) and b). These trajectories define the boundaries of the atom and the molecular graph.

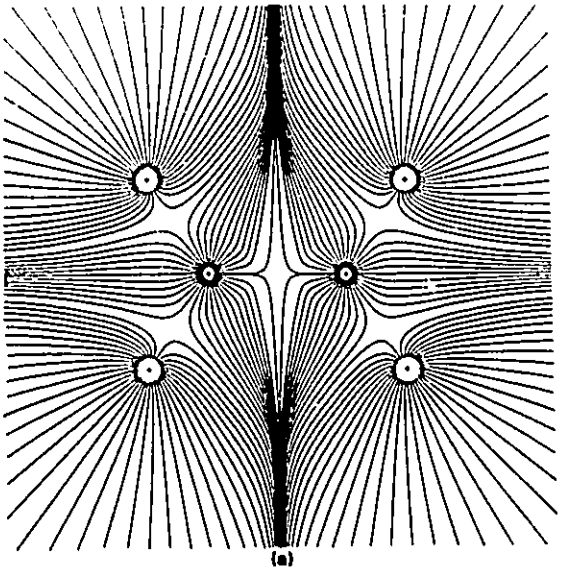

(a)

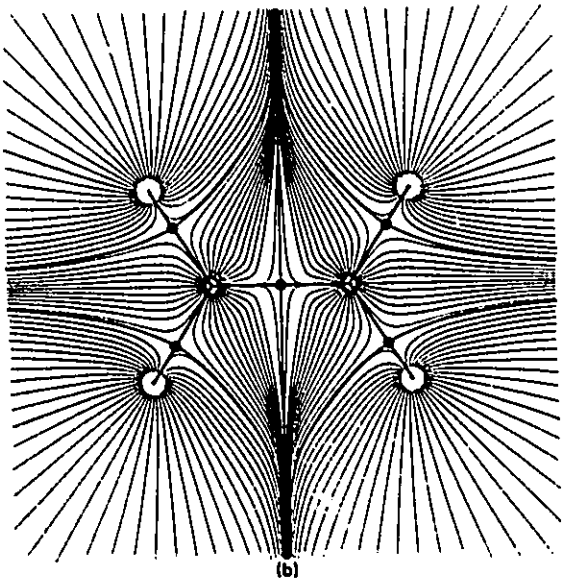

(b)